



# Design study of a Laser Plasma Wakefield Accelerator with an externally injected 10-MeV electron beam coming from a photoinjector

Ke Wang

## ► To cite this version:

Ke Wang. Design study of a Laser Plasma Wakefield Accelerator with an externally injected 10-MeV electron beam coming from a photoinjector. Accelerator Physics [physics.acc-ph]. Université Paris-Saclay, 2019. English. NNT : 2019SACLS179 . tel-02285456

**HAL Id: tel-02285456**

**<https://theses.hal.science/tel-02285456>**

Submitted on 12 Sep 2019

**HAL** is a multi-disciplinary open access archive for the deposit and dissemination of scientific research documents, whether they are published or not. The documents may come from teaching and research institutions in France or abroad, or from public or private research centers.

L'archive ouverte pluridisciplinaire **HAL**, est destinée au dépôt et à la diffusion de documents scientifiques de niveau recherche, publiés ou non, émanant des établissements d'enseignement et de recherche français ou étrangers, des laboratoires publics ou privés.

# Design study of a Laser Plasma Wakefield Accelerator with an externally injected 10-MeV electron beam coming from a photoinjector

Thèse de doctorat de l'Université Paris-Saclay  
préparée à l'Université Paris-Sud

Ecole doctorale n°576 Particules, Hadrons, Énergie, Noyau, Instrumentation, Imagerie,  
Cosmos et Simulation (PHENIICS)  
Spécialité de doctorat : physique des accélérateurs

Thèse présentée et soutenue à Orsay, le 2 Juillet 2019, par

**KE WANG**

Composition du Jury :

Fabien CAVALIER Directeur de Recherche - Université Paris-Sud (LAL)	Président
Mme. Cristina VACCAREZZA Directrice de Recherche - Istituto Nazionale di Fisica Nucleare	Rapporteur
M. Philippe BALCOU Directeur de Recherche - Université de Bordeaux (CELIA)	Rapporteur
M. Phu Anh Phi NGHIEM Directeur de Recherche - CEA/DRF/IRFU/DACM	Examineur
M. Arnd SPECKA Directeur de Recherche - Laboratoire Leprince-Ringuet	Examineur
M. Nicolas DELERUE Chargé de recherche - Université Paris-Sud (LAL)	Directeur de thèse

# Résumé

**Titre:** Étude d'un accélérateur à champ de sillage laser-plasma avec un faisceau d'électrons de 10 MeV injectés depuis un photoinjecteur

**Mots clés:** Accélérateur laser-plasma, compression de paquet d'électrons, transport de faisceau d'électrons, simulations du début à la fin, capillaire diélectrique creux.

Le champ électrique généré dans le plasma en raison de la modulation de la densité des électrons du plasma peut atteindre l'ordre de 100 GV/m, soit trois ordres de plus que celui des structures RF classiques, ce qui permet de générer rapidement des faisceaux d'électrons de haute énergie intervalle. Le gain en énergie en une étape a récemment été porté à 8 GeV, tandis que la qualité et la stabilité du faisceau d'électrons ne sont toujours pas comparables à celles obtenues avec les accélérateurs classiques. Une des manières possibles d'améliorer la qualité et la stabilité du faisceau au niveau des accélérateurs RF consiste à combiner un injecteur RF classique avec une structure d'accélération laser-plasma, c'est-à-dire générer une source d'électrons accordable, de haute qualité et stable basée sur un injecteur RF et l'injecter dans le plasma pour obtenir une accélération efficace, la qualité du faisceau peut être maintenue en faisant correspondre le groupe d'électrons externe au sillage dans le plasma. Dans cette thèse, l'accélération d'une série d'électrons de 10 MeV provenant d'un photoinjecteur RF dans un champ électrique à fort gradient excité dans un plasma par un laser de forte puissance est étudiée. La configuration d'une telle expérience est étudiée et des simulations de bout en bout sont présentées. La mise en correspondance du groupe d'électrons avec le champ de sillage du plasma est l'une des difficultés du schéma d'injection externe. Avant d'être injecté dans l'onde de plasma, le paquet d'électrons doit être compressé pour être beaucoup plus court (généralement plusieurs femtosecondes ou sous la femtoseconde) que la longueur d'onde du plasma afin de minimiser la dispersion en énergie, la taille du paquet radial doit être beaucoup plus petite (typiquement la taille du point laser pour obtenir une force de focalisation constante dans la direction radiale est un défi pour le groupe d'électrons dominé par la charge d'espace (10 MeV, 10 pC). Nous commençons l'interaction plusieurs longueurs de Rayleigh avant le plan focal laser pour obtenir une taille de point laser plus grande, la condition d'adaptation pour la taille transversale est assouplie à plusieurs centaines de micromètres et un groupage de vitesse est également effectué entre le plan

de départ et le plan focal du laser, la condition d'appariement pour la durée du paquet longitudinal est assouplie à plusieurs centaines de femtosecondes (inférieure à la moitié de la longueur d'onde du plasma). Dans le sens longitudinal, le groupe d'électrons externe 10MeV est comprimé en deux étapes. La première étape est réalisée à l'aide d'une chicane dogleg composée de deux dipôles, de quatre quadripôles et de deux sextupoles; les quadripôles servent à ajuster la fonction bêta dans la chicane et à faire correspondre les termes de dispersion de premier ordre R16 et R26 à zéro, les sextupôles servant à faire correspondre T566 terme avec la courbure RF et d'accorder les termes de dispersion de second ordre T166, T266. La chicane est conçue avec MADX, IMPACT-T et CSRTRACK sont utilisés pour réaliser des études de simulation sur la dynamique du faisceau avec effet de charge d'espace (SC) et rayonnement synchrotron cohérent (CSR) inclus. Nos résultats montrent que l'écart d'énergie induit par le CSR est inférieur à 0.009% et a donc moins d'effet sur le paquet d'électrons. En conséquence, le groupe d'électrons est comprimé à 69 fs à la sortie de la chicane. La deuxième étape est réalisée avec le groupage de vitesse dans le plasma, la phase d'injection ainsi que la distance entre le plan d'injection et le plan focal laser sont ajustées pour optimiser le processus de groupage de vitesse, un code PIC statique WAKE est utilisé pour étudier l'interaction. En conséquence, le groupe d'électrons est comprimé à 3 fs avant une accélération efficace et près de 80% des électrons injectés sont piégés et accélérés. Dans le sens transversal, le paquet d'électrons est focalisé avec un solénoïde avant d'être injecté dans le plasma. Une longue cellule est utilisée pour créer un plasma commençant plusieurs longueurs de Rayleigh avant le plan focal laser, relâchant les contraintes sur la taille du paquet transverse. La cellule s'étend sur plusieurs longueurs de Rayleigh après le plan focal du laser pour supprimer la divergence angulaire du paquet d'électrons. Nous démontrons que le paquet d'électrons à la sortie du plasma a une énergie de plus de 100 MeV, une émittance inférieure à  $1 \mu\text{m}$ , une charge supérieure à 7 pC et une dispersion d'énergie FWHM inférieure à 1.5%. Afin d'étendre la section d'accélération et d'augmenter le gain d'énergie, le guidage du faisceau laser avec un capillaire diélectrique creux est étudié. Pour un tel guidage, le profil transversal de l'intensité du laser à l'entrée du capillaire a une forte influence sur les fluctuations du champ de sillage du plasma transverse pendant la propagation du laser. Les effets de ces fluctuations sur l'accélération d'un paquet d'électrons sont analysés en détail. Nos résultats montrent que même dans les meilleures conditions d'appariement, le profil transversal gaussien habituellement utilisé conduit à de fortes fluctuations générées par la diffraction des arêtes du laser à l'entrée du capillaire. Nous démontrons qu'en réduisant cette diffraction grâce à l'utilisation d'un profil laser gaussien aplati, il est possible d'obtenir une accélération efficace du paquet d'électrons sur plusieurs longueurs de Rayleigh, c'est-à-dire que dans la configuration étudiée dans cette thèse, le paquet d'électrons est accéléré à 375 MeV dans un capillaire de 15 cm.



# Abstract

**Title:** Design study of a Laser Plasma Wakefield Accelerator with an externally injected 10 MeV electron beam coming from a photoinjector

**Keywords:** Laser Plasma Wakefield Accelerator, electron bunch compression, electron beam transport, start to end simulations, hollow dielectric capillary.

The acceleration of an externally injected 10 MeV electron bunch coming from a RF photoinjector in a high gradient electric field excited in a plasma by a high power laser is studied. In this thesis the configuration of such an experiment is studied and start to end simulations are presented. As an ultrashort electron bunch (several femtoseconds) is required to maintain a low energy spread beam in the plasma, the 10 MeV electron bunch coming from the photoinjector is compressed in two stages. The first stage is realized using a dogleg chicane which compresses the electron bunch to 69 fs, the second stage is realized with velocity bunching in the plasma that further compresses the electron bunch to 3 fs before efficient acceleration. The electron bunch is transversely focused with a solenoid before being injected into the plasma. A long cell is used to create a plasma starting several Rayleigh lengths before the laser focal plane, allowing the velocity bunching in the first part of the plasma and relaxing constraints on the transverse bunch size. The cell extends several Rayleigh lengths after the laser focal plane to suppress the angular divergence of the electron bunch. We demonstrate that the electron bunch at the exit of the plasma has an energy of more than one hundred MeV, with an emittance smaller than  $1\text{ }\mu\text{m}$ , a charge greater than 7 pC and a FWHM energy spread smaller than 1.5%. To extend the acceleration section, the guiding of the laser beam with a hollow dielectric capillary is studied, the results show that even in the best matching conditions, the usual laser Gaussian transverse profile is not optimum, mainly because of the diffraction of the laser on the edges at the entrance of the capillary, a flattened Gaussian laser profile is then suggested to suppress this diffraction and the electrons can be accelerated over more than ten Rayleigh lengths.

# Acknowledgements

I want to thank my doctoral advisor, Dr. Nicolas DELERUE for accepting me as his PhD student and guiding me to this interesting field of research. Thank for his helpful discussion and support in the lab, and also for the help in daily life i.e. CROUS, CAF and RDV with a doctor...

I would like to express my very great appreciation to Prof. Dr. Gilles MAYNARD at LPGP for the guidance and help in the simulation work and paper writing.

I would like to thank Dr. Viacheslav KUBYTSKYI for the useful discussion on LPWA and advice on my thesis, thank Dr. Antoine CHANCE and Dr. Christelle BRUNI for the discussion on beam optics, thank Dr. Hayg GULER for the support on the parallel calculation on the machine. I would like to give my sincere acknowledge to all my colleagues at LAL.

Finally, thank for the support of my family.

# Contents

<b>1</b>	<b>Introduction</b>	<b>1</b>
<b>2</b>	<b>Electron dynamics and Laser-Plasma Wakefield acceleration in the linear regime</b>	<b>6</b>
2.1	Electron dynamics . . . . .	6
2.1.1	Equation of motion . . . . .	6
2.1.2	Hill equation and Courant-Snyder (Twiss) parameters . . . . .	8
2.1.3	Beam optics . . . . .	10
2.1.4	Interaction between particles . . . . .	11
2.1.4.1	Space charge effect . . . . .	11
2.1.4.2	Coherent synchrotron Radiation . . . . .	14
2.1.5	Longitudinal compression of electron bunch . . . . .	18
2.1.5.1	Compression with velocity difference . . . . .	19
2.1.5.1.1	Ballistic Compression . . . . .	19
2.1.5.1.2	Velocity bunching . . . . .	21
2.1.5.2	Compression with trajectory difference . . . . .	22
2.2	Laser plasma wakefield acceleration . . . . .	23
2.2.1	Basic properties of the plasma and the laser beam . . . . .	24
2.2.1.1	Ionization of the gas . . . . .	24
2.2.1.2	Basic parameters of plasma . . . . .	27
2.2.1.3	Basic parameters of the laser . . . . .	28
2.2.2	Electrons move in a plane electromagnetic field . . . . .	30
2.2.3	Pondermotive force . . . . .	34
2.2.4	Establishment of the laser plasma wakefield . . . . .	35
2.2.5	The self-focusing of the laser beam . . . . .	37
2.2.6	Injection of the electrons . . . . .	39
2.2.7	Limitation of the energy gain . . . . .	41
<b>3</b>	<b>Electron bunch compression and matching before the plasma</b>	<b>43</b>
3.1	The PHIL Beam line . . . . .	44
3.2	Generating an energy chirp in a standing wave cavity . . . . .	46
3.3	Beam optics of a dogleg chicane . . . . .	48
3.3.1	Emittance growth in a dogleg chicane . . . . .	48
3.3.2	Linear optics in thin lens approximation . . . . .	50
3.3.3	Optical matching with MADX . . . . .	54
3.4	Study of the beam dynamics in the dogleg . . . . .	58

3.4.1	Benchmark of the codes . . . . .	58
3.4.2	Beam dynamics in the dogleg chicane . . . . .	60
3.5	Transverse focusing before the plasma . . . . .	66
3.6	Summary . . . . .	70
<b>4</b>	<b>Beam capture and acceleration in the plasma wakefield</b>	<b>71</b>
4.1	Simulation code . . . . .	72
4.2	Density profile in the plasma cell . . . . .	74
4.3	Considerations related to the configuration . . . . .	75
4.3.1	Energy gain in the plasma wave . . . . .	75
4.3.2	Longitudinal capture and compression of the electron bunch in the plasma wave . . . . .	80
4.4	Simulation study of the electron-plasma wakefield interaction in the plasma cell . . . . .	85
4.4.1	Longitudinal Phase space manipulation with the laser configuration	85
4.4.2	Evolution of the transverse parameters of the electron bunch . . .	93
4.4.3	Optimization of the injection configuration for different plasma densities . . . . .	95
4.5	Summary . . . . .	97
<b>5</b>	<b>Extending the acceleration length with the laser being guided by a hollow dielectric capillary</b>	<b>98</b>
5.1	Capillary guiding of a laser beam with a Gaussian radial profile . . . . .	99
5.2	Capillary guiding of a laser beam with flattened Gaussian radial profile .	108
5.2.1	Properties and the focusing of Flattened Gaussian beams . . . . .	108
5.2.2	Propagation of a laser beam in the dielectric capillary . . . . .	110
5.2.3	Simulation of the laser propagation and the acceleration of the electrons in the hollow dielectric capillary . . . . .	116
5.3	Extending the acceleration length for the ESCULAP frame . . . . .	123
5.4	Compensating the dephasing effect with a plasma up density ramp . . . .	129
5.5	summary . . . . .	131
<b>6</b>	<b>Conclusion</b>	<b>133</b>
	<b>Bibliography</b>	<b>135</b>

# Chapter 1

## Introduction

High energy electron beams have been one of the most important tools for scientific research, facilities used to accelerate the electron beam are called accelerators. In conventional accelerators, the electron beam is accelerated by a radio-frequency (RF) electric field inside a metallic cavity, the acceleration gradient is limited by the break-down threshold of the cavity material (i.e. the SLAC S-Band Linac operated at 17 MV/m [1], the X-band cavity of the Global Linear Collider (GLC) test facility operates at 65 MV/m [2], and the X-band cavity for CERN based Compact Linear Collider (CLIC) is designed to generate an acceleration gradient of 100 MV/m [3]). Thus, many kilometers long of acceleration structures are required to get a high energy beam of tens GeV [4, 5] or TeV [6]. In order to make the facility more compact and cut the costs, a high gradient acceleration structure is strongly desired.

The electric field generated in the plasma due to the density modulation of plasma electrons can reach the order of  $\sim 100$  GV/m, which is three orders larger than the maximum field in conventional RF structures and provides the possibility to produce high energy electron beams in meter range. The plasma electron density can be modulated by the field of an intense laser beam or of a high-intensity particle beam, depending on the drive beam, this acceleration process is known as Laser-driven plasma wakefield acceleration (LPWA) or beam-driven plasma wakefield acceleration (PWFA). The LPWA was firstly proposed by Tajima and Dawson [7] in 1979, however the laser intensity could not reach the level required by LPWA until the development of the Chirped Pulse Amplification (CPA) technique [8] in 1985, in some early experiments, the laser pulse had a duration comparable with the plasma wave [9, 10], in the early 2000s high-power ( $\sim 10$  TW) femtosecond laser pulses began to be used in experiments, and an acceleration gradients of 100 GV/m, and an energy gain of 100 MeV have been demonstrated [11–14], however,

the beam were of poor quality with an exponential energy spectra. A dramatic breakthrough was achieved in 2004, electron bunches of better quality ( $>100$  MeV, with an energy spread of few percent) were produced by three independent groups [15–17], while the maximum energy is limited by the diffraction of the laser. Two years later, with the laser pulse being guided by the plasma channel in a 3.3 cm discharge capillary, a GeV acceleration has been demonstrated by experiment [18]. The energy gain in a single stage has been further pushed to  $\sim 4.2$  GeV in 2014 [19, 20] and to 8 GeV recently [21]. The dephasing between electron bunch and plasma wave as well as the depletion of the laser become the new obstacles to go to higher energy. The quasi-phase-matched acceleration (a periodic structure is used) [22] and the plasma density ramp [23–25] have the potential to compensate the phase mismatch between plasma wave and electron bunch, the recently developed curved plasma channel [26, 27] provides an opportunity to study the multi-stage acceleration scheme by experiment, with these techniques, a higher energy gain is foreseeable.

In addition to the effort on the high energy gain, many researches aim at improve the quality and stability of the electron bunch, that are greatly affected by the injection process. In the breakthrough achieved in 2004, the electron bunch was injected by the wave breaking induced self-injection, with this self-injection mechanism an electron beam of high charge and narrow energy spread (a few percent to 10%) can be achieved, but the process is affected by the non-linear self-focusing and self-compression [28–33] of the laser pulse, the beam is unstable and untunable. Then injection mechanisms such as ionization injection [34–37], density gradient injection [38–40] and laser colliding injection [41–44] have been developed, they make the injection process controllable, while the stability and quality of the electron beams are still not compatible with that produced by conventional RF accelerators.

A possible way to improve the beam quality and stability is to combine the conventional RF injector with a laser-plasma acceleration structure, that is to generate a tunable, high quality and stable electron source with a RF injector, then inject it into the high gradient plasma wakefield to get efficient acceleration. The beam quality can be maintained by matching the external electron bunch with the plasma wakefield, to minimize the energy spread growth during the acceleration, the duration of the external bunch should be significantly shorter than the period of the plasma wave (typically of the order of 100 fs), thus a bunch compressor is usually implemented before the plasma to compress the electron bunch to several femtoseconds or sub-femtosecond, to reduce the emittance growth during the acceleration, the Twiss parameters of the electron bunch should also be matched with the plasma wakefield [45], the matched bunch size is typically a few micrometers. The beam stability relies on the precise control of all the sub-systems, eg. the synchronization between the drive laser, the photo cathode laser, and the RF phase

of the cavity (as they affect the time stability the electron beam arriving at the plasma structure), the RF power, laser and plasma stability (directly affect beam parameters).

Though, the external injection system is much more complicated, it provides an opportunity to improve the beam quality to the level of the conventional RF accelerators, there are several running and planned projects worldwide aiming to study the external injection scheme [46–50], some of them will be shortly summarized below. In SINBAD at DESY, a 100 MeV external electron beam will be compressed to sub-femtosecond duration by velocity bunching and a magnetic chicane with a collimator located between the second and third dipole[51, 52], with this configuration, most electrons are lost at the collimator (i.e 2.7 pC out of 10 pC can pass), the bunch arrival time jitter is expected to be smaller than 10 fs, the acceleration gradient in the plasma is expected to be larger than 200 MeV/m [53]. In SPARC lab, the 20 pC,  $\sim 100$  MeV electron bunch will be firstly compressed to 70 fs by velocity bunching and then to 29 fs by a dogleg chicane, two configurations are planned in the plasma, one with the laser not being guided and another with the laser being guided by a capillary tube, the final energy is respectively 120 MeV and 630 MeV with energy spread smaller than 1%[49, 54]. In REGAE, the 5 MeV electron bunch is compressed to few femtoseconds with ballistic compression, a S-band gun and a S-band booster are used, the longitudinal phase space is linearised with the help of the space charge effect [50, 55], the bunch charge at the plasma entrance is of the order of fC, while some of the studies such as the design of the focusing solenoid at the plasma entrance [56, 57] have important enlightenment for us.

In LAL, the photo injector PHIL [58] provides a low energy (5 MeV) short pulses (ps) electron beam [58], while the Ti:Sapphire laser LASERIX [59] can produce a 2 J laser beam, with these existing facilities, the ESCULAP project [60] was proposed to perform experimental study on the external injection scheme. As the energy of the electron bunch is quite low, the space charge effect which decreases with  $\gamma_e^2$  is significant, it is expected to work in a low charge range ( $\sim 10$  pC), a booster will be implemented after the gun to accelerate the electron bunch to  $\sim 10$  MeV with an energy chirp, then a dogleg chicane and a solenoid will be put downstream to match the electron bunch with the plasma wakefield. The laser will be focused to a spot size of  $\sim 50 \mu\text{m}$  which yield a Rayleigh length of 1 cm, with a FWHM duration of 45 fs, the maximum intensity and amplitude of the laser yield  $I_0 = 1.04 \times 10^{18} \text{W/cm}^2$ ,  $a_0 = 0.70$ , the plasma wakefield field is in the linear regime. The object of this thesis is to perform parameters studies for the project, and propose a configuration that will be set up for the subsequent experimental study, the beam manipulation before the plasma and the injection, acceleration process in the plasma are all covered.

In SINBAD and SPARC the beam energy is 100 MeV, both velocity bunching and magnetic compression will be implemented, a two stages magnetic compression has also been proposed for SINBAD. While for ESCULAP, the beam energy is low (10 MeV with a booster), due to the limited space in the PHIL experiment room, it is difficult to add Linacs or perform two stages compression, with only one stage magnetic compression, it's not realistic to compress the electron beam from  $\sim 1$  ps to several femtoseconds. Thus the idea is to compress the electron bunch to  $\sim 100$  fs (shorter than half of the plasma wave) with a magnetic chicane, and then perform velocity bunching with a relatively weak wakefield in the plasma, after the electron bunch being compressed to few femtoseconds, a strong wakefield will accelerate the bunch to higher energy.

The longitudinal compression chicane and the transverse transport line are designed and studied in this thesis, normally the TWISS parameters after the magnet chicane can be tuned by the TWISS parameters at the chicane entrance, thus several quadrupoles can be set before the magnetic chicane to pre-match the TWISS parameters, this can reduce the length of the transport line after the magnet chicane, and suppress the bunch length growth there. While in the low energy case, the electron bunch is space charge dominated, especially when it is compressed, the actual TWISS parameters vary a lot from the optical design values, thus in our case the transverse matching and longitudinal compression are performed separately. After the booster, a dogleg chicane is used to compress the electron bunch to  $\sim 60$  fs, then a solenoid is used to focus the electron bunch to a size of  $\sim 25 \mu\text{m}$  much smaller than the laser spot size at the injection plane (the injection plane is several Rayleigh lengths away from the laser focal plane).

In the plasma, the laser plasma interaction begins several Rayleigh lengths before the laser focal plane, where the wakefield is weak, the electron bunch is injected near the zero crossing phase of the electric field to perform velocity bunching. In the meanwhile, the electron bunch slips backward due to the dephasing effect (electrons move slower than the plasma wave). The electron bunch slips to the field crest and is compressed to several femtoseconds close to the laser focal plane, then it is efficiently accelerated to  $\sim 150$  MeV. Here, the laser beam is not guided, the efficient acceleration section is only within one Rayleigh length before and after the laser focal plane, the interaction ends several Rayleigh length after the laser focal plane, thus the angular divergence of the electron bunch is reduced, this is beneficial for the subsequent extraction beam line.

To further increase the bunch energy, the laser guiding with a hollow dielectric capillary is studied, the simulation results show that with normal Gaussian radial profile, the field at the capillary inner wall at the entrance is not zero, the diffraction at the capillary entrance modulates the radial profile of the laser and excites a defocusing force at the focusing phase, in that case most electrons are lost during the propagation. In this thesis



a focused Flattened Gaussian beam[61] is suggested to eliminate the diffraction at the capillary entrance, the propagation of the focused flattened Gaussian beam in a dielectric capillary is investigated, with the focused Flattened Gaussian beam, the electron loss during the propagation is efficiently suppressed. With the dielectric capillary and the focused Flattened Gaussian beam, an upgrade configuration for the ESCULAP project is studied.

This thesis is organized as follows. In chapter 2, the basic theory of beam dynamics and frequently used bunch compression techniques are introduced. The generation of the laser plasma wakefield, the technique related to bunch injection and the limitation of the bunch energy are reviewed. In Chapter 3, the design of the dogleg and the transport line as well as the simulation results are presented. In chapter 4, the laser-plasma configuration and the injection phase of the electron bunch are tuned to optimize the velocity bunching process. The optimal injection conditions at different plasma densities are presented, the evolution of the bunch parameters under the optimal injection condition are investigated. In chapter 5, a hollow dielectric capillary is implemented to guide the laser beam and extend the acceleration length, the propagation of the laser beam in a dielectric capillary is studied. With a Gaussian and a focused Flattened Gaussian radial profile of the drive laser, the propagation of the electron bunch in the plasma wakefield is studied.

## Chapter 2

# Electron dynamics and Laser-Plasma Wakefield acceleration in the linear regime

### 2.1 Electron dynamics

#### 2.1.1 Equation of motion

In particle accelerators, the electron beam is usually accelerated by an electric field and guided by a magnetic field, the equation of motion for electrons in the presence of an electromagnetic field takes the form

$$\frac{d\vec{p}}{dt} = e\vec{E} + e\vec{v} \times \vec{B} \quad (2.1)$$

Without loss of generality, let's assume that the electrons move in the  $z$  direction,  $x$ ,  $y$  are respectively the horizontal and vertical direction. For simplicity, the particles are usually described using a Cartesian coordinate system that follows with the reference or ideal trajectory (the reference electron is located at the origin of the coordinate  $O$ ), a 6D trace space  $(x, x', y, y', z, \delta)$  can be used to fully describe the electrons. Recognizing the momentum of the reference electron as  $(p_{x0}, p_{y0}, p_0)$ , and the momentum of a general electron as  $(p_x, p_y, p_z)$ , then one has  $\delta = (p_z - p_{z0})/p_{z0}$ .

With the reference coordinates, the equation of motion takes the form [62]:

$$x'' = -(1 + k_{x0}x)k_x + k_{x0} \quad (2.2)$$

Here  $k_{x0} = \frac{eB_{y0}}{p_{z0}}$ ,  $k_x = \frac{eB_y}{p_z}$  refer to the curvatures of the electron trajectory, and the subscript 'x0' indicates the parameters for the reference particle. A development of the magnetic field in a magnet is:

$$B_y = B_{0y} + gx + \frac{1}{2}s(x^2 - y^2) + \dots \quad (2.3a)$$

$$B_x = B_{0x} + gy + sxy + \dots \quad (2.3b)$$

The three terms in the right hand of the equations are respectively the 0th order (dipole) component, the 1st order (quadrupole) component and the 2nd order (sextupole) component.

The 0th order component may exert a deflective force on the reference particle, while the higher order components are related to the coordinates, they are invisible for the reference electron ( $k_{x0} = 0$ ), but they are capable of focusing the general electrons to oscillate around the reference electron.

The momenta  $\frac{1}{p_z}$  can be expanded w.r.t. the reference momenta  $\frac{1}{p_{z0}}$  in the following form

$$\frac{1}{p_z} = \frac{1}{p_{z0}(1 + \delta)} = \frac{1}{p_{z0}}(1 - \delta + \delta^2 - \delta^3 + O(\delta^4)) \quad (2.4)$$

Thus we have  $k_x = k_{x0}(1 - \delta + \delta^2 - \delta^3 + O(\delta^4))$ , substituting it into equation 2.2 and only keeping the linear term of  $\delta$  we have  $x'' = -k_{x0}^2 x + k_{x0}\delta + k_{x0}^2 x\delta$ . Where  $k_{x0}$  can be replaced with the magnetic field in the corresponding magnet shown in formula 2.3, ignoring the cubic order of  $\delta$ ,  $x$ , the equations of motion in dipoles, quadrupoles and sextupoles can be written with

$$x'' + \frac{x}{\rho_0^2} = \frac{\delta}{\rho_0} + \frac{x\delta}{\rho_0^2} \quad (2.5a)$$

$$x'' + \frac{e}{p_{z0}}gx = \frac{e}{p_{z0}}gx\delta \quad (2.5b)$$

$$x'' = -\frac{1}{2}\frac{e}{p_{z0}}s(x^2 - y^2) \quad (2.5c)$$

Where  $\rho_0 = p_{z0}/(eB_{0y})$  is the bend radius in the dipole. For a monochromatic beam the equations of motion in a dipole and a quadrupole become homogeneous equations, but in real case we can never get a monochromatic beam, electrons with different energies are focused differently and the image becomes blurred. While, according to the equation of motion in a sextupole, it is independent of  $\delta$  and is capable of compensating the chromatic aberration introduced in the dipole the quadrupole. But one should note that, here only the quadratic order of  $\delta$ ,  $x$  are included, if we go to higher order, sextupoles will introduce higher order chromatic aberrations.

### 2.1.2 Hill equation and Courant-Snyder (Twiss) parameters

If a monochromatic particle is considered, the equations of motion in previous section can be written as Hill's equation

$$x'' + Kx = 0 \quad (2.6)$$

The solution for Hill's equation depends on the express of  $K$ , with a constant  $K$  in a length of  $L$ , the solution follows

**$K \geq 0$**

$$\begin{bmatrix} x \\ x' \end{bmatrix} = \begin{bmatrix} \cos(\sqrt{K}L) & \frac{1}{\sqrt{K}}\sin(\sqrt{K}L) \\ -\sqrt{K}\sin(\sqrt{K}L) & \cos(\sqrt{K}L) \end{bmatrix} \begin{bmatrix} x_0 \\ x'_0 \end{bmatrix} \quad (2.7)$$

**$K < 0$**

$$\begin{bmatrix} x \\ x' \end{bmatrix} = \begin{bmatrix} \cosh(\sqrt{|K|}L) & \frac{1}{\sqrt{|K|}}\sinh(\sqrt{|K|}L) \\ -\sqrt{|K|}\sinh(\sqrt{|K|}L) & \cosh(\sqrt{|K|}L) \end{bmatrix} \begin{bmatrix} x_0 \\ x'_0 \end{bmatrix} \quad (2.8)$$

if  $\sqrt{K}L \ll 1$ , the transfer matrix can be simplified with  $\cos(\sqrt{K}L) \approx 1$ ,  $\sin(\sqrt{K}L) \approx \sqrt{K}L$ , thus when  $K \geq 0$  one has

$$\begin{bmatrix} x \\ x' \end{bmatrix} = \begin{bmatrix} 1 & L \\ -KL & 1 \end{bmatrix} \begin{bmatrix} x_0 \\ x'_0 \end{bmatrix} \quad (2.9)$$

Compare with a convex lens, where  $f = \frac{1}{KL}$  is the focal length, the thin lens approximation is usually used in simple analysis of the transport line, it is a good approximation when  $KL^2 = L/f \ll 1$ .

The transport line can be described with the scalar product of a series of transfer matrices. In the periodic system  $K(s) = K(s+C)$ ,  $C$  is the length of a period, Hill's equation has a solution as a harmonic oscillator[63]

$$x(s) = A\sqrt{\beta(s)}\cos(\psi(s) + \psi_0) \quad (2.10)$$

where  $\beta(s)$  and  $\psi(s)$  are respectively the amplitude and phase functions which varies along the beam line, while  $A$  and  $\psi_0$  are constants determined by the initial conditions.  $\psi(s)$  and  $\beta(s)$  are related by

$$\psi(s) = \int \frac{1}{\beta(s)} ds \quad (2.11)$$

It is customary to define two other functions to describe the angular divergence

$$\alpha(s) = -\frac{1}{2} \frac{d\beta(s)}{ds} \quad (2.12)$$

$$\gamma(s) = \frac{1 + \alpha(s)^2}{\beta(s)} \quad (2.13)$$

$\alpha > 0$  indicates that the particle is converging to the axis and vice versa,  $A\sqrt{\gamma}$  is the angular divergence.  $\alpha(s)$ ,  $\beta(s)$ , and  $\gamma(s)$  are the so-called Twiss or Courant Snyder parameters. The trajectory of particles satisfy the relation

$$\gamma(s)x^2 + 2\alpha(s)xx' + \beta(s)x'^2 = A^2 \quad (2.14)$$

With the Twiss parameters, equations 2.7, 2.8 can be rewritten as[64]

$$\begin{bmatrix} x \\ x' \end{bmatrix}_s = \begin{bmatrix} \sqrt{\frac{\beta_{x.s}}{\beta_{x.0}}} (\cos(\Delta\psi) + \alpha_{x.0}\sin(\Delta\psi)) & \sqrt{\beta_{x.s}\beta_{x.0}}\sin(\Delta\psi) \\ -\frac{(1+\alpha_{x.s}\alpha_{x.0})\sin(\Delta\psi) + (\alpha_{x.0}-\alpha_{x.s})\cos(\Delta\psi)}{\sqrt{\beta_{x.s}\beta_{x.0}}} & \sqrt{\frac{\beta_{x.0}}{\beta_{x.s}}} (\cos(\Delta\psi) - \alpha_{x.s}\sin(\Delta\psi)) \end{bmatrix} \begin{bmatrix} x \\ x' \end{bmatrix}_{s0} \quad (2.15)$$

Equation 2.14 is the general equation of an ellipse centered at the origin of the  $x - x'$  space, the ellipse varies along the transport line, but the area is kept constant. Equation 2.14 describes only a single particle, it can also be extended to describe the trace space of a particle beam by replacing the oscillation amplitude with  $A\sqrt{\beta} = \sqrt{\langle x^2 \rangle}$ , defining the area of the phase space as the trace emittance  $\epsilon_{x.tr} = A^2$ , then the corresponding Twiss parameters are

$$\beta = \frac{\langle x^2 \rangle}{\epsilon_{x.tr}}, \gamma = \frac{\langle x'^2 \rangle}{\epsilon_{x.tr}}, -\alpha = \frac{\langle xx' \rangle}{\epsilon_{x.tr}}, \quad (2.16)$$

And we have

$$\epsilon_{x.tr} = \sqrt{\langle x^2 \rangle \langle x'^2 \rangle - \langle xx' \rangle^2} \quad (2.17)$$

Obviously, the trace emittance decreases along with the acceleration of the beam, thus it is customary to normalize the trace emittance with the energy

$$\epsilon_{x.n.tr} = \frac{\bar{p}}{m_0 c} \epsilon_{x.tr} \quad (2.18)$$

$\bar{p}$  denotes the average longitudinal momentum, there are two other common ways to define the emittance, the normalized RMS emittance and the geometric emittance

$$\epsilon_{x.n.rms} = \frac{1}{m_0 c} \sqrt{\langle x^2 \rangle \langle p_x^2 \rangle - \langle xp_x \rangle^2}, \epsilon_{x.rms} = \frac{\epsilon_{x.n.rms}}{\bar{p}_z / m_0 c} \quad (2.19)$$

The normalized RMS emittance is usually used in numerical codes, thus the 6D phase space  $(x, p_x, y, p_y, z, \delta)$  is generally used instead of the trace space. According to Liouville's theorem, the 6D phase space is constant, and it is also valid to the 3 projected planes if they are not correlated, and we have  $\epsilon_{x.n.rms} = \epsilon_{x.n.tr}$  close to the beam waist[65].

### 2.1.3 Beam optics

According to the solution for the equation of motion 2.7, 2.8, the evolution of a single particle's trajectory can be described with the transfer matrix

$$\begin{bmatrix} x \\ x' \end{bmatrix} = \begin{bmatrix} R_{11} & R_{12} \\ R_{21} & R_{22} \end{bmatrix} \begin{bmatrix} x_0 \\ x'_0 \end{bmatrix} \quad (2.20)$$

The matrix  $\mathbf{R}$  depends on the properties of the magnet, according to equation 2.20, the transfer equation for a particle beam follows that

$$\langle x^2 \rangle = R_{11}^2 \langle x_0^2 \rangle + R_{12}^2 \langle x_0'^2 \rangle + 2R_{11}R_{12} \langle x_0x_0' \rangle \quad (2.21a)$$

$$\langle x'^2 \rangle = R_{21}^2 \langle x_0^2 \rangle + R_{22}^2 \langle x_0'^2 \rangle + 2R_{21}R_{22} \langle x_0x_0' \rangle \quad (2.21b)$$

$$\langle xx' \rangle = R_{11}R_{21} \langle x_0^2 \rangle + R_{12}R_{22} \langle x_0'^2 \rangle + (R_{11}R_{22} + R_{12}R_{21}) \langle x_0x_0' \rangle \quad (2.21c)$$

Compare with the definition of the Twiss parameters in equation 2.16, the transfer matrix of the Twiss parameters is written as

$$\epsilon_{x.tr} \begin{bmatrix} \beta_x \\ \gamma_x \\ \alpha_x \end{bmatrix} = \epsilon_{x0.tr} \begin{bmatrix} R_{11}^2 & R_{12}^2 & -2R_{11}R_{12} \\ R_{21}^2 & R_{22}^2 & -2R_{21}R_{22} \\ -R_{11}R_{21} & -R_{12}R_{22} & R_{11}R_{22} + R_{12}R_{21} \end{bmatrix} \begin{bmatrix} \beta_{x0} \\ \gamma_{x0} \\ \alpha_{x0} \end{bmatrix} \quad (2.22)$$

Usually a matrix  $\boldsymbol{\sigma}$  is defined by the Twiss parameters

$$\boldsymbol{\sigma}_x = \epsilon_{x.tr} \begin{bmatrix} \beta_x & -\alpha_x \\ -\alpha_x & \gamma_x \end{bmatrix} \quad (2.23)$$

Refer to equation 2.22, the  $\boldsymbol{\sigma}_x$  matrix evolves as

$$\boldsymbol{\sigma}_x = \mathbf{R}\boldsymbol{\sigma}_{x0}\mathbf{R}^T \quad (2.24)$$

This transfer matrix could be also extended to the 6D trace space, only considering the linear optics (first order), we have

$$\begin{bmatrix} x \\ x' \\ y \\ y' \\ z \\ \delta \end{bmatrix} = \begin{bmatrix} R_{11} & R_{12} & R_{13} & R_{14} & R_{15} & R_{16} \\ R_{21} & R_{22} & R_{23} & R_{24} & R_{25} & R_{26} \\ R_{31} & R_{32} & R_{33} & R_{34} & R_{35} & R_{36} \\ R_{41} & R_{42} & R_{43} & R_{44} & R_{45} & R_{46} \\ R_{51} & R_{52} & R_{53} & R_{54} & R_{55} & R_{56} \\ R_{61} & R_{62} & R_{63} & R_{64} & R_{65} & R_{66} \end{bmatrix} \begin{bmatrix} x_0 \\ x'_0 \\ y_0 \\ y'_0 \\ z_0 \\ \delta_0 \end{bmatrix} \quad (2.25)$$

The dispersion function  $R_{16}$  and it's derivative  $R_{26}$  are coming from the  $\frac{\delta}{\rho_0}$  in equation 2.5a.

Substituting higher order  $\delta$  of equation 2.4 into the equation of motion, and recognizing the elements of the second and third order transfer matrix as  $T_{ijk}$ ,  $U_{ijkl}$ , the transfer matrix is written as

$$x_i = \sum_{j=1}^6 R_{ij} x_{j0} + \sum_{j=1}^6 \sum_{k=1}^6 T_{ijk} x_{j0} x_{k0} + \sum_{j=1}^6 \sum_{k=1}^6 \sum_{l=1}^6 U_{ijkl} x_{j0} x_{k0} x_{l0} + O(4) \quad (2.26)$$

To study the the transfer matrix of a transport line, let's recognize the transfer matrix at the entrance of magnet A as  $M_{en}$  (matrix elements at the entrance are recognized with a subscript of  $en$ ), and recognize the transfer matrix of A as  $M_A$  (matrix elements are recognized with a subscript of  $A$ ), then the transfer matrix at the exit of A take the form that

$$\begin{aligned} R_{ij.ex} &= \sum_{p=1}^6 R_{ip.A} R_{pj.en} \\ T_{ijk.ex} &= \sum_{p=1}^6 R_{ip.A} T_{pjk.en} + \sum_{p,q=1}^6 T_{ipq.A} (R_{pj.en} R_{qk.en} + R_{pk.en} R_{qj.en}) \end{aligned} \quad (2.27)$$

In general, a transport line is composed of dipoles and quadrupoles, the  $(x, x')$  and  $(y, y')$  planes are uncoupled, they are analyzed separately, while for particle beams with sufficient energy spread, the dispersion function should be considered.

## 2.1.4 Interaction between particles

So far, we have treated only the forces of external fields on a particle, another important issue is the effects of the beam's own electromagnetic field on itself, in this thesis, just the space charge and the Coherent synchrotron radiation (CSR) are investigated, while the wakefield is usually important for high repetition beam, it is out of the scope of this thesis.

### 2.1.4.1 Space charge effect

Firstly, assume a long beam uniformly distributed in longitudinal and azimuthal direction, moving with velocity  $v$ , thus we have only the radial electric field and azimuthal

magnetic field, in the particle beam they take the form that

$$E_r = \frac{q}{\epsilon_0 r} \int_0^r \rho(r) r dr \quad (2.28a)$$

$$B_\theta = \frac{qv\mu_0}{r} \int_0^r \rho(r) r dr \quad (2.28b)$$

Where  $q$  is the charge of a single particle,  $\rho$  is the density of the particles,  $\epsilon_0$  and  $\mu_0$  are respectively the vacuum permittivity and the vacuum permeability. The radial Lorentz force is  $F_r = qE_r - qvB_\theta = qE_r(1 - \beta^2)$ ,  $\beta = \frac{v}{c}$  is the Lorentz factor and  $c$  is the speed of light. For relativistic beams,  $1 - \beta^2 \approx \frac{1}{\gamma^2}$ , thus

$$F_r = \frac{q^2}{\epsilon_0 r \gamma^2} \int_0^r \rho(r) r dr \quad (2.29)$$

It's a defocusing force and decreases with  $\gamma^2$ , thus it is more significant in the low energy regime.

In real case, particle beams have finite length, an ellipsoidal bunched model is usually used to study the beam envelop, here we follow the model in [66, 67]

Consider a particle beam uniformly distributed in an ellipse, then the semi axes is related to the RMS size by  $r_i = \sqrt{5}\sigma_i = \sqrt{5 \langle i^2 \rangle}$ ,  $i = x, y, z$ , the electric field inside the bunch follows that

$$E_x = \frac{3I\lambda(1-f)}{4\pi\epsilon_0 c(r_x + r_y)} \frac{x}{r_x} \quad (2.30a)$$

$$E_y = \frac{3I\lambda(1-f)}{4\pi\epsilon_0 c(r_x + r_y)} \frac{y}{r_y} \quad (2.30b)$$

$$E_z = \frac{3I\lambda f}{4\pi\epsilon_0 c r_x r_y} \frac{z}{r_z} \quad (2.30c)$$

Where  $\lambda$  is the RF wavelength,  $I$  is the average current over a RF period,  $f$  is the ellipsoid form factor and is a function of the parameter  $p = \gamma r_z / \sqrt{r_x r_y}$ , it is expressed in equation 2.32 and shown in Figure 2.1. According to equation 2.30 the field is linearly related to the coordinate, the envelop equations can be derived by substituting the field expressions into Hill's equation and they are given by [63]

$$\sigma_x'' + k_x(s)\sigma_x - \frac{\epsilon_{x,tr}^2}{\sigma_x^3} - \frac{3K(1-f)}{(\sigma_x + \sigma_y)\sigma_z} = 0 \quad (2.31a)$$

$$\sigma_y'' + k_y(s)\sigma_y - \frac{\epsilon_{y,tr}^2}{\sigma_y^3} - \frac{3K(1-f)}{(\sigma_x + \sigma_y)\sigma_z} = 0 \quad (2.31b)$$

$$\sigma_z'' + k_z(s)\sigma_z - \frac{\epsilon_{z,tr}^2}{\sigma_z^3} - \frac{3Kf}{\sigma_x \sigma_y} = 0 \quad (2.31c)$$



$$f = \frac{1}{1-p^2} \begin{cases} 1 - \frac{p}{\sqrt{1-p^2}} \arccos(p) & p < 1 \\ 1 - \frac{p}{\sqrt{p^2-1}} \operatorname{arccosh}(p) & p > 1 \end{cases} \quad (2.32)$$

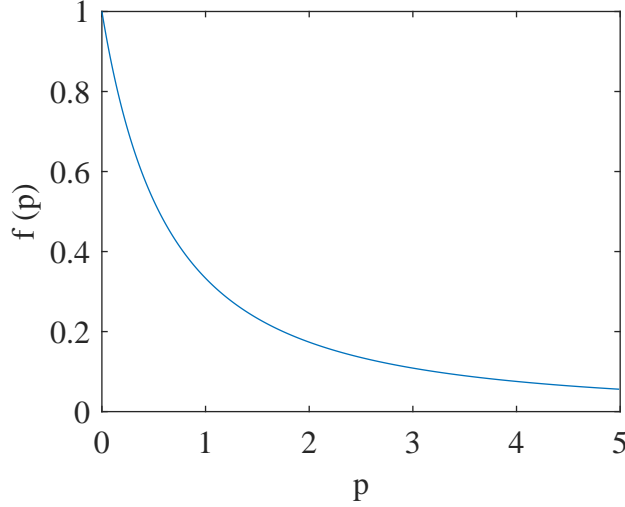


FIGURE 2.1: The ellipsoid form factor

Where  $K = eI\lambda/(20\sqrt{5}\epsilon_0 mc^3 \gamma^3 \beta^2)$  is the 3-dimensional space charge parameter. This is a good approximation for any distribution with ellipsoidal symmetry. In formula 2.31a, 2.31b and 2.31c, the second term represents the external focusing force, the third term represents the outward pressure due to the normalized RMS emittance, and the fourth term represents the space charge term.

In a space charge dominated beam (i.e in the gun), the term of emittance can be ignored, one can easily derive the matching condition which lead to a constant envelop ( $\sigma'_{x,y,z} = 0$ ). i.e  $k_x(s) = 3K(1-f)/(\sigma_{x,match}(\sigma_{x,match} + \sigma_y)\sigma_z)$ . However, the geometry varies in the longitudinal direction, thus the matching condition varies between slices, it is shown that in a slightly mismatched slice the x envelop oscillates with  $\sin \sqrt{2k_x z}$ , while the emittance oscillates with  $|\sin \sqrt{2k_x z}|$ . In a real electron bunch, the space charge effect varies along the electron bunch, thus the betatron oscillation frequency is different between slices, this may lead to the decoherence between slices, and increase the projected emittance, an external force is required to compensate the emittance growth[68]. The mismatch factor defined by [69] which can be used to check the decoherence between slices.

$$M_s = B_{mag} + \sqrt{B_{mag}^2 + 1} \quad (2.33)$$

where  $B_{mag}$  yield

$$B_{mag} = \frac{1}{2}(\beta_1 \gamma_2 + \beta_2 \gamma_1 - 2\alpha_1 \alpha_2) \quad (2.34)$$

$\beta_{1,2}$  and  $\alpha_{1,2}$  are the Twiss parameters of two different slices, with  $M_s = 1$  the phase space of two slices are similar.

In an emittance dominated beam, the space charge effect can be ignored, the beam size should be matched with the external force, and from equation 2.31a, one has

$$k_{x.match}(s) = \epsilon_{x.tr}^2 / \sigma_{x.match}^4(s) = 1/\beta_x^2 \quad (2.35)$$

For a precise study, a 3D numerical simulation is required.

#### 2.1.4.2 Coherent synchrotron Radiation

Particles radiate energy when they are accelerated, in a curved trajectory, the radiation field emitted by the particles in the tail may overtake the head of the bunch. The radiation from a relativistic electron bunch moving in a magnetic field is usually in a wide frequency spectrum, the spectral distribution is characterized by a critical wavelength  $\lambda_{rad.c} = (4/3)\pi\rho\gamma^{-3}$ , the radiation power at wavelengths shorter than  $\lambda_{rad.c}$  is 50% of the total radiation power [70]. The radiation is coherent in the frequency range of  $\omega_{rad} \ll c/l_b$ ,  $c$  is the speed of light in vacuum, and  $l_b$  is the bunch length,  $\rho$  is the bending radius and  $\gamma$  is the Lorentz factor of the electron.

Here we simply review the theory of synchrotron radiation (SR) beginning with vector and scalar inhomogeneous wave equations, in this section, all the equations are listed in SI unit unless specified otherwise.

$$\Delta^2 \vec{A} - \frac{1}{c^2} \frac{\partial^2 \vec{A}}{\partial t^2} = -\mu_0 \vec{J} \quad (2.36)$$

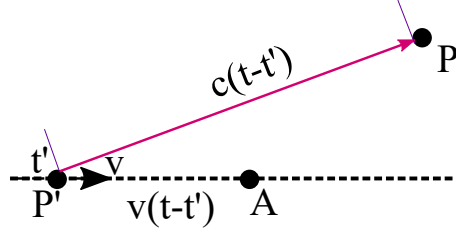
$$\Delta^2 \Phi - \frac{1}{c^2} \frac{\partial^2 \Phi}{\partial t^2} = -\frac{\rho}{\epsilon_0} \quad (2.37)$$

The retarded solution for equation 2.36, 2.37 can be derived with Green's function [71]

$$\vec{A}(\vec{r}, t) = \frac{\mu_0}{4\pi} \int \vec{J}(\vec{r}', t') \frac{d\vec{r}'}{|\vec{r} - \vec{r}'|} \quad (2.38)$$

$$\Phi(\vec{r}, t) = \frac{1}{4\pi\epsilon_0} \int \rho(\vec{r}', t') \frac{d\vec{r}'}{|\vec{r} - \vec{r}'|} \quad (2.39)$$

In equations 2.38, 2.39, the vector/scalar in position  $\vec{r}$  at time  $t$  is excited by the current/electron source in position  $\vec{r}'$  at time  $t'$ ,  $t - t' = |\vec{r}(t) - \vec{r}'(t')|/c$  is the retard time.


 FIGURE 2.2: Radiation of an electron moving with velocity  $\vec{v}$ 

To describe it in detail, let's start with considering an electron moving with velocity  $\vec{v}$ , referring to Figure 2.2, when the electron moves from  $P'$ , it radiates an electromagnetic field, the radiation travels with velocity  $c$ , at time  $t$  the radiation arrives at  $P$ , while the electron arrives at  $A$ . All the parameters in formulas 2.38, 2.39 with superscript ' describe the state of the electron at time  $t'$ . In order to do the calculation we need to transform them into the same time coordinate, assuming that from  $t'$  to  $t$ , there is no disturbance then the transformations follow that

$$\vec{v}'(\vec{r}', t') = \vec{v}(\vec{r}' + (t - t')\vec{v}', t) = \vec{v} \quad (2.40)$$

$$\vec{J}(\vec{r}', t - \frac{|\vec{r} - \vec{r}'|}{c}) = \vec{J}(\vec{r}' + \vec{v}\frac{|\vec{r} - \vec{r}'|}{c}, t) \quad (2.41)$$

$$\rho(\vec{r}', t - \frac{|\vec{r} - \vec{r}'|}{c}) = \rho(\vec{r}' + \vec{v}\frac{|\vec{r} - \vec{r}'|}{c}, t) \quad (2.42)$$

Let's call the right hand of formula 2.41/2.42 the retarded current/charge, substitute them into formula 2.38, 2.39, we have

$$\vec{A}(\vec{r}, t) = \frac{\mu_0}{4\pi} \int \vec{J}(\vec{r}' + \vec{v}\frac{|\vec{r} - \vec{r}'|}{c}, t) \frac{d(\vec{r}' + \vec{v}\frac{|\vec{r} - \vec{r}'|}{c})}{|\vec{r} - (\vec{r}' + \vec{v}\frac{|\vec{r} - \vec{r}'|}{c})|} \quad (2.43)$$

$$\Phi(\vec{r}, t) = \frac{1}{4\pi\epsilon_0} \int \rho(\vec{r}' + \vec{v}\frac{|\vec{r} - \vec{r}'|}{c}, t) \frac{d(\vec{r}' + \vec{v}\frac{|\vec{r} - \vec{r}'|}{c})}{|\vec{r} - (\vec{r}' + \vec{v}\frac{|\vec{r} - \vec{r}'|}{c})|} \quad (2.44)$$

If only one electron is considered, equations 2.43, 2.44 are reduced to the following formalization

$$\vec{A}(\vec{r}, t) = \frac{\mu_0 e}{4\pi} \frac{\vec{v}}{|\vec{r} - \vec{r}'|(1 - \vec{n} \cdot \vec{\beta})} \quad (2.45)$$

$$\Phi(\vec{r}, t) = \frac{e}{4\pi\epsilon_0} \frac{\vec{v}}{|\vec{r} - \vec{r}'|(1 - \vec{n} \cdot \vec{\beta})} \quad (2.46)$$

With the relation that  $E = -\nabla \Phi - \partial \vec{A}/\partial t$ , and  $B = \nabla \times \vec{A}$ , the electric field yields

$$\vec{E} = \frac{e}{4\pi\epsilon_0} \left( \frac{\vec{n} - \vec{\beta}}{\gamma^2(1 - \vec{n} \cdot \vec{\beta})^3|\vec{r} - \vec{r}'|^2} + \frac{\vec{n} \times [(\vec{n} - \vec{\beta}) \times \dot{\vec{\beta}}]}{c(1 - \vec{n} \cdot \vec{\beta})^3|\vec{r} - \vec{r}'|} \right) \quad (2.47)$$

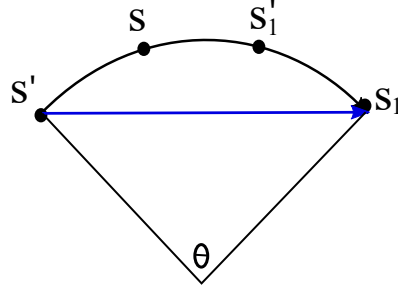


FIGURE 2.3: Two electrons move in a circular trajectory

Here,  $\vec{\beta} = \vec{v}/c$  is the normalized velocity,  $\dot{\vec{\beta}} = d\vec{\beta}/dt$  refers to the acceleration. It should be noted that formulas 2.38, 2.39 are derived without assumption or approximation, while formula 2.47 is derived with the assumption that from  $t'$  to  $t$ , the velocity of the electron didn't change. The 3D electromagnetic field can be calculated from the distribution of the electrons, however, it is usually time consuming.

For an electrons moving in a circular trajectory, according to the theory in [72], the electron bunch can be treated as line distribution if the transverse size is so small that the Derbenev criterion is satisfied, then the radiation force can be divided into 1D CSR (the second part in equation 2.47) and Coulomb force (the first part in equation 2.47), the Derbenev criterion is

$$\frac{\sigma_r}{\sigma_z} \ll \left( \frac{\rho}{\sigma_z} \right)^{1/3} \quad (2.48)$$

Where  $\rho$  is the bend radius, with the 1D CSR model, consider two electrons moving in a circular trajectory, see Figure 2.3, at time  $t'$ , they are located at  $s'$  and  $s'_1$ , at time  $t$ , they reaches  $s$  and  $s_1$  and the electric field of the back electron produced at point  $s'$  overtakes the front electron, the overtaken length is

$$\Delta s = s'_1 - s' = \rho\theta - |s's_1|\beta \approx (1 - \beta)\rho\theta + \rho\theta^3/24 \quad (2.49)$$

For an electron bunch, with a length of  $l_b$ , in the total coherent regime where the electron bunch is smaller than the critical radiation wavelength  $l_b \ll \lambda_{rad.c}$ , the energy loss gradient is given by [73]

$$\frac{dE_e}{dct} = \frac{N^2 e^2 \gamma_e^4 s}{3\pi \epsilon_0 \rho^2 l_b} \quad (0 \leq s \leq l_b) \quad (2.50)$$

The total energy loss due to the radiation can be obtained from the integration

$$P = - \int_0^{l_b} ds \zeta(s) \frac{dE_e}{dt} \quad (2.51)$$

Where  $\zeta(s)$  is the line density of the electrons. The integration is proportional to  $N^2 e^2 \gamma_e^4$ ,

that means the electron in a short bunch radiates as a single particle with the charge of  $Ne$ , the radiation power also depends on the energy of the electron bunch.

While if  $l_b \gg \lambda_{rad.c}$ , there is still low frequency radiation, which is coherent, the energy loss gradient along the bunch is given by [72, 73]

$$\frac{dE_e}{dct} \approx -\frac{2e^2}{4\pi\epsilon_0 3^{1/3} \rho^{2/3}} \int_{-\infty}^{s_1} \frac{1}{(s_1 - s)^{1/3}} \frac{d\zeta(s)}{ds} \quad (2.52)$$

For a Gaussian distributed electron beam, the line density denotes  $\zeta(s) = \frac{N}{\sqrt{2\pi}l_b} \exp(-\frac{s^2}{2l_b^2})$ , the integrated result is derived in [72–74], it follows the form that

$$\frac{dE_e}{dct} = \frac{Ne^2}{2\sqrt{2}\pi^{3/2}\epsilon_0 3^{1/3} \rho^{2/3} l_b^{4/3}} F\left(\frac{s}{l_b}\right) \quad (2.53)$$

Where  $F(\frac{s}{l_b})$  is given by

$$F(x) = \int_{-\infty}^x \frac{dx'}{(x - x')^{1/3}} \frac{d}{dx'} \exp(-x'^2/2) \quad (2.54)$$

The energy loss along the bunch  $dE_e/dct$  is shown in Figure 2.4, the bunch head (right) get energy while the bunch tail (left) lost energy. The total power loss can be obtained by substituting equation 2.53 into 2.51, it yields

$$P = -\frac{N^2 e^2}{\rho^{2/3} l_b^{4/3}} \frac{3^{1/6} (\Gamma(2/3))^2}{2^{2/3} \pi^2 \epsilon_0} \quad (2.55)$$

Where  $\Gamma(x) = \int_0^\infty \frac{t^{x-1}}{e^t} dt$ , the radiation is also proportional to the square of the electron number, but the radiation power depends on the bunch length and is independent of the bunch energy.

Thus CSR effect is significant for the case of short bunch length and high bunch charge, assume the CSR induced energy deviation is  $\delta_{CSR}$ , the bunch properties can be modified with the dispersion terms i.e.  $x = x_0 + R_{16}\delta_{CSR}$ , the effect of CSR should be checked carefully in bending planes, especially in magnetic compressors.

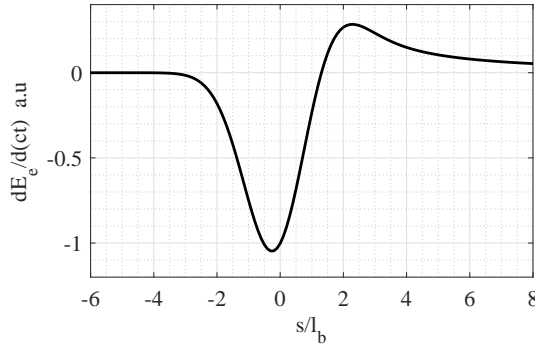


FIGURE 2.4: The CSR induced energy change of a line charge with Gaussian density distribution, the bunch head is on the right side

### 2.1.5 Longitudinal compression of electron bunch

The general way to compress an electron bunch in the longitudinal direction is to utilize the energy-position correlation, that is to properly match the  $R_{56}$  and  $R_{65}$  terms of the transfer line. Assuming an electron bunch with initial energy deviation (uncorrelated)  $\delta_0$ , an energy-position correlation is imparted as

$$\delta = k_0\delta_0 + k_1z_i + k_2z_i^2 + k_3z_i^3 + (4) \quad (2.56)$$

When it traverses a dispersed beam line the transfer equation is

$$z = z_i + h_1\delta + h_2\delta^2 + h_3\delta^3 + (4) \quad (2.57)$$

$h_1$ ,  $h_2$  and  $h_3$  are respectively  $R_{56}$ ,  $T_{566}$  and  $U_{5666}$  in the transfer matrix, while  $k_1$ ,  $k_2$  and  $k_3$  are respectively  $R_{65}$ ,  $T_{655}$ ,  $U_{6555}$ . Usually  $k_0$  is introduced by the energy change of the reference particle.

Only remain the terms  $z_i^m, \delta^m$ , with  $m < 3$ , after the dispersed beam line we have

$$\begin{aligned} z^2 = & h_1k_0^2\delta_0^2 \\ & + 2h_1k_0\delta_0(1 + k_1h_1)z_i \\ & + [(1 + k_1h_1)^2 + 2h_1k_0\delta_0(k_2h_1 + k_1^2h_2)]z_i^2 \end{aligned} \quad (2.58)$$

The RMS bunch length is

$$\sigma_z \approx \sqrt{h_1^2k_0^2\sigma_{\delta_0}^2 + [(1 + k_1h_1)^2 + 2R_{56}k_0\delta_0(k_2h_1 + k_1^2h_2)]\sigma_{z_i}^2} \quad (2.59)$$

According to equation 2.59, the minimum bunch length can be achieved with the full compression condition

$$h_1 = -1/k_1, \quad h_2 = -k_2 h_1 / k_1^2 \quad (2.60)$$

Under full compression, the minimum bunch length is limited by the initial uncorrelated energy spread.

Generally, the energy chirp terms  $k_i$ ,  $i = 0, 1, 2, \dots$ , are generated by off crest acceleration in a RF field, there are also studies on generating energy chirp with the space charge effect[75].

The dispersion terms  $h_i$ ,  $i = 1, 2, 3, \dots$  can be generated directly by the velocity difference in low energy regime, and by the trajectory difference in the high energy regime.

### 2.1.5.1 Compression with velocity difference

The two frequently used compression methods in low energy regime are ballistic compression and velocity bunching. The ballistic compression is to impart an energy chirp ( $R_{65}$ ) by off crest acceleration in a RF field, the electron bunch will be compressed in the downstream drift by the velocity difference, while velocity bunching relies on the longitudinal phase-space rotation of the electrons and the phase slippage between the electrons and the RF wave which both occur during the acceleration of non-ultra-relativistic electrons.

**2.1.5.1.1 Ballistic Compression** To study the energy chirp generated by the acceleration in a RF field, assume that the reference particle has an energy of  $E_{i0}$  at the entrance, and then is accelerated to the nominal energy  $E_{f0}$  with an RF phase  $\phi_0$ . For a general electron which is located at  $z_i$  with respect to reference particle, and has an energy of  $E_i$  at the entrance, the energy after acceleration yields

$$E_f = E_i + \frac{E_{f0} - E_{i0}}{\cos(\phi_0)} \cos(\phi_0 + 2\pi z_i / \lambda) \quad (2.61)$$

$\lambda$  is the wavelength of the acceleration field in the RF structure, generally,  $z_i \ll \lambda/2\pi$  and the relative energy deviation can be expanded as

$$\delta_f \approx \frac{E_{i0}}{E_{f0}} \delta_0 - \left(1 - \frac{E_{i0}}{E_{f0}}\right) \frac{2\pi}{\lambda} z_i \tan(\phi_0) - \left(1 - \frac{E_{i0}}{E_{f0}}\right) \frac{1}{2} \left(\frac{2\pi}{\lambda} z_i\right)^2 + \left(1 - \frac{E_{i0}}{E_{f0}}\right) \frac{1}{6} \left(\frac{2\pi}{\lambda} z_i\right)^3 \tan(\phi_0) \quad (2.62)$$

Here  $\delta_f = (E_f - E_{f0})/E_{f0}$ ,  $\delta_0 = (E_i - E_{i0})/E_{i0}$ .

Referring to equation 2.56, we have

$$\begin{cases} k_0 = \frac{E_{i0}}{E_{f0}} \\ k_1 = (1 - \frac{E_{i0}}{E_{f0}}) \frac{2\pi}{\lambda} \tan(\phi_0) \\ k_2 = (1 - \frac{E_{i0}}{E_{f0}}) \frac{1}{2} (\frac{2\pi}{\lambda})^2 \end{cases} \quad (2.63)$$

The relative position of electrons can be modified by the velocity difference in the low energy regime, consider a reference electron with a velocity  $v_0$ , and a general electron with velocity  $v_0 + \Delta v$ , they are coincident in  $z_0$ , when the reference electron travels to  $z$ , the longitudinal shift between the two electrons is

$$\Delta z = \Delta v \frac{z - z_0}{v_0} = \frac{\Delta \beta}{\beta_0} (z - z_0) \quad (2.64)$$

Where  $\beta = \frac{v}{c}$  is the normalized velocity,  $\gamma = \frac{1}{\sqrt{1-\beta^2}}$  is the Lorentz factor. With the momentum deviation being defined by  $\delta = \frac{\Delta \beta \gamma}{\beta_0 \gamma_0}$ , expanding equation 2.64 about the center momenta  $\beta_0 \gamma_0$ , we have

$$\Delta z = \frac{1}{\beta_0} \left[ \frac{d\beta}{d(\beta\gamma)} \right]_{\beta_0 \gamma_0} \Delta(\beta\gamma) + \frac{1}{2} \frac{d^2\beta}{d(\beta\gamma)^2} \Big|_{\beta_0 \gamma_0} \Delta(\beta\gamma)^2 + \frac{1}{6} \frac{d^3\beta}{d(\beta\gamma)^3} \Big|_{\beta_0 \gamma_0} \Delta(\beta\gamma)^3 + O(4) (z - z_0) \quad (2.65)$$

Since we have

$$\begin{cases} \frac{d\beta}{d\beta\gamma} = \frac{1}{\gamma^3} \\ \frac{d^2\beta}{d\beta\gamma^2} = -\frac{3\beta}{\gamma^4} \\ \frac{d^3\beta}{d\beta\gamma^3} = -\frac{15\beta^2 - 3}{\gamma^5} \end{cases} \quad (2.66)$$

Substituting equation 2.66 into equation 2.65 and compare with equation 2.57 we have

$$\begin{cases} h_1 = \frac{z - z_0}{\gamma_0^2} \\ h_2 = -\frac{3\beta_0^2}{2\gamma_0^2} (z - z_0) \\ h_3 = [-\frac{\beta_0^2}{2\gamma_0^2} + \frac{5\beta_0^4}{2\gamma_0^2}] (z - z_0) \end{cases} \quad (2.67)$$

One should be aware that an assumption of  $\beta \approx 1$  was made in equation 2.62, so that  $\frac{d\beta\gamma}{d\beta_0\gamma_0} \approx \frac{\Delta\gamma}{\gamma_0}$ .

Only taking the linear order in equation 2.65, we have  $R_{56} = \frac{(z - z_0)}{\gamma_0^2}$ , to obtain equal shift, the required drift length increases with  $\gamma_0^2$ . Consider a 5 MeV ( $\gamma_0 = 10$ ) electron beam with an energy spread of  $\delta = 1\%$ , the longitudinal shift in 1 m's propagation is  $\Delta z = 0.1$  mm, while for a 50 MeV ( $\gamma_0 = 100$ ) electron beam with the same energy spread, the longitudinal shift in 1 m's propagation is only  $\Delta z = 0.001$  mm. Normally the electron bunch has a size of several millimeters, thus in the low energy regime, the



velocity difference is capable of rearranging the longitudinal distribution over several meters, by pre-setting a proper energy chirp  $R_{65}$ , the bunch can be compressed. While in the high energy regime, hundreds meter's drift are required to achieve equal shift, usually a bend section is used to generate sufficient  $R_{56}$  by trajectory difference.

To obtain a short electron bunch, usually the second order full compression condition (see 2.60) should also be satisfied, usually another cavity is used to linearize the phase space and match the second order terms[76, 77], the energy gain and the acceleration phase in two cavities should meet the following conditions [78]

$$\frac{\Delta E_1 \sin(\phi_1)}{\lambda_1^2} = -\frac{\Delta E_2 \sin(\phi_2)}{\lambda_2^2} \quad (2.68a)$$

$$\frac{\Delta E_1 \cos(\phi_1)}{\lambda_1^3} = -\frac{\Delta E_2 \cos(\phi_2)}{\lambda_2^3} \quad (2.68b)$$

The parameters in two cavities are respectively identified with subscripts "1" and "2",  $\lambda$  is the RF wavelength,  $\Delta E$  is the maximum energy gain in the cavity and  $\phi$  is the acceleration phase in the cavity. If  $\lambda_1 = \lambda_2$ , the energy gain in the two cavities are canceled ( $\Delta E_1 \sin(\phi_1) = -\Delta E_2 \sin(\phi_2)$ ) according to equation 2.68, thus usually a high harmonic cavity is used to match the second order terms.

Another interesting topic is that the space charge effect may expand the longitudinal phase space, and two cavities with the same frequency can also be used to linearize the phase space, the detailed study can be found in [55], but the second cavity needs to work at a deceleration phase, the bunch energy is quite low after compression.

**2.1.5.1.2 Velocity bunching** Velocity bunching is realized by off crest acceleration in the RF field, electrons in the head get less energy while electrons in the tail get more energy, the phase space rotates during the acceleration. Velocity bunching is beneficial for high current where the space charge effect can be reduced by the acceleration, but longer, multi-cavities are required for the compression.

The acceleration phase  $\phi$  evolves as  $d\phi = k_{rf}(v_e - v_{rf})dt = k_{rf}(1 - \frac{v_{rf}}{v_e})ds$ , where  $k_{rf}$  is the wave number of the RF field,  $v_{rf}$  and  $v_e$  are respectively the velocity of the RF field and the electron, usually we take  $v_{rf} \approx c$  for simplification, energy  $\gamma$  in the RF cavity evolves as  $d\gamma = ak_{rf} \sin(\phi)ds$ , and  $a = \frac{E_0}{k_{rf}mc^2}$  is defined as dimensionless vector potential amplitude of the wave, thus we have

$$\frac{d\phi}{ds} = k_{rf}\left(1 - \frac{\gamma}{\sqrt{\gamma^2 - 1}}\right) \quad (2.69a)$$

$$\frac{d\gamma}{ds} = ak_{rf} \sin(\phi) \quad (2.69b)$$

Using a separation of variables approach, one can get[79]

$$a \cos(\phi) + \gamma - \sqrt{\gamma^2 - 1} = C \quad (2.70)$$

Where  $C$  is a constant that can be decided by the initial condition  $C = a \cos(\phi_0) + \gamma_0 - \sqrt{\gamma_0^2 - 1}$ , usually the electron beam is relativistic after velocity bunching, two approximations are made for simplification,  $\gamma - \sqrt{\gamma^2 - 1} \approx 0$ , and  $\gamma_0 - \sqrt{\gamma_0^2 - 1} \approx \frac{1}{2\gamma_0}$ , substituting them into equation 2.70, one has

$$\phi = \arccos(\arccos(\phi_0) + \frac{1}{2a\gamma_0}) \quad (2.71)$$

Expanding equation 2.71 to the first order of  $\phi_0$  and  $\gamma_0$ , one can get the final phase extension

$$\Delta\phi = \frac{\sin(\phi_0)}{\sin(\phi)} \Delta\phi_0 + \frac{1}{2a\gamma_0^2 \sin(\phi)} \Delta\gamma_0 \quad (2.72)$$

Ignoring the initial energy spread, the compression factor follows  $\frac{\Delta\phi}{\Delta\phi_0} = \frac{\sin(\phi_0)}{\sin(\phi)}$ , the maximum compression is achieved with  $\phi = 0$ .

### 2.1.5.2 Compression with trajectory difference

For an ultra relativistic electron bunch, the velocity difference is quite small, the compression is usually realized with the trajectory difference in a bend section.

Dipoles are used to bend the electron beam, dispersion terms in a dipole can be achieved by solving equation 2.5a, the first order horizontal dispersion term is  $R_{16} = \rho(1 - \cos(\theta))$ ,  $\rho$  and  $\theta$  are the bend radius and the bend angle of the dipole, the first and second order longitudinal dispersion terms  $R_{56}$  and  $T_{566}$  are given by[80]

$$R_{56} = - \int \frac{R_{16}}{\rho} ds \quad (2.73a)$$

$$T_{566} = - \int \left[ \frac{T_{166}}{\rho} + \frac{1}{2} R_{26}^2 + \frac{1}{2} \left( \frac{R_{16}}{\rho} \right)^2 \right] ds \quad (2.73b)$$

The integration of the transverse dispersion gives the longitudinal dispersion, and usually several dipoles are used to get a closed transverse dispersion. The frequently used configurations are the Dogleg chicane, C-chicane, S-chicane, and FODO arc as shown in Figure 2.5.

By convention the bunch head is the  $z < 0$  direction, thus  $R_{56}$  is positive in the dogleg and the FODO arc, and negative in the C-type and S-type chicane. Using thin lens

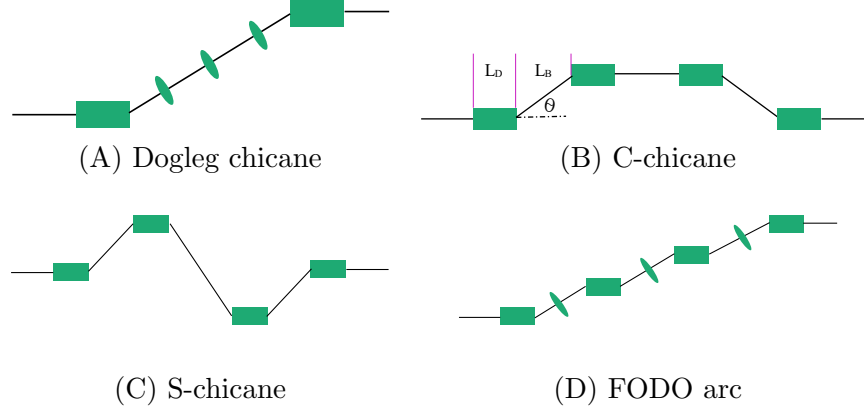


FIGURE 2.5: different types of magnetic compressor

approximation, the exact longitudinal dispersion value of C-chicane is given by

$$h_1 = R_{56} = -2\theta^2(L_D + \frac{2}{3}L_B), h_2 = T_{566} = -\frac{3}{2}R_{56} \quad (2.74)$$

For a dogleg chicane one has

$$h_1 = R_{56} = 2\rho(\sin \theta - \theta) + \frac{\Delta s}{\gamma^2} \quad (2.75)$$

The dogleg chicane and FODO arc are usually used to shift the beamline, and extra quadrupole are used to close the dispersion, while in C-type and S-type chicanes, the transverse dispersion is maturely closed, by tuning the phase advance in S-type chicane, the CSR induced emittance growth can be suppressed[81–83].

## 2.2 Laser plasma wakefield acceleration

When a drive beam (i.e laser, electron or proton beam) is injected into a plasma cell which is filled with gas, the electric field of the drive beam may ionize the gas into ions and electrons, they have equal charge, and are locally uniformly distributed. After ionization, they will be further driven by the external electric field and oscillate in the plasma cell, electron and ion have different oscillation frequency due to the large difference in mass, thus the local electrical neutrality is broken, and a periodic electromagnetic field is generated after the drive beam, this is the plasma wakefield.

The wakefield in the plasma can be described with Maxwell's equation, in differential form they can be written as

$$\nabla \cdot \vec{E} = \frac{\rho}{\epsilon_0} \quad (2.76)$$

$$\nabla \times \vec{E} = -\frac{\partial \vec{B}}{\partial t} \quad (2.77)$$

$$\nabla \cdot \vec{B} = 0 \quad (2.78)$$

$$\nabla \times \vec{B} = \mu_0 \epsilon_0 \frac{\partial \vec{E}}{\partial t} + \mu_0 \vec{J} \quad (2.79)$$

$$\nabla \cdot \vec{J} = -\frac{\partial \rho}{\partial t} \quad (2.80)$$

Since  $\nabla \times \nabla \vec{m} = 0$ ,  $\nabla \times \nabla \cdot \vec{m} = 0$ ,  $\vec{m}$  is an arbitrary vector, the magnetic vector potential and the electric scalar potential are defined as

$$\vec{B} = \nabla \times \vec{A} \quad (2.81)$$

$$\vec{E} = -\frac{\partial \vec{A}}{\partial t} - \nabla \Phi \quad (2.82)$$

The scalar potential given in equation 2.82 can be derived with equation 2.77 and 2.81, substituting 2.81 and 2.82 into 2.79, we have

$$\nabla \times \nabla \times \vec{A} = \nabla \nabla \cdot \vec{A} - \nabla^2 \vec{A} = -\mu_0 \epsilon_0 \left( \frac{\partial^2 \vec{A}}{\partial t^2} + \nabla \frac{\partial \Phi}{\partial t} \right) + \mu_0 \vec{J} \quad (2.83)$$

With Lorentz gauge condition  $\nabla \cdot \vec{A} = -\mu_0 \epsilon_0 \frac{\partial \Phi}{\partial t}$ , equation 2.83 is reduced to the wave equation

$$\nabla^2 \vec{A} - \mu_0 \epsilon_0 \frac{\partial^2 \vec{A}}{\partial t^2} = -\mu_0 \vec{J} \quad (2.84)$$

These formulas will be used in the subsequent derivation which follows the courses of S. Karsch [84].

## 2.2.1 Basic properties of the plasma and the laser beam

The plasma wakefield is generated by the different distribution of electrons and ions ionized from the gas, thus to derive the plasma wakefield one needs to study the ionization of the gas and the motion of electrons and ions under the external field from the drive beam (in our case, it is the laser pulse). In this section the ionization of the gas and the properties of the plasma and the laser beam are briefly introduced.

### 2.2.1.1 Ionization of the gas

The ionization process of the gas atom (hydrogen in this thesis) under the external field of the laser depends on the laser frequency and the laser intensity. In an atom, the electron is bound to the nuclei by the Coulomb force, when the laser frequency is so

high that  $\hbar\omega_L > E_{ion}$  ( $\hbar$  is the Planck constant,  $\omega_L$  is the frequency of the laser,  $E_{ion}$  is the ionization energy of the material and it is 13.6 eV for the ground state of hydrogen), the electron can overcome the potential barrier by absorbing one photon, this is called the photoelectric effect. With a Ti:sapphire laser ( $\lambda_L = 800 \mu\text{m}$ ), the energy of the photon is  $\hbar\omega_L = 1.6 \text{ eV}$ , much smaller than the Coulomb potential between nuclei and electron, thus the gas can't be fully ionized by the photoelectric effect.

When  $\hbar\omega_L < E_{ion}$ , the ionization process depends on the laser intensity, with a low intensity laser beam, the electric field of the laser can be ignored in comparison with the Coulomb force, the molecules are mainly ionized by absorbing multiple photons, this is the multiple photon ionization (MPI)[85], the ionization rate is related to the cross section of the atoms  $\sigma_a$  and the laser intensity  $I_L$ , in the case where  $n$  photons are needed for ionization, the ionization rate is given by

$$\Gamma = \sigma_a^n I_L^n \quad (2.85)$$

As the increase of the laser intensity, if the electric field is comparable to the Coulomb force, the barrier potential is modified, the electric potential created by an atom is

$$\Phi_a(r) = -\frac{1}{4\pi\epsilon_0} \frac{Ze^2}{r} \quad (2.86)$$

The potential of the laser follows that

$$\Phi_L(x, t) = -eE_L(t)r \quad (2.87)$$

The superposition of the two fields forms a new potential barrier as shown in Figure 2.6, due to the uncertainty principle, the electron at  $r_1$  may go to  $r_2$  and escapes from the nuclei, this is called tunnel ionization[86, 87].

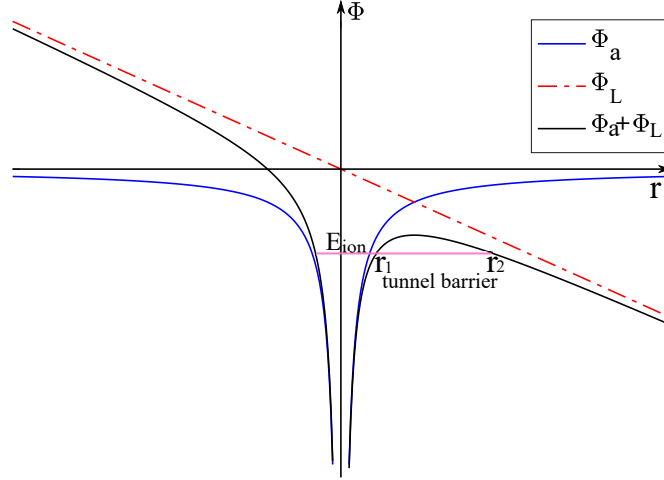


FIGURE 2.6: The tunnel ionization

The tunneling rate is given by

$$\Gamma \propto e^{-2 \left| \int_{r_1}^{r_2} \frac{\sqrt{2m(\Phi_p(r) + \Phi_L(r) - E_{ion})}}{\hbar} dr \right|} \quad (2.88)$$

If the laser intensity is so high that the modified potential is below the ionization potential, the electrons can leave the atom directly, without tunneling, as shown in Figure 2.7, this is the barrier suppression ionization (BSI) [88]. With the modified bar-

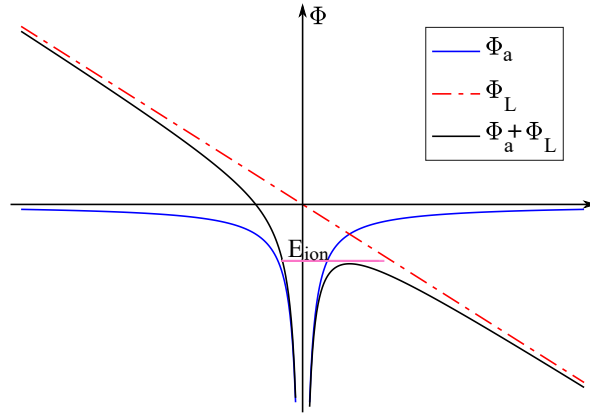


FIGURE 2.7: The barrier suppression ionization

rier potential being  $\Phi(r) = \Phi_a + \Phi_L$ , let  $d\Phi/dr = 0$ , the maximum value of  $\Phi$  yields  $\Phi_{max} = \sqrt{Ze^3 E_L / (\pi \epsilon_0)}$ . Let  $\Phi_{max} = E_{ion}$ , and with  $I_L = \frac{\epsilon_0 c E_L^2}{2}$ , the threshold laser intensity for BSI can be derived

$$I_{L.BSI} = \frac{\pi^2 \epsilon_0^3 c}{2 Z^2 e^6} E_{ion}^4 \quad (2.89)$$

For hydrogen  $E_{ion} = -13.6$  eV,  $I_{L.BSI}$  yields  $1.4 \times 10^{14} \text{ W/cm}^2$ .

In a laser plasma wakefield accelerator, the laser intensity is usually stronger than  $1 \times 10^{17} \text{W/cm}^2$ , three orders larger than the BSI intensity, thus the gas is fully ionized by the raising edge of the laser, it can be treated as a plasma in the subsequent discussion.

### 2.2.1.2 Basic parameters of plasma

Plasma is a state of matter in which an ionized gaseous substance becomes highly electrically conductive to the point that long-range electric and magnetic fields dominate the behavior of matter. It is a an electrically neutral medium of unbound positive and negative particles.

The thermal motion of the electrons and ions in the plasma are described by the plasma temperature  $T_e$ ,  $T_i$ , and we have

$$\frac{1}{2}m_e v_e^2 = k_B T_e \quad (2.90a)$$

$$\frac{1}{2}m_i v_i^2 = k_B T_i \quad (2.90b)$$

Where  $k_B$  is the Boltzmann's constant,  $m_e$ ,  $m_i$  are the mass of the electron and the ion,  $v_e$ ,  $v_i$  are the velocity of the electron and the ion, for equal ion and electron temperatures,  $\frac{v_e}{v_i} = \sqrt{\frac{m_i}{m_e}} \approx \frac{1}{43A_Z}$ ,  $A_Z$  is the proton number ( $A_Z = 1$  for hydrogen atom), thus ions are almost stationary on the electron time scale. The oscillation frequency of the electrons and ions are given by [89]

$$\omega_e = \sqrt{\frac{ne^2}{\epsilon_0 m_e}}, \quad \omega_i = \sqrt{\frac{ne^2}{\epsilon_0 m_i}} \quad (2.91)$$

Where  $\epsilon_0$  is the vacuum permittivity. As  $v_e \gg v_i$ , the current in the plasma is mainly generated by the motion of the electrons, the frequency of the electron is used as the plasma frequency.

The Debye length  $\lambda_D$  is a parameter that can define the quasi-neutrality scale in the plasma, the electrons in the plasma may rearrange themselves under the external field, and with one  $\lambda_D$  the externally applied potential drops to  $1/e$ . Thus on scales  $L \gg \lambda_D$ , the plasma is quasi-neutral, while for  $L \leq \lambda_D$  a localized electric field can occur in the plasma, it is given by

$$\lambda_D = \sqrt{\frac{\epsilon_0 k_B T_e}{ne^2}} \quad (2.92)$$

### 2.2.1.3 Basic parameters of the laser

The LASERIX laser will be used as the drive beam, it has an energy of 2 J, the intensity is distributed in the longitudinal and the transverse direction with a Gaussian profile and takes the form

$$I(r, z, t) = I_m(s) e^{-\frac{2r^2}{w(s)^2}} e^{-\frac{2(ct-z)^2}{L^2}} \quad (2.93)$$

Where,  $r$  is the radial distance to the laser center,  $z$  refers to the longitudinal distance to the laser center,  $L$  is the laser length (defined as the laser intensity falling to  $1/e^2$  of the maximum value),  $w(s)$  and  $I_m(s)$  are respectively the transverse size and maximum intensity of the laser, they evolve as the distance to the laser focal plane.

The laser power  $P$  and laser intensity  $I$  are related by

$$P = \int 2\pi r I dr = \int 2\pi r I_m e^{-\frac{2r^2}{w(s)^2}} e^{-\frac{2(ct-z)^2}{L^2}} dr = \frac{\pi}{2} I_m w(s)^2 e^{-\frac{2(ct-z)^2}{L^2}} \quad (2.94a)$$

$$E = \int P dt = \sqrt{\frac{\pi}{2}} \frac{\pi}{2} I_m w(s)^2 2L = \sqrt{\pi/2} P_m L \quad (2.94b)$$

The electric field of the laser is  $E_L = \sqrt{2I/(\epsilon_0 c)}$ , the laser amplitude is defined as  $a = \frac{eE_L}{m_e c \omega}$ ,  $\frac{eE_L}{\omega}$  is the maximum oscillation momentum of the plasma electron in the laser field (discussed in section 2.2.2), thus it indicates whether the electron motion is relativistic or not.

Consider a laser with a Gaussian distribution in the longitudinal direction, the intensity envelop and the corresponding electric field and field profile are shown in Figure 2.8, the half laser duration  $L$  is  $\sim 19$  fs, with a wavelength of  $\lambda_L = 800 \mu\text{m}$ , the peak intensity is  $1.04 \times 10^{18} \text{ W/cm}^2$ .



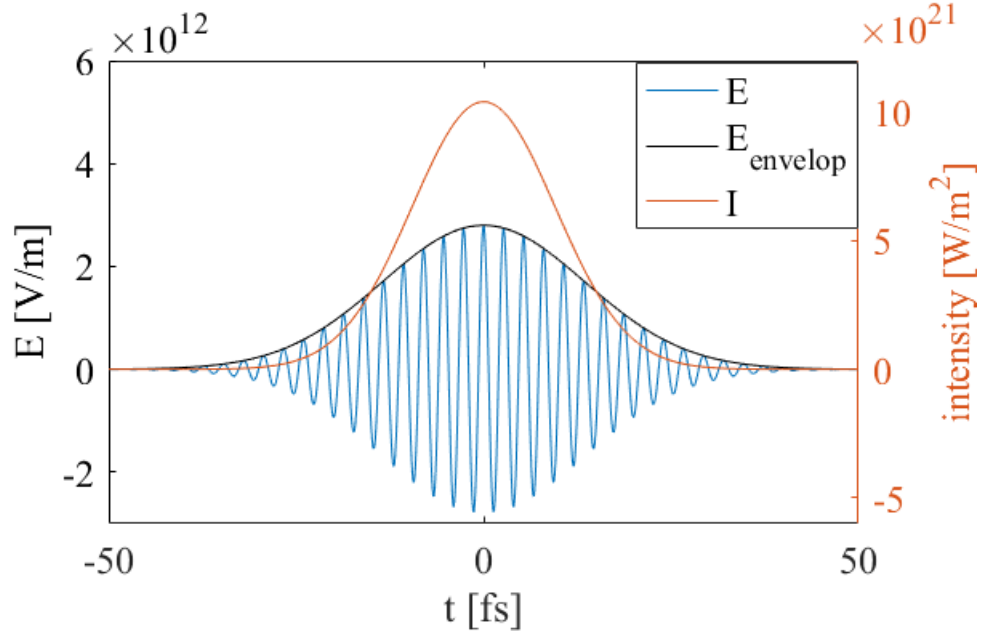


FIGURE 2.8: The laser intensity profile and the related electric field and field envelope

When propagating in an uniform media, the transverse envelop of a focused laser is shown in Figure 2.9, the transverse size is given by

$$w(s) = w_0 \sqrt{1 + \frac{s^2}{l_r^2}} \quad (2.95)$$

$l_r$  is the Rayleigh length and it is given by  $l_r = \pi w_0^2 / \lambda_L$ ,  $w_0$  is the waist of the laser,  $\lambda_L$  is the wavelength of the laser.

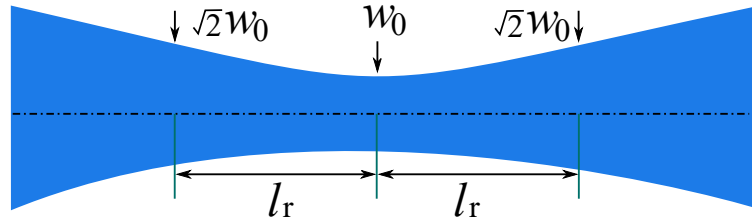


FIGURE 2.9: The transverse envelop of a focused laser beam

### 2.2.2 Electrons move in a plane electromagnetic field

Let's consider an electron moving in a plane electromagnetic wave which propagates along the  $z$  axis, the momentum equation is:

$$d\vec{p}/dt = -e(\vec{E} + \vec{v} \times \vec{B}) \quad (2.96)$$

In the plane electromagnetic wave, without loss of generality, let's assume that the electric field is in the  $x$  direction while the magnetic field is in the  $y$  direction, the electric field can be depicted with  $E_x = E_m \cos(\omega_L t - k_L z)$ ,  $\omega_L$  and  $k_L$  are respectively the angular frequency and wave number. According to the formula 2.79, 2.82, we have  $B_y = E_x/c$ ,  $A_x = \frac{E_m}{\omega_L} \sin(\omega_L t - k_L z)$ ,  $B_m = E_m/c = \frac{\omega_L}{c} A_m$  ( $\Phi$  is due to density modulation of plasma electrons, it is ignored here). Firstly, let's compare the maximum force exerted on the electron by the electric field and the magnetic field

$$F_{Emax} = -eE_m \quad (2.97a)$$

$$F_{Bmax} = -ev \times B_m = -ev \times \frac{E_m}{c} \quad (2.97b)$$

We have  $\frac{F_{Bmax}}{F_{Emax}} = \frac{v}{c}$ , which indicates that if  $v \ll c$ , the magnetic field can be ignored in the analysis, while if  $v$  is comparable to the speed of light  $c$ , the magnetic field must be included in the analysis. To estimate the value of  $v$ , consider an electron at rest at  $t = 0$ , it oscillates in the transverse direction under a periodic electric field  $F_x = eE_m \cos(\omega_L t - k_L z)$ , integrating this formula with  $t$ , the oscillation momentum follows that  $P_{os} = \frac{eE_m}{\omega_L} \sin(\omega_L t)$ . Then a conventionally used parameter  $a$  can be introduced as the quotient of  $P_{os}$  and  $mc$

$$a = \frac{eE_m \sin(\omega_L t)}{m\omega_L c} = \frac{eA}{mc} \quad (2.98)$$

The maximum value  $a_m = \frac{eE_m}{m\omega_L c} = \frac{eA_m}{mc}$  indicates whether the oscillation is in the relativistic regime or not. If  $a_m > 1$ , the maximum oscillation velocity is comparable with the speed of light  $c$ , the force of the magnetic field is comparable with that of the electric field. To study the motion of an electron in a plane electromagnetic wave (the laser intensity is constant in the 3D space volume), we will go to the momentum equation. Substituting 2.82, 2.81 into 2.96, we have

$$\frac{d\vec{p}}{dt} = e\nabla\Phi + e\frac{\partial\vec{A}}{\partial t} - e\vec{v} \times (\nabla \times \vec{A}) \quad (2.99)$$

With the relation that  $\frac{\partial \vec{A}}{\partial t} = \frac{d\vec{A}}{dt} - (\vec{v} \cdot \nabla) \vec{A}$ , and substituting equation 2.81 into equation 2.99, we have

$$\frac{d\vec{p}}{dt} = e \frac{d\vec{A}}{dt} - e \nabla(\vec{v} \cdot \vec{A}) \quad (2.100)$$

The second part in the right hand side is zero, thus we have the relation.

$$\vec{p} - e\vec{A} = C_1 \quad (2.101)$$

Since  $\vec{A} = (A_m \sin(\omega_L t - K_L z), 0, 0)$ , equation 2.101 is reduced to

$$p_x = eA \quad (2.102)$$

Since the magnetic field has no contribution to the electron energy, we have

$$\frac{d\gamma}{dt} = -\frac{e}{mc^2} \vec{v} \cdot \vec{E} = -\frac{e}{mc^2} v_x E_0 \cos(\omega_L t - k_L z) = -a_m \omega_L \beta_x \cos(\omega_L t - k_L z) \quad (2.103)$$

Let's write the momentum equation 2.96 in the x,y,z direction respectively, for the sake of convenience, the normalized momentum are used, i.e  $(\hat{p}_x, \hat{p}_y, \hat{p}_z) = (p_x, p_y, p_z)/(mc) = \gamma(\beta_x, \beta_y, \beta_z)$

$$\frac{d}{dt}(\hat{p}_x) = -a_m \omega_L \cos(\omega_L t - k_L z)(\beta_z - 1) \quad (2.104a)$$

$$\frac{d}{dt}(\hat{p}_y) = 0 \quad (2.104b)$$

$$\frac{d}{dt}(\hat{p}_z) = -a_m \omega_L \beta_x \cos(\omega_L t - k_L z) \quad (2.104c)$$

Comparing 2.104c and 2.103, we have

$$\frac{d\gamma}{dt} = \frac{d}{dt}(\hat{p}_z) \quad (2.105)$$

Integrating equation 2.105 yields

$$\gamma - \hat{p}_z = C_2 \quad (2.106)$$

For an electron which is at rest initially,  $C_1$  in equation 2.102 yields 0,  $C_2$  in equation 2.106 yields 1. Simultaneous  $\gamma^2 = 1 + \hat{p}_x^2 + \hat{p}_y^2 + \hat{p}_z^2$  and equation 2.106, 2.102, we obtain the relation  $\hat{p}_z = \frac{1}{2}\hat{p}_x^2$ , the motion of the electron in a electromagnetic plane wave can

be described with

$$\hat{p}_x = a \quad (2.107a)$$

$$\hat{p}_y = 0 \quad (2.107b)$$

$$\hat{p}_z = \frac{1}{2}\hat{p}_x^2 = \frac{1}{2}a^2 \quad (2.107c)$$

$$\gamma = 1 + \hat{p}_z = 1 + \frac{1}{2}a^2 \quad (2.107d)$$

The dimensionless parameter  $a$  takes the form that  $a = a_m \sin(\omega_L t - k_L z)$ , to calculate the electron trajectory, an integration is required, here a small trick is performed letting  $\omega_L \tau = \theta = \omega_L t - k_L z$ , then  $\tau = t - z/c$ , this is the so-called laser co-moving coordinate, we have the relation

$$\frac{d}{dt} = \frac{d}{d\tau} \frac{d\tau}{dt} = \frac{d}{d\tau} \left(1 - \frac{1}{c} \frac{dz}{dt}\right) = \left(1 - \frac{1}{\gamma} \hat{p}_z\right) \frac{d}{d\tau} = \frac{1}{\gamma} \frac{d}{d\tau} \quad (2.108)$$

Then equation 2.107a-2.107d can be rewritten with

$$\frac{dx}{d\tau} = ca_m \sin(\omega_L \tau) \quad (2.109a)$$

$$\frac{dy}{d\tau} = 0 \quad (2.109b)$$

$$\frac{dz}{d\tau} = \frac{c}{2} a_m^2 \sin^2(\omega_L \tau) \quad (2.109c)$$

Assume the electron is initially located at the origin ( $x = y = z = 0$ ), then it's trajectory follows

$$x = \frac{ca_m}{\omega_L} - \frac{ca_m}{\omega_L} \cos(\omega_L \tau) \quad (2.110a)$$

$$y = 0 \quad (2.110b)$$

$$z = \frac{ca_m^2}{8\omega_L} (2\omega_L \tau - \sin(2\omega_L \tau)) \quad (2.110c)$$

Equation 2.110a and 2.110c, indicate that: in the x direction, the electron oscillates with the frequency of the laser, and the amplitude depends linearly on  $a_m$ . In the z direction, the electron drifts forward and also oscillates with twice the laser frequency, the amplitude scales with the square of the laser strength  $a_m^2$ . Let's replace  $\tau$  with  $\tau = t - z/c$  and ignore the oscillation part, we have  $z = ca_m^2(t - z/c)/4$ , the drift distance yields

$$z = \frac{ca_m^2}{4 + a_m^2} t \quad (2.111)$$

In the laboratory frame, for  $a_m = 0.5$ , and  $a_m = 1$ , the electron trajectory in the  $x - z$  plane is shown in Figure 2.10, the oscillation amplitude in the x direction is proportional

to the laser amplitude  $a_m$ , while that in the  $z$  direction is proportional to  $a_m^2$ . In a primed frame, the coordinate moves with the mean velocity of the electron in the  $z$  direction, the trajectory of the electron for different laser amplitude is shown in Figure 2.11, for  $a_m = 1$ , the oscillation amplitude in the  $x$  direction is  $0.127 \mu\text{m}$ , and in the  $z$  direction is  $0.016 \mu\text{m}$ .

With a laser of finite length, the electron may oscillate in the  $x$  direction driven by the electric field at first, and then moves forward and oscillates in the  $z$  direction driven by the magnetic field, however, the motion stops after been overtaken by the back of the laser pulse, and returns back to static.

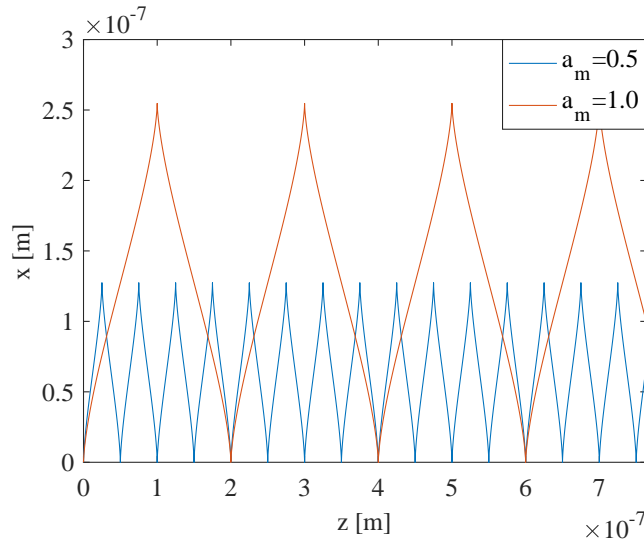


FIGURE 2.10: The trajectory of an electron in a plane electromagnetic field in the laboratory frame, with  $a_m = 0.5$  and  $a_m = 1.0$

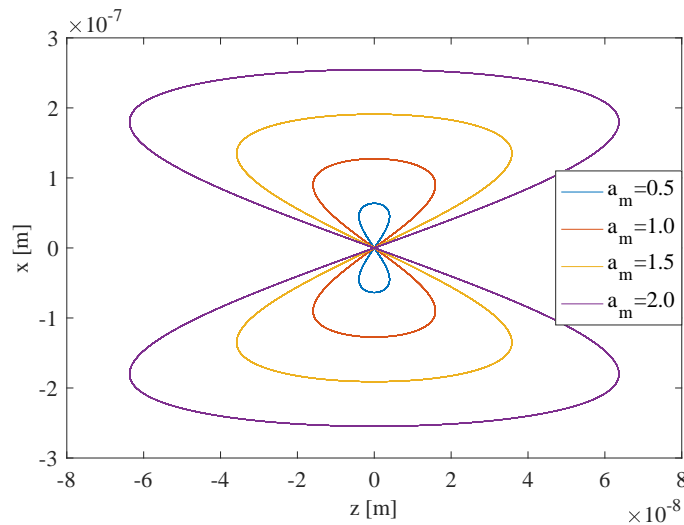


FIGURE 2.11: The trajectory of an electron in a plane electromagnetic field in the primed frame, with  $a_m$  from 0.5 to 2

### 2.2.3 Pondermotive force

In the previous section, the electron motion in a plane electromagnetic field has been discussed, where the laser is assumed to be uniform. However, in the real case the laser intensity has a distribution in the 3D volume, the pondermotive force introduced by the laser intensity profile will be discussed in this section.

Rewriting the momentum equation 2.99 with the normalized parameters and note that  $\frac{d}{dt} = \frac{\partial}{\partial t} + \vec{v} \cdot \nabla$ , we have

$$\frac{\partial \vec{p}}{\partial t} + (\vec{v} \cdot \nabla) \vec{p} = \frac{e}{mc} \nabla \Phi + \frac{\partial \vec{a}}{\partial t} - \vec{v} \times (\nabla \times \vec{a}) \quad (2.112)$$

This equation is usually solved order by order, i.e.  $\vec{a}(\vec{r}, t) = \vec{a}(r, t)|_{\vec{r}=0} + (\Delta \vec{r} \cdot \nabla) \vec{a}(r, t)|_{\vec{r}=0} + \dots$ , the first order is spatially independent, but it displaces the electrons, and a the second order force is exerted on the electron and 2.112 can be divided into

$$\frac{\partial \vec{p}_1}{\partial t} = \frac{\partial \vec{a}}{\partial t} \quad (2.113a)$$

$$\frac{\partial \vec{p}_2}{\partial t} = -(\vec{v}_1 \cdot \nabla) \vec{p}_1 + \frac{e}{mc} \nabla \Phi - \vec{v}_1 \times (\nabla \times \vec{a}) \quad (2.113b)$$

The first order motion is driven by the periodic electric field, while the second order motion is driven by the gradient of laser intensity. Generally, the second order parameters change much more slowly than the first order, the variables used in the second order are the average values of the first order in a period.

Equation 2.113a indicates that  $\vec{p}_1 = \vec{a} = \gamma \vec{v}_1 / c$ , the third term in the right side of 2.113b can be written with  $\vec{v}_1 \times (\nabla \times \vec{a}) = (\vec{v}_1 \cdot \vec{a}) \nabla - (\vec{v}_1 \cdot \nabla) \vec{a}$ . Without considering the restoring force of the electron potential, we have

$$\frac{\partial \vec{p}_2}{\partial t} = \frac{c}{\gamma} \nabla < -\vec{a} \cdot \vec{a} > \quad (2.114)$$

With  $\vec{F} = mc \frac{d\vec{p}}{dt}$ , the pondermotive force is derived

$$\vec{F}_p = \frac{m_e c^2 \nabla \vec{a}_m^2}{4 \langle \gamma \rangle} \quad (2.115)$$

The pondermotive force is introduced by the spatial distribution of the laser intensity, with the pondermotive force, electrons are expelled from the higher laser intensity region to the lower intensity region.

### 2.2.4 Establishment of the laser plasma wakefield

In the previous sections, the electron motion in the laser field has been discussed, where only the response of the electron to the laser is considered. In the plasma, the motion of electrons will lead to a charge density modulation, this density modulation in turn will introduce a coulomb restoring force to the electrons. The plasma density can be described with the continuity equation, while the restoring force can be described with Poisson's equation, just taking into consideration the second order motion of electrons, the electrons can be fully described with:

$$\frac{\partial \vec{\beta} \gamma}{\partial t} = \frac{e}{mc} \nabla \Phi - \frac{c}{\gamma} \nabla \langle \frac{\vec{a}^2}{2} \rangle \quad (2.116a)$$

$$\frac{\partial n_e}{\partial t} + \nabla \cdot (\vec{v} n_e) = 0 \quad (2.116b)$$

$$\nabla^2 \Phi = \frac{e(n_e - \alpha_i n_i)}{\epsilon} \quad (2.116c)$$

Here  $n_e$ ,  $n_i$  are respectively the electron and ion density,  $\alpha_i$  is the ion charge number, taking hydrogen for example  $\alpha_i = 1$ . The ions can be treated as static when studying the electrons motion, thus  $n_i$  is constant. Let's consider the case of the linear regime, where  $a \ll 1$ ,  $\gamma \approx 1$ , and the electron density perturbation is small, recognizing  $n_e - n_i$  with  $n_d$ , equation 2.116a-2.116c yield

$$\frac{\partial \vec{\beta}}{\partial t} = \frac{e}{mc} \nabla \Phi - c \nabla \langle \frac{\vec{a}^2}{2} \rangle \quad (2.117a)$$

$$\frac{\partial n_d}{\partial t} + \nabla \cdot (\vec{v} n_i) = 0 \quad (2.117b)$$

$$\nabla^2 \Phi = \frac{e n_d}{\epsilon} \quad (2.117c)$$

By further simplifying the previous equations, the three variable  $\vec{v}$ ,  $\Phi$ , and  $n_d$  can be described as

$$(\frac{1}{c^2} \frac{\partial^2}{\partial t^2} + k_p^2) n_d = n_i \nabla^2 \langle \frac{\vec{a}^2}{2} \rangle \quad (2.118a)$$

$$(\frac{1}{c^2} \frac{\partial^2}{\partial t^2} + k_p^2) \Phi = \frac{n_i e}{\epsilon} \langle \frac{\vec{a}^2}{2} \rangle \quad (2.118b)$$

$$(\frac{1}{c^2} \frac{\partial^2}{\partial t^2} + k_p^2) v = -\frac{\partial}{\partial t} (\nabla \langle \frac{\vec{a}^2}{2} \rangle) \quad (2.118c)$$

Because the laser and the wakefield propagates close to the speed of light, a co-moving coordinate  $\xi = ct - z$  is used to simplify the equation, the wake potential  $\Phi$  behind the laser can be solved by using Green's function [90]

$$\Phi = \frac{n_0 e}{2\epsilon} \int_{\xi_0}^{\xi} \sin k_p (\xi' - \xi_0) \langle a(\vec{\xi}')^2 \rangle d\xi' \quad (2.119)$$

Where  $\xi_0$  is the front of the laser,  $\langle \vec{a}^2 \rangle$  is the average value in a period, it only relies on the spatial distribution of the laser, e.g.  $\vec{a}^2$  usually takes the form that  $\vec{a}^2(\xi) = h_r(r, s)h_z(s)\vec{a}_m^2 \sin^2(k_L \xi)$ , while  $\langle \vec{a}^2 \rangle = \frac{1}{2}h_r(r, s)h_z(s)\vec{a}_m^2$ , here  $h_r$  and  $h_z$  are respectively the transverse and longitudinal shape function of the laser intensity, and  $\xi$  refers to the distance to laser front. For a Gaussian distribution,  $h_r$  and  $h_z$  takes the form

$$h_r = \exp\left(-\frac{2r^2}{w(s)^2}\right) \quad (2.120a)$$

$$h_z = \exp\left(\frac{2z^2}{L^2}\right) \quad (2.120b)$$

Where  $w(s)$  is the waist of the laser.  $z$  is the relative position to the laser peak,  $s$  is the distance to the laser focal plane.

Substituting the form factors of the laser beam into formula 2.119, and integrating in the laser duration, the wake potential after the laser yields

$$\Phi = \sqrt{\pi} \frac{a_m^2}{4\sqrt{2}} \frac{m_e c^2}{e} k_p L \exp(-k_p^2 L^2 / 8) \sin(k_p \xi) \exp\left(\frac{-2r^2}{w(s)^2}\right) \quad (2.121)$$

The expression  $x \exp(-x^2/8)$  takes a maximum value at  $x = 2$ , thus we can get a maximum wake potential with  $L = \frac{2}{k_p} = \frac{\lambda_p}{\pi}$ , the amplitude of the wake potential (normalized with the maximum value) versus  $\frac{L}{\lambda_p}$  is shown in figure 2.12. That means the laser duration should be matched with the plasma density to transfer maximum laser energy to the wakefield. With  $E = -\nabla \Phi$ , the longitudinal electric field and the transverse electric field yield

$$E_z = \sqrt{\pi} \frac{a_0^2}{4\sqrt{2}} \frac{m_e c \omega_p}{e} k_p L \exp(-k_p^2 L^2 / 8) \cos(k_p \xi) \exp\left(\frac{-2r^2}{w(s)^2}\right) \quad (2.122a)$$

$$E_r = \sqrt{\frac{\pi}{2}} a_0^2 \frac{m_e c^2 r}{e w(s)^2} k_p L \exp(-k_p^2 L^2 / 8) \sin(k_p \xi) \exp\left(\frac{-2r^2}{w(s)^2}\right) \quad (2.122b)$$



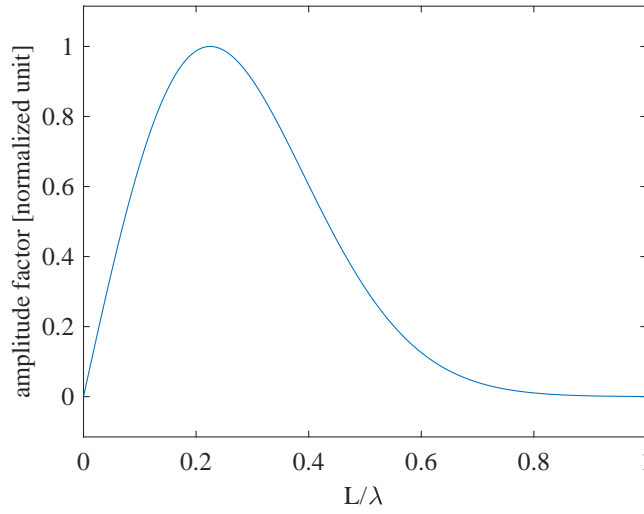


FIGURE 2.12: normalized wake potential versus laser length

From equation 2.117c, the electric field reaches its upper limit when all the electrons are expelled and the spatial oscillation amplitude is equal to the plasma wavelength  $\lambda_p$ , this is the so called wave breaking amplitude, with  $\nabla \cdot E_z = k_p E_z = \frac{n_i - n_0}{\epsilon}$ , and  $n_e = 0$ , the electric field yields  $E_{wb} = \frac{m_e c \omega_p}{e}$ , however, in the relativistic case, this formula should be corrected with

$$E_{wb.r} = E_{wb} \sqrt{2 \left( \frac{\omega_L}{\omega_p} - 1 \right)} \quad (2.123)$$

With  $n_e = 2 \times 10^{17}/\text{cm}^3$ ,  $\lambda_L = 0.8 \mu\text{m}$ ,  $\omega_p/\omega_L = 0.0107$ , and  $E_{wb} = 43.00 \text{ GV/m}$ ,  $E_{wb.r} = 13.59 E_{wb} = 584.36 \text{ GV/m}$ .

### 2.2.5 The self-focusing of the laser beam

Considering the propagation of an electromagnetic wave in a plasma, the electric field  $E_L$  and the magnetic field  $B_L$  can be described with

$$\nabla \times \vec{E}_L = -\frac{\partial \vec{B}_L}{\partial t} \quad (2.124a)$$

$$c^2 \nabla \times \frac{\partial \vec{B}_L}{\partial t} = \frac{1}{\epsilon_0} \frac{\partial J}{\partial t} + \frac{\partial^2 \vec{E}_L}{\partial t^2} \quad (2.124b)$$

Here  $J$  is the current generated by the electron motion in the plasma, the electrons are driven by the electric field and one has

$$m_e \frac{\partial v_e}{\partial t} = -e E_L, \quad J = -en_e v_e \quad (2.125)$$

With  $\frac{\partial}{\partial t} = i\omega_L$ ,  $\frac{\partial}{\partial z} = ik_L$ , combine 2.124 and 2.125 one has

$$(\omega_L^2 - c^2 k_L^2) \vec{E}_L = \frac{n_e e^2}{\epsilon_0 m_e} \vec{E}_L = \omega_p^2 \vec{E}_L \quad (2.126)$$

The dispersion relation in a plasma yields

$$\omega_L^2 = \omega_p^2 + k_L^2 c^2 \quad (2.127)$$

The phase velocity is then

$$v_{ph} = \frac{\omega_L}{k_L} = \frac{c}{\sqrt{1 - \frac{\omega_p^2}{\omega_L^2}}} = \frac{c}{\eta} > c \quad (2.128)$$

Where  $\eta$  refers to the plasma refractive index, the group velocity yields

$$v_g = \frac{\partial \omega_L}{\partial k_L} = \frac{k_L c^2}{\sqrt{\omega_p^2 + k_L^2 c^2}} = c\eta < c \quad (2.129)$$

The phase velocity is larger than the speed of light while the group velocity is smaller than the speed of light, with  $\omega_p > \omega_L$  the plasma reacts so fast that the external field is shielded and can't propagate in the plasma. For a given laser beam, the critical density  $n_c$  is given by

$$n_c = \frac{\omega_L^2 \epsilon_0 m_e}{e^2} \quad (2.130)$$

When  $n_e > n_c$  the plasma is under dense, the laser can propagate in the plasma, when  $n_e < n_c$  the plasma is over dense, the laser is completely reflected.

The refractive index depends on the ratio between the plasma frequency and the laser frequency, in case  $\omega_p^2/\omega_L^2 \ll 1$  the plasma has almost no effect to the propagation of the laser beam.

However, if the effect of the plasma can't be ignored, with  $\omega_p \propto \sqrt{n_e/m_e}$ , both the density of the electrons and the mass of the electrons (Lorentz factor  $\gamma$  in relativistic case should be considered) have influence on the refractive index, the nonlinear relativistic optics (i.e. transverse relativistic self focusing, longitudinal pulse compression, self-phase modulation) should be considered.

The plasma density can be affected by the initial gas density, ionization process, and also the pondermotive force from the laser, with the pondermotive force electrons are expelled from the axis where the laser intensity is higher, thus the electron density increase with the distance to the propagation axis. With  $r_2 > r_1$ , one has  $n_e(r_2) > n_e(r_1)$ , thus

$\eta(r_1) > \eta(r_2)$ ,  $v_{ph}(r_1) < v_{ph}(r_2)$ , the wave front of the energy flux is tilted to the axis, the laser is focused by the electron density distribution.

The electrons are driven by the laser field and move with a Lorentz factor of  $\gamma_e = 1 + a^2/2$ , the average value in one period is  $\langle \gamma_e \rangle = 1 + a_m^2/4$ , as  $a_m \propto I\lambda_L^2$ ,  $\langle \gamma_e \rangle = 1 + a_m^2/4$  increases with the laser intensity. For the Gaussian distributed laser, with  $r_2 > r_1$ , one has  $\langle \gamma_e(r_1) \rangle > \langle \gamma_e(r_2) \rangle$  and  $\eta(r_1) > \eta(r_2)$ , the laser experiences a focusing force from the relativistic effect (self-focusing), this focusing effect counteracts the defocusing force from diffraction, and the balance takes place if

$$P_c[\text{GW}] = 17.4 \frac{\omega_L^2}{\omega_p^2} \quad (2.131)$$

With a given plasma density, the self-focusing effect increases with the laser power.

### 2.2.6 Injection of the electrons

In the previous analysis, the plasma electrons only oscillates under the electromagnetic field of the laser and form the plasma wave, it is also an important issue to inject electrons into the plasma wave and get efficient acceleration.

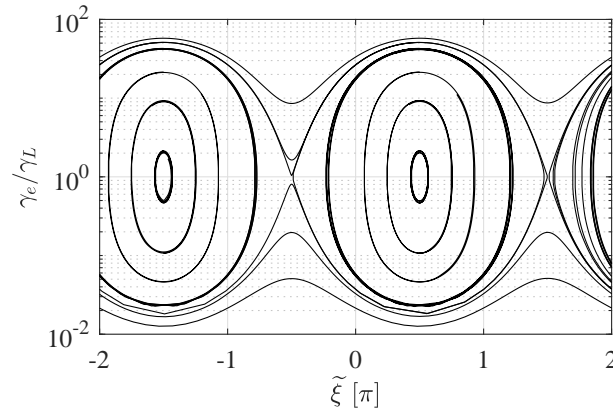


FIGURE 2.13: The orbits of single particle in the phase energy space, the horizontal axis  $\tilde{\xi}$  is the acceleration phase and the vertical axis is the Lorentz factor of the electron over that of the laser beam.

The longitudinal motion of the electrons in the plasma wave can be described with their energy  $\gamma_e$  and the acceleration phase  $\xi$ , for simplicity, the phase  $\xi$  is normalized with  $k_p$  and we have  $\tilde{\xi} = k_p \xi$ , the evolution of the  $(\gamma_e, \tilde{\xi})$  depend on their injection phase, injection energy and the strength of the plasma wakefield, the orbit of single particles in the energy-phase space can be achieved by solving the 1-D equation of motion 4.6, i.e with the normalized longitudinal electric field being set to  $\tilde{E}_z = E_z/E_{wb} = 0.13$ ,

the Lorentz factor of the laser beam being set to  $\gamma_L = 97$ , the orbits of electrons with different injection phase and energy are shown in Figure 2.13, only the electrons in the closed orbits can get efficient acceleration from the plasma wave. Thus the injection of the electrons is to tune the injection phase, the energy of the electrons and the strength of the plasma wakefield to make the electrons in the closed orbits.

A relatively simple injection method is the "self-injection", where the plasma wave amplitude is close to the wave-breaking threshold, the velocity of the quiver motion is close to the phase velocity of the plasma wave, the background electrons can be trapped by the plasma wave and then be accelerated [11, 12, 15, 91], a high charge electron bunch with energy spread of several percent can be produced. However, it is difficult to control the injection process because the self-injection is usually related to the non-linear effects of the laser (i.e relativistic self-focusing and self compression [30]), the electron beam is untunable and usually unstable.

Other methods such as the ionization injection, colliding-pulse injection, density ramp injection can also be used to inject electrons in the plasma wave. Ionization injection takes places in high-Z gas, the electrons in low energy level can be ionized by the edge of the laser field, where the laser intensity is relatively lower (typically  $I < 10^{16} \text{W/cm}^2$ ), the inner electrons are ionized near the crest of the laser, they may be trapped by the plasma wave [34–37], however, the injection happens all along the propagation, thus the energy spread of the electron bunch is relatively large. In colliding-pulse injection, two laser pulses are used, one is for the excitation of the plasma wave, another is for the injection of the electrons [92], the widely used scheme is that two laser pulses counter propagate and collide in the plasma [41–44], the interference generates a laser beat-wave which can accelerate the plasma electrons to help them to be trapped by the plasma wave, the position of the interference point can be tuned to adjust the injection phase, the injected electron bunch has a duration of several femtoseconds, the initial bunch volume can also be tuned by the injection laser pulse, however, the system is quite complicated as two laser pulses are used, femtosecond level synchronization and micrometer level alignment are required. In plasma density ramp injection, a down density ramp is used to slow down the phase velocity of the plasma wave, thus electrons are easier to be trapped, it has been demonstrated to be an efficient and stable method for electrons injection [38–40], the energy spread is in the 10% range.

However, with the previous injection methods, the stability, and quality (emittance, energy spread) of the electron beam is still not comparable with that of the beam produced by conventional RF accelerators. One possible way to improve the beam quality is to combine the RF injector and the plasma structure, by injecting an external electron bunch from the RF injector into the plasma wave, the electron bunch from the

RF injector is more stable and tunable, it can be manipulated to match the electric field of the plasma wave [93], thus the beam quality can be optimized, several running and planned project are aiming to study the external injection scheme [46, 49, 50, 94]. Due to the short period duration of the accelerating plasma buckets (typically on the order of 10 fs to 300 fs,) synchronization accuracy of a few femtoseconds is required, the bunch duration should also be compressed to femtoseconds level before being injected into the plasma wave.

### 2.2.7 Limitation of the energy gain

One of the limitation to the energy gain of the electrons in the plasma wave is the divergence of the laser, the effective acceleration section is only within one Rayleigh length before and after the laser focal plane. Several methods have been developed to extend the propagation length of the laser.

Relativistic self-focusing [95, 96] is one of the most commonly employed method, for the simplicity of its implementation, the laser defocusing effect can be fully counteracted if the laser power is larger than the critical power  $P_c = 17.4 GW \omega_L^2 / \omega_p^2$ . The principle of relativistic self-focusing has been discussed before, the radial profile of the laser leads to a radial profile of  $\gamma_e$  of the plasma electrons, thus the plasma refractive index varies with radius, that acts as a positive lens and exerts a focusing force on the laser.

Hollow capillary tube is another tool used to guide the laser, the laser energy is maintained by the reflection at the inner walls of the capillary tube. The capillary tube can be a metallic tube or a dielectric tube, a metallic tube can be used to guide the laser without loss at the inner wall, while it's surface is usually not optically smooth for the interested laser wavelength and tube size. With a dielectric tube, the inner wall can be easily manufactured to be optically smooth, but partial energy loss occurs at the inner walls. These have been studied in [97, 98], in this thesis, the guiding of the laser beam with a hollow dielectric capillary tube will be studied in chapter 5.

Another important topic on laser guiding is the plasma channel, the radial plasma density profile is modified thus it is capable of compensating the diffraction of the laser, the density is minimum on the laser propagation axis, the exact density profile required to focus the laser is dependent on the laser profile. A parabolic plasma channel can be used to guide a Gaussian beam with constant spot size, the radial density profile is given by  $n_e(r) = n_e(0) + \Delta n_c(r^2/w_0^2)$  [96, 99], where  $\Delta n_c = 1/(\pi r_e w_0^2)$  is the channel depth [100], with  $r_e = e^2/mc^2$  is the classical electron radius. The plasma channel is usually generated by an external electrical discharge [101–104], or by a heating laser

pulse [16, 105]. The plasma channel is formed by the expansion of the heated plasma, thus the synchronization is quite important, and the system is more complicated.

Even when the laser is properly guided, the energy gain of the electron bunch is limited by the dephasing length of the electrons [106] and the depletion length of the laser [107]. The dephasing length is defined as the length over which the electrons slip to the decelerating phase of the electric field. Recognize the velocity of the electron and plasma wave as  $v_e$  and  $v_p$ , thus in the 1D (only considering the longitudinal direction) linear regime the dephasing length  $L_d$  is given by

$$\int_0^{L_d} (1 - \beta_g/\beta_e) ds = \lambda_p/2 \quad (2.132)$$

In the ultra-relativistic case, it can be simplified to  $L_d = \lambda_p/(2(1 - \beta_p)) \approx \frac{\omega_L^2}{\omega_p^2} \lambda_p$ , if the transverse field is taken into consideration, the acceleration and focusing phase region is  $\lambda/4$ , the dephasing length denotes  $L_d = \frac{\omega_L^2}{2\omega_p^2} \lambda_p$ . While, it has been found that this dephasing process can be compensated with an up plasma density ramp, the plasma wavelength decreases with the increase of the plasma density, with proper plasma density profile, the acceleration phase can be fixed during the propagation [25, 108, 109].

The laser pump depletion length is defined as the length  $L_{pd}$  over which the energy contained in the plasma wave equals that of the laser beam, in the linear regime, it is given by [107]

$$L_{pd} = \frac{\omega_L^2}{\omega_p^2} \frac{c\tau_L}{a_0^2} \quad (2.133)$$

Where  $\tau_L$  is the laser duration, the Lorentz factor of the plasma wave  $\gamma_p$ , the dephasing length and the depletion length in the linear regime, the nonlinear regime and 3D bubble regime are summarized in [110], and are shown in Table 2.1

TABLE 2.1: The dephasing length and the depletion length in different regimes.

	$a_0$	$\gamma_p$	$L_d$	$L_{pd}$
Linear	$<1$	$\frac{\omega_L}{\omega_p}$	$\frac{\omega_L^2}{2\omega_p^2} \lambda_p$	$\frac{\omega_L^2}{\omega_p^2} \frac{c\tau_L}{a_0^2}$
1D nonlinear	$>1$	$\sqrt{a_0} \frac{\omega_L}{\omega_p}$	$4a_0^2 \frac{\omega_L^2}{\omega_p^2} \lambda_p$	$\frac{1}{3} \frac{\omega_L^2}{\omega_p^2} c\tau_L$
3D nonlinear	$>1$	$\frac{1}{\sqrt{3}} \frac{\omega_L}{\omega_p}$	$\frac{4}{3} \frac{\omega_L}{\omega_p} \frac{\sqrt{a_0}}{k_p}$	$\frac{\omega_L^2}{\omega_p^2} c\tau_L$

In the linear regime, if  $\lambda_p/2 > c\tau_L/a_0^2$  then the energy is mainly limited by the laser depletion, otherwise the energy gain is limited by the dephasing of the electron.

## Chapter 3

# Electron bunch compression and matching before the plasma

The RF gun PHIL has a photo cathode and a 2.5 cell standing wave cavity that can generate an electron beam up to an energy of 6 MeV, and another S-band booster is available to accelerate the electron beam to more than 10 MeV, the bunch duration at the gun exit is  $\sim 1$  ps RMS, it is much longer than the plasma wave packet, thus an efficient compression of the electron bunch is required.

In this chapter, a dogleg chicane is designed to compress the electron bunch longitudinally before the plasma. The dogleg is composed of two dipoles, four quadrupoles and two sextupoles, the dipoles are used to bend the electrons thus the electrons with higher energy (bunch head) travels a longer trajectory than the electrons with lower energy (bunch tail), this is the principle of the bunch compression. The quadrupoles are mainly used to cancel the transverse dispersion terms  $R_{16}$  and  $R_{26}$  which lead to the emittance growth. The sextupoles are capable of matching the second order terms  $T_{566}$  with the RF curvature, and suppressing the emittance growth caused by  $T_{166}$  and  $T_{266}$ . The beam optics is studied analytically with thin lens approximation, and then numerically with the optical designing code Madx, the beam dynamics is studied with the combination of four different codes: ELEGANT, ASTRA, IMPACT-T and CSRTrack.

In the simulation, the effects of space charge and CSR are mainly checked, to verify the simulation result, Impact-T and CSRTrack are used for cross-checking.

After the dogleg chicane, the electron bunch should be transversely focused to match the plasma wakefield, we present the design of a transfer line composed of a quadrupole doublet and a quadrupole triplet that matches the  $\alpha_{x,y}$  to 0 and  $\beta_{x,y}$  to 0.1. While referring to the subsequent acceleration in the plasma, it's difficult to define the matching

condition at the plasma entrance, the electron bunch is just need to be focused to a size much smaller than the laser beam, thus a solenoid is used to focus the 10 MeV beam.

### 3.1 The PHIL Beam line

The AlphaX gun PHIL[111] will be used as the external electron source, it is composed of a copper photocathode and a 2.5 cell S-band standing wave cavity located just after the cathode, a layout of the beginning of the PHIL beamline is shown in Figure 3.1.

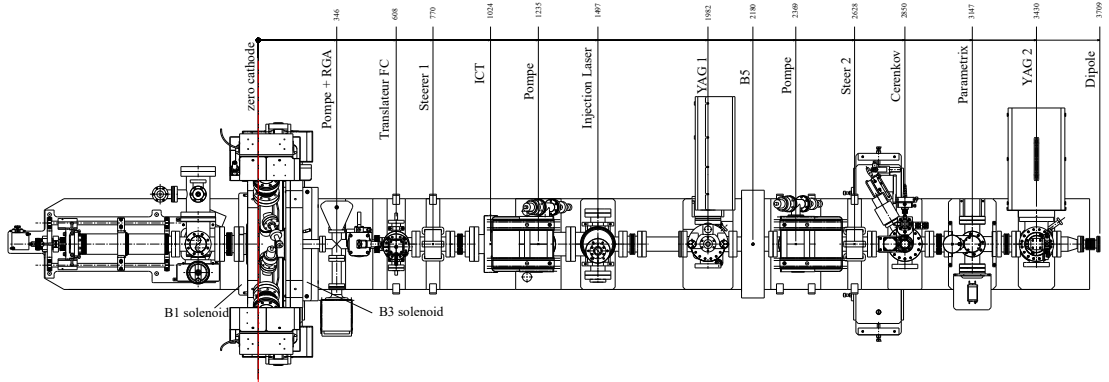


FIGURE 3.1: The layout of the original PHIL beamline.

Three solenoids B1, B3 and B5 are used, the B3 solenoid is located 14 cm after the photocathode, it is used to optimize the bunch transverse emittance at the RF-gun exit by emittance compensation process [68, 112]. The transverse emittance at the entrance of the B5 solenoid versus the maximum magnetic field of B3 is shown in Figure 3.2. The B1 solenoid is used to cancel the magnetic field on the photocathode produced by B3, B5 is located 2.18m after the cathode, it is used to transversely focus the electron bunch, that will be used to tune the beta function at the dogleg entrance.



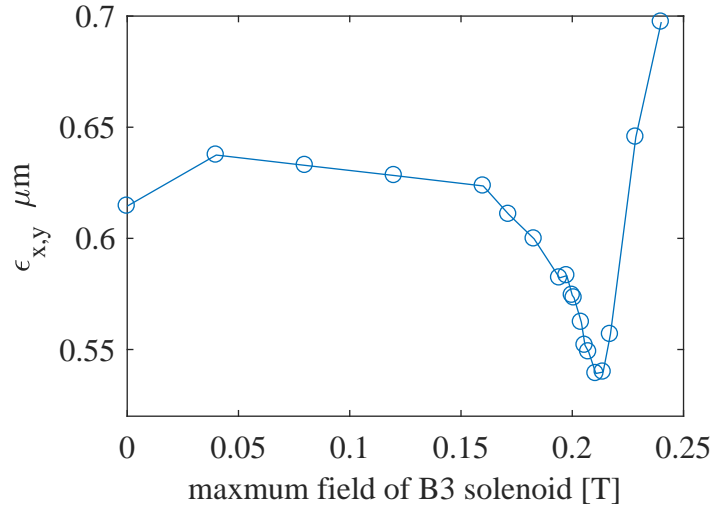


FIGURE 3.2: The transverse emittance at the entrance of the B5 solenoid versus the maximum field of the B3 solenoid.

The profile of the on axis normalized acceleration field is shown in Figure 3.3, at a field gradient of 92 MV/m, the gun is expected to deliver electron beams with an energy of up to 6 MeV [58].

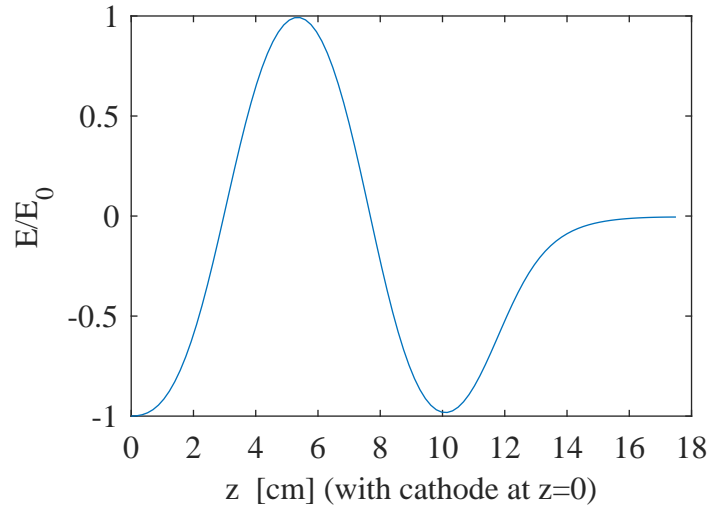


FIGURE 3.3: Normalized profile of the on axis longitudinal electric field of the PHIL 2.5 cell photocathode RF-gun.

For the ESCULAP project, the PHIL photo-injector will be upgraded by implementing a S-band accelerating section downstream of the gun, and then extract the beam with a dipole at  $z = 2.5$  m. The accelerating section is capable of accelerating the beam to  $\sim 10$  MeV and also generating an energy chirp, the normalized profile of the on axis longitudinal field of the accelerating section is shown in Figure 3.4.

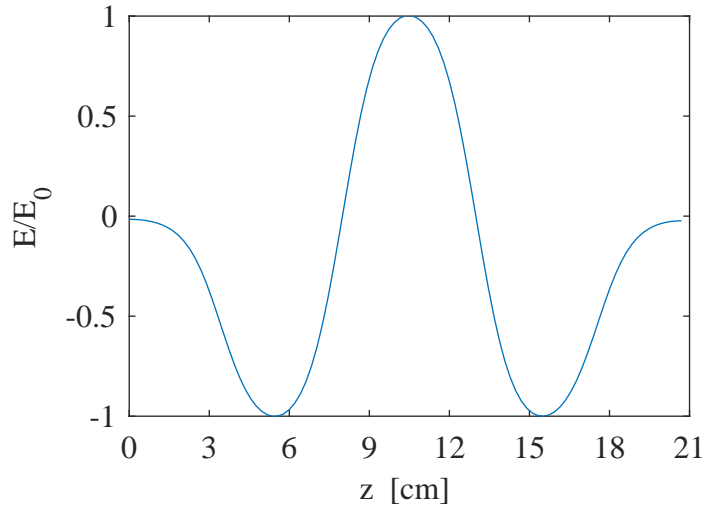


FIGURE 3.4: Normalized profile of the on axis longitudinal electric field of the standing wave booster.

### 3.2 Generating an energy chirp in a standing wave cavity

In a traveling wave structure, the longitudinal field takes the form  $E = E_0 \cos(\omega t - k_{rf} z)$ , the electron beam moves together with the RF wave and rides on a specific phase, assume the reference electron is riding on phase  $\phi_0$ , then the electric field witnessed by a general electron at the same time is shown in formula 2.61, and the energy-position correlation can be described with formula 2.62. But in a standing wave cavity, the acceleration phase witnessed by the electron is changing along the cavity, the energy-position correlation in a standing wave structure will be discussed here.

The longitudinal electric field in a standing wave cavity is  $E_z = E_0(z) \cos(\omega_{rf} t)$ ,  $E_0(z)$  is symmetric with respect to the midpoint of the structure, the field witnessed by the reference particle is

$$E_z = E_0(z) \cos(\omega_{rf} t + \phi_0) \quad (3.1)$$

$\phi_0$  is the reference phase, and concerning that the velocity of the reference electron  $v_e$  is approximately equal to the phase velocity of the RF wave  $v_{ph.rf}$ , 3.1 can be written as

$$E_z = E_0(z) \cos(k_{rf} z + \phi_0) \quad (3.2)$$

$z$  is then the position of the reference electron, thus the electric field witnessed by a general electron at the same position is

$$\begin{aligned} E_z &= E_0(z) \cos(k_{rf} z + k_{rf} \Delta z + \phi_0) \\ &= E_0(z) \cos(k_{rf} z) \cos(k_{rf} \Delta z + \phi_0) - E_0(z) \sin(k_{rf} z) \sin(\Delta z + \phi_0) \end{aligned} \quad (3.3)$$

Ignoring the relative longitudinal position change in the short cavity (in a long cavity, this should be considered, and which results in the velocity bunching), then  $\Delta z$  is constant, by integrating the longitudinal electric field along the cavity, the energy gain of a general electron yields

$$\Delta E_e = e \int_{-L/2}^{L/2} [E_0(z) \cos(k_{rf}z) \cos(k_{rf}\Delta z + \phi_0) - E_0(z) \sin(k_{rf}z) \sin(\Delta z + \phi_0)] dz \quad (3.4)$$

$L$  is the length of the cavity, then  $E_0(z)$  and  $\cos(k_{rf}z)$  have even symmetry, while  $\sin(k_{rf}z)$  has odd symmetry, thus the sin term vanishes. Identify  $\int_{-L/2}^{L/2} e[E_0(z) \cos(k_{rf}z)] dz$  as the maximum energy gain  $\Delta E_{e,max}$ , the energy gain of a general electron is then  $\Delta E_e = \Delta E_{e,max} \cos(k_{rf}\Delta z + \phi_0)$ , it has the similar form with that in the traveling wave cavity. The energy change of the reference electron is then  $E_{e0} = \Delta E_{e,max} \cos \phi_0$ , the energy position correlation after the cavity is then

$$\delta = \frac{E_{i0}}{E_{f0}} \delta_0 - \frac{\Delta E_{e0}}{E_{f0}} \tan(\phi_0) k_{rf} z_i - \frac{1}{2} \frac{\Delta E_{e0}}{E_{f0}} k_{rf}^2 z_i^2 + \frac{1}{6} \frac{\Delta E_{e0}}{E_{f0}} \tan(\phi_0) k_{rf}^3 z_i^3 \quad (3.5)$$

The parameter used here has the same definition as that in a traveling wave cavity, that is,  $E_{i0}$  and  $E_{f0}$  are respectively the energy of the reference electron at the cavity entrance and exit,  $\Delta E_{e,max} \cos(\phi_0) = E_{f0} - E_{i0}$ ,  $\delta_0$  refers to the normalized energy deviation at the cavity entrance.

The RF gun PHIL is capable of producing a stable electron beam at 5 MeV,  $E_{f0}$  is set to 10 MeV considering the capture of the electrons in subsequent plasma wave, thus  $\Delta E_{e0} = 5$  MeV, the corresponding  $R_{56}$  for full compression is  $R_{56} = 2/(k_{rf} \tan \phi_0)$ . By setting  $\Delta E_{e0} = 5$  MeV, the required field gradient of the booster and the  $R_{56}$  required for full compression versus acceleration phase in the booster is shown in Figure 3.5.

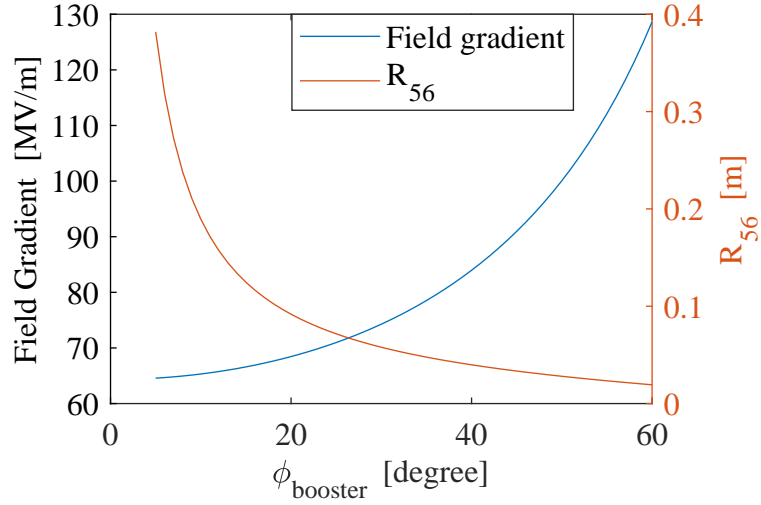


FIGURE 3.5: Energy gain in the gun and the booster are both set to 5 MeV, then the field gradient needed for the booster versus the acceleration phase, and the corresponding  $R_{56}$  that satisfying the full compression condition.

The required gradient increases with the acceleration phase, while the full compression  $R_{56}$  decreases with the acceleration phase, a relatively small  $R_{56}$  may reduce the requirement to the bend dipoles, and also suppress the radiation in a bend section. But the gradient can not go beyond 100 MV/m, thus to get a full compression, the minimum longitudinal dispersion should be  $R_{56} > 0.028$ , i.e with a gradient of 90 MV/m, one should have  $R_{56} = 0.033m$ .

### 3.3 Beam optics of a dogleg chicane

#### 3.3.1 Emittance growth in a dogleg chicane

The longitudinal matching of  $R_{56}$  and the energy chirp has been discussed in the previous section, since an energy chirp should be imparted to the beam before the dogleg, the beam has a relatively large energy spread, the transverse emittance caused by transverse dispersion terms should be studied. Identify the x-x' plane as the bending plane, identify the status of the electron at the dogleg entrance as  $X_0 = (x_0; x'_0)$ , and recognize the first and second order of transverse dispersion terms as  $\eta_x = (R_{16}; R_{26})$ ,  $T_x = (T_{166}; T_{266})$ , thus the emittance after the dogleg takes the form that

$$\begin{aligned} \epsilon_{x.tr} &\stackrel{det}{=} < XX^T > \\ &\stackrel{det}{=} < (RX_0 + \eta_x \delta_0 + T_x \delta_0^2)(RX_0 + \eta_x \delta_0 + T_x \delta_0^2)^T > \end{aligned} \quad (3.6)$$

Assume no correlation between  $x_0$ ,  $x'_0$  and  $\delta_0$ , then formula 3.6 reduced to

$$\epsilon_{x.tr} \stackrel{det}{=} < RX_0 X_0^T R^T + \eta_x \eta_x^T \delta_0^2 + T_x T_x^T \delta_0^4 > \quad (3.7)$$

The first term in equation 3.7 results from the initial emittance and it is invariant, the second term is the first order dispersion, it can be matched to 0 with quadrupoles between two dipoles, while the third term is the second order dispersion, extra sextupoles are needed to eliminate it.

Assume that the first order has been eliminated, the emittance in the x direction is then

$$\begin{aligned} \epsilon_{x.tr} &\stackrel{det}{=} \left\langle \epsilon_{x0.tr} R \begin{bmatrix} \beta_{x0} & -\alpha_{x0} \\ -\alpha_{x0} & \gamma_{x0} \end{bmatrix} R^T + T T^T \delta_0^4 \right\rangle \\ &\stackrel{det}{=} \left\langle \epsilon_{x0.tr} \begin{bmatrix} \beta_x & -\alpha_x \\ -\alpha_x & \gamma_x \end{bmatrix} + \delta_0^4 \begin{bmatrix} T_{166}^2 & T_{166} T_{266} \\ T_{166} T_{266} & T_{266}^2 \end{bmatrix} \right\rangle \\ &= \sqrt{\epsilon_{x0.tr}^2 + \epsilon_{x0.tr} \delta_0^4 (T_{166}^2 \gamma_x + T_{266}^2 \beta_x + 2T_{166} T_{266} \alpha_x)} \end{aligned} \quad (3.8)$$

While in the y direction, there is no dispersion terms, thus the emittance is invariant from the beam optics of view. However, as will be discussed later, sextupoles will be introduced to tune the second order longitudinal dispersion  $T_{566}$ , the sextupoles will also introduce second order aberration terms (i.e  $T_{336}$ ,  $T_{346}$ ,  $T_{436}$ ,  $T_{446}$ ), and also the coupling terms (i.e  $T_{331}$ ,  $T_{332}$ ,  $T_{341}$ ,  $T_{342}$ ,  $T_{431}$ ,  $T_{432}$ ,  $T_{441}$ ,  $T_{442}$ ), that will contribute to the emittance growth in the y direction, by defining that  $Y = [y, y']$ ,  $T_y = [T_{336}, T_{346}; T_{436}, T_{446}]$ , the formula for emittance growth shall be quite complex if all terms are included, ignoring the coupling terms, the emittance follows that

$$\begin{aligned} \epsilon_{y.tr} &\stackrel{det}{=} < Y Y^T > \\ &\stackrel{det}{=} < (R + T_y \delta_0) Y_0 Y_0^T (R + T_y \delta_0)^T > \end{aligned} \quad (3.9)$$

By submitting the Twiss parameters into  $Y_0 Y_0^T$ , the emittance in the y direction after the dogleg yields

$$\begin{aligned} \epsilon_{y.tr}^2 / \epsilon_{y0.tr}^2 = & 1 + (T_{346} T_{436} - T_{336} T_{446})^2 \delta_0^4 \\ & + \gamma_{y0} (\beta_y T_{446}^2 + 2\alpha_y T_{346} T_{446} + \gamma_y T_{346}^2) \delta_0^2 \\ & + \beta_{y0} (\beta_y T_{436}^2 + 2\alpha_y T_{336} T_{436} + \gamma_y T_{336}^2) \delta_0^2 \\ & - 2\alpha_{y0} (\beta_y T_{436} T_{446} + \alpha_y T_{336} T_{446} + \alpha_y T_{346} T_{436} + \gamma_y T_{336} T_{346}) \delta_0^2 \end{aligned} \quad (3.10)$$

Because the longitudinal dispersion term  $R_{56}$  determines the longitudinal compression, while the transverse dispersion determines the emittance growth, the design of the dogleg chicane is mainly focused on matching the dispersion terms.

### 3.3.2 Linear optics in thin lens approximation

In this section the dispersion terms  $R_{16}$ ,  $R_{26}$ ,  $R_{56}$  will be derived under thin lens approximation. The 6D transfer matrix of a dipole, a quadrupole and a drift take the form

$$M_B(\rho, \theta) = \begin{bmatrix} \cos(\theta) & \rho \sin(\theta) & 0 & 0 & 0 & \rho - \rho \cos(\theta) \\ -\sin(\theta)/\rho & \cos(\theta) & 0 & 0 & 0 & \sin(\theta) \\ 0 & 0 & 1 & \rho \sin(\theta) & 0 & 0 \\ 0 & 0 & 1 & 0 & 0 & 0 \\ -\sin(\theta) & \rho \cos(\theta) - \rho & 0 & 0 & 1 & \frac{\rho\theta}{\gamma^2} + \rho \sin(\theta) - \rho\theta \\ 0 & 0 & 0 & 0 & 0 & 1 \end{bmatrix} \quad (3.11)$$

$$M_Q(f) = \begin{bmatrix} 1 & 0 & 0 & 0 & 0 & 0 \\ \frac{-1}{f} & 1 & 0 & 0 & 0 & 0 \\ 0 & 0 & 1 & 0 & 0 & 0 \\ 0 & 0 & \frac{1}{f} & 1 & 0 & 0 \\ 0 & 0 & 0 & 0 & 1 & 0 \\ 0 & 0 & 0 & 0 & 0 & 1 \end{bmatrix} \quad (3.12)$$

$$M_D(L) = \begin{bmatrix} 1 & L & 0 & 0 & 0 & 0 \\ 0 & 1 & 0 & 0 & 0 & 0 \\ 0 & 0 & 1 & 0 & 0 & 0 \\ 0 & 0 & 0 & 1 & 0 & 0 \\ 0 & 0 & 0 & 0 & 1 & \frac{L}{\gamma^2} \\ 0 & 0 & 0 & 0 & 0 & 1 \end{bmatrix} \quad (3.13)$$

Where  $\rho$  and  $\theta$  are the bend radius and bend angle of the dipole,  $\rho\theta$  is the path length in the dipole,  $f$  is the focal length of the quadrupole, and  $L$  is the length of the drift.

One should note that the transfer matrix of a quadrupole in thin lens approximation should be  $M_{Q.thin}(L_Q, f) = M_D(L_Q/2)M_Q(f)M_D(L_Q/2)$ , here we only show the focusing term  $M_Q(f)$ , to be more accurate, the quadrupole can be described with several slices.

Several quadrupoles are usually arranged between two dipoles to tune the dispersion terms and the beam size [113, 114], the transfer matrix between two dipoles can be assumed to be

$$M_{tune} = \begin{bmatrix} M_{tune.11} & M_{tune.12} & 0 & 0 & 0 & 0 \\ M_{tune.21} & M_{tune.22} & 0 & 0 & 0 & 0 \\ 0 & 0 & M_{tune.33} & M_{tune.34} & 0 & 0 \\ 0 & 0 & M_{tune.43} & M_{tune.44} & 0 & 0 \\ 0 & 0 & 0 & 0 & 1 & M_{tune.56} \\ 0 & 0 & 0 & 0 & M_{tune.65} & 1 \end{bmatrix} \quad (3.14)$$

Thus the transfer matrix of the dogleg is  $M_{dl} = M_B(\rho, \theta)M_{tune}M_B(-\rho, -\theta)$ , by calculating with Mathematica, the  $R_{16}$ ,  $R_{26}$  and  $R_{56}$  are given by

$$R_{16} = \rho - \sin \theta * (M_{tune.12} \cos \theta + M_{tune.22} \rho \sin \theta) - \rho \cos \theta \\ - (M_{tune.11} \cos \theta + M_{tune.21} \rho \sin \theta)(\rho - \rho \cos \theta) \quad (3.15a)$$

$$R_{26} = \sin \theta - (M_{tune.21} \cos \theta - (M_{tune.11} \sin \theta)/\rho)(\rho - \rho \cos \theta) \\ - \sin \theta (M_{tune.22} \cos \theta - (M_{tune.12} \sin \theta)/\rho) \quad (3.15b)$$

$$R_{56} = M_{tune.56} - 2\rho\theta + 2\rho \sin \theta + (2\rho\theta)/\gamma^2 + (M_{tune.21} + M_{tune.11} \sin \theta)(\rho - \rho \cos \theta) \\ + \sin \theta (M_{tune.22}(\rho - \rho \cos \theta) + M_{tune.12} \sin \theta) \quad (3.15c)$$

Comparing equation 3.15a, 3.15b and 3.15c, one can easily find that

$$R_{56} = M_{tune.56} - 2\rho\theta + 2\rho \sin \theta + (2\rho\theta)/\gamma^2 - R_{16} \sin \theta + R_{26}\rho(1 - \cos \theta) \quad (3.16)$$

Where  $M_{tune.56} \approx L_{tune}/\gamma^2$  refers to formula 2.67, thus  $M_{tune.56} + (2\rho\theta)/\gamma^2 \approx L_{dl}/\gamma^2$  is the terms resulted by velocity difference, where  $L_{tune}$  is the length between two dipoles, and  $L_{dl}$  is the total length of the dogleg.

It is notable that from 3.16 if the transverse dispersion  $R_{16}$  and  $R_{26}$  vanished,  $R_{56}$  depends only on the bend angle and bend radius of the dipoles (ignore the dispersion introduced by velocity difference), thus one can only tune the  $R_{56}$  at the expense of unclosed transverse dispersion.

Normally the transverse dispersion terms are tuned to zero, then the longitudinal dispersion yields  $R_{56} = 2\rho(\sin \theta - \theta)$ . Due to the limited space in PHIL, the dogleg has a length of  $\sim 2$  m,  $\theta$  should not beyond  $50^\circ$ . The magnetic field is related to the bend radius by  $B = E_e/(\rho c)$ ,  $E_e$  is the energy of the electron beam, considering a 10 MeV

electron beam, the magnetic field versus bend radius is shown in Figure 3.6, the corresponding  $R_{56}$  with a bend angle of  $40^\circ$ ,  $45^\circ$ ,  $50^\circ$  are also shown in Figure 3.6. The bend radius should be larger than 0.28m with the premise that the iron of the dipole begins to saturate at 1200 Gs (the dipole in the lab that is available now), it has also been discussed in the previous section that  $R_{56}$  should be larger than 2.8 cm due to the limited acceleration gradient of the cavity, considering also the dipole size, the bend radius is set to 0.32m with a bend angle of  $45^\circ$ , then the  $R_{56}$  yields 4.5 cm, the simulation results have been published in [115].

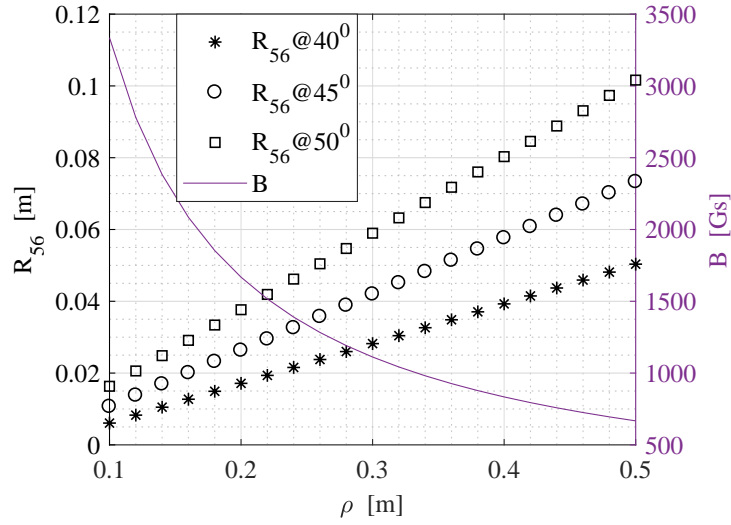


FIGURE 3.6: The longitudinal dispersion terms  $R_{56}$  and the required magnetic field versus bend radius.

Considering the first order matching, the dogleg shown in Figure 3.7 will be used for bunch compression, in this symmetry configuration, according to equation 2.27, if  $R_{16}$  is matched to 0 in the middle point, then  $R_{16}$  and  $R_{26}$  yield 0 at the end of the dogleg.

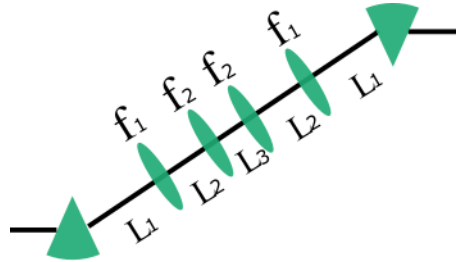


FIGURE 3.7: The analytical model of the symmetry dogleg, with the middle quadrupoles chops into 2 slices



Thus the required condition to eliminate the transverse dispersion reduced to

$$M_{hf,16} = 0, \quad M_{hf} = M_D(L_3/2)M_Q(f_2)M_D(L_2)M_Q(f_1)M_D(L_1)M_B(-\rho, -\theta) \quad (3.17)$$

According to space available in the PHIL, the variables are set with  $\theta = 45^\circ$ ,  $\rho = 0.32m$ ,  $L_1 = 0.45m$ ,  $L_2 = 0.3m$ ,  $L_3 = 0.12m$ , then the quadrupole strength that satisfying equation 3.17 is shown in Figure 3.8

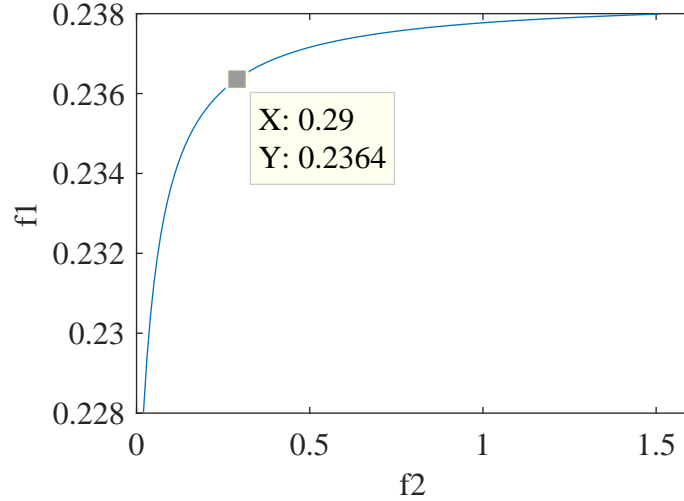


FIGURE 3.8: The focal length of the quadrupoles, that vanishes the first order transverse dispersion and it's derivative.

With the quadrupoles having a thickness of  $L_Q = 0.1m$ , and a focal length  $f = 0.25m$ , this doesn't satisfy the hypothesis of the thin lens approximation  $L_Q/f \ll 1$ , however, this can be a good estimation, and the conclusion that the longitudinal dispersion only depends on bend angle and bend radius when the transverse dispersion vanishes also applies to the general case.

Another feature of this symmetric configuration is that, if  $\alpha_x = 0$  in the midpoint, the beta function  $\beta_x$  has mirror symmetry and therefore returns to it's initial value at the exit, this has been studied by [114]. Even without this symmetry, the Twiss parameters at the dogleg exit can also be tuned by the quadrupoles before the chicane, for example in the SINBAD beam line, this is beneficial for the transverse matching after the chicane (i.e. reduce the length of the transport line). However, in our case, as the energy is low, the space charge effect is significant, the simulation results are different to the design results, thus the longitudinal compression and transverse matching will be performed separately.

### 3.3.3 Optical matching with MADX

The first order transfer matrix has been studied in the thin lens approximation, and one know that, in this symmetric configuration, if  $R_{16}$  in the dogleg middle is tuned to zero, then one can get a closed transverse dispersion and it's derivative, that is  $R_{16} = R_{26} = 0$  at the dogleg exit. With a closed transverse dispersion, the longitudinal dispersion is constant at the dogleg exit and takes the form  $R_{56} = 2\rho(\sin\theta - \theta) - \frac{L_{dl}}{\gamma^2}$ . In this section, the codes MADX and ELEGANT are used to do the matching with the second order terms included.

The bend angle and bend radius are set to  $\theta = \pi/4$ ,  $\rho = 0.32m$  according to the previous analysis in Figure 3.5 and 3.6. Two free variables are available in the dogleg (the strength of the two outer quadrupoles, and of the inner quadrupoles), but there is only one constrain  $R_{16} = 0$  in the dogleg middle, thus another variable can be used to tune the betatron function.

As shown in Figure 3.8, for each pair of  $(f_1, f_2)$  in the curvature, the transverse dispersion can vanish, there is still one degree of freedom to control the beam size, here we use this freedom to minimize the angular divergence in the midpoint, to get nearly mirror symmetry for the envelop in the dogleg. The Twiss parameters at the dogleg entrance are  $\beta_x = 1.47m$ ,  $\beta_y = 1.47m$ ,  $\alpha_x = 2.36$ ,  $\alpha_y = 2.36$ , in a matched result, the quadrupole strength are respectively  $k_{q1} = 39.665/m^2$ ,  $k_{q2} = -15.758/m^2$ , for a 10 MeV electron beam, this corresponds to a field gradient of 1.397T/m and 1.015T/m, it's easy to achieve. The transverse dispersion and it's derivative are shown in Figure 3.9, the nominal beta function is shown in Figure 3.10.

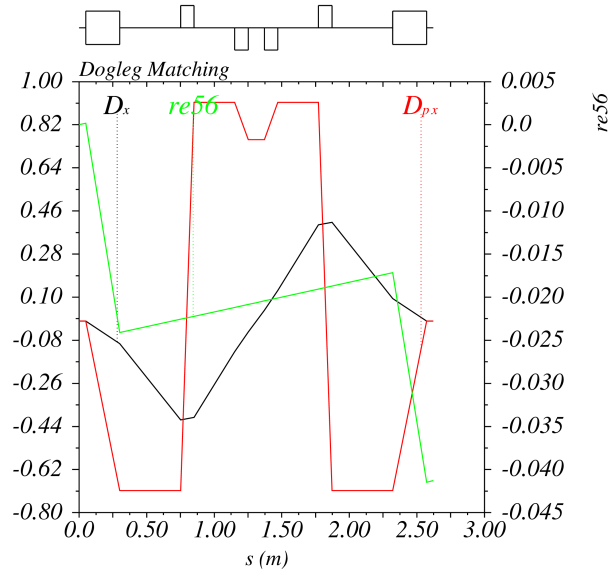


FIGURE 3.9: The dispersion terms along the dogleg, matched with MADX, where  $D_x$  refers to  $R_{16}$ , and  $D_{px}$  refers to  $R_{26}$ .

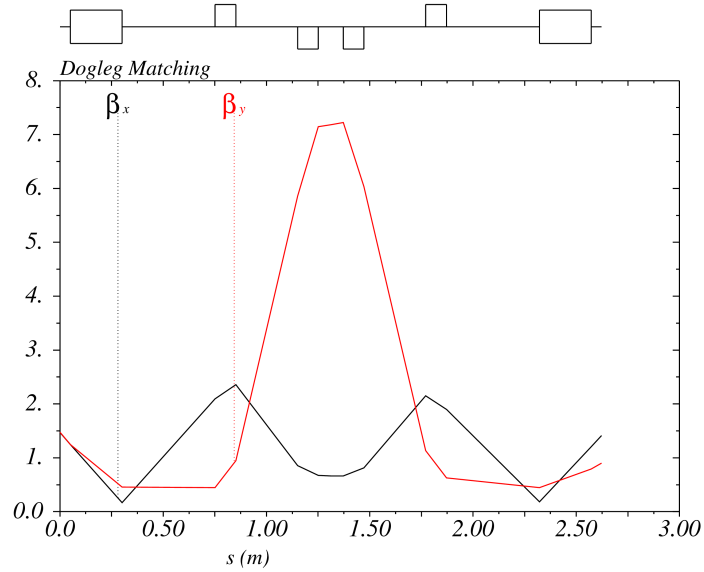


FIGURE 3.10: The nominal beta function along dogleg.

The beta function is smaller than 5.50 m, that corresponds to a RMS transverse size of 0.43 mm for a 10 MeV electron beam with a normalized emittance of  $0.65 \mu\text{m}$  (the actual emittance at the dogleg entrance).

The  $R_{56}$  of the dogleg is 0.0449 m, according to formula 3.5 one can get the exact acceleration phase in the booster  $\phi_0$  and the second order dispersion terms for the matching condition, they are summarized in Table 3.1

TABLE 3.1: The desired value of the parameters to meet the match condition

$R_{56}$	$k_1$	$\phi_0$	$k_2$	$T_{566}$
0.0449 m	22.8/m	38.507°	987.339m	0.063m

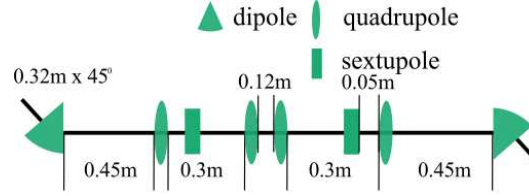


FIGURE 3.11: The layout of the dogleg with sextupoles to tune the second order dispersion.

At the dogleg entrance, the RMS energy spread is  $\sigma_{\delta 0} = 6.60 \times 10^{-4}$ , while the RMS transverse beam size and RMS angular divergence are respectively  $x_{rms} = y_{rms} = 2.02 \times 10^{-4}$ m,  $x'_{rms} = y'_{rms} = 2.90 \times 10^{-4}$ mrad, when going to second order matrix, the energy deviation  $\delta^2$  is much larger than the other terms, thus two sextupoles are implemented as shown in Figure 3.11 to tune the second order dispersion  $T_{166}$ ,  $T_{266}$ ,  $T_{566}$ . The emittance growth in x,y direction are estimated with the formula 3.8, 3.10, it is shown again here

$$\epsilon_{x.tr} = \sqrt{\epsilon_{x0.tr}^2 + \epsilon_{x0.tr} \delta_0^4 (T_{166}^2 \gamma_x + T_{266}^2 \beta_x + 2T_{166}T_{266}\alpha_x)} \quad (3.18)$$

$$\begin{aligned} \epsilon_{y.tr}^2 / \epsilon_{y0.tr}^2 = & 1 + (T_{346}T_{436} - T_{336}T_{446})^2 \delta_0^4 \\ & + \gamma_{y0}(\beta_y T_{446}^2 + 2\alpha_y T_{346}T_{446} + \gamma_y T_{346}^2) \delta_0^2 \\ & + \beta_{y0}(\beta_y T_{436}^2 + 2\alpha_y T_{336}T_{436} + \gamma_y T_{336}^2) \delta_0^2 \\ & - 2\alpha_{y0}(\beta_y T_{436}T_{446} + \alpha_y T_{336}T_{446} + \alpha_y T_{346}T_{436} + \gamma_y T_{336}T_{346}) \delta_0^2 \end{aligned} \quad (3.19)$$

Recognize the factor  $(T_{166}^2 \gamma_x + T_{266}^2 \beta_x + 2T_{166}T_{266}\alpha_x)$  as  $cof_{ex}$ , and identify  $\epsilon_{y.tr}^2 / \epsilon_{y0.tr}^2$  as  $cof_{ey}$  then the strength of sextupoles that can match the second order longitudinal dispersion terms are shown in Figure 3.12, with each pair of the sextupole strength, the corresponding  $cof_{ex}$ ,  $cof_{ey}$  are also shown in Figure 3.12. With  $ks_1 = -600/m^3$ ,  $ks_2 = 245/m^3$ , one can get the minimum value of  $cof_{ex}$ , which yield 0.775 m, while the strength of sextupoles has less effect on  $cof_{ey}$

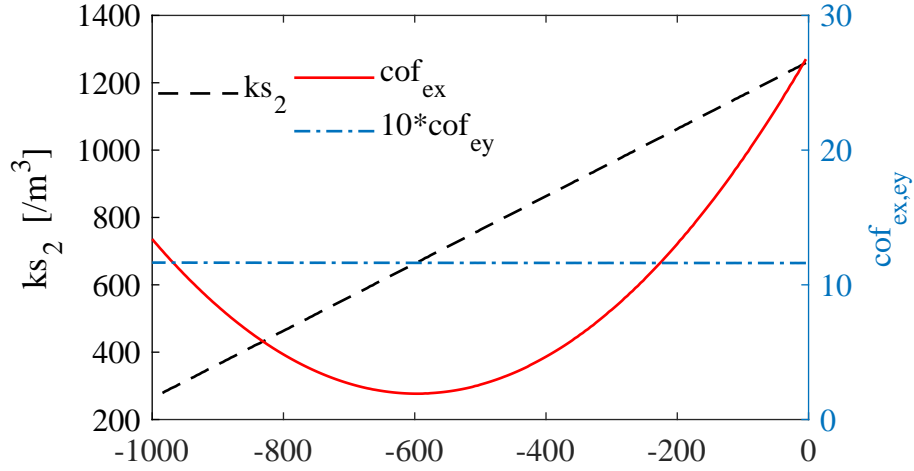


FIGURE 3.12: The strength of two sextupoles that vanish the  $T_{566}$  terms, and the corresponding emittance growth factor  $\delta_e$ .

One should note that, the sextupoles can also couple the x plane to y plane, the emittance growth formula here only consider the energy correlated terms. With the initial emittance being  $\epsilon_{x.n.tr} = \epsilon_{y.n.tr} = 0.617\mu\text{m}$ , the emittance at dogleg exit can be calculated according to formula 3.18 and 3.19 and is shown in Figure 3.13, the emittance calculated from ELEGANT (up to 3rd order matrix) are also shown in Figure 3.13 for comparison.

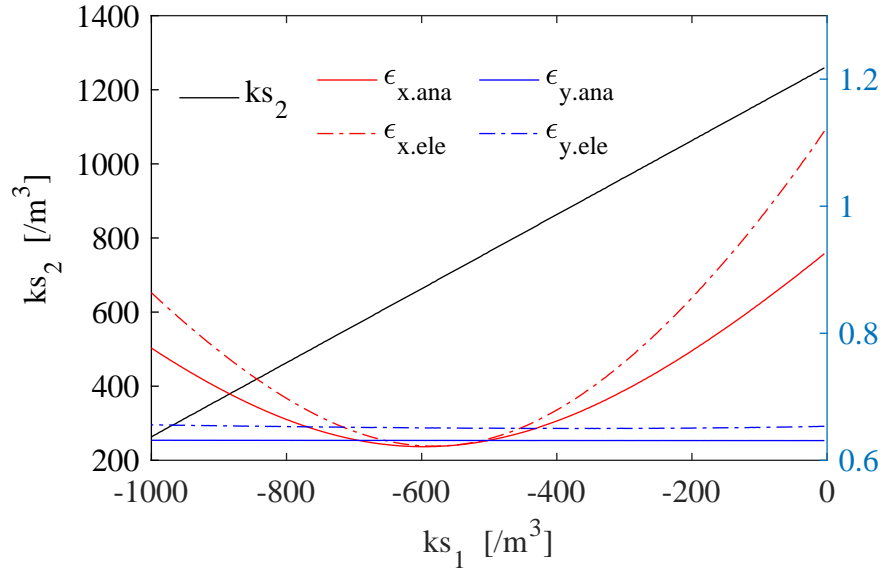


FIGURE 3.13: With sextupoles strength that tune the longitudinal term  $T_{566}$  to full compression condition, the corresponding emittance at dogleg exit in x and y directions are calculated with ELEGANT, the initial emittance are  $\epsilon_{x0} = \epsilon_{y0} = 0.617\mu\text{m}$ .

According to Figure 3.13, on the hypothesis that  $T_{566}$  term has been matched by sextupoles, the emittance growth in the x direction can be suppressed by tune the sextupoles strength, while the emittance growth in y direction are not sensitive to sextupoles strength. The emittance growth by analytical estimation in x direction is in good agreement with the result in Elegant which perform the tracking with transfer matrix up to 3rd order.

### 3.4 Study of the beam dynamics in the dogleg

The dogleg has been designed on the basis of beam optics, however, the collective effects like space charge and coherent synchrotron radiation (CSR) still need to be studied. ELEGANT is used to check the optics design and estimate the CSR effect, then the codes Impact-T[116] and CSRtrack[117] are used to study beam dynamics in the dogleg.

ELEGANT is capable of tracking the 6D phase space with transfer matrix up to the 3rd order, longitudinal space charge impedance can be included in the drift space, and a 1-D CSR model is available in bend sections, while the transverse space charge effect is not included.

Impact-T is a fully three-dimensional quasi-static beam dynamics code in the time domain, the Liénard–Wiechert (L-W) potential is divided into space charge and the 1-D CSR. In CSRTrack both the 1-D CSR model as in Impact-T and the sub-bunch model are available, in the 1-D model the particles are projected to the z axis, and the 1-D L-W potential is calculated, thus both space charge and CSR effect has only one dimension, in the sub-bunch model, all the particles are projected onto the bending plane, the retarded positions are derived by backtracking excluding the self-force, then the macro electrons in retarded positions are replaced by 3-D Gaussian sub-bunches, the sub-bunch to electron L-W potential is then calculated.

#### 3.4.1 Benchmark of the codes

As discussed before, different models are implemented in the codes Impact-T and CSRTrack for the calculation of self-force, they are however expected to give consistent results when tracking particles in a straight line (where there is no CSR). These two codes have already been bench marked by [113] in detail, it is shown that the vertical space charge is absent due to the symmetry of the sub bunches, but the volume of the beam depends on the vertical size of the sub-bunch  $\sigma_{v.sub}$ , if  $\sigma_{v.sub}$  is smaller than the bunch size, then the space charge effect will be overestimated, thus  $\sigma_{v.sub}$  should be set to the vertical bunch size.

As the benchmark in [113] was done using an electron bunch of 1-5 pC with a duration between 1-5 fs, and we are aiming at studying an 10 pC electron bunch with a duration of several tens of fs to 100 fs, a new benchmark is done here, for a detailed comparison of the two codes one can refer to [113].

In a drift space, the acceleration terms in L-W potential is absent, thus the self force of the two codes are expected to be the same, a 10 pC 10 MeV electron bunches with a duration of 30 fs, 60 fs, 100 fs are tracked by ASTRA, IMPACT-T, and CSRTrack in a 0.1 m drift, ASTRA here is used as a reference. The initial emittance and transverse bunch size are respectively set to  $\epsilon_{nx0} = \epsilon_{ny0} = 0.6 \mu\text{m}$ ,  $\sigma_{x0} = \sigma_{y0} = 300 \mu\text{m}$ . Referring to the sub-bunch model in CSRTrack, all the horizontal sub bunch size is set to  $15 \mu\text{m}$ , all the longitudinal sub bunch size is set to 0.05 of the local bunch size, while the vertical sub bunch sizes are set to 1, 0.2, 0.1, 0.05 of the local bunch size for comparison.

The horizontal and vertical bunch size growth after the drift are shown in Figure 3.14, from Figure 3.14a, the three codes are in good agreement if the vertical sub bunch size  $\sigma_{v.sub}$  is set to the vertical bunch size  $\sigma_v$ , but with  $\sigma_{v.sub}$  much smaller than  $\sigma_v$ , the horizontal bunch size growth calculated by CSRTrack is larger than that calculated by ASTRA and Impact-T, the space charge is overestimated. Referring to Figure 3.14b, the bunch size growth in vertical direction, ASTRA and Impact-T is in good agreement, while in CSRTrack the vertical bunch size seems to be constant, the space charge effect is absent.

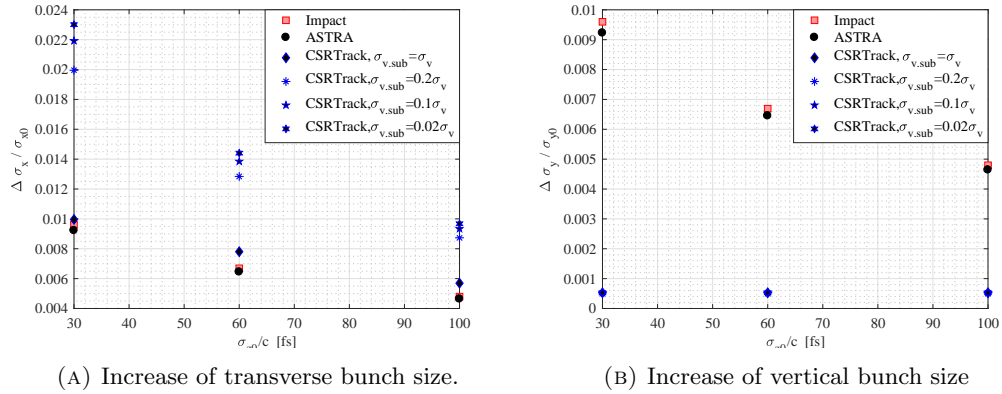


FIGURE 3.14: The increase of the bunch size in a 0.1 m drift, tracked by ASTRA, Impact-T and CSRTrack with different vertical sub bunch size.

The bunch length growth is shown in Figure 3.15, Impact-T and ASTRA are in good agreement with each other for all the cases. The result from CSRTrack is dependent on the initial bunch duration, in the case  $\sigma_{z0} = 100$  fs, the result coincides with Impact-T and is independent of the sub-bunch size, in the case  $\sigma_{z0} = 60$  fs the result is in agreement with Impact-T only with  $\sigma_{v.sub} = \sigma_v$ , a slightly larger duration growth is resulted with  $\sigma_{v.sub} \ll \sigma_v$ , in the case  $\sigma_{z0} = 30$  fs, the duration growth is underestimated

with  $\sigma_{v.sub} = \sigma_v$  and is overestimated with  $\sigma_{v.sub} \ll \sigma_v$ . This can be explained because with a longer bunch the space charge effect is not significant, the absence of the vertical space charge or the overestimation of the horizontal space charge has less effect on the bunch duration, while with a shorter bunch, the space charge effect is significant, with  $\sigma_{v.sub} = \sigma_v$  the vertical space charge effect is absent, thus the bunch duration growth is underestimated, with  $\sigma_{v.sub} \ll \sigma_v$  the vertical space charge is still absent but the horizontal space charge is overestimated and this leads to a growth of the bunch duration.

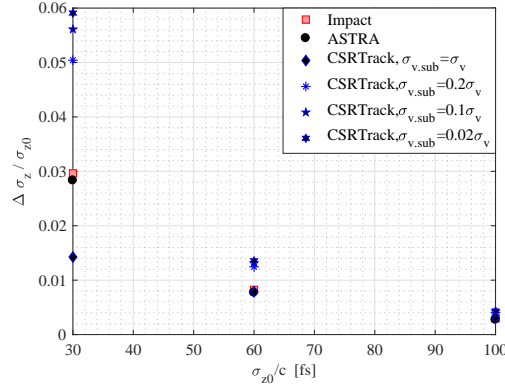


FIGURE 3.15: The growth of the bunch length in a 0.1 m drift, tracked by ASTRA, Impact-T and CSRTrack with different vertical sub bunch size.

In our case, the electron bunch has a duration of  $\sim 60$  fs after the magnetic compression, thus in the subsequent simulation with CSRTrack, the vertical sub-bunch size is set to the local vertical bunch size, as a result, the horizontal bunch parameters and the bunch duration is expected to be in agreement with Impact-T, while the vertical bunch size should be smaller than that in Impact-T.

### 3.4.2 Beam dynamics in the dogleg chicane

From photo cathode to the dogleg entrance the electron bunch is tracked with ASTRA, 50000 macro particles are used in the simulation, the longitudinal phase space at the dogleg entrance is shown in Figure 3.16, the chirp is calculated with

$$k_1 = \langle z\delta \rangle / \langle z^2 \rangle \quad (3.20)$$



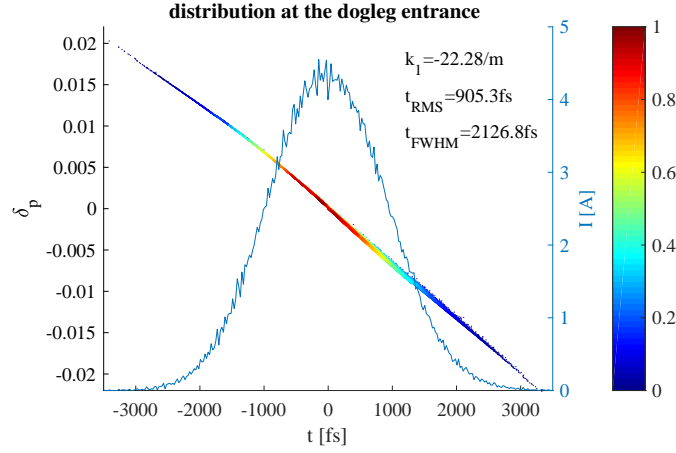


FIGURE 3.16: Longitudinal phase space of the electron bunch at the dogleg entrance.

In the dogleg, the electron bunch is firstly tracked with Impact-T without space charge or CSR effect, the longitudinal phase space at the dogleg exit is shown in Figure 3.17, the electron bunch is compressed to 28.5 fs FWHM and 63.3 fs RMS, with a peak current of  $\sim 200$  A one should note that the FWHM value is smaller than the RMS value, because the electrons are distributed with a sharp peak and long tails, thus the FWHM value is more meaningful for subsequent study in the plasma.

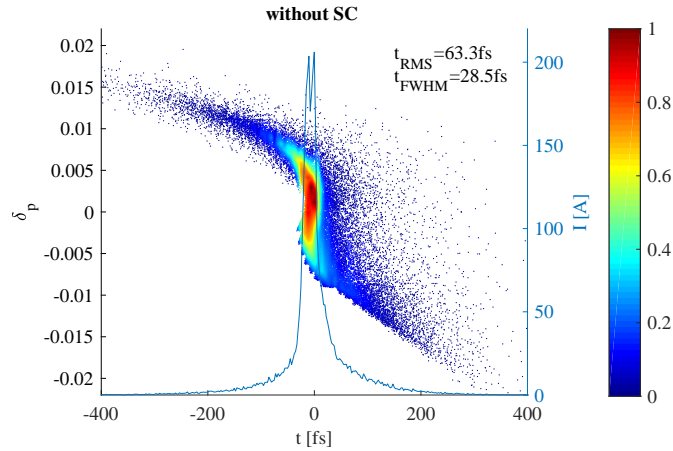


FIGURE 3.17: Longitudinal phase space of the electron bunch at the dogleg exit, tracked with Impact-T without self force.

Then the space charge effect is turned on in Impact-T, the phase space of the electron bunch at the dogleg exit is shown in Figure 3.18, the FWHM duration increased to 170.6 fs and the peak current reduced to  $\sim 50$  A.

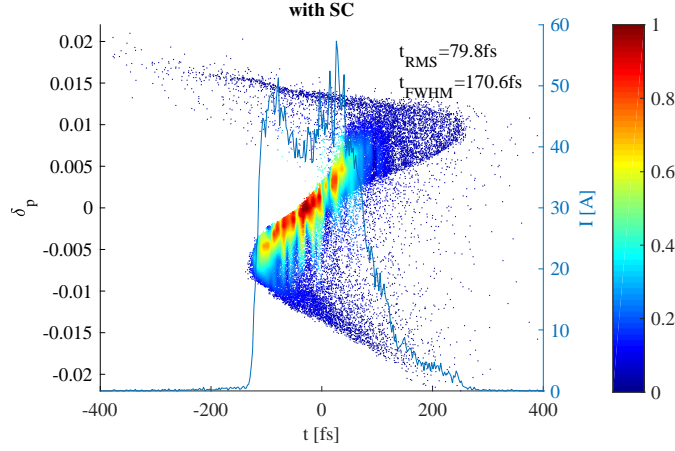


FIGURE 3.18: Longitudinal phase space of the electron bunch at the dogleg exit, tracked with Impact-T with space charge included.

According to the phase space distribution, the electron bunch is over compressed, this is due to the fact that, the space charge may stretch the electron bunch and increase the energy chirp, this can be compensated by further decreasing the initial energy chirp at the dogleg entrance, and an optimized result is shown in Figure 3.19, the energy chirp at the dogleg entrance is  $k_1 = -22.17/\text{mm}$ , after compression, electron bunch has a duration of 69.5 fs RMS and 53.2 fs FWHM, with a peak current of  $\sim 150$  A.

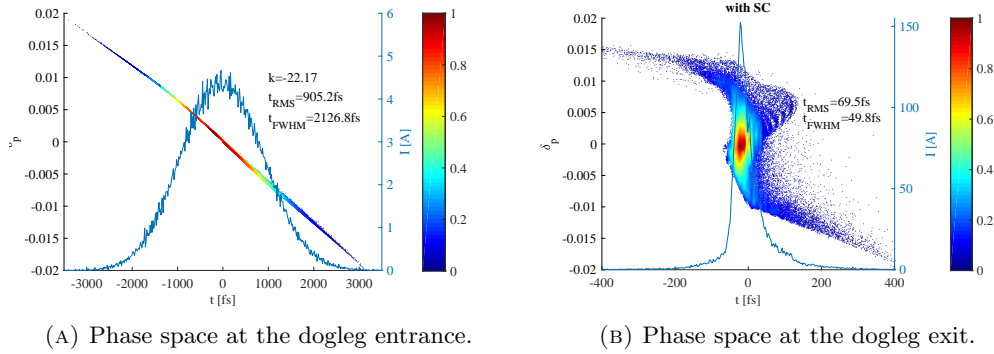


FIGURE 3.19: Longitudinal phase space of the electron bunch at the dogleg entrance and the dogleg exit, tracked with Impact-T with space charge included and CSR excluded

ELEGANT is used to estimate the energy loss along the electron bunch in the two dipoles caused by CSR. In the first dipole, the electron bunch is relatively longer  $\sim 0.27$  mm and the CSR effect is weaker, the maximum energy change is approximately 25 eV, while in the second dipole, the electron bunch is compressed by a factor of  $\sim 10$ , the maximum energy change along the electron bunch is 900 eV, much larger than in the first dipole, however that corresponding to only 0.009% of the reference beam energy, thus it can be ignored.

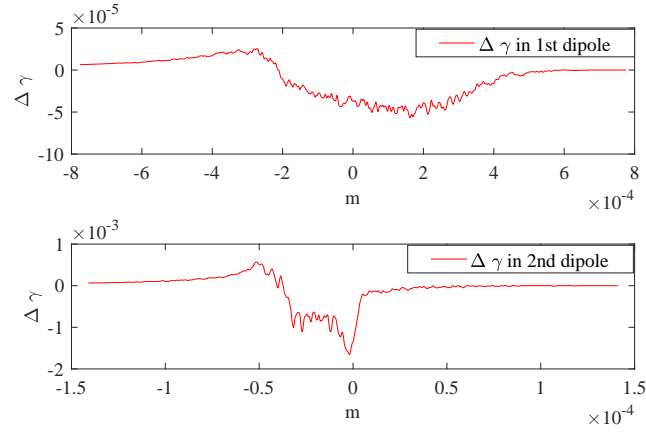
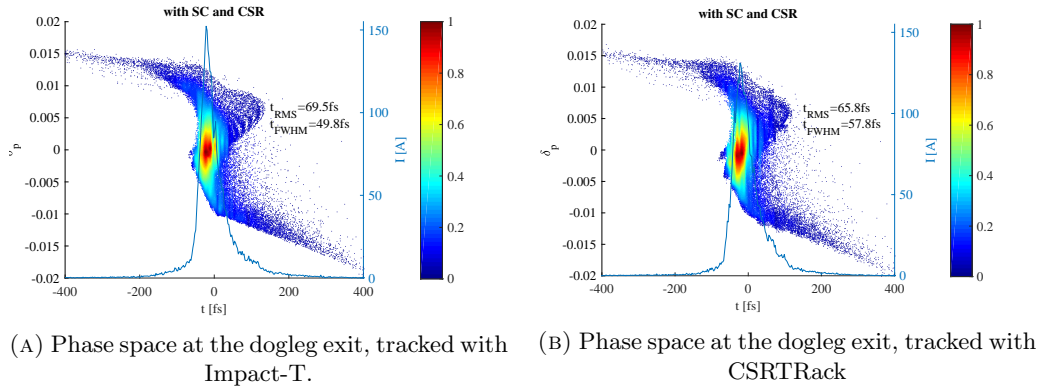


FIGURE 3.20: The CSR induced energy change along the electron bunch in two dipoles of the dogleg, the CSR effect is estimated with steady state model in ELEGANT.

With both SC and CSR turned on in Impact-T, the phase space of the electron bunch at the dogleg exit is shown in figure 3.21a, comparing with Figure 3.19b, CSR has almost no effect on the phase space distribution. This is then cross-checked with CSRTrack, the longitudinal phase space is shown in Figure 3.21b, it is slightly different than that in Impact-T, because different self force models are used in the two codes. However, in both codes the electron bunch is compressed to several tens of femtoseconds, this confirm the validity of the bunch compression.



(A) Phase space at the dogleg exit, tracked with Impact-T. (B) Phase space at the dogleg exit, tracked with CSRTrack

FIGURE 3.21: Longitudinal phase space of the electron bunch at the dogleg entrance and the dogleg exit, the electron bunch in the dogleg is tracked with Impact-T with Space charge and CSR effects included.

The transverse emittance growth and the bunch size after the compression is shown Table 3.2, the initial emittance and bunch size are  $\epsilon_{nx0} = \epsilon_{ny0} = 0.62 \mu\text{m}$ ,  $\sigma_x = \sigma_y = 0.22 \text{mm}$ . According to our simulation result with ImpactT, SC leads to significant emittance growth ( $\sim 76\%$ ) in the x direction (bend plane), while only 4.7% in the y direction. The CSR induced emittance change in the X and the Y directions are both smaller than 4%, and can be ignored.

TABLE 3.2: Emittance growth and bunch size after compression.

code	SC	CSR	$\frac{\Delta\epsilon_{nx}}{\epsilon_{nx0}}$	$\frac{\Delta\epsilon_{ny}}{\epsilon_{ny0}}$	$\sigma_x(\text{mm})$	$\sigma_y(\text{mm})$
ImpactT	off	off	3.65%	4.73%	0.23	0.22
ImpactT	on	off	79.40%	7.31%	0.29	0.21
ImpactT	on	on	82.61%	4.42%	0.30	0.21
CSRtrack	on	on	85.13%	4.26%	0.30	0.21

The emittance growth in the y direction is  $\sim 4\%$  in both Impact-T and CSRTrack, and it is interesting that in Impact-T, the emittance in the vertical plane is slightly reduced by the CSR effect.

In the previous simulation, the electron bunch is fully compressed at the dogleg exit, while after the dogleg, the electron bunch will be transversely focused to match the plasma wakefield, a significant increase of the bunch duration is expected due to the space charge effect and the velocity difference (the bunch head moves faster than the bunch tail), i.e. with  $\gamma_e = 20$ , energy deviation  $\delta = 0.005$ , the relative position shift after 1 meter drift is  $\Delta z/c = (\gamma_e^2 c) \delta = 41.67 \text{ fs}$  according to equation 2.67, it is comparable to the bunch duration. The evolution of the bunch duration is shown in Figure 3.22, with the dogleg exit located at 5.03 m, after the dogleg it is a drift space.

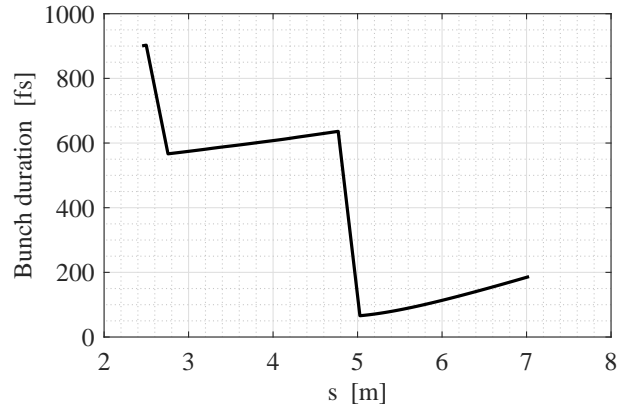


FIGURE 3.22: The evolution of the bunch duration, with the dogleg located at 2.5 m to 5.03 m.

To suppress the increase of the bunch length, a short focus line is desired, here we also try with an over compressed bunch, that is at the dogleg exit, the bunch head has less energy while the bunch tail has more energy, the bunch length may be slightly reduced downstream of the dogleg. To get an over compressed bunch, we slightly increase the phase of the booster, the electric field is also increased to keep a constant energy of 10 MeV, with different phase, the evolution of the RMS bunch length after the dogleg

is shown in Figure 3.23. One can find that the optimal condition is depend on the extraction position (the plasma entrance), if the plasma entrance is before 5.4 m, a shorter bunch can be achieved with a full compressed bunch, otherwise, an over compressed bunch is preferable.

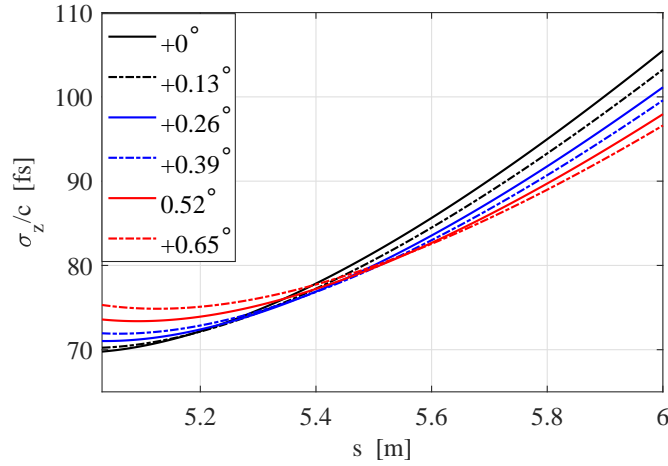


FIGURE 3.23: The evolution of the bunch duration in the subsequent drift space downstream of the dogleg.

It is notable that, according to the bunch length evolution after the dogleg, if the plasma entrance is set close to  $s = 5.4\text{m}$ , the bunch length is less sensitive to the acceleration phase of the booster, this will makes the tuning of the dogleg easier, a solenoid will be used to focus the electron bunch quickly, the plasma entrance is set to 5.46 m, this will be discussed in the section 3.5. With a full compression condition at the dogleg exit (5.03 m), the bunch duration at 5.46 m (plasma entrance) is 78.6 fs RMS, 60 fs FWHM, the longitudinal phase space is shown in Figure 3.24a, with the booster phase increased by  $0.39^\circ$ , a minimum RMS bunch duration of 77.4 fs is achieved at 5.46 m, while the FWHM duration increased to 65 fs, the longitudinal phase space is shown in Figure 3.24b. At 5.46 m, there is less difference between the full compression and over compression case, the FWHM bunch duration is slightly shorter with the full compression case, the full compression will be applied in the subsequent study.

Considering the whole line from the gun to plasma entrance, since the gun and the booster are powered by the same klystron, they have the same phase error, for different phase errors, the RMS bunch duration at the plasma entrance (5.62 m) is shown in Figure 3.25, to obtain a bunch duration shorter than 100 fs, the phase error should be smaller than  $1.5^\circ$ , that corresponding to 1.38 ps.

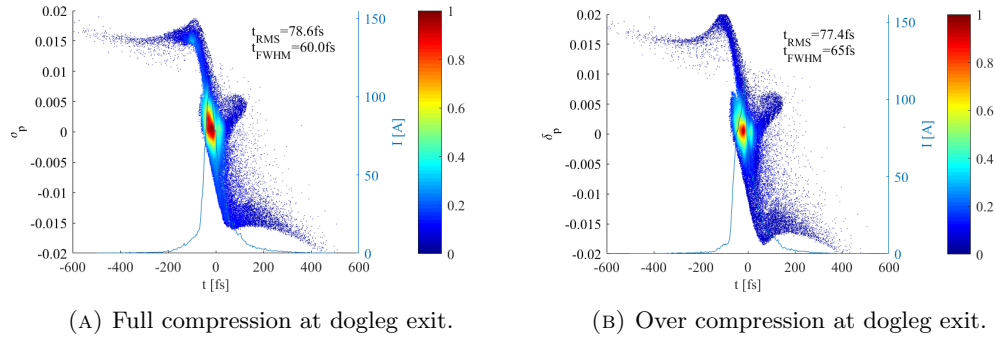


FIGURE 3.24: Longitudinal phase space of the electron bunch at 5.46 m, the dogleg exit is located at 5.03 m.

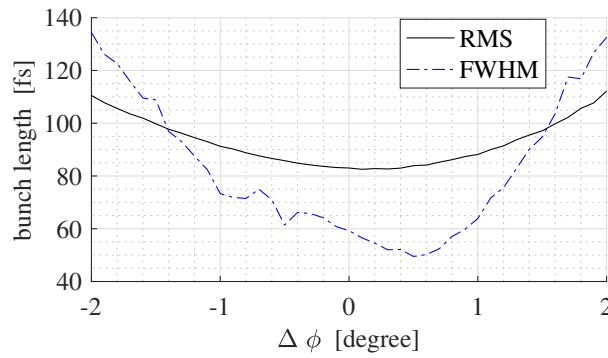


FIGURE 3.25: The bunch duration at the plasma entrance versus the RF phase error.

### 3.5 Transverse focusing before the plasma

The longitudinal phase space of the electron bunch has been manipulated to improve the capture in the plasma, however, before being injected into the plasma, the transverse parameters should also be tuned to suppress the emittance growth in the plasma.

The transverse motion of the electrons can be described with the Hill's equation 2.6, with  $d^2x/dz^2 = F_x/(\gamma_e m_e c^2)$ , we have  $K = F_x/(\gamma_e m_e c^2 x)$ , for a mono energetic, and short beam, if the focusing force is linear related to the transverse coordinate ( $K$  in equation 2.6 is independent of the transverse or longitudinal coordinate) then the beam emittance is conserved during the propagation [45, 118]. But this assumption usually doesn't hold in reality, i.e. if the initial electron bunch length can't be neglected comparing with the plasma wavelength, then  $K$  varies between bunch slices, the phase space ellipses of bunch slices will rotate with different betatron frequencies, this will lead to the decoherence between bunch slices and increase the project emittance. Also the beam is usually not mono energetic, concerning the energy spread, the correlated energy spread may lead to the decoherence between slices while the uncorrelated energy spread may lead to

the decoherence in bunch slices, they both lead to the degradation of the projected emittance.

In a constant focusing channel (the focusing field varies much slower than the betatron function), the emittance growth from betatron decoherence can be efficiently mitigated by matching of the beams with the electromagnetic field. The matching condition can be derived from the beam envelop equation 2.31a, in emittance dominated beam (the space charge effect can be neglected), the matching condition is given by [93, 119]

$$\alpha_{x,y} = 0, \beta_{x,y} = \frac{1}{\overline{k_{\beta,x,y}}} = \frac{1}{\sqrt{K}} \quad (3.21)$$

$\alpha_{x,y}$ , and  $\beta_{x,y}$  are the Twiss parameters in x and y direction, while  $\overline{k_{\beta,x,y}}$  is the mean betatron oscillation wave number of the electrons,  $K$  is the focus strength of the plasma wakefield, it yields  $K = \frac{e}{\gamma_e m_e c^2} \partial_r E_r |_{r=0}$ ,  $E_r$  is the transverse electric field as giving in equation 2.122b. For  $r \ll w(s)$ , the matching condition in the linear regime follows that

$$\alpha_{x,y} = 0, 1/\beta_{x,y} = \left\langle \sqrt[4]{\frac{\pi}{2}} \sqrt{\frac{a_0^2}{\gamma_e w(s)^2} k_p L \exp(-k_p^2 L^2/8) \sin(k_p \xi)} \right\rangle \quad (3.22)$$

Where  $w(s)$ ,  $a_0(s)$  are the waist and the amplitude of the laser,  $k_p \xi$  is the acceleration phase in the plasma wave. But one should note that this matching condition is valid for the case of a uniform focusing channel, where the acceleration phase varies slowly during the propagation, the relative position of the electrons are fixed (decide the average value). Usually the betatron function needs to be tuned to a small value (few  $\mu\text{m}$ ), it has been shown that an up ramp of the plasma density[120] and the focusing of the laser as shown in Figure 3.26 may relax the requirement for  $\beta_{x,y}$ , since the plasma wakefield helps to focus the electron bunch.

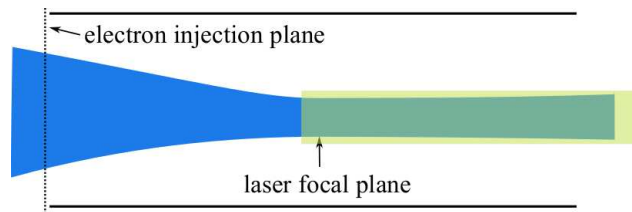


FIGURE 3.26: The focusing laser configuration.

Referring to the focusing laser configuration, the matching condition in equation 3.21 is for the uniform acceleration section (after the laser focal plane in Figure 3.26), the matching condition at the injection plane can be found by backtracking a matched electron bunch from the uniform acceleration section.

While for the plasma configuration in ESCULAP, the laser focusing section is mainly used to perform velocity bunching, the initial bunch length is almost half the plasma wave length, the relative longitudinal position of electrons are rearranged and many electrons are lost during the propagation, also the laser beam will not be guided for the first experiment, thus there is no uniform acceleration section. The matching condition is not validate in our case, but it is still necessary to focus the electron bunch to be much smaller than the laser beam.

The 10 MeV electron bunch can be focused with several quadrupoles or a solenoid, with quadrupoles the TWISS parameters in x and y plane can be tuned separately, but several quadrupoles are needed to focus the beam in both direction, electrons may require strong defocusing before focusing, thus a long space is required. With a solenoid, the electron bunch experience the same focus force in x and y plane thus it can be focused directly, but the problem is that x-y plane can't be tuned separately.

A transport line composed of a quadrupole doublet and a quadrupole triplet has been designed and presented in [115], it matches  $\alpha_{x,y}$  to 0 and  $\beta_{x,y}$  to 0.1 m. The matching is performed with MADx, the space charge effect is compensated by slightly tuning the quadrupoles strength referring to the mismatch factor  $M_s$  in equation 2.33, the Twiss parameters are shown in Figure 3.27, the dogleg exit is located at 5.03 m.

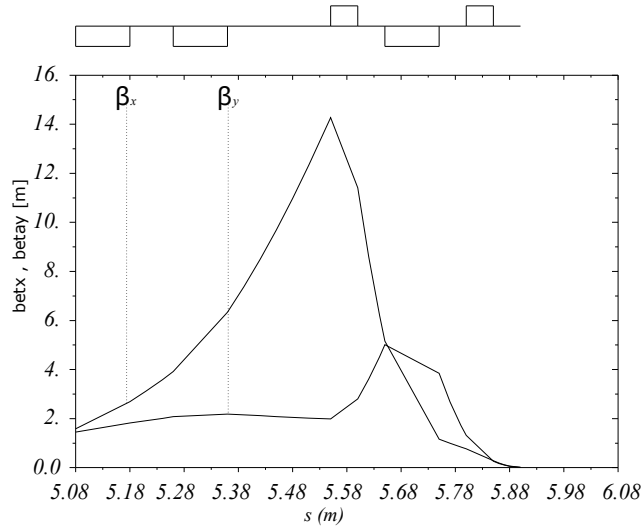


FIGURE 3.27: Betatron function along the transfer line.

However, as discussed before, it's hard to define the matching condition at the plasma entrance in our case, here the electron bunch is just focused to a size much smaller than the laser beam. The bunch size at dogleg exit is  $\sim 300 \mu\text{m}$  (see table 3.2), the spot size of the laser beam at the laser focal plane is  $w_0 = 50.46 \mu\text{m}$ , assume the injection plane is 4 Rayleigh lengths from the focal plane, the laser beam size at the injection plane



is  $\sim 200 \mu\text{m}$ , here a solenoid with  $\int B(z)^2 dz = 0.045 \text{T}^2\text{m}$  is put at  $s = 5.3 \text{m}$  to focus the electron beam, the transverse beam size and the emittance from the dogleg exit to plasma entrance is shown in Figure 3.28. The transverse beam size at the plasma entrance are  $\sigma_x = 26.2 \mu\text{m}$ ,  $\sigma_y = 25.3 \mu\text{m}$ , the emittance in the y plane increases fast due to the aberrations and the coupling between x-y plane.

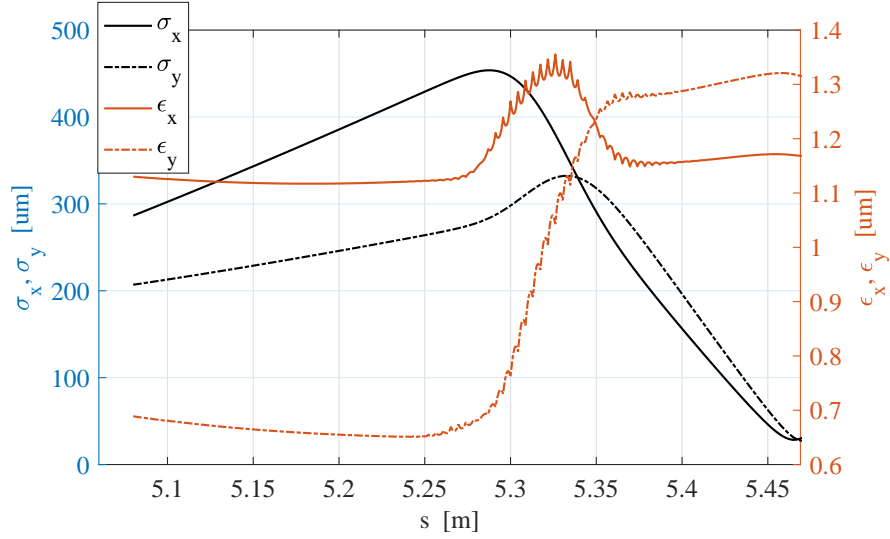


FIGURE 3.28: The evolution of the transverse bunch size and emittance by focusing with a solenoid.

The bunch length increases to  $82 \text{fs}$  at the plasma entrance as shown in Figure 3.29, the longitudinal phase space at the dogleg entrance is shown in Figure 3.30

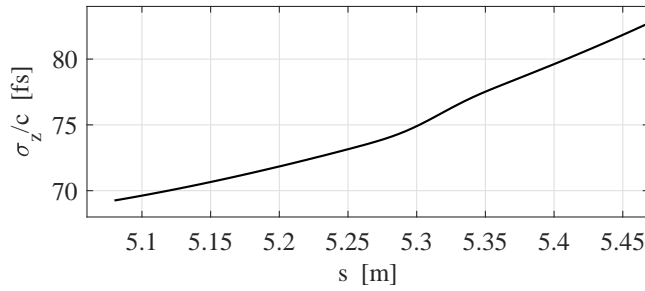


FIGURE 3.29: The evolution of the bunch length by focusing with a solenoid.

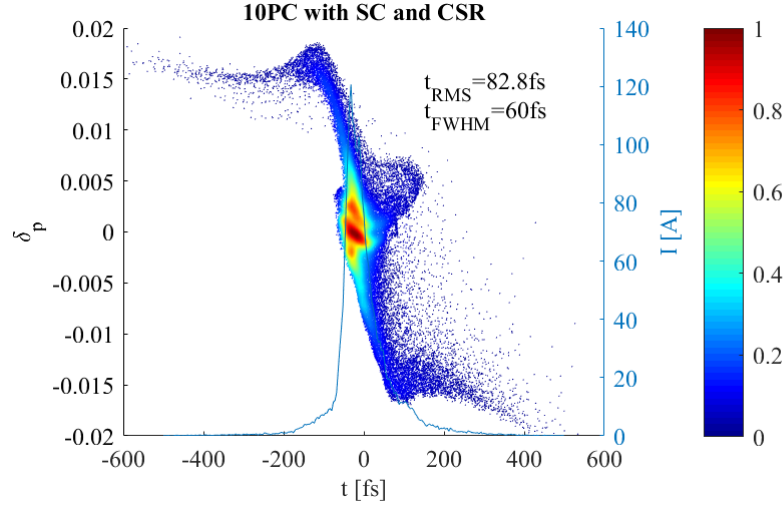


FIGURE 3.30: The longitudinal phase space of the electron bunch at plasma entrance.

### 3.6 Summary

The optical design of the dogleg chicane and the simulation study of the beam dynamics has been presented, the beam dynamics is studied with Impact-T and CSRTrack for cross-checking, the results are in good agreement. The duration of the electron bunch at the dogleg exit is 65.9 fs RMS, 50 fs FWHM.

After the dogleg, the bunch length increases quickly so that it should be injected into the plasma quickly, a solenoid is used to focus the electron bunch to a smaller size with respect to the spot size of the laser beam at the injection plane. The dogleg exit is at 5.03 m, while the solenoid is set at 5.3 m, and the plasma entrance is located at 5.46 m. At the plasma entrance the RMS bunch duration is 83 fs, while the FWHM duration is 60 fs.

## Chapter 4

# Beam capture and acceleration in the plasma wakefield

In this chapter, the electron bunch injection and acceleration in the plasma are studied. At the plasma entrance, the electron bunch has been longitudinally compressed to  $\sim 83$  fs RMS, it is comparable with the linear plasma wavelength (i.e  $249 \text{ fs} @ 2 \times 10^{17} \text{ cm}^{-3}$ ), if it is directly accelerated, the energy spread will be large, thus a further compression before the acceleration is strongly desired.

The external electron bunch has an energy of  $\sim 10 \text{ MeV}$ , due to this low energy, the relative longitudinal positions of the electrons are not frozen, velocity bunching can be performed, that is to inject the electron bunch at a specific phase where the bunch tail gets more energy than the bunch head, thus the bunch will be compressed during the propagation, this has already been discussed in the first chapter, lower electric field and longer propagation length is beneficial for the compression. By analogy with the curve of sine like electric field, maximum compression can be achieved at the zero crossing phase where the field gradient is maximum. Whereas for the acceleration process, the electron bunch is expected to lie in the acceleration field crest to get efficient acceleration with minimum energy spread.

So different phases are required for compression and acceleration, this can be realized by dephasing, the external electron bunch moves slower than the laser initially and slips backward, then due to the acceleration in the plasma wakefield it will catch up the laser beam and slip forward. The electron bunch is expected to be injected at the zero crossing phase of the longitudinal field to get maximum compression, and then slips to the field crest to get maximum acceleration. Since the relative position change of the electron in  $1 \text{ m}$ 's propagation is proportional to  $\delta/\gamma_e^2$ , the acceleration field at the injection plane should be weaker to keep the small  $\gamma_e$ . On the other hand, a strong electric field is

required to accelerate the bunch to catch up the laser beam before slipping into the defocusing phase, when the electron bunch catches up the laser beam a strong electric field is also desired to efficiently accelerate the bunch to higher energy before it slips forward away from the field crest.

The weak electric field at the injection plane, and the strong electric field at the acceleration section is realized by starting the laser plasma interaction several Rayleigh length (assume  $n$  Rayleigh length) before the laser focal plane, thus the electric field at the injection plane is  $1/n^2$  the electric field at the laser focal plane. It will also be shown that by ending the laser plasma interaction several Rayleigh length after the laser focal plane may significantly reduce the angular divergence of the electron bunch thus increase the chromatic length and relax the requirement on the magnets of the subsequent extraction line.

The evolution of the longitudinal phase space of the electron bunch is of vital importance in our case, it is tuned by varying the injection phase of the electron bunch and the distance between the plasma start plane (injection plane) and the laser focal plane. The evolution of the longitudinal phase space is studied by solving the 1-D equation of motion and then with PIC (particle in cell) simulation, the optimal injection condition are achieved for several plasma densities, the evolution of the energy spread, emittance, transverse size and longitudinal duration of the electron bunch are also studied.

## 4.1 Simulation code

The ESCULAP project aims at studying the acceleration of an externally injected electron bunch in quasi linear regime, with a plasma cell of length of  $\sim 10$  cm. To perform studies over a large ensemble of parameters in a long interaction distance, very heavy calculations are expected with the commonly used 3D particle in cell (PIC) simulation. Thus, a quasi-static code WAKE-EP [121], an upgrade of the code WAKE [122] is used to model the interaction in the plasma.

WAKE is a 2D (Cartesian/Cylindrical) fully relativistic, non-linear code, it is valid in the case  $\omega_p/\omega_L \ll 1$ ,  $\omega_p$  and  $\omega_L$  are respectively the angular frequency of the plasma and the laser. In WAKE, the electron motion is separated into a fast quiver motion driven by the high frequency laser field and a slow varying motion driven by the pondermotive force, the laser is assumed to be fixed when a plasma electron transit through the laser, thus the time scale in the simulation is the plasma period. WAKE-EP is an improved version of WAKE, in which the fields generated by the relativistic electrons are calculated and added to the wakefield, following the same procedure as in [123]. As an example, the

laser intensity and electron density calculated by WAKE-EP in linear regime is shown in 4.1.



FIGURE 4.1: The laser intensity and the plasma electrons density in WAKE-EP.

In fact, the laser amplitude in our study is  $a_0 = 0.7$ , it is in quasi linear regime, the nonlinear effect has contribution to the wakefield, the longitudinal wakefield calculated by WAKE-EP, and by the linear theory are shown in Figure 4.2. The acceleration field crest tilts forward while the deceleration field crest tilts backward under the effect of the nonlinearities.

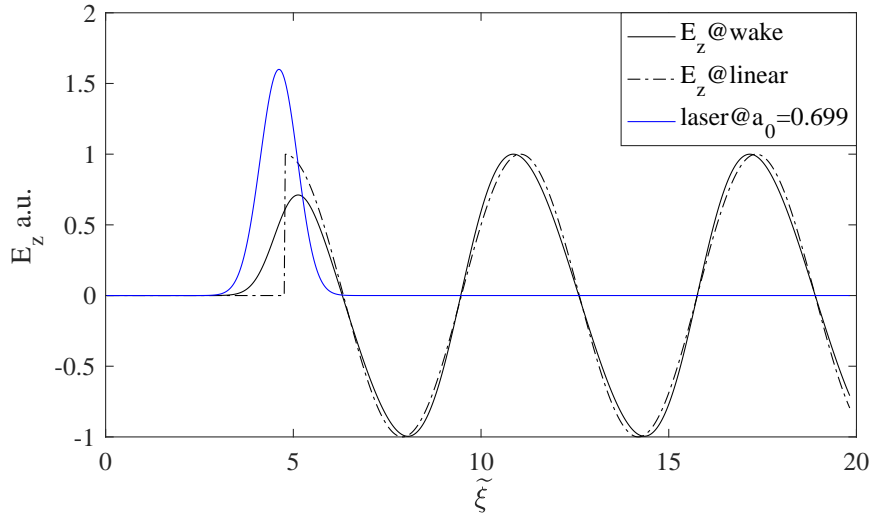


FIGURE 4.2: Longitudinal electric field calculated by WAKE-EP and the linear theory, with laser amplitude  $a_0 = 0.699$ , plasma density  $n_e = 2 \times 10^{17} \text{ cm}^{-3}$ .

To perform parameters study, a code named WAKETRAJ[124] was also developed, that can calculate the linear plasma wakefield, or read the field potential calculated by WAKE-EP, then do the particle tracking with space charge effect excluded. For the same laser-plasma configuration, the wakefield is fixed, we can use WAKE-EP to calculate the

field potential, then use WAKETRAJ to read the field potential and search for the optimal injection phase, this further reduce the computation time. With the optimal injection phase found by WAKETRAJ, the space charge effect is checked with WAKE-EP.

## 4.2 Density profile in the plasma cell

Before the simulation study of the interaction between laser and plasma, the plasma density is checked. A plasma cell will be used in the experiment as shown in Figure 4.3 (a preliminary design for ESCULAP that will be used to produce an uniform density profile), the plasma density we are concerned is around  $2 \times 10^{17}/\text{cm}^{-3}$  (this will be discussed in next section).

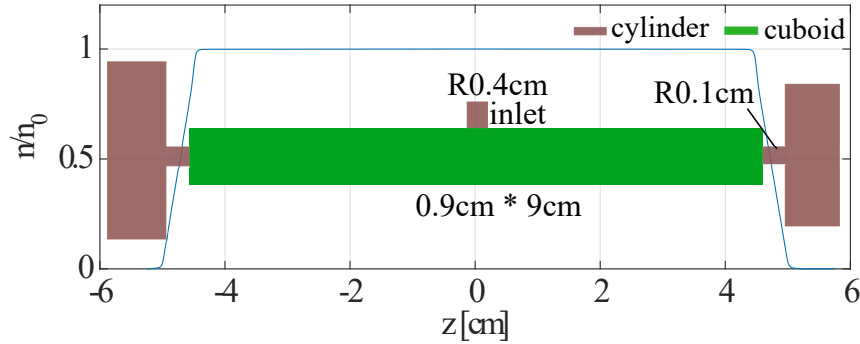


FIGURE 4.3: The plasma cell and the on axis plasma density.

In a gas, molecules not only strike the wall but also undergo frequent collisions, let  $\omega$  denote the collision frequency, consider a gas with  $N_0$  molecules, after a period  $t$ , there are still  $N$  particles that have not undergone collision, then we have  $-dN = N\omega dt$ , integrating this equation, we have

$$N = N_0 e^{-\omega t} \quad (4.1)$$

$t$  can be replaced by  $l/v_a$ ,  $l$  is the path that has been traversed by a molecule without suffering collision during interval  $t$ ,  $v_a$  is the average velocity, the mean free path length  $L$  is defined as the mean path length over which molecules travel without collision, thus  $\omega = \frac{v_a}{L}$ , then the fraction of molecules that are still traveling without suffering a collision in the distance  $l$  follows that

$$\phi(l) = \frac{N}{N_0} = e^{-l/L} \quad (4.2)$$

In a plasma cell, the gas flow can be described by three regimes depending on the ratio of mean free path length ( $L$ ) and the transverse size of the tube ( $a$ ).

(A) viscous regime:  $L/a < 0.01$ .

(B) molecular regime:  $L/a > 1$ .

(C) transition regime:  $0.01 < L/a < 1$

In the viscous regime collisions mainly happen between molecules, thus it is easily to reach thermal equilibrium, the flow is continuous. In the molecular flow, the gas density is quite low thus the collision mainly happens between molecule and the wall. The molecular motion in different regimes are shown in Figure 4.4

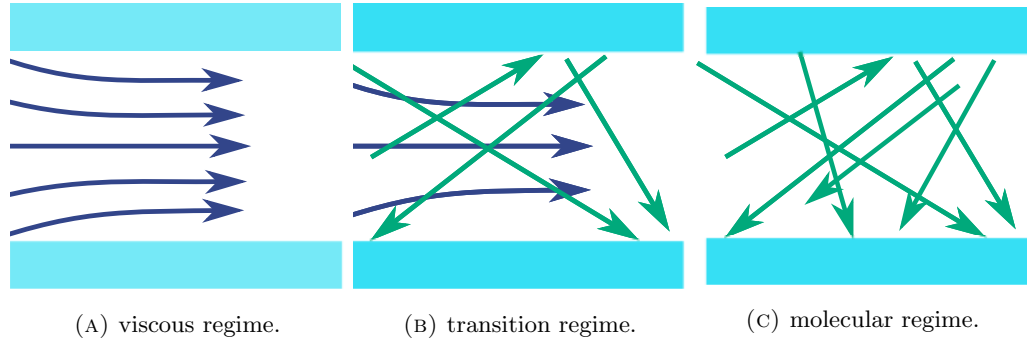


FIGURE 4.4: The motion of molecules in different regimes.

The mean free path length is related to the temperature  $T$ , the molecular cross section  $\sigma$  and pressure  $P$ , is given by [125]

$$L = \frac{2.331 \times 10^{-17} T}{P_{Tor} \sigma^2} \quad (4.3)$$

For hydrogen at  $T = 298.15K$ , with a density of  $1 \times 10^{17}/\text{cm}^{-3}$  (corresponding to an electron density of  $2 \times 10^{17}/\text{cm}^{-3}$  under full ionization), one has  $L \approx 29.8\mu\text{m}$ . With  $a = 0.9\text{cm}$ ,  $L/a \approx 0.0031$ , the gas density in the plasma cell should be studied with the viscous flow model.

The laminar flow model is used and a finite element method (FEM) is applied to calculate the gas density, the velocity of the gas molecules in the main cell is lower than 10 m/s, the density profile is shown in Figure 4.3.

## 4.3 Considerations related to the configuration

### 4.3.1 Energy gain in the plasma wave

The advantage of the LWFA is the high acceleration gradient, thus it is important to have a basic understanding of the magnitude of the achievable acceleration field and

the energy gain, for the first step of ESCULAP, the laser is not guided, thus the energy gain is mainly achieved within one Rayleigh length before and after the laser focal plane. It has been discussed before, to efficiently excite the field potential in the plasma, the length of the laser beam  $L$  should be matched with the plasma density  $n_e$  (which further decides the plasma wave number  $k_p$ ), with a fixed laser amplitude, the resonant condition was shown in Figure 2.12, while for a laser with fixed energy, the shape factor i.e the laser length  $L$ , laser waist  $w$  also decides the laser amplitude and directly affect the amplitude of the potential, one has  $a \propto \frac{1}{w\omega_L} \sqrt{E_L/L}$  according to the discussion in section 2.2.4. Consider a laser beam laser which has an energy  $E_L = 2\text{J}$  (the case of LASERIX), with a Gaussian distributed profile in both longitudinal and radial direction, by setting the spot size to  $w_0 = 50.46\mu\text{m}$  at the focal plane, the Rayleigh length yields  $L_R = \pi r_{s0}^2/\lambda_L = 1\text{cm}$ , the wakefield potential, wakefield strength versus plasma density  $n_e$  and laser duration are show in Figure 4.5.

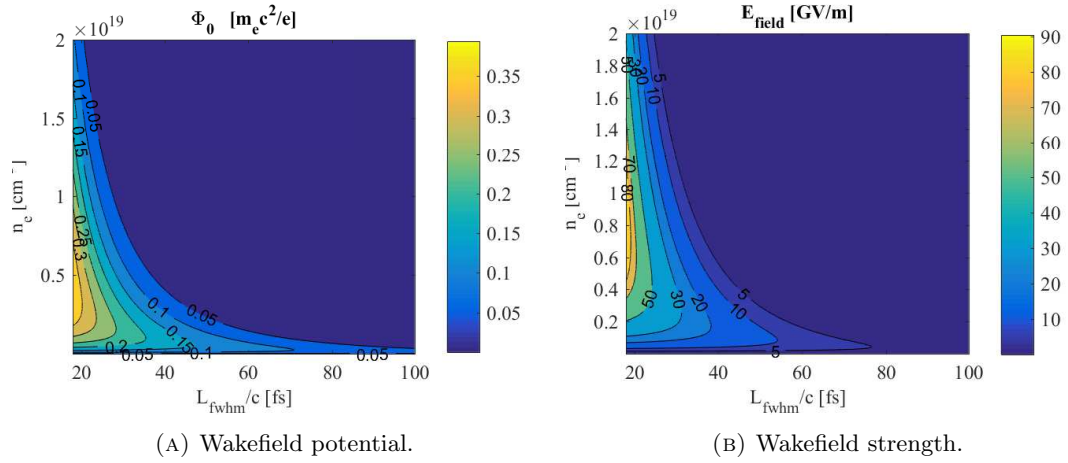


FIGURE 4.5: With the LASERIX laser  $E_L = 2\text{J}$ , by setting the laser waist to  $r_s = 50.46\mu\text{m}$ , the achievable maximum wake potential and longitudinal electric field with various plasma density and laser length.

Compare Figure 4.5a with Figure 4.5b, the resonant condition for the wake potential and the wakefield are different, since the wakefield can be described with the product of wake potential and the field of the wave breaking  $E_{wb}$ ,  $E_{wb}$  is also related to the plasma density by  $E_{wb} \propto \sqrt{n_e}$ . However, a shorter laser duration is desired to achieve both higher wakefield potential and wakefield, with a laser duration of 20 fs, an acceleration gradient as high as 90 GV/m can be achieved with a plasma density of  $n_e \approx 8 \times 10^{18} \text{cm}^{-3}$ . The laser beam has a wavelength of  $\lambda_L = 0.8\mu\text{m}$ , the critical density  $n_c = \epsilon_0 m_e \omega_L^2 / e^2$  yields  $1.74 \times 10^{21} \text{cm}^{-3}$ , the plasma density should below this value for the propagation of the laser, this is not conflict with the resonant condition.

However, for the ESCULAP project, the external electron bunch achieved in the previous chapter at the plasma entrance is shorter than  $\sim 85\text{fs}$ , the plasma wave duration should be at least longer than 170 fs, thus most electrons are injected at the focusing phase.



The plasma wave period  $T_p$  is proportional to  $\sqrt{1/n_e}$ ,  $T_p$  versus  $n_e$  is shown in Figure 4.6.

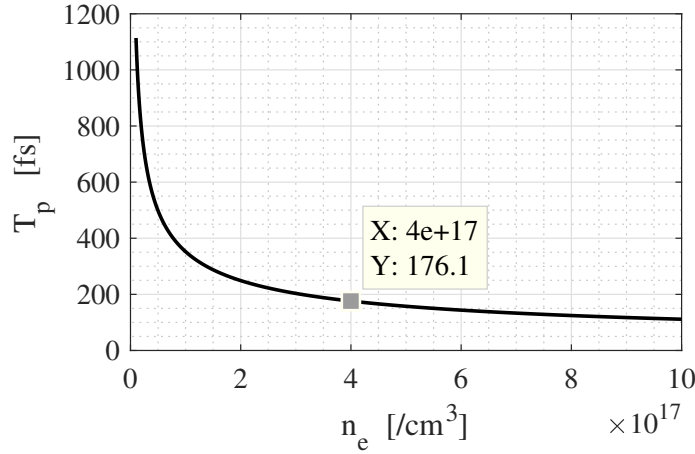


FIGURE 4.6: The plasma wave duration versus plasma density.

According to Figure 4.6, with a plasma density of  $4 \times 10^{17} / \text{cm}^3$ , the plasma wave duration yields 176 fs, it is two times the electron bunch duration. With the 2 J laser beam, by setting the density range to  $n_e < 4 \times 10^{17} / \text{cm}^3$ , the laser amplitude versus laser duration is shown in Figure 4.7a, the wakefield potential, wakefield strength and energy gain of the electron within two Rayleigh length versus the laser duration and plasma density are respectively shown in Figure 4.7b, 4.7c and 4.7d.

From Figure 4.7a, with a laser duration longer than 20 fs, the laser amplitude is smaller than 1, that is the linear regime, according to Figure 4.7b, 4.7c, 4.7d, in the interested density range, shorter laser duration and higher plasma density is desired to obtain higher acceleration field and energy gain. With a plasma density of  $n_e = 4 \times 10^{17} \text{cm}^3$ , and a laser duration of 20 fs the maximum longitudinal electric field is  $\sim 12 \text{ GV/m}$ , the efficient energy gain of the electron bunch within one Rayleigh length before and after the laser focal plane yields  $\Delta\gamma_e \approx 460$ .

However, given the current status of LASERIX, the pulse duration is 45 fs FWHM, without additional compression of the laser pulse, only the laser waist spot size  $w_0$  can be tuned,  $w_0$  has effect on the field potential and the field strength but has less effect on the energy gain of the electron bunch since  $a_0^2 L_R$  (the acceleration field is in proportional to  $a_0^2$ ) is independent of the laser waist. With the FWHM laser duration being fixed to 45 fs, the laser amplitude versus laser spot size is shown in Figure 4.8a, the wakefield potential, wakefield strength and energy gain of the electron over two Rayleigh lengths versus the laser duration and plasma density are respectively shown in Figure 4.8b, 4.8c, 4.8d.

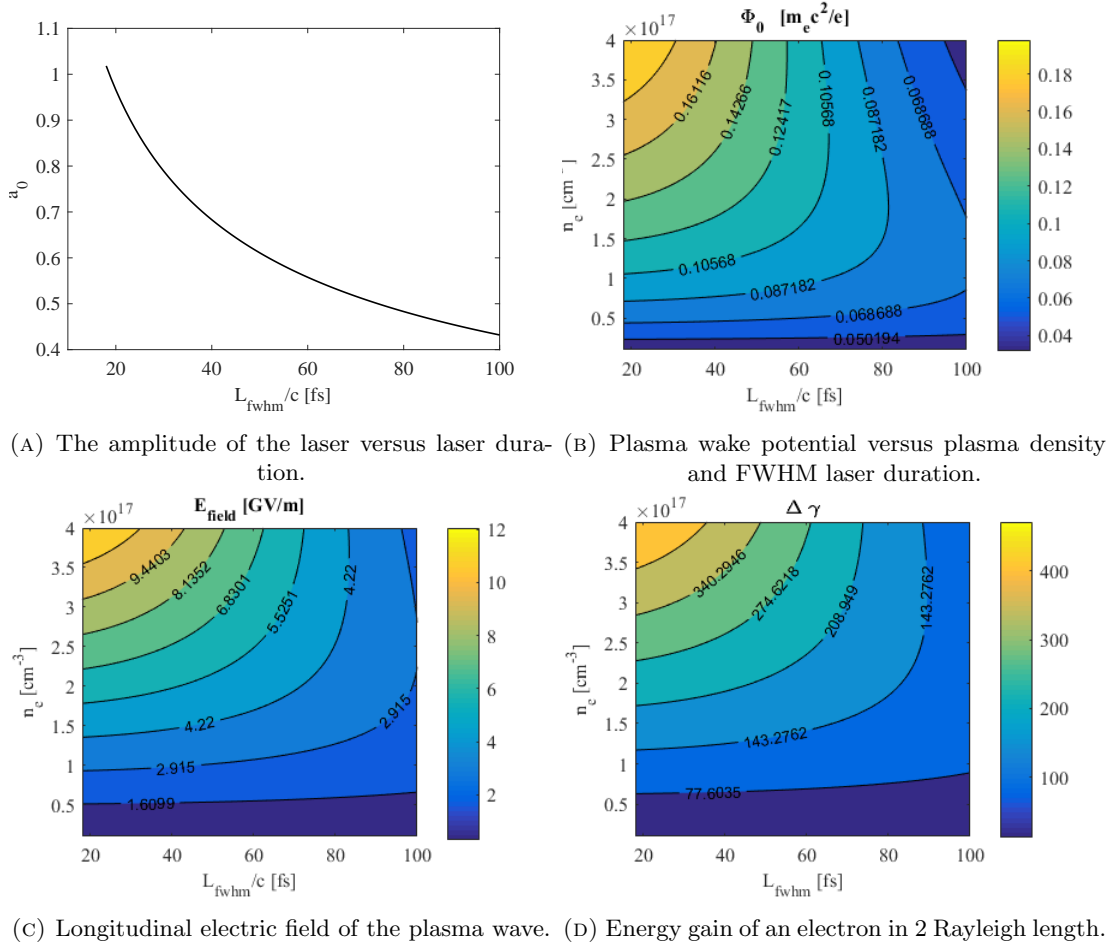


FIGURE 4.7: With the LASERIX laser  $E_L = 2 \text{ J}$ , by setting the laser waist to  $r_s = 50.46 \mu\text{m}$ , the amplitude of the laser versus laser length at focal plane is shown in A). The achievable maximum wake potential and longitudinal electric field with various plasma density and laser length are shown in B and C, the longitudinal electric field multiplied by two Rayleigh length is shown in D.

One can find from Figure 4.8 that, by tightly focusing the laser to a spot size of  $25 \mu\text{m}$ , with a plasma density of  $\sim 4 \times 10^{17} \text{ cm}^{-3}$ , an accelerating electric field as high as  $40 \text{ GV/m}$  can be achieved in the quasi-linear regime. While the spot size of the laser has no effect on the energy gain.

It is notable that in our case, the capture of the electrons and the final beam quality depends on the velocity bunching process in the plasma, according to the previous discussion a low electric field and long distance is preferred for the velocity bunching, that calls for a large laser waist. Thus, in the following study, the laser FWHM duration and laser waist are respectively fixed to  $\tau_L = 45 \text{ fs}$ ,  $w_0 = 50.46 \mu\text{m}$  (giving a Rayleigh length of  $1 \text{ cm}$ ), the injection configuration for different plasma densities are studied.

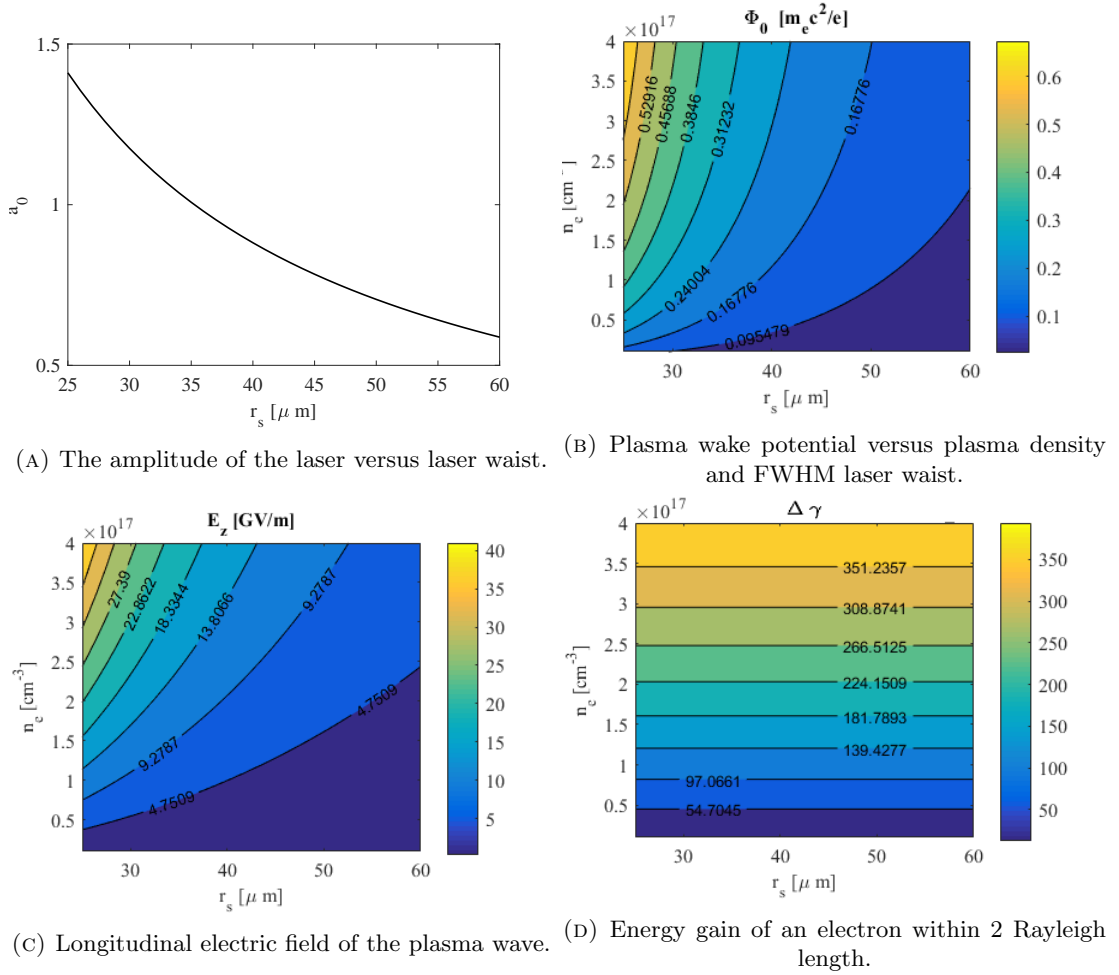


FIGURE 4.8: With the current LASERIX parameters, the energy is  $E_L = 2 \text{ J}$ , the FWHM laser duration is 45 fs, the amplitude of the laser versus laser waist at focal plane is shown in A). The achievable maximum wake potential and longitudinal electric field with various plasma density and laser waist are shown in B and C, the longitudinal electric field multiply two Rayleigh length is shown in D.

### 4.3.2 Longitudinal capture and compression of the electron bunch in the plasma wave

The external electron bunch has an energy of 10 MeV which corresponding to a Lorentz factor of  $\gamma_e = 20$ , with a uniform plasma density, the phase velocity of the plasma wave is the group velocity of the laser, as the Lorentz factor is used to describe the energy and velocity of the electron bunch, for consistency it is also used to describe the velocity of the laser beam, in a plasma the Lorentz factor of the laser  $\gamma_L$  is proportional to  $\sqrt{1/n_e}$ , with the LASERIX laser beam,  $\gamma_L$  versus  $n_e$  is shown in Figure 4.9. For the density range of interest  $n_e < 4 \times 10^{17} \text{ cm}^{-3}$ , we have  $\gamma_L > 65$ , thus the external electrons moves slower than the plasma wave and slips backward at the entrance of the plasma.

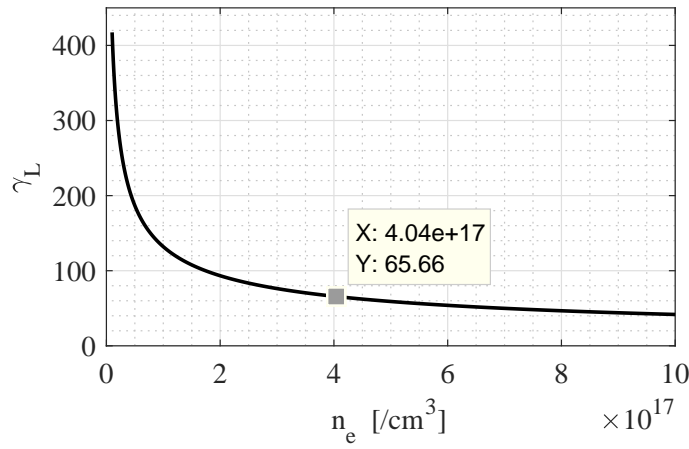


FIGURE 4.9: The plasma wave duration versus plasma density

The electric field of the plasma wakefield in the linear regime in the co-moving frame has been derived in formula 2.122, they are shown again here

$$E_z = \sqrt{\pi} \frac{a_0^2}{4\sqrt{2}} \frac{m_e c \omega_p}{e} k_p L \exp(-k_p^2 L^2 / 8) \cos(k_p \xi) \exp\left(\frac{-2r^2}{w(s)^2}\right) \quad (4.4a)$$

$$E_r = \sqrt{\frac{\pi}{2}} a_0^2 \frac{m_e c^2 r}{e w(s)^2} k_p L \exp(-k_p^2 L^2 / 8) \sin(k_p \xi) \exp\left(\frac{-2r^2}{w(s)^2}\right) \quad (4.4b)$$

Note that there is a phase difference of  $\pi/2$  between the longitudinal electric field and the transverse field, thus we have

$$\begin{aligned}
 2n\pi + 0 < k_p\xi < 2n\pi + \pi/2 & \quad \text{focus and deceleration} \\
 2n\pi + \pi/2 < k_p\xi < 2n\pi + \pi & \quad \text{focus and acceleration} \\
 2n\pi + \pi < k_p\xi < 2n\pi + 3\pi/2 & \quad \text{defocus and acceleration} \\
 2n\pi + 3\pi/2 < k_p\xi < 2n\pi + 2\pi & \quad \text{defocus and deceleration}
 \end{aligned}$$

The electric field calculated with the linear theory are shown in Figure 4.10, with negative value of  $E_z$  referring to the acceleration field, positive value of  $E_r$  refers to the focusing field. For the sake of simplicity, the terms  $2n\pi$  is ignored in the following analysis, the  $k_p\xi$  refers to the acceleration phase, it is recognized as  $\phi$  for simplicity. In the regime in which we are interested, the external electron bunch is slower than the plasma wave, thus when injected, the electrons slip backward behind the plasma wave, the phase increases during the propagation. The electron bunch is expected to be injected between 0 and  $\pi$ , in transverse direction the electrons are focused, in longitudinal direction, the bunch head get less energy than the bunch tail, it is compressed. Consider the wakefield, at phase  $\phi = \pi/2$  a maximum field gradient is achieved thus the electron bunch gets a maximum compression there, at phase  $\phi = \pi$ , a minimum field gradient but a maximum field strength is achieved, the electrons can be accelerated with higher energy and smaller energy spread.

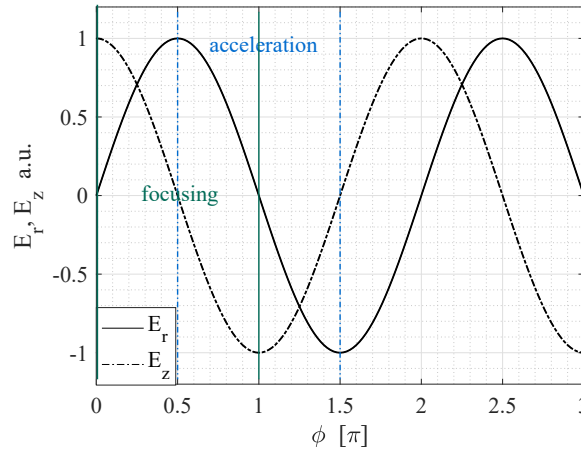


FIGURE 4.10: The radial and longitudinal electric field from the linear theory, with amplitude not to scale,  $\phi = 0$  refers to the middle of the laser, laser tail is in right side.

The longitudinal motion of the electrons in the plasma wave can be described with the acceleration phase  $\phi = k_p\xi$  and the normalized electron energy  $\gamma = E_e/m_e c^2$ ,

$$\frac{dp_i}{dt} = eE_i \quad (4.5a)$$

$$\frac{d\phi}{dt} = k_p(v_g - v_e) \quad (4.5b)$$

Where  $i = x, y, z$ , in the x and y direction,  $E_{x,y} = E_{x0,y0} \sin \phi$ , while in the z direction  $E_z = E_{z0} \cos(\phi + \phi_0)$ , in the following study, normalized parameters are used and they are distinguished with the symbol  $\sim$ , they yield  $\tilde{p} = p/m_e c$ ,  $\tilde{t} = \omega_p t$ ,  $\tilde{E}_i = E_i/E_{wb} = E_i \frac{e}{m_e c \omega_p}$ ,  $\tilde{\xi} = k_p \xi$ ,  $\tilde{s} = s/L_R$ , note that  $\xi$  refers to the distance to laser peak while  $s$  refers to the distance from the electron bunch to the laser focal plane and it is normalized with the Rayleigh length. Thus the normalized motion equation in the z direction yield

$$\frac{d\tilde{p}_z}{d\tilde{t}} = \tilde{E}_z \quad (4.6a)$$

$$\frac{d\tilde{\xi}}{d\tilde{t}} = \beta_g - \beta_e = \beta_g - \frac{\tilde{p}_z}{\sqrt{1 + \tilde{p}_z^2}} \quad (4.6b)$$

Where  $\beta_e, \beta_g$  are respectively the velocity of the electron and the group velocity of the laser normalized by c. As shown in formula 4.4, one has  $E_{z0} \propto \frac{\omega_p^2}{\omega_L^2} \frac{1}{w_0^2(1+\tilde{s}^2)}$ , the plasma density and the distance between the injection plane (the plasma start plane as shown in Figure 4.11) and the laser focal plane  $\tilde{s}_f$ , and also the injection phase can be adjusted to tune the evolution of  $(\tilde{\xi}, \tilde{p}_z)$  phase space of the electron bunch in the plasma.

For the sake of clarity, the configuration of the laser envelop as well as the parameters  $\tilde{\xi}, \tilde{s}$  are shown in Figure 4.11, and LASERIX parameters will be used in the study, the laser waist is set to  $w_0 = 50.46 \mu\text{m}$  (giving a Rayleigh length of 1 cm).

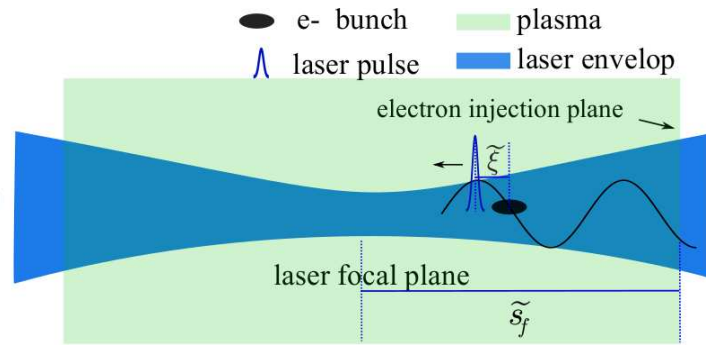


FIGURE 4.11: The configuration of the laser laser envelop and the plasma cell.

The motion equation 4.6 can be solved with the Runge-Kutta method. Here an ellipse is used to represent the envelop of the phase space of the initial electrons as shown in Figure 4.12, it is initially distributes in  $0 < \tilde{\xi} < \pi$ . By setting the plasma density to

$2 \times 10^{17} \text{ cm}^{-3}$ , with various  $\tilde{s}_f$ , the phase space envelop at the laser focal plane is shown in Figure 4.13. With the increase of  $\tilde{s}_f$ , the electron bunch is closer to the field crest, and is more compressed at the laser focal plane, however, part of the electrons slips to the next wave period when  $\tilde{s}_f = 5$ . It is also notable that, in the range of  $\pi < \tilde{\xi} < 2\pi$ , the transverse field has a defocusing force, particles slips close to this range may get lost (i.e the case of  $\tilde{s}_f = 5$ ). With  $\tilde{s}_f = 4$ , the electron bunch can catch up the laser before slipping into the deceleration phase, and can be efficiently compressed by the plasma wakefield, then it can to be accelerated by the subsequent plasma wakefield with smaller energy spread.

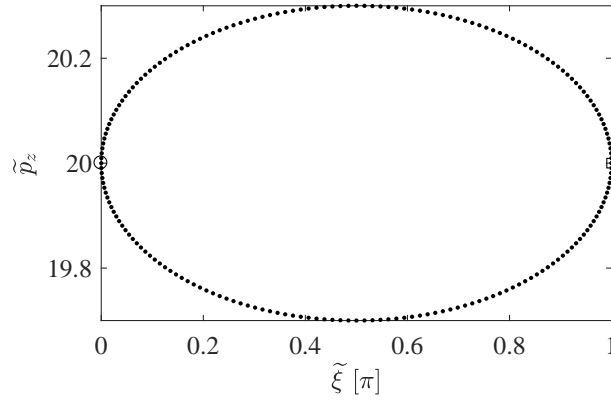


FIGURE 4.12: The phase space envelop of the initial electron bunch.

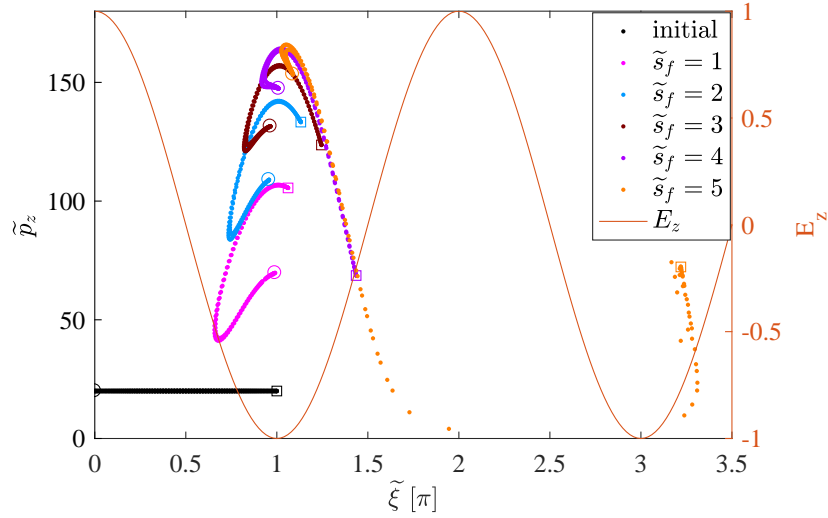


FIGURE 4.13: The phase space envelop of the electron bunch at the plasma entrance and after being accelerated to the laser focal plane, the distance from the electron injection plane to laser focal plane  $\tilde{s}_f$  is varied, the plasma density is uniformly  $2 \times 10^{17} \text{ cm}^{-3}$ .

Regarding the ESCULAP project, the uniform plasma density is then replaced with the

density profile in Figure 4.3, and the maximum density is set to  $2 \times 10^{17} \text{cm}^{-3}$ . The phase space envelop at the laser focal plane with various  $\tilde{s}_f$  is shown in Figure 4.14.

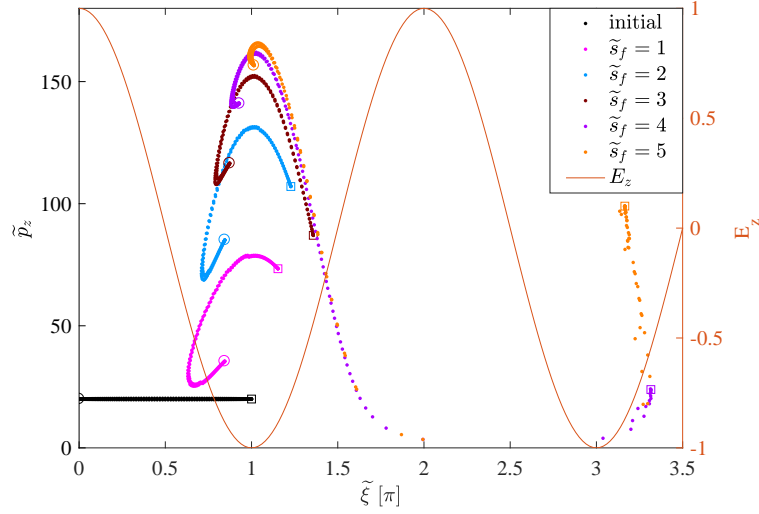


FIGURE 4.14: The phase space envelop of the electron bunch at the plasma entrance and after acceleration to the laser focal plane, the distance from electron injection plane to the laser focal plane  $\tilde{s}_f$  is varied, the plasma density profile is from figure 4.3 with a maximum density of  $2 \times 10^{17} \text{cm}^{-3}$ .

Referring to the plasma density profile, it starts from 0 and rises to 90% of the maximum density at 0.75cm, the length of the rising edge is comparable with the Rayleigh length, thus it has effect on the electric field. Comparing Figure 4.13 with Figure 4.14, one can find that the envelop is more stretched in the latter case, because in the rising edge the electric field is weaker, the plasma wavelength is longer, electrons are not distributed in the desired phase range. One can also note that the rising edge has more effect on the electron bunch energy if  $\tilde{s}_f$  is small, this is due to the fact that if the interaction starts near the laser focal plane, the electric field with uniform density is sufficient high to accelerate the electron bunch, the low density in the rising edge may affect the final energy, if the interaction starts far away from the laser focal plane, the electric field is weak, the rising edge has less effect on the final energy.

Thus the electron bunch is more compressed with uniform density, it's better to shorten the rise edge of the plasma density profile. With a smaller aperture at the ends of the main plasma cell, one can get a sharper rising edge, but this has more requirement on the mechanical manufacture.

In the previous discussion the transverse field is absent and the longitudinal electric field is assumed to be uniform in the radial direction, for an accurate study, a PIC simulation will be performed in the next section.



## 4.4 Simulation study of the electron-plasma wakefield interaction in the plasma cell

It has been discussed in the previous section, with the linear wakefield, by setting the injection plane (plasma start plane) several Rayleigh length before the laser focal plane, the external electron bunch which is injected in a phase range of  $0 \leq \tilde{\xi} \leq \pi$  can be efficiently compressed when propagating towards the laser focal plane, while the effect of the transverse field was not included. In this section, the interaction in the plasma is simulated with the WAKE-EP code, the best injection configuration for different plasma densities are studied, the effect of the space charge is analyzed.

The initialization of the moving window in WAKE-EP is shown in Figure 4.15, in the radial direction, the size of the simulation window  $R_{iar}$  is set to 20 times the laser waist at the focal plane  $R_{iar} = 20w_0$ , the grid number in  $w_0$  is larger than 60. In longitudinal direction, we have  $z_{bl} = 4L$  and  $z_{wake} = 15L$  the grid number in  $L$  is larger than 60.

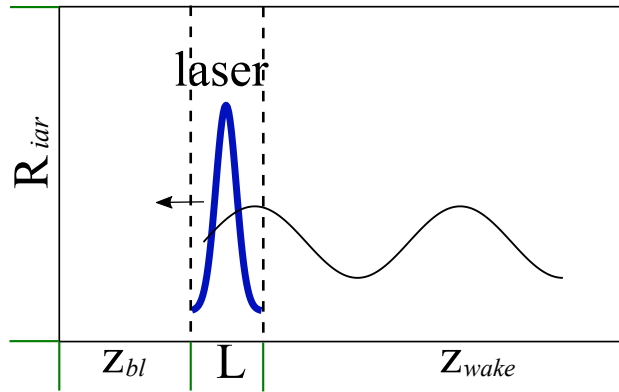


FIGURE 4.15: The moving window in WAKE-EP

### 4.4.1 Longitudinal Phase space manipulation with the laser configuration

In the previous study, only the 1-D longitudinal electric field is considered, the electrons are injected in the phase range  $0 \leq \tilde{\xi} \leq \pi$ , where the transverse electric field exerts a focusing force on the electron bunch. For the simulation with WAKE-EP, the  $\tilde{s}_f$  defined in Figure 4.11 and the injection phase  $\tilde{\xi}_0$  are tuned to find the optimum configuration, note that  $\tilde{\xi}_0 = k_p \xi_0$ ,  $k_p$  is the nominal plasma wave number,  $\xi_0$  is the distance from the injection position to the laser peak. The plasma density profile in Figure 4.3 is used in the following study, it is uniform in the main cell (9 cm in length), this uniform density is recognized as the nominal plasma density  $n_0$ .

With different  $\tilde{s}_f$  and  $\tilde{\xi}_0$  the longitudinal distribution of the electrons at the laser focal plane is shown in Figure 4.16. We can see that with the increase of  $\tilde{s}_f$  the electron bunch is more compressed at the laser focal plane, and slips more backward, when  $\tilde{s}_f$  is increased to 4.75, the peak current starts to decrease, this is consistent with the result in Figure 4.14. Here  $2\pi$  refers to the nominal plasma wavelength  $74.66 \mu\text{m}$  ( $249.04 \text{ fs}$  in duration), the peak current at the laser focal plane reaches  $1166 \text{ A}$  with  $\tilde{s}_f = 4.5$  and  $\tilde{\xi}_0 = 0$ . With  $\tilde{\xi}_0 = 0$ , some electrons are injected in the defocusing region, this may be due to the fact that at the start position both the laser amplitude and the plasma density is low, the electric field is weak thus the low energy electrons slip quickly to the focusing region before getting lost.

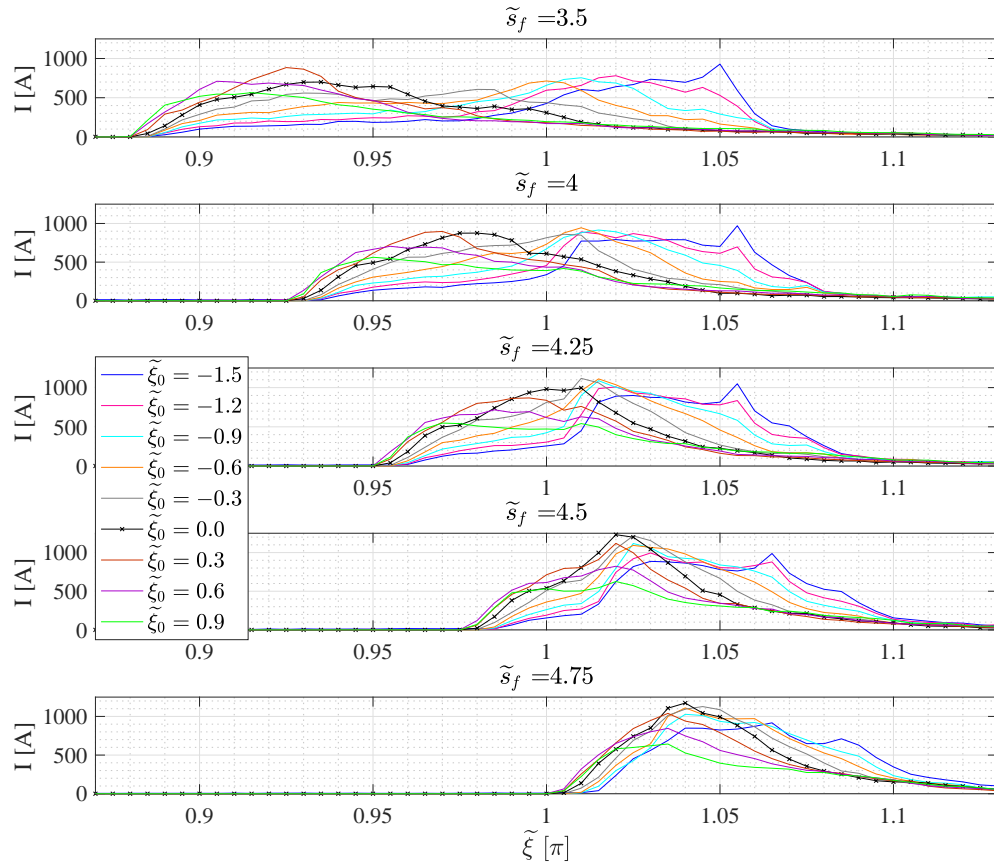


FIGURE 4.16: The longitudinal distribution of the electrons at laser focal plane, with different start position and injection phase, bin size is  $0.005\pi$ .

With the electron bunch being compressed near the laser focal plane, the energy spread is expected to be relatively small after the acceleration, with all the configuration in Figure 4.16, the energy distribution of the main electron bunch at the plasma cell exit is reported in Figure 4.17, one can find that with the electron bunch being well compressed at the laser focal plane, the energy spectrum is more sharp at the plasma exit.

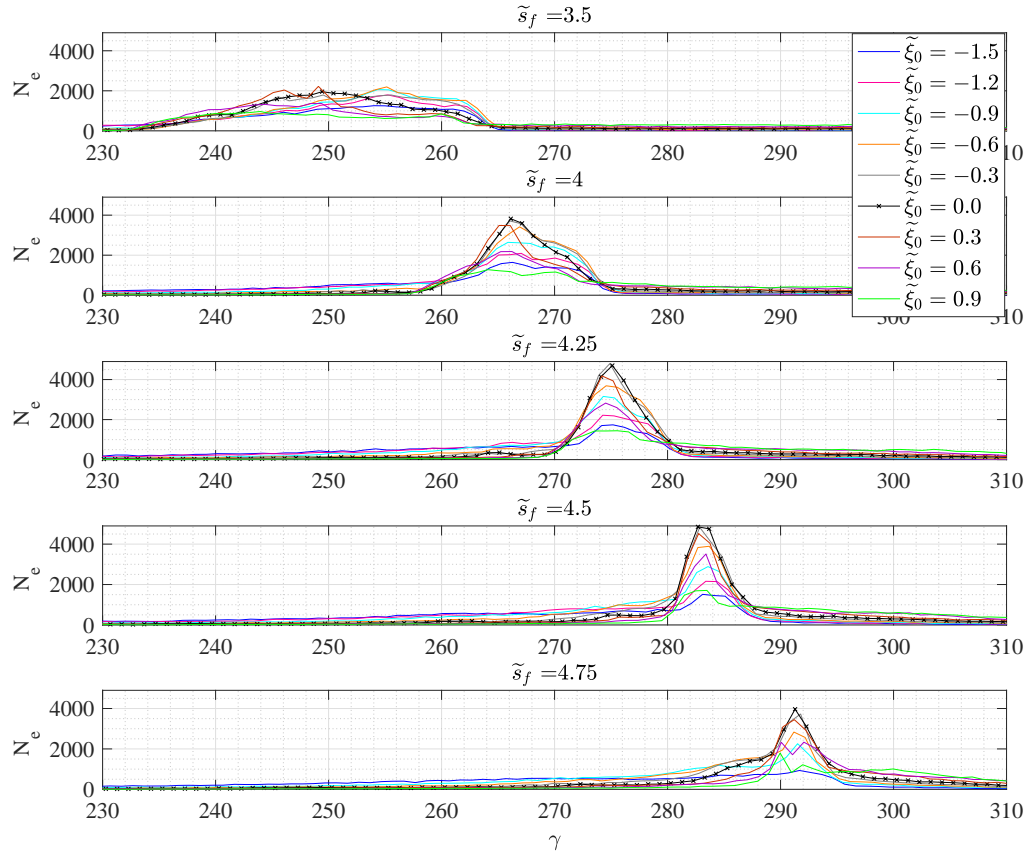


FIGURE 4.17: The energy distribution of the electrons at the exit of the plasma cell, with different start position and injection phase, bin size is 1.

Regarding to the optimal injection configuration ( $\tilde{s}_f = 4.5$ ,  $\tilde{\xi} = 0$ ), the longitudinal phase space ( $\tilde{\xi}$ ,  $\gamma$ ) (left axis) together with the values of  $E_z$  (right axis) at four different positions are reported in Figure 4.18.

At the entrance of the plasma both the plasma density and the laser amplitude is low, thus the electric field is not sufficient to change the electron energy.

When propagated to near 0.8 cm the plasma density rises to  $0.9n_0$ , the laser amplitude is approximately 0.18, the plasma wakefield field is excited in linear regime. The first deceleration peak is located at  $\tilde{\xi} = 0.1\pi$ , while the first acceleration peak is located at  $\tilde{\xi} = \pi$ , thus the first half period is shorter under the effect of the laser. The core of the electron bunch is situated at  $\xi \approx 0.15\pi$ , the electrons are mainly distributed between  $\tilde{\xi} = 0.1\pi$  and  $\tilde{\xi} = 0.7\pi$ , in this phase region, the electrons experiences a transversely focusing force from the transverse electric field, while in the longitudinal direction, electrons at the bunch head get less energy (deceleration) than that at the bunch tail, thus the phase space is rotated and longitudinally compressed during the propagation. Most of

the electrons are slightly decelerated w.r.t the energy at the plasma entrance and are slower than the plasma wave, they will slip backward (toward large phase) during the propagation.

Near the laser focal plane, the laser amplitude increased to  $\sim 0.7$ , the maximum acceleration field increased to  $0.137E_{wb}$  corresponding to 5.89 GV/m, thus the electron bunch can get an efficient acceleration. The electron bunch has already been compressed in the previous propagation and slipped just to the acceleration field crest (the derivative of the field is minimum), thus the electron bunch can be accelerated to higher energy with smaller energy spread. One may find that the first acceleration field crest tilt slightly backward (located at  $\tilde{\xi} \approx 1.085\pi$ ), because at the laser focal plane the laser amplitude is 0.7, the nonlinearity has effect on the electric field.

At the plasma exit, the electron bunch slips slightly forward from  $\tilde{\xi} = \pi$  w.r.t the distribution at the laser focal plane, because the electron bunch moves faster than the plasma wave ( $\gamma_L > 93.3$ ) since the laser focal plane. A short electron bunch with high energy is clearly identified at the plasma exit, a small part of the electrons slip to the second period, they are also accelerated to high energy, however they are only 1.26% of all the electrons.

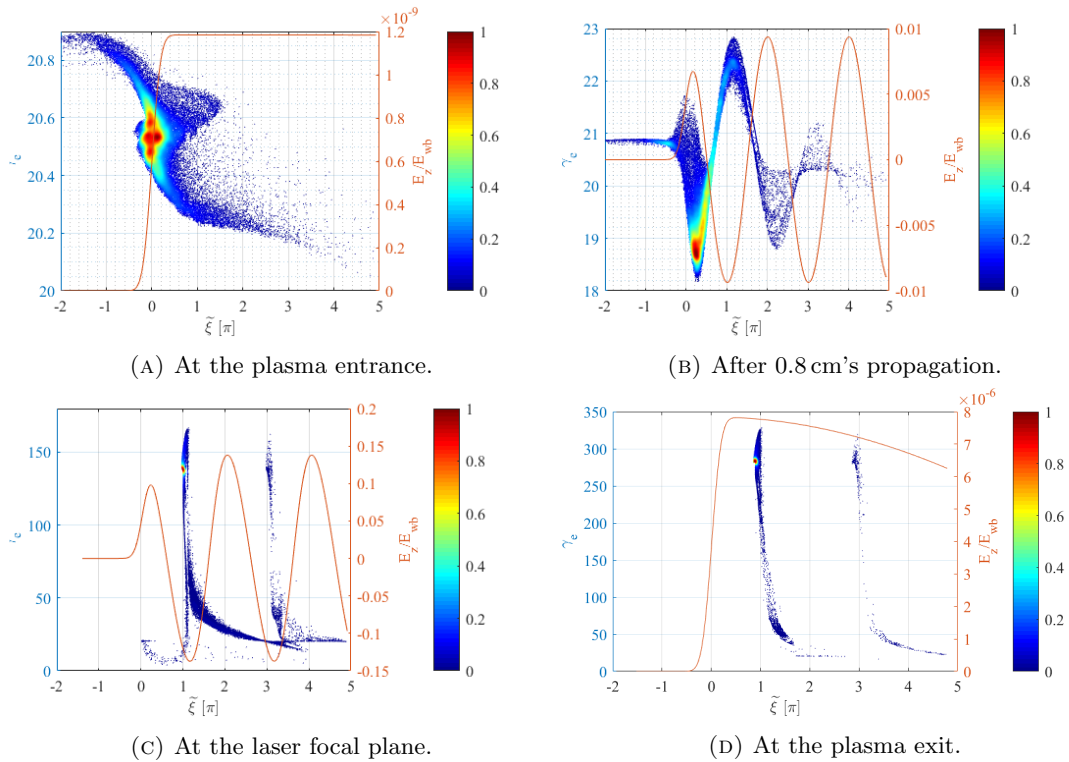


FIGURE 4.18: With  $\tilde{s}_f = 4.5$ ,  $\tilde{\xi} = 0.2$ , the longitudinal phase space of the electron bunch and longitudinal electric field in reduced units at four positions, (A) at the entrance of the plasma, (B) after 0.8 cm's propagation where the plasma density rise to  $0.99n_0$ , (C) at the laser focal plane, (D) at the plasma exit.

The bunch charge at the plasma entrance is 10 pC, 50000 macro particles are used in the simulation, 39713 macro particles survived to the plasma exit. Due to the long tail in both energy and position, the energy spread calculated with all the particles seems meaningless.

The longitudinal position distribution of the electrons at the plasma exit is shown in Figure 4.19, almost 95% electrons are distributed at  $\tilde{\xi} < \pi$ , while 98.5% electrons are distributed at  $\tilde{\xi} < 1.5\pi$ . With the consideration that a few high energy electrons are distributed near  $\tilde{\xi} = \pi$ , thus the electrons distributed at  $\tilde{\xi} < 1.5\pi$  are assumed to belong to the main bunch, their energy distribution will be discussed in the subsequent study. Due to the long bunch tail, the bunch duration is described with it's FWHM value, it is approximately  $0.045\pi$  at the plasma exit, which yields 5.6 fs ( $2\pi$  refers to the period of the plasma wave 249fs).

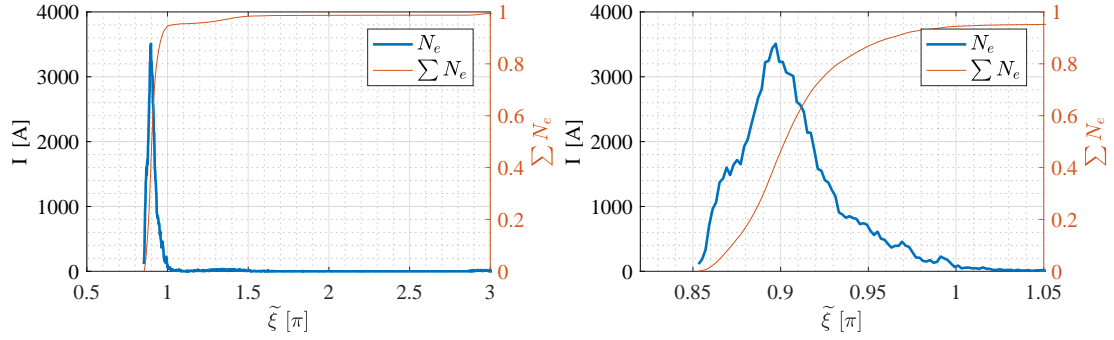


FIGURE 4.19: The longitudinal distribution of the particles at plasma exit (blue line, left axis), bin size is  $0.005\pi$ , and the sum of the particle number normalized with the total particles number (red line, right axis). The figure at the right side is the zoom of the left one.

Only consider the main bunch with  $\tilde{\xi} < 1.5\pi$ , the distribution of the  $\gamma_e$  is shown in Figure 4.20.

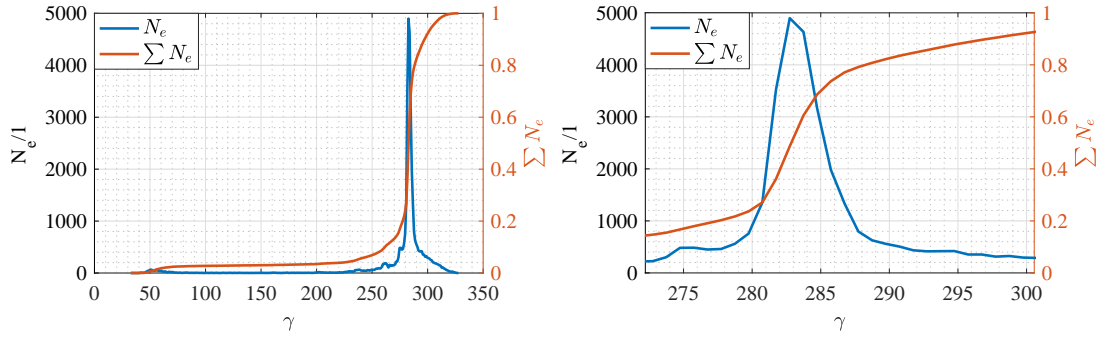


FIGURE 4.20: The energy distribution of the selected particles at the exit of the plasma cell (blue line, left axis), bin size is 1, and the sum of the particle number normalized with the total particles number (red line, right axis), the figure in the left is the zoom of left one.

In the main bunch, the average  $\gamma_e$  yields 282.67,  $\sim 90\%$  electrons have a  $\gamma_e$  larger than 260, the energy spread of these electrons is  $\sigma_\delta = 3.27\%$ ,  $\sim 95\%$  electrons have a  $\gamma_e$  larger than 230, they yield an energy spread of  $\sigma_\delta = 4.48\%$ . Because the energy spectrum has a sharp peak and long tails, the energy spread is quite sensitive to the selecting window, in the previous paper in [126], 95% high energy electrons are selected to calculate the energy spread, here the FWHM energy spread is calculated to avoid the effect of the long tails, the full width of the half maximum value of the energy spectrum is considered as the absolute energy spread, it is then normalized with the average energy and recognized as  $\sigma_{\delta, fwhm}$ , it yields 1.2% at the plasma exit.

Cutting the low energy tail is reasonable since they have a larger radial size and angular divergence, and may be lost or can be easily collimated during the subsequent transport. The distribution of the main bunch in the transverse plane is shown in Figure 4.21a, more than 94% of the electrons are distributed in a radius of  $90\ \mu\text{m}$  (see the red circle in the figure), the distribution of these electrons in the circle in the  $\tilde{\xi} - \gamma_e$  plane is shown in Figure 4.21b. Comparing with the distribution of all the electrons in Figure 4.18d, one can find that the electrons with lower energy are distributed at larger radial size, they surround the bunch core as a halo.

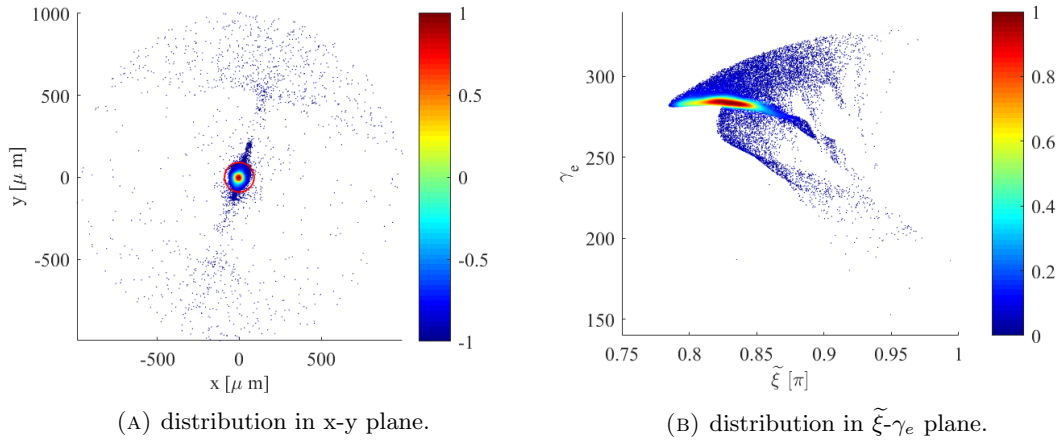


FIGURE 4.21: (A) The distribution of the electrons in the transverse plane, the red line shows a circle with a radius of  $90 \mu\text{m}$ , (B) the longitudinal phase space of the electrons in the circle.

To check the evolution of the bunch length and the energy spread during the propagation, only the 94% high energy macro particles in the main bunch are counted, the RMS and FWHM bunch duration and the energy spread are respectively shown in Figure 4.22a and Figure 4.22b. The evolution of the RMS value and the FWHM value have the same trend during the propagation, a sharp peak and long tails in the distribution is indicated if the RMS value is larger than the FWHM value. The bunch length reduces quickly between 1 cm and 4 cm, that means the velocity bunching is mainly performed in this range. The energy spread increases between 0 and 2.5 cm, because the energy chirp for the velocity bunching is generated in this range, then the energy spread decreases from 3 cm to 5.5 cm due to the near crest acceleration. It can be inferred that with a longer on crest acceleration range, the energy spread may decrease to a smaller value.

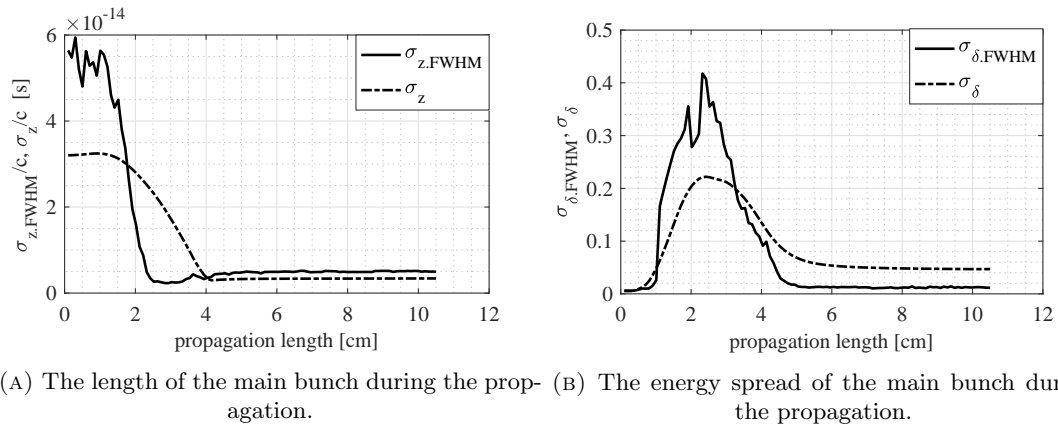


FIGURE 4.22: Evolution of the bunch length and energy spread in the plasma cell.

The average Lorentz factor of the electrons  $\langle\gamma_e\rangle$  during the propagation in the plasma is shown in Figure 4.23,  $\langle\gamma_e\rangle$  slightly decreases before 1 cm, and continuously increases to

283 at the plasma exit, that means the bunch center is suited at the zero acceleration phase  $\tilde{\xi} = \pi/2$  after 1 cm of propagation, and then slips to the acceleration field crest and get efficient acceleration during the propagation. The energy gain is mainly happened between 3.5 cm to 5.5 cm, within one Rayleigh length before and after the laser focal plane.

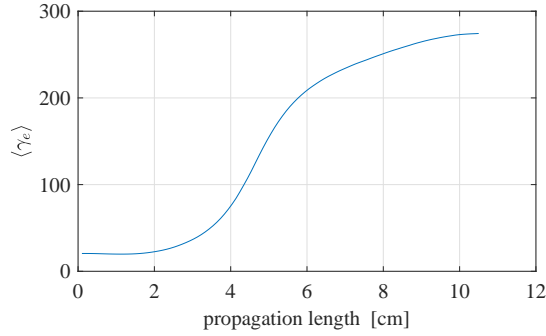


FIGURE 4.23: The average Lorentz factor of the electron bunch versus the propagation distance in the plasma.

The optimal configuration is searched with WAKETraj with space charge effect excluded, and then confirmed with WAKE-EP with space charge effect included. Near the laser focal plane (4.5 cm), the electron bunch has a minimum volume thus the space charge effect is most significant. The value of the longitudinal field at 1 cm after the laser focal plane is shown in Figure 4.24a, the difference in the longitudinal field values with and without beam loading is shown in Figure 4.24b. The electric field excited with the plasma is  $\sim 5000$  times that excited by the electron bunch, thus the space charge can be ignored in our case.

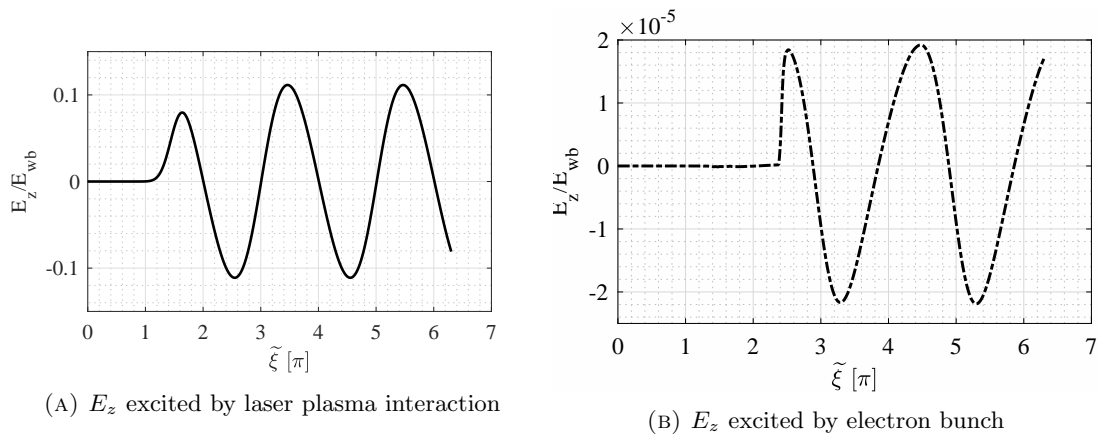


FIGURE 4.24: Longitudinal on axis electric field  $E_z$  in units of  $E_{w.b} = m_e c \omega_p / e$ , at 0.5 cm after the laser focal plane. The electric field excited with laser plasma interaction is reported in (A), while the difference in  $E_z$  with and without beam loading is reported in (B).



In the previous study, the injection phase is scanned, however, only the electron bunch being injected in the first period of the plasma wave are studied, the optimal injection condition is  $\tilde{s}_f = 4.5$ ,  $\tilde{\xi} = 0$ . Actually we can get a mostly similar compression with the electron bunch being injected in the subsequent period, i.e. with  $\tilde{s}_f = 4.5$ ,  $\tilde{\xi} = 2\pi$ , the phase space of the electrons is shown in Figure 4.25, the distribution of the main bunch is almost similar with that in the previous simulations, the major difference is that a few electrons (less than 1.5%) are captured before the main bunch and form a pre-pulse, from this point, it is prevalent to inject the electron bunch in the first period.

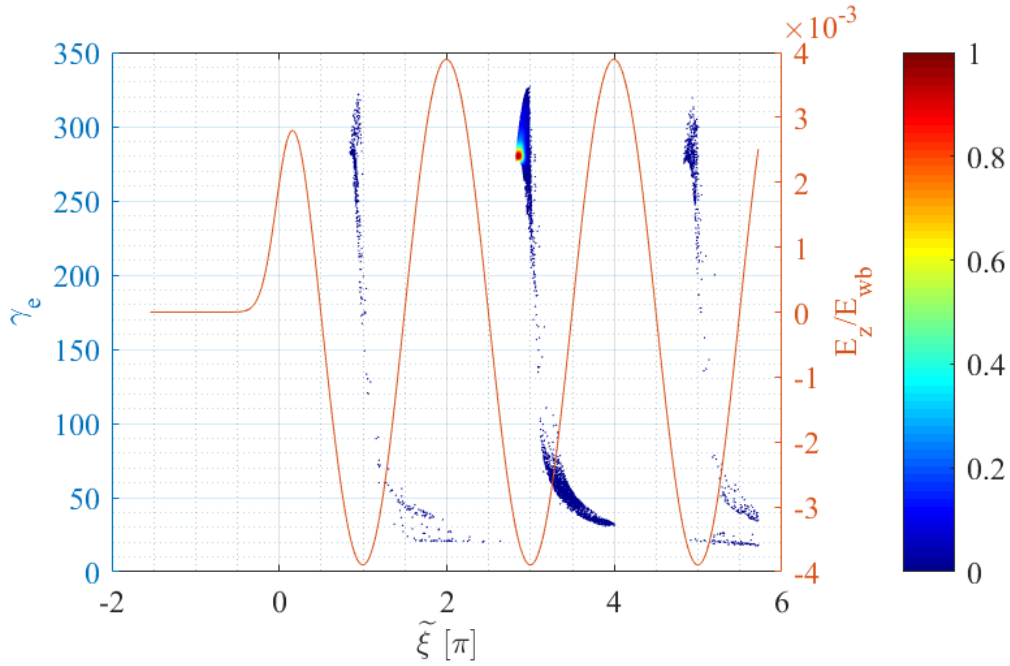


FIGURE 4.25: The longitudinal phase space of the electron bunch at plasma exit, with the configuration  $\tilde{s}_f = 4.5$ , and the injection phase  $\tilde{\xi} = 2.2\pi$ .

#### 4.4.2 Evolution of the transverse parameters of the electron bunch

In previous chapter, we discuss mainly the longitudinal parameters. In this section, the evolution of the transverse parameters in the plasma are checked. To calculate the transverse parameters, the 94% high energy electrons in the main bunch are used. The transverse size and the emittance of the main bunch during the propagation is shown in Figure 4.26, the bunch size evolves smoothly and is almost symmetric to the laser focal plane. The oscillation of the emittance is only significant before 6 cm, at the plasma exit, the emittance in x and y plane are smaller than  $1\ \mu\text{m}$ . Note that, only the captured 7.35 pC higher energy electrons are counted in the analysis, thus the the bunch size at the entrance is smaller than the 10 pC injected bunch  $\sigma_x = 26.2\ \mu\text{m}$ ,  $\sigma_y = 25.3\ \mu\text{m}$  as shown in Figure 3.28.

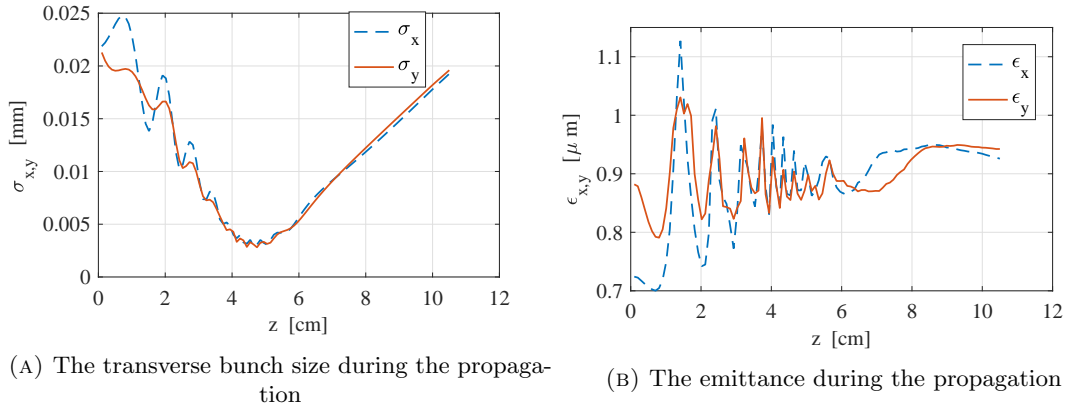


FIGURE 4.26: Evolution of the transverse size and emittance of the 95% high energy electrons, the beam size at plasma entrance are  $\sigma_x = 26.2 \mu\text{m}$ ,  $\sigma_y = 25.3 \mu\text{m}$

Actually, different beam sizes have been tried to minimize the emittance growth, we noticed that, with a larger or smaller beam size, significant oscillation of the beam size before the laser focal plane can be observed, the emittance at the plasma exit is larger than the case shown in Figure 4.26. i.e by slightly increasing the solenoid strength, the beam size at the focal plane is  $\sigma_x = 13.8 \mu\text{m}$ ,  $\sigma_y = 15.4 \mu\text{m}$ , the transverse size and the emittance of the main bunch during the propagation is shown in Figure 4.27, the oscillation of the bunch size and the emittance go worse, a larger emittance is obtained at the plasma exit, i.e  $\epsilon_{nx} \approx 1.4 \mu\text{m}$ .

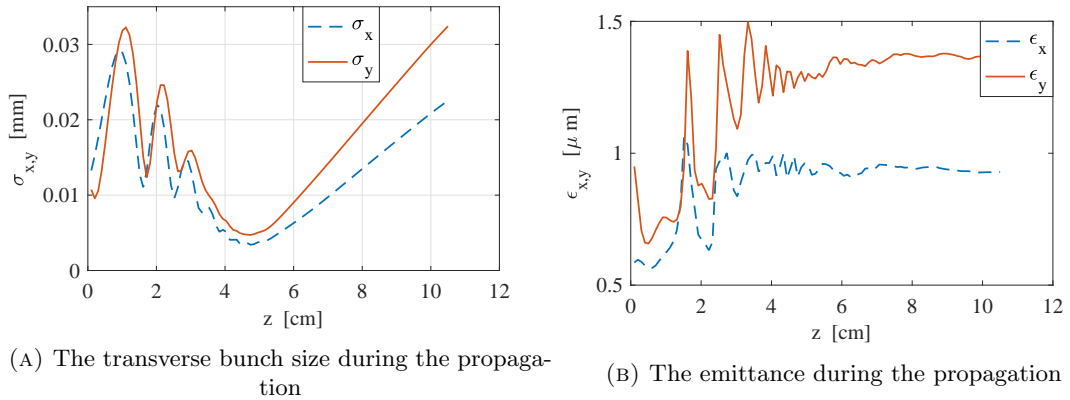


FIGURE 4.27: Evolution of the transverse size and emittance of the 95% high energy electrons, the beam size at plasma entrance are  $\sigma_x = 13.8 \mu\text{m}$ ,  $\sigma_y = 15.4 \mu\text{m}$

The evolution of the angular divergence is shown in Figure 4.28, it decreases from 2.5 mrad at the laser focal plane to 0.17 mrad at the plasma exit, this may relax the requirement on the magnets of the subsequent extraction line.

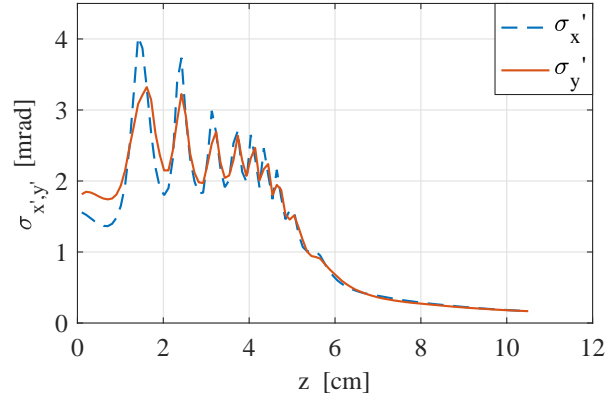


FIGURE 4.28: The evolution of the transverse angular dispersion in the plasma cell

#### 4.4.3 Optimization of the injection configuration for different plasma densities

With the previous analysis, the region before the plasma focal plane is mainly aimed to manipulate the longitudinal phase space of the electron bunch, and the region after the plasma focal plane is mainly for the extraction of the electron bunch. With the same plasma cell, the longitudinal optimal injection configuration with plasma density of  $1.5, 2.5 \times 10^{17} \text{ /cm}^{-3}$  are also studied, the energy distribution of the electron bunch at the plasma exit with different injection condition ( $\tilde{s}_f$  and  $\tilde{\xi}$ ) for plasma density of  $1.5, 2.5 \times 10^{17} \text{ /cm}^{-3}$  are respectively shown in Figure 4.29 and Figure 4.30. The optimal injection condition and the corresponding bunch charge and energy spread at the plasma exit is summarized in Table 4.1.

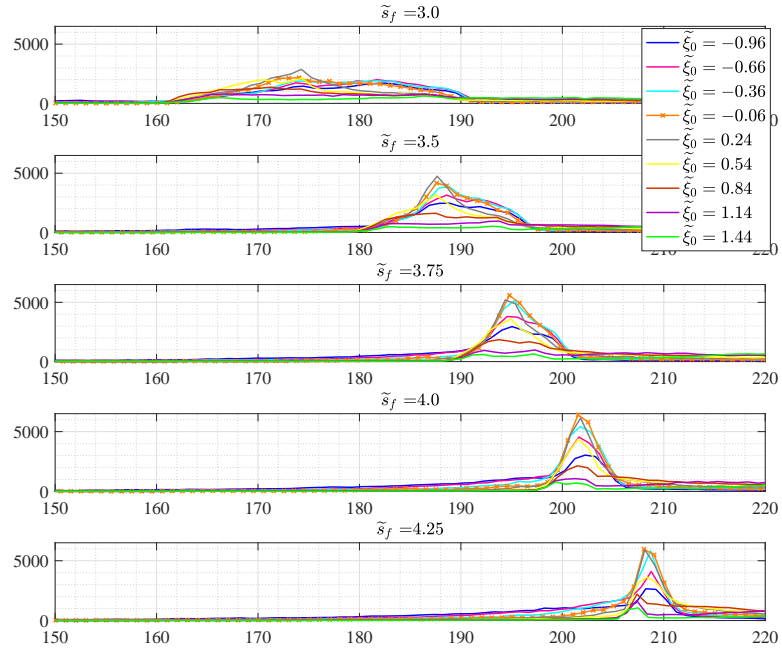


FIGURE 4.29: The energy distribution of the electrons at the exit of the plasma cell, with different starting position and injection phase, bin size is 1, the plasma density is  $1.5 \times 10^{17}/\text{cm}^3$ .

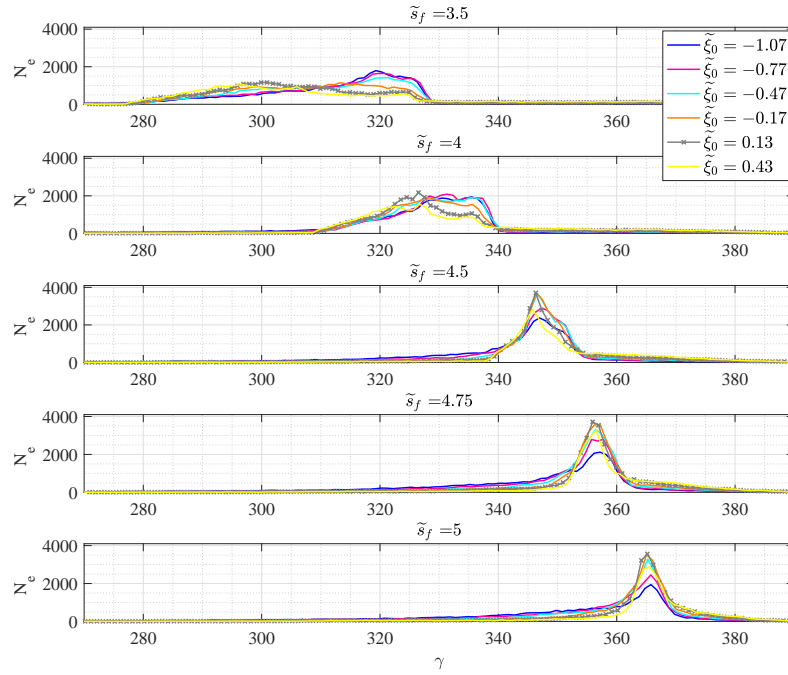


FIGURE 4.30: The energy distribution of the electrons at the exit of the plasma cell, with different starting position and injection phase, bin size is 1, the plasma density is  $2.5 \times 10^{17}/\text{cm}^3$ .

TABLE 4.1: The optimal injection configuration and the corresponding bunch characteristics at various plasma densities.

$\rho$ [ $10^{17}/\text{cm}^3$ ]	$\tilde{s}_f$	$\tilde{\xi}_0$	$\langle \gamma \rangle$	Q [pC]	$\sigma_\delta$	$\sigma_{\delta.FWHM}$
1.5	4	-0.06	201.86	7.99	4.65%	1.19%
2.0	4.5	0.00	282.67	7.89	4.48%	1.17%
2.5	4.75	0.13	355.17	6.88	4.18%	1.17%

With higher plasma density, the optimal injection plane is farther away from the laser focal plane, this may due to the fact that the electric field is stronger in higher density plasma, while the velocity bunching is more efficient with lower electric field and long interaction distance, thus the optimal injection plane moves farther from the laser focal plane to decrease the electric field.

The initial bunch charge is 10 pC, we can observe in this table the general trend of an increase in energy with a plasma density, compensated by a reduction of the trapped electron percentage. Because the electric field increases with plasma density while the plasma wavelength decreases with plasma density, however there are still more than 68% of electrons that can be captured.

## 4.5 Summary

In this chapter, the capture and the acceleration of the electron bunch in the plasma wakefield have been studied. A plasma cell is used as the plasma media, the density map is calculated with a laminar flow model by FEM, the laser-plasma-electron interaction is simulated with the PIC code WAKE-EP.

In the plasma, by starting the interaction plane several Rayleigh length before the laser focal plane, and injecting the low energy electron bunch near the zero crossing phase, the electron bunch can be efficiently compressed to  $\sim 3$  fs at the laser focal plane, optimal injection configuration for different plasma densities have been found. By terminating the interaction several Rayleigh length after the laser focal plane, the angular divergence is efficiently reduced, i.e  $0.17 \text{ mrad}@n_e = 2 \times 10^{17}/\text{cm}^3$ . The energy spectrum of the electron bunch has long tails, with a plasma density of  $n_e = 2 \times 10^{17}/\text{cm}^3$ , at the plasma exit the RMS energy spread of 95% high energy electrons is  $\sim 4.5\%$ , while the FWHM energy spread is  $\sim 1.2\%$ .

## Chapter 5

# Extending the acceleration length with the laser being guided by a hollow dielectric capillary

In the previous study, the energy of the electron bunch is mainly limited by the diffraction of the laser, the efficient acceleration range is only within one Rayleigh length before and after the laser focal plane, it has also been discussed under Figure 4.22 that the energy spread may decrease with a longer range acceleration. Thus, in this chapter, a dielectric capillary is introduced from the laser focal plane to guide the laser.

It will be shown that with Gaussian radial profile of the laser, even in the matching condition [97] (capillary radius being 1.55 times of the laser waist), the diffraction of the laser edge at the capillary entrance may lead to a fast fluctuation of the laser intensity, and further modulate the laser radial profile, as a result, the near axis electric field exerts a defocusing force on the electrons in the focusing phase, most electrons are lost during the propagation.

The using of a Flattened Gaussian beam (FGB) is then proposed to reduce the diffraction at the capillary entrance, the FGB here refers to the beam that has a Flattened Gaussian radial profile, it is actually the superposition of a series of Laguerre Gaussian beams with the same waist size. By focusing the Flattened Gaussian beam, the radial intensity falls fast to zero at the focal plane, thus the diffraction at the capillary entrance can be eliminated. The FGB and its focusing will be shortly reviewed, the propagation of a focused Flattened Gaussian beam in the capillary tube is studied.

The acceleration of the electron bunch with drive laser beams of different radial profiles (Flattened Gaussian and Gaussian) are studied. For a general study, the simulation

starts from the capillary entrance, with a matched electron bunch being injected into the plasma, then based on the simulation results, an upgrade configuration for the ESCULAP is studied.

## 5.1 Capillary guiding of a laser beam with a Gaussian radial profile

It has been studied in [97] that, to guide a laser beam from the focal plane, that has a Gaussian distributed intensity profile in the radial direction, the radius of the capillary should be 1.55 times the laser waist ( $R_{cap} \approx 1.55w_0$ ), thus the maximum laser energy (98%) is coupled to the fundamental  $EH_{11}$  mode which has interesting properties for the laser wakefield excitation, 1% of the energy is coupled to higher order modes and the remaining 1% is outside the capillary tube.

With the configuration found in the previous chapter,  $n_e = 2 \times 10^{17} \text{cm}^{-3}$ ,  $\tilde{s}_f = 4.5$ ,  $\tilde{\xi}_0 = 0$ , a capillary tube with radius  $R_{cap} = 1.55w_0 = 78.4 \mu\text{m}$  is put at the laser focal plane ( $s = 0$ ), the on axis laser intensity and the accelerated macro particles along the propagation length is shown in Figure 5.1.

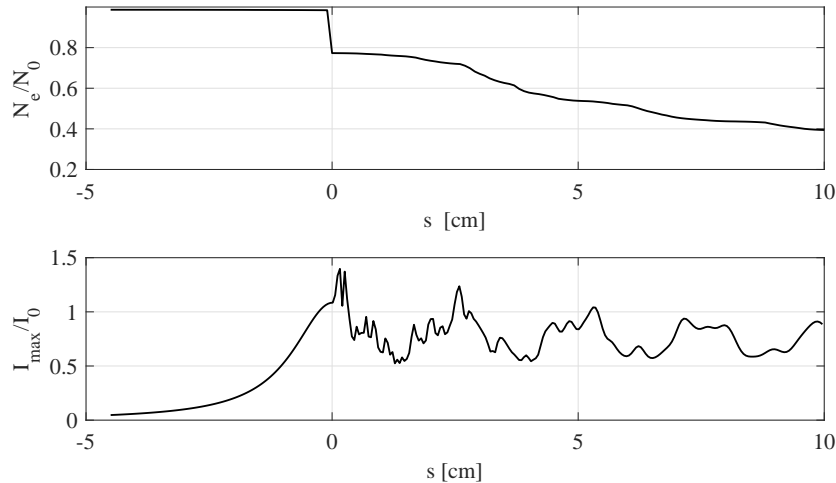


FIGURE 5.1: The number of trapped electrons and the maximum laser intensity during the propagation with laser focal plane and capillary entrance at  $s=0$ .

The low frequency oscillations of the laser intensity with a period of  $\sim 2.4$  cm is due to the dephasing between hybrid modes this will be discussed later, while the fast fluctuation of the maximum intensity which is introduced at the capillary entrance, then gradually damped during the propagation, is due to the diffraction of the laser edges at the capillary entrance. Referring to the electrons, almost 20% of the electrons are lost at the capillary

entrance, and another 40% lost during the propagation in the capillary. The electrons lost at the capillary entrance have a radial size larger than the capillary radius and have lower energy, thus they are essentially not captured by the plasma wave, the capillary works as a collimator, while the loss of electrons in the capillary is mainly due to the fast fluctuation of the laser intensity, this will be discussed in the following text.

Between  $s = 0$  and  $s = 2\text{cm}$  where the fast fluctuation is more significant, the radial laser profiles are shown in Figure 5.2, the radial laser profiles are modulated by the diffraction, and at some positions, the maximum laser intensity is no longer situated at axis, thus the plasma wave exerts a defocusing force on the par-axial electrons at focusing phase. For the sake of clarity, the radial electric field at  $s=0$  and  $s=0.2\text{ cm}$  are shown in Figure 5.3 for comparison.

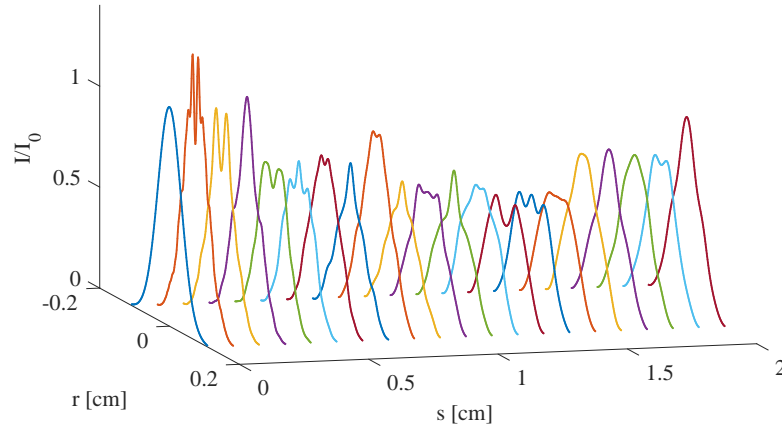
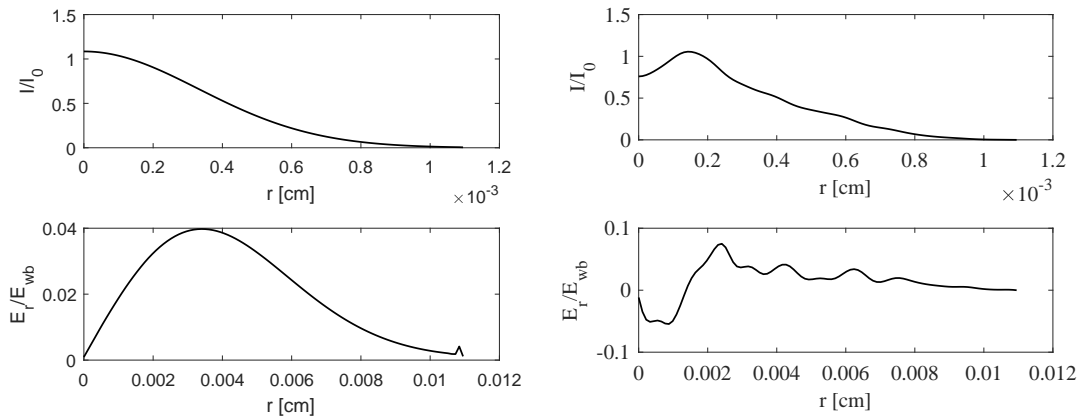


FIGURE 5.2: The radial laser profile during the first 2 cm of propagation in the capillary

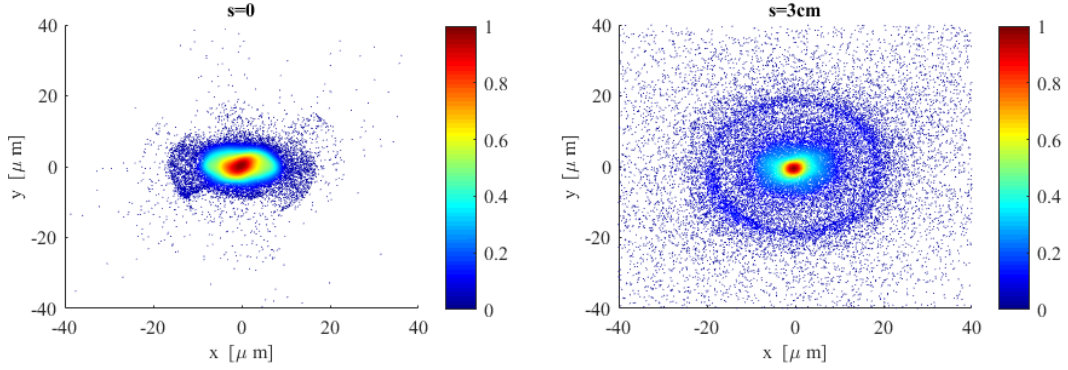


(A) The radial laser profile and the excited trans- (B) The radial laser profile and the excited trans-  
verse electric field at  $s=0$  verse electric field at  $s=0.2\text{cm}$

FIGURE 5.3: The radial laser profile and the excited transverse electric field at different positions



At  $s=0$ , as shown in Figure 5.3a the radial laser intensity profile is in Gaussian distribution, the transverse electric field is positive along the radial direction, that exerts a focusing force on the external electrons, while at  $s=0.2$  cm, the radial laser profile is modulated, the near axis transverse electric field is no longer linearly related to the radial size, the emittance is not conserved during the propagation, worse still, the transverse electric field changes sign at  $r = 13.5 \mu\text{m}$ , the electrons at  $r < 13.5 \mu\text{m}$  will be kicked from the axis, while electrons with larger radial size are focused towards the axis, thus the electron bunch is divided according to the phase and amplitude of the betatron oscillation (radial decoherence). As the decoherence of the electron bunch in radial direction, the emittance increases during the propagation and at some places an electron ring can be observed. As shows in Figure 5.4 the distribution of the electrons in the  $x - y$  plane at the capillary entrance and 3 cm after the capillary entrance, an electron ring is clearly identified at  $s=3$  cm.



(A) The electron distribution in  $x$ - $y$  plane at  $s=0$  (B) The electron distribution in  $x$ - $y$  plane at  $s=3$  cm

FIGURE 5.4: The transverse distribution of the electrons at different positions.

The longitudinal electric field is proportional to the laser intensity which varies also in the radial direction, but normally the energy of the electrons are independent of the radial size due to the betatron oscillation, even though the slice energy spread may increase during the propagation [127]. However, if the electrons are divided into several sub bunches, and the amplitude of the betatron oscillation varies between the sub bunches as shown in Figure 5.4b, then the longitudinal phase space of the electrons may also be split into several parts during the propagation, the longitudinal phase space at  $s=0$ ,  $s=1.3$  cm,  $s=3$  cm and  $s=9.5$  cm are shown in Figure 5.5.

It is notable that the low frequency oscillation of the laser intensity also has contribution to the loss of electrons, the acceleration field crest tilted backward due to the nonlinearity at high laser intensity as shown in Figure 4.2, the acceleration field crest is the zero crossing point of the transverse field, it separates the focusing and defocusing force, thus the boundary of the focusing force also moves with the laser intensity. It tilts toward larger phase (away from electron bunch) at higher laser intensity and returns at lower

laser intensity (close to the electron bunch). Thus when the laser intensity decreases, the transverse field exerted on the electrons decreases not only due the laser amplitude but also due to the shift of the zero crossing point, some electrons may even situated at the defocusing phase when the laser intensity decreased to the local minimum value. As the electron bunch moves faster than the plasma wave in the capillary, thus the electron bunch is closest to the acceleration field crest when the laser intensity decreased to it's first minimum value, that is  $s=1.3\text{cm}$  according to Figure 5.1, the longitudinal phase space of the electron bunch and the electric field of the plasma wave at  $s=1.3\text{cm}$  are shown in Figure 5.5b, only few electrons are in the defocusing phase, most electrons, especially the bunch core is still in the focusing phase.

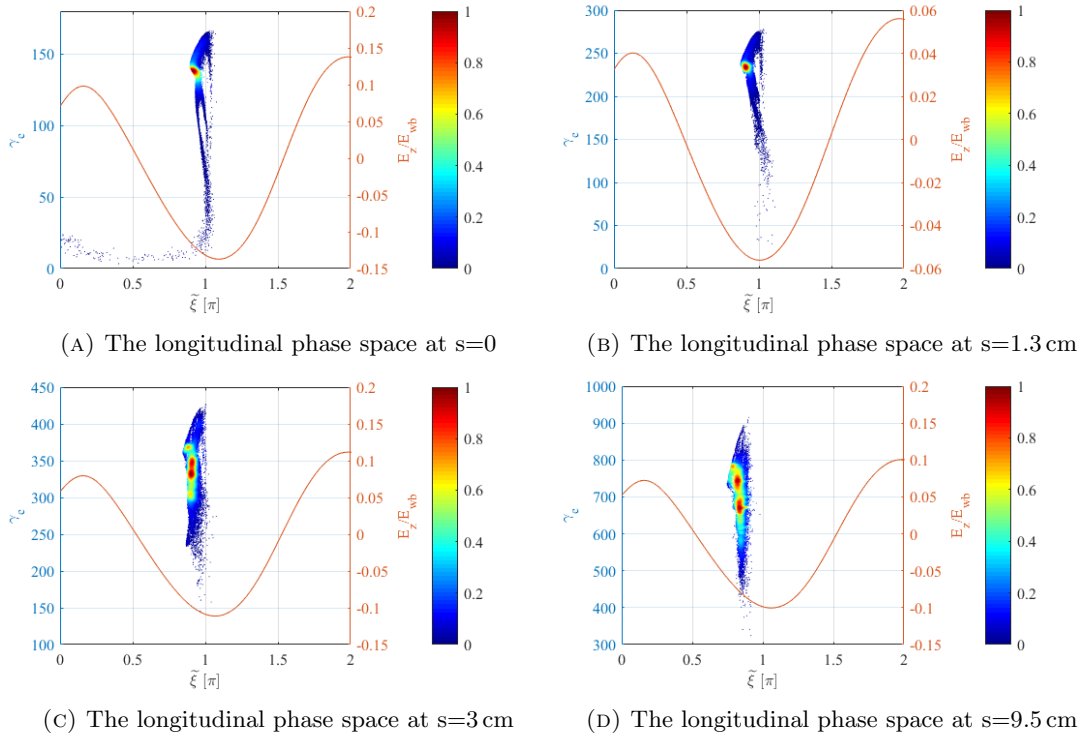


FIGURE 5.5: The longitudinal phase space of the electron bunch and the longitudinal electric field of the plasma wave at different positions.

Comparing Figure 4.18c with Figure 5.5a, the longitudinal phase space of the electron bunch at the laser focal plane without and with capillary tube, the electrons at the defocusing phase are collimated by the capillary entrance. Then, as shown in figure 5.5c and 5.5d the energy distribution is stretched and split during the propagation in the capillary.

However, one may note that in Figure 5.1 the laser intensity is slightly larger than the nominal laser intensity at the capillary entrance, this is due to the self-focusing of the laser in the plasma, thus the radial laser size is smaller than the nominal size at the capillary entrance, the matching capillary size is changed. To eliminate this effect,

a laser beam with Gaussian radial profile starting at it's focal plane with a radius of  $w_0 = 50.46 \mu\text{m}$  propagating in a capillary tube with a radius of  $R_{cap} = 1.55w_0 = 78.21 \mu\text{m}$  is studied, with vacuum in the capillary the laser intensity during the propagation is shown in Figure 5.6

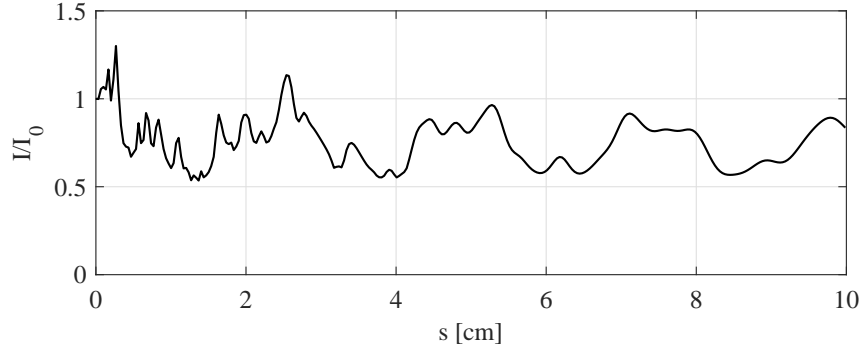


FIGURE 5.6: The maximum laser intensity during the propagation in the capillary with matching condition,  $w_0 = 50.46 \mu\text{m}$ ,  $R_{cap} = 1.55w_0 = 78.21 \mu\text{m}$ , with vacuum in the capillary.

The fast fluctuation is still obvious in the first 3 cm and then damped during the propagation, the self-focusing has less effect on the laser propagation in the capillary tube, the radial profiles in the first 2 cm are shown in Figure 5.7, the modulation of the radial profile still occurs during the propagation.

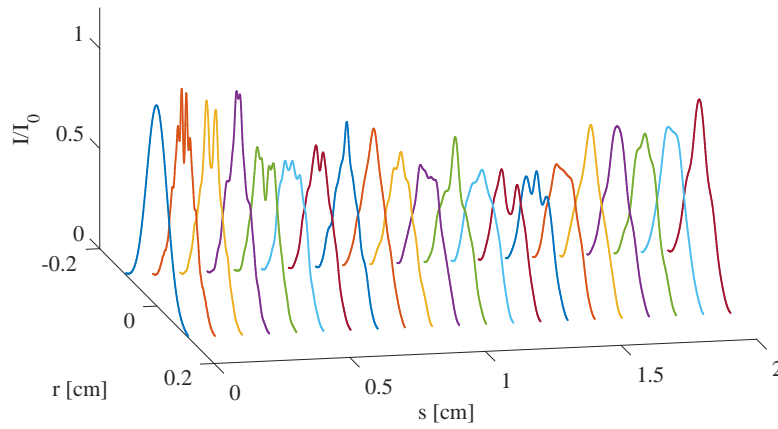


FIGURE 5.7: The radial laser profile during the first 2 cm propagation in the capillary which is filled with vacuum

As discussed before, the loss of electrons may result from the joint effect of the fast fluctuations, lower frequency oscillations of the laser intensity, and also the non-linearity induced field crest tilt.

To evaluate their effects for general case, we do simulations starting from the capillary entrance (also is the laser focal plane), an electron bunch in transverse matching condition is used, firstly a laser beam with Gaussian radial profile is used, while the electron bunch is injected on different phases  $0.92\pi$  and  $0.87\pi$  for comparison,  $0.92\pi$  is the acceleration phase at the focal plane in the previous study,  $0.87\pi$  is to make sure all the electrons are in the transverse focusing phase even with the existing of nonlinearities. Then a laser beam with Airy-like profile (available in WAKE-EP) [128] is used, with the electron being injected at  $0.92\pi$ , the Airy-like beam takes the form that  $E(r) = AJ_1(u_1 r/R_{cap})/r$ ,  $R_{cap}$  is the radius of the capillary, it is set also to 1.55 times of the Gaussian beam waist, the radial profiles for the Gaussian and Airy-like beam are shown in Figure 5.8, since the field falls to zero at the capillary wall with the Airy beam, thus there is no diffraction at the capillary entrance.

The properties of the electron bunch and the laser beam are set according to the parameters at the laser focal plane in the previous study. The laser amplitude is  $a_0 = 0.699$ , the Lorentz factor of the initial electron beam is  $\gamma_e = 150$  with an energy spread of 1%, the bunch size and duration is set according to according to Figure 4.22a and 4.27a, the RMS transverse bunch size is set to  $5\text{ }\mu\text{m}$ , RMS bunch duration is set to 3 fs, the Twiss parameter is calculated according to the matching condition in equation 3.21.

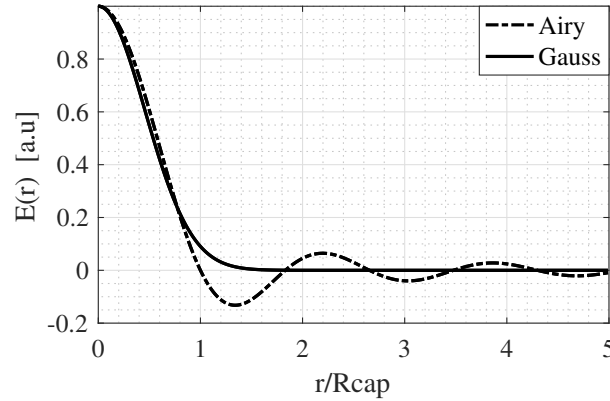


FIGURE 5.8: The radial profile of the Airy beam and the Gaussian beam.

The maximum intensity of the laser during the propagation in the capillary for the Gaussian beam and the Airy beam are shown in Figure 5.10 for comparison, the radial profiles of the Airy laser during the first 2 cm's propagation are reported in Figure 5.9 for comparison with the Gaussian case in Figure 5.7.

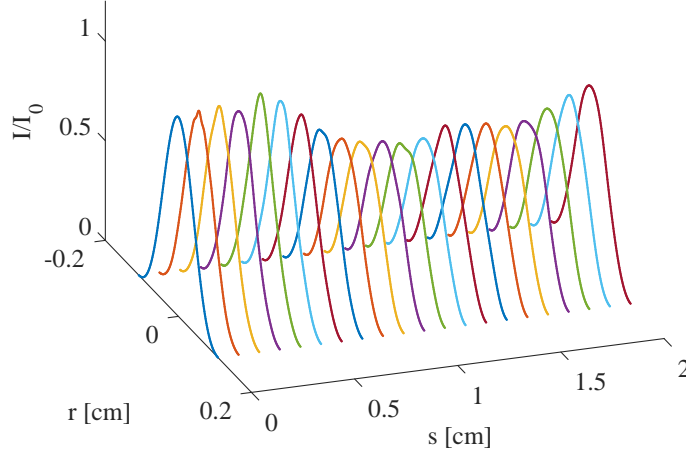


FIGURE 5.9: The radial profile of the Airy-like beam during the propagation

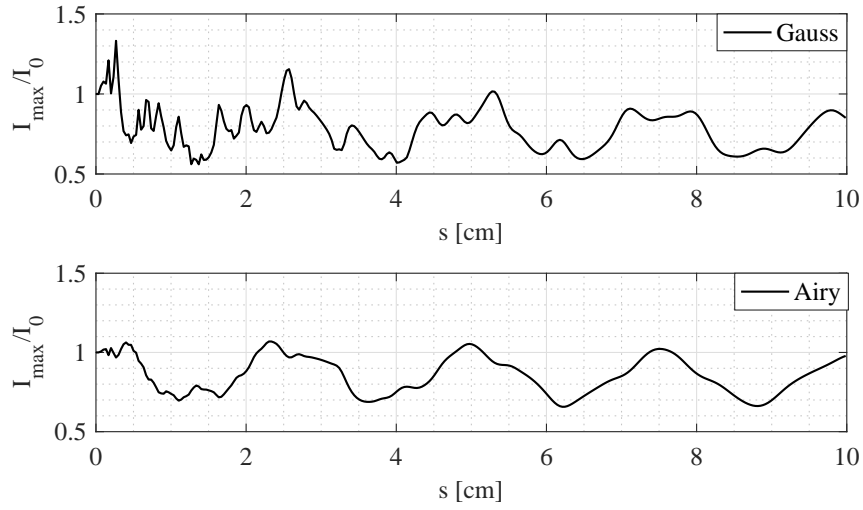


FIGURE 5.10: The evolution of the maximum laser intensity during the propagation, the initial radial profile of the laser are respectively in Gaussian and Airy-like distribution.

The fast fluctuation of the laser intensity is eliminated with the Airy beam, the modulation of the radial profile is efficiently suppressed. Then the trapped electrons during the propagation for Gaussian beam with injection phase of  $0.87\pi$ ,  $0.92\pi$ , and for Airy beam with injection phase of  $0.92\pi$  are shown in Figure 5.11, with the Airy profile, almost no electrons are lost during the propagation, while with the Gaussian profile more than 50% of the electrons are lost. For the Gaussian profile, more electrons are lost for the case injected at  $0.87\pi$ , this indicates that the tilt of the acceleration peak has less effect on the electron loss.

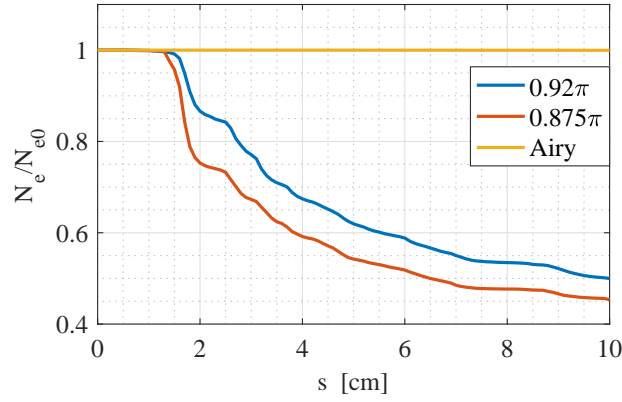


FIGURE 5.11: The number of electrons normalized with the initial number of electrons during the propagation

With the electron bunch being injected at  $0.92\pi$  of the plasma wave, the longitudinal electron phase space at the capillary entrance and at 1.3 cm, 9.5 cm after the entrance, driving by a laser beam with Gaussian radial profile are shown in Figure 5.12a, 5.12c and 5.12e, for comparison, the phase space at same position but driving by a laser beam with Airy radial profile are shown in Figure 5.12b, 5.12d and 5.12f. With the Airy intensity profile laser, an energy chirp is introduced to the longitudinal phase space of the electron bunch by the field gradient, while with the Gaussian intensity profile drive laser, the chirp is only identified in the core at  $s=1.3\text{cm}$ , and then the phase space is stretched by the laser intensity fluctuation.

It's notable that the laser amplitude is the same for Gaussian and Airy laser beam (compare the electric field at Figure 5.12a and 5.12b), while the energy difference of the electron bunch is due to the difference of the laser intensity oscillation amplitude as shown in Figure 5.10.

In conclusion, with a Gaussian driven beam, a fast fluctuation of the laser intensity is introduced by the diffraction at the capillary entrance even in the best matching condition, the self focusing has less effect on the laser propagation. The fast fluctuation of laser intensity may modulate the radial laser profile so that that a transverse defocusing force is excited near the axis and a focusing force is excited far away from the axis in the focusing phase region, as a result, the electron bunch is separated into several sub-bunches according to the betatron frequency and amplitude, the electrons with large betatron amplitude get less energy from the wakefield, thus the energy distribution is stretched. With the fast fluctuation and low frequency oscillation of the laser amplitude, most electrons may be lost during the propagation, while with an Airy-like laser, the laser intensity falls to zero at the inner capillary wall at the capillary entrance, the diffraction induced fast fluctuation can be eliminated, then almost no electrons are lost

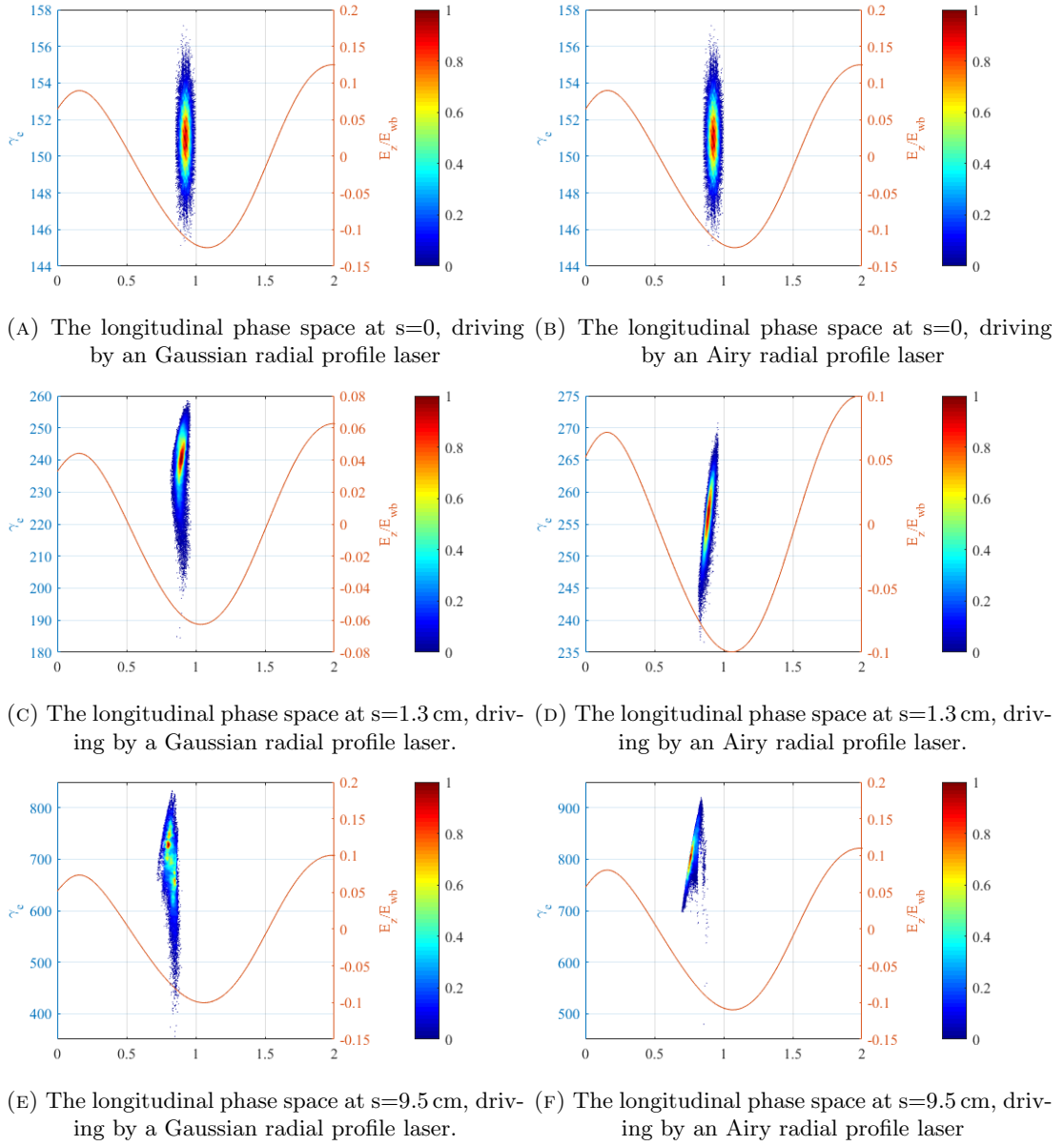


FIGURE 5.12: The longitudinal phase space of the electron bunch and the longitudinal electric field of the plasma wave at different position, the injection phase is  $0.92\pi$  for all case.

during the propagation. In the next section, the generation of the laser profile with field amplitude falling to zero at the capillary entrance will be mainly studied.

## 5.2 Capillary guiding of a laser beam with flattened Gaussian radial profile

The radial laser profile may be modulated by the diffraction of the laser edge at the capillary entrance, to eliminate this diffraction the laser intensity should fall to zero at the capillary entrance. According to the results shown in [61], this can be realized by focusing a Flattened Gaussian beam [129], for the sake of clarity, the flattened Gaussian beam and its focusing will be shortly reviewed and then its propagation in a capillary tube will be studied.

### 5.2.1 Properties and the focusing of Flattened Gaussian beams

The Flattened Gaussian beam (FGB) is defined in [129], the electric field takes the form that

$$E_N(r) = A \exp(-(N+1)r^2/w_0^2) \sum_{m=0}^N \frac{1}{m!} \left( \frac{(N+1)r^2}{w_0^2} \right)^m \quad (N = 0, 1, 2, \dots) \quad (5.1)$$

With the relation that [130]

$$x^{2m} = \frac{m!}{2^m} \sum_{n=0}^m (-1)^n \binom{m}{n} L_n(2x^2) \quad (m = 0, 1, 2, \dots) \quad (5.2)$$

Where  $L_n$  is the  $n$ th Laguerre polynomial, and  $\binom{B}{A}$  is the binomial coefficient, they follow that

$$\binom{m}{n} = \frac{m!}{n!(m-n)!}$$

$$L_n(x) = \sum_{k=0}^n \binom{n}{k} \frac{(-1)^k}{k!} x^k$$

With equation 5.2 formula 5.1 can be rewritten as

$$E_N(r) = A \sum_{n=0}^N c_n^N L_n \left( \frac{2(N+1)r^2}{w_0^2} \right) \exp \left( -\frac{(N+1)r^2}{w_0^2} \right) \quad (5.3)$$

Where the coefficients  $c_n^{(N)}$  take the form that

$$c_n^{(N)} = (-1)^n \sum_{m=n}^N \frac{1}{2^m} \binom{m}{n} \quad (5.4)$$



According to formula 5.3, the  $N$ th order FGB is the superposition of the first  $N$  Laguerre Gauss beams (LGB) with weights of  $c_n^{(N)}$ . The waist of the LGB is

$$w_{LGf-N} = \frac{w_0}{\sqrt{N+1}} \quad (5.5)$$

The Profiles of FGB of different orders are shown in Figure 5.13

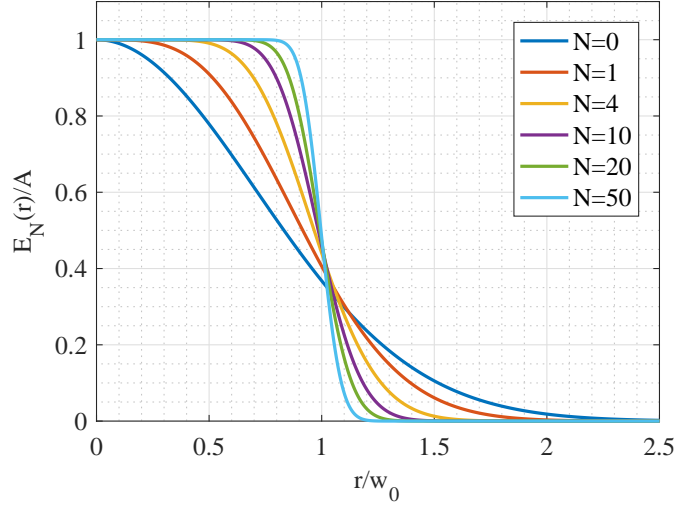


FIGURE 5.13: The profiles of FGB of orders 0, 1, 4, 10, 20, 50.

Then the focusing of the FGB is studied in [61], the field at focal plane takes the form that

$$E_N(r) = \frac{-iAk w_0^2}{2(N+1)f} \exp\left(i\left(kf + \frac{k}{2f}r^2\right)\right) \exp\left(\frac{k^2 w_0^2}{4(N+1)f^2}r^2\right) \sum_{n=0}^N c_n^N (-1)^n L_n \left(\frac{k^2 w_0^2}{2(N+1)f^2}r^2\right) \quad (5.6)$$

The waist of the Laguerre Gaussian beam at the focal plane is

$$w_{LG0-N} = \frac{2\sqrt{N+1}f}{kw_0} = \frac{2f}{kw_{LGf-N}} = \frac{f\lambda}{\pi w_{LGf-N}} \quad (5.7)$$

Where  $w_{LGf-N}$  indicates the waist of the Laguerre Gaussian beam before focusing. Note that, the Gaussian beam is a special case of the FGB with  $N = 0$ , in that case, the waist before focusing is  $w_{Gf} = w_0$ , the waist at the focal plane is  $w_{G0} = f\lambda/(\pi w_0)$ , thus the waist of the LGB before focusing and at the focal plane are respectively  $w_{LGf-N} = w_{Gf}/\sqrt{N+1}$ ,  $w_{LG0-N} = w_{G0}\sqrt{N+1}$ . The radial profiles of the focused FGB at the focal plane are shown in Figure 5.14

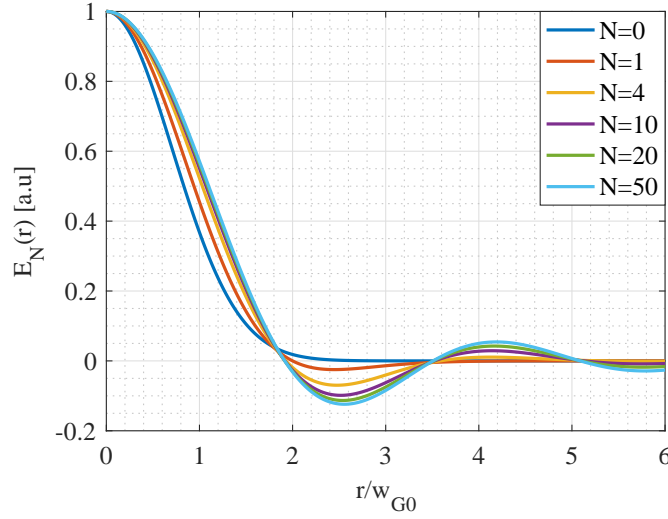


FIGURE 5.14: The radial profiles of the FGB of orders 0, 1, 4, 10, 20, 50 at the focal plane, with maximum field normalized to 1

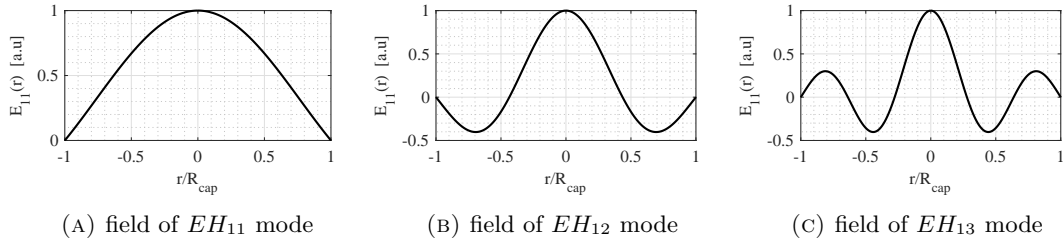
At the laser focal plane, the field falls fast to zero near  $r \approx 1.9w_{G0}$ , the capillary radius can be set to the first zero crossing radius of the field to eliminate the diffraction at the capillary entrance.

### 5.2.2 Propagation of a laser beam in the dielectric capillary

The propagation of the laser in the capillary tube can be studied by solving the wave equation with the dielectric capillary wall describing the continuity of the field, the eigen modes in the capillary can be obtained, and an incident linearly polarized laser beam can be efficiently coupled to the linearly polarized family of  $EH_{1m}$  modes ( $m=1,2,\dots$ ), this has been studied in[98]. For the sake of clarity, it is shortly discussed here, in the par-axial approximation ( $\lambda \ll R_{cap}$ ), the field for  $EH_{1m}$  modes takes the form [97]

$$E_{1m} = A_m J_0(k_{\perp m} r) \exp(-k_m^l z) \cos(\omega_L t - k_{zm} z) \quad (5.8)$$

For the mode of order  $m$ ,  $A_m$  is the amplitude,  $J_0$  is the first kind of Bessel function of order zero,  $k_{\perp m}$  and  $k_{zm}$  are respectively the transverse and longitudinal wave number,  $k = \sqrt{k_{\perp m}^2 + k_{zm}^2}$ ,  $k = \omega_L/c$  is the wave number in free space, recognize the  $m$ th root of  $J_0$  as  $u_m$ , then  $k_{\perp m} = u_m/R_{cap}$ . While  $k_m^l$  is the damping coefficient and it follows that  $k_m^l = u_m^2(1 + \epsilon_r)/(2k^2 R_{cap}^3 \sqrt{\epsilon_r - 1})$ ,  $\epsilon_r$  is the dielectric constant of the wall. The damping coefficient increases fast with  $m$ , thus the higher modes damp faster than the fundamental mode.


 FIGURE 5.15: The electric field of the first three  $EH_{1m}$  modes

The amplitude coefficient  $A_m$  can be calculated by making the scalar product, they are given by [97]

$$A_m = \frac{\int_0^1 x E_N(x) J_0(u_m x) dx}{\int_0^1 x J_0(u_m x) J_0(u_m x) dx} = \frac{2 \int_0^1 x E_N(x) J_0(u_m x) dx}{J_1^2(u_m)} \quad (5.9)$$

Where  $x = r/R_{cap}$ , refer to formula 5.6  $E_N$  is the field of the laser with the amplitude normalized to 1, the energy percentage of different modes can be calculated by

$$C_m = \frac{\int_0^1 (A_m J_0(x u_m))^2 x dx}{\int_0^1 x E_N^2(x) dx} = \frac{2 [\int_0^1 x E_N(x) J_0(u_m x) dx]^2}{J_1^2(u_m) \int_0^1 x E_N^2(x) dx} \quad (5.10)$$

Another important parameter is the energy percentage of the incident laser that can be coupled into the capillary, it can be derived as

$$\eta = \frac{\int_0^1 x E_N^2(x) dx}{\int_0^\infty x E_N^2(x) dx} \quad (5.11)$$

Consider a FGB, the field in focal plane has been described in formula 5.6, the first zero crossing radius  $r_0$  in unit of the corresponding Gaussian beam waist  $w_{G0}$  for different orders  $N$  are calculated. With the capillary radius equal to  $r_0$ , the percentage of energy coupled into the capillary  $\eta$  and the coupling coefficients  $C_m$  can be calculated by substituting formula 5.6 into formula 5.11 and 5.10, they are summarized in Table 5.1,  $N = 0$  refers to the Gaussian beam,  $r_0$  is set to 1.55 times of the waist.

TABLE 5.1: Coupling coefficients and first zero crossing radius of FGB of different orders

N	0	1	2	4	5	8	10	20	50
$r_0$	1.5500e0	2.0000e0	1.9503e0	1.9278e0	1.9241e0	1.9195e0	1.9183e0	1.9165e0	1.9160e0
$\eta$	9.9181e-1	9.9634e-1	9.8894e-1	9.7447e-1	9.6834e-1	9.5377e-1	9.4640e-1	9.2346e-1	8.9698e-1
$C_{11}$	9.8884e-1	9.4498e-1	9.6925e-1	9.8250e-1	9.8514e-1	9.8902e-1	9.9027e-1	9.9268e-1	9.9406e-1
$C_{12}$	5.2060e-3	5.4851e-2	3.0427e-2	1.7167e-2	1.4538e-2	1.0697e-2	9.4601e-3	7.0820e-3	5.7360e-3
$C_{13}$	1.4628e-3	1.2630e-4	2.7386e-4	2.8530e-4	2.7392e-4	2.4473e-4	2.3143e-4	1.9919e-4	1.7627e-4
$C_{14}$	9.1461e-4	2.8377e-5	3.6387e-5	3.5241e-5	3.3793e-5	3.0413e-5	2.8907e-5	2.5250e-5	2.2619e-5
$C_{15}$	6.2400e-4	6.6581e-6	8.1100e-6	7.7660e-6	7.4497e-6	6.7250e-6	6.4039e-6	5.6235e-6	5.0599e-6
$C_{16}$	4.4520e-4	2.0679e-6	2.4674e-6	2.3527e-6	2.2574e-6	2.0409e-6	1.9452e-6	1.7125e-6	1.5442e-6
$C_{17}$	3.3131e-4	7.7842e-7	9.1906e-7	8.7442e-7	8.3916e-7	7.5936e-7	7.2411e-7	6.3841e-7	5.7636e-7
$C_{18}$	2.5531e-4	3.3640e-7	3.9472e-7	3.7509e-7	3.6000e-7	3.2594e-7	3.1092e-7	2.7436e-7	2.4788e-7
$C_{19}$	2.0239e-4	1.6128e-7	1.8849e-7	1.7897e-7	1.7179e-7	1.5559e-7	1.4845e-7	1.3107e-7	1.1848e-7
$A_{11}$	8.7024e-1	7.3881e-1	8.0175e-1	8.4890e-1	8.6046e-1	8.7963e-1	8.8659e-1	9.0150e-1	9.1116e-1
$A_{12}$	9.6339e-2	2.7158e-1	2.1673e-1	1.7120e-1	1.5948e-1	1.3958e-1	1.3221e-1	1.1617e-1	1.0560e-1
$A_{13}$	6.4013e-2	-1.6335e-2	-2.5774e-2	-2.7665e-2	-2.7440e-2	-2.6463e-2	-2.5921e-2	-2.4422e-2	-2.3204e-2
$A_{14}$	-5.9107e-2	9.0417e-3	1.0971e-2	1.1354e-2	1.1255e-2	1.0894e-2	1.0698e-2	1.0154e-2	9.7067e-3
$A_{15}$	5.4947e-2	-4.9291e-3	-5.8291e-3	-5.9987e-3	-5.9473e-3	-5.7652e-3	-5.6668e-3	-5.3930e-3	-5.1669e-3
$A_{16}$	-5.1064e-2	3.0224e-3	3.5376e-3	3.6327e-3	3.6021e-3	3.4945e-3	3.4363e-3	3.2745e-3	3.1406e-3
$A_{17}$	4.7728e-2	-2.0091e-3	-2.3392e-3	-2.3995e-3	-2.3795e-3	-2.3094e-3	-2.2716e-3	-2.1661e-3	-2.0788e-3
$A_{18}$	-4.4894e-2	1.4152e-3	1.6426e-3	1.6840e-3	1.6700e-3	1.6212e-3	1.5949e-3	1.5216e-3	1.4608e-3
$A_{19}$	4.2472e-2	-1.0412e-3	-1.2061e-3	-1.2360e-3	-1.2258e-3	-1.1902e-3	-1.1710e-3	-1.1175e-3	-1.0731e-3

According to Table 5.1,  $\eta$  decrease with  $N$ , that means by setting the capillary radius to the first zero crossing radius of the FGB at the focal plane, less energy can enter the capillary with higher order FGB. For the Gaussian beam ( $N = 0$ ) there is a slow decrease of the amplitude with the mode number, so a large number of modes can contribute to the field in the capillary, while for a focused flattened Gaussian beam the decrease is much faster. The amplitude of the fundamental mode increases with  $N$  while the amplitude of the higher modes decreases with  $N$ , thus with higher order FGB, a more approximate mono mode beam can be obtained in the capillary with the sacrifice of the total energy.

Since the diffraction at the capillary entrance can be avoided with the FGB, in our case (low plasma density and laser amplitude), the radial profile of the laser in the capillary depends on the evolution of hybrid modes. To study the evolution of hybrids modes, their phase velocities and the damping are mainly concerned. In order to be consistent with previous studies, the laser wavelength is set to  $\lambda = 0.8 \mu\text{m}$ , the laser waist of the Gaussian beam before focusing and at the focal plane are respectively set to  $w_{Gf} = 2.5 \text{ cm}$  and  $w_{G0} = 50.46 \mu\text{m}$ , the dielectric constant of the glass capillary is  $\epsilon_r = 2.25$ .

According to the previous discussion, the longitudinal wave number of the  $EH_{1m}$  modes are

$$k_{zm} = \sqrt{k^2 - k_{\perp m}^2} = \sqrt{k^2 - u_m^2/R_{cap}^2} \approx k(1 - \frac{u_m^2}{2k^2 R_{cap}^2}) \quad (5.12)$$

The beating length  $L_{bm}$  is defined as the propagation length, over which the phase shift between the fundamental mode  $EH_{11}$  and the  $EH_{1m}$  mode is  $2\pi$ , that is

$$L_{bm} = 2\pi/(k_{z1} - k_{zm}) = \frac{4\pi k^2 R_{cap}^2}{(u_m^2 - u_{m-1}^2)} \quad (5.13)$$

Thus after a propagation length of  $\frac{n}{2}L_{bm}$ ,  $n = 1, 3, 5, \dots$  the field of the  $E_{1m}$  mode changed sign, the radial profile may be modulated by the phase slippage between the hybrid modes.

The damping length of the modes is defined with the reciprocal of the damping coefficient  $k_m^l$  in formula 5.8, that is  $L_{dpm} = 1/k_m^l$ , it refers to the propagation length, over which the field decreases to  $1/e$ ,

With  $N = 4$  as an example, the capillary radius is then  $R_{cap} = 1.9278w_{G0}$ , the beating length then yield  $L_{b2} = 3.78$  cm,  $L_{b3} = 1.35$  cm. The damping length yield  $L_{dp1} = 6.76$  m,  $L_{dp2} = 1.28$  m,  $L_{dp3} = 0.52$  m, thus the damping in several centimeters' propagation can almost be ignored. By substituting the coefficient in Table 5.1 into formula 5.8, with  $t = zk_{z1}/\omega_L$ , only consider the first two modes the radial profile of the laser field at  $z = 0$  and  $z = 0.5L_{b2}$  are calculated and shown in Figure 5.16

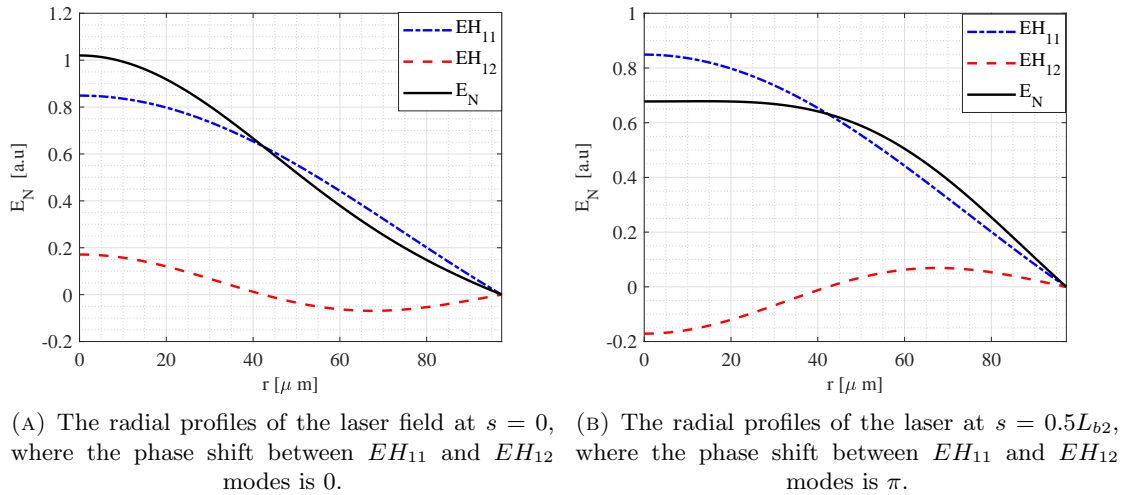


FIGURE 5.16: The radial profile of the laser field at  $s = 0$  and  $s = 0.5L_{b2}$ , started with a focused FGB with order of  $N=4$ .

One can find that at  $0.5L_{b2}$  the amplitude of the field decreases to 0.68 of the initial value, this only results from the dephasing between the first two hybrid modes. Refer to the radial profile, the maximum field is no longer located at the axis ( $r = 0$ ), there is a flat top near the axis. To study the contribution of higher modes, the evolution of the radial profile with the first 50 modes are checked, we find that near  $s = 1.7$  cm we get

the minimum on axis field, the field profile at  $s = 1.7$  cm calculated with first  $N$  orders are shown in Figure 5.17, with  $N = 2, 4, 8, 10, 20, 50$ .

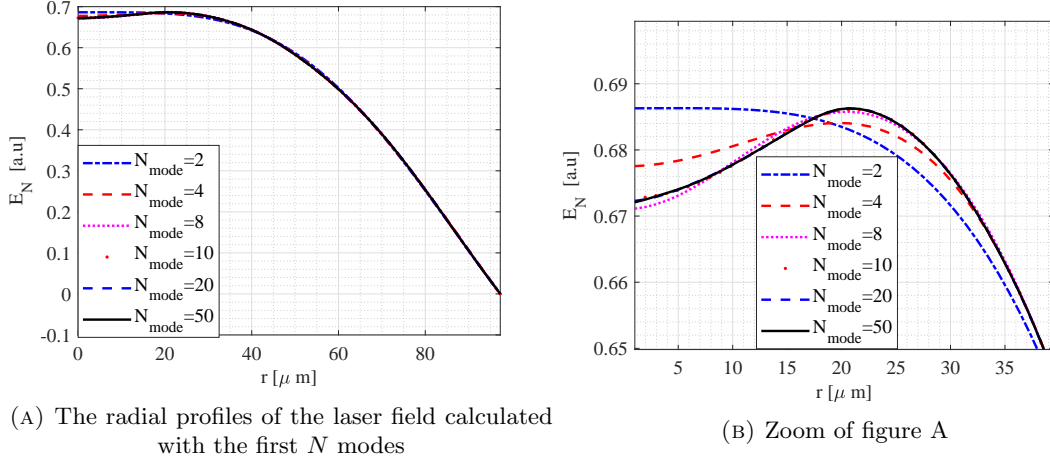


FIGURE 5.17: The radial profile of the laser field at  $s = 1.7$  cm, starting with a focused FGB with order of  $N=4$

According to Figure 5.17a, the field far away from the axis can be approximately calculated with the first 2 modes, while the higher order modes may contribute to the field near the axis since their energy are mainly distributed near the axis, according to Figure 5.17b, the near axis field can be estimated with the first 8 modes, the energy percentage and normalized amplitude of the  $EH_{18}$  mode are respectively  $3.75 \times 10^{-7}$  and  $1.68 \times 10^{-3}$ . Thus referring to the coupling coefficients in Table 5.1, even with a FGB up to 50th orders, the higher modes may contribute to the field profile, with  $N = 50$ , the radial profile of the laser field at 1.64 cm is shown in Figure 5.18, the field near axis is also modulated. Thus a real mono mode profile is required to completely eliminate this radial profile modulation, and according to the table 5.1, with a FGB the energy of the higher modes decreases faster than the GB, thus the dephasing induced modulation of the radial profile in a GB is more serious.

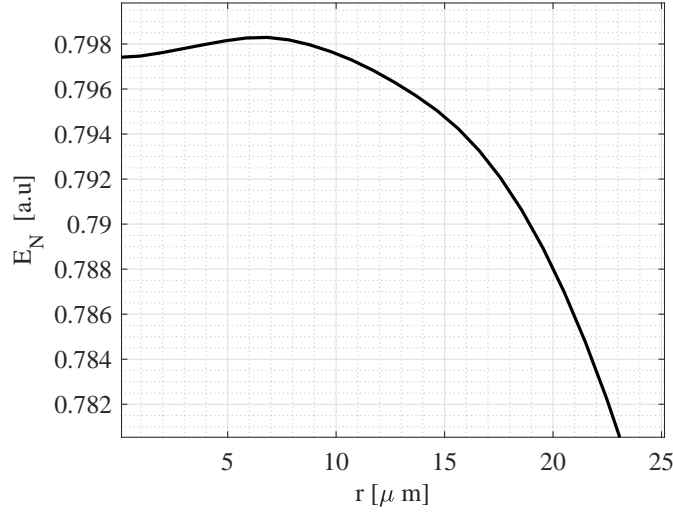


FIGURE 5.18: The near axis field of the laser at  $s = 1.64$  cm, starting with a focused FGB with order of  $N=50$

Comparing Figure 5.17 with Figure 5.18, the modulation of the radial profile exists in both cases, but with higher order FGB, the difference between the on axis field and the maximum field is much smaller, that means the defocusing force near the axis is smaller, since the field far from the axis is focusing, the electrons may not lost due to the defocusing field. However, due to the fast oscillation of the field profile, the emittance of the electron bunch may increase during the propagation, this may further lead to an increase of the bunch size, thus electrons may be lost during the propagation. As an example the evolution of the near axis radial profile in Figure 5.18, from  $s = 1.61$  cm to  $s = 1.68$  cm are shown in Figure 5.19. The acceleration of the electrons will be studied in the next section.

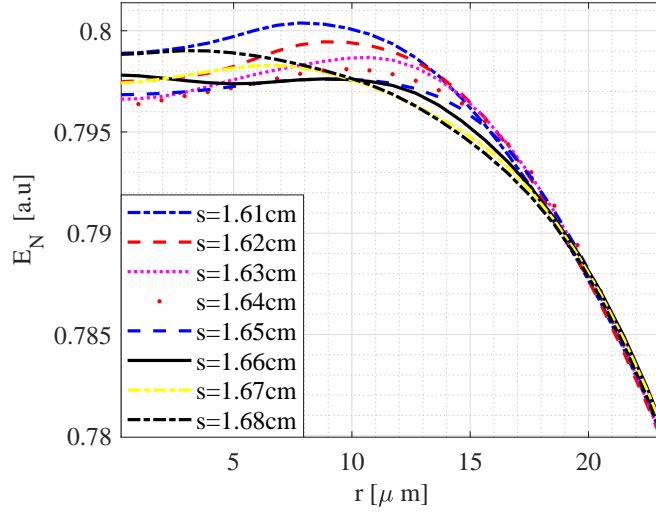


FIGURE 5.19: The evolution of the near axis field of the laser from  $s = 1.61$  cm to  $s = 1.68$  cm, starting with a focused FGB with order of  $N=50$

### 5.2.3 Simulation of the laser propagation and the acceleration of the electrons in the hollow dielectric capillary

The evolution of the laser intensity profile when propagating in a capillary without plasma has been analytically discussed in the previous section, it shows that the laser intensity profile is dependent on the propagation of the hybrid modes, the dephasing between hybrid modes may modulate the radial intensity profile. In this section, the laser propagation in the plasma and the acceleration of the electrons will be studied by simulation.

The simulation starts from the capillary entrance, where is also the focal plane of the laser beam, firstly the propagation of a FGB of order  $N = 4$ ,  $N = 20$  and  $N = 50$  without plasma in a capillary are studied to compare with the analytical results, the laser parameters are the same with that in the previous study, that is  $w_{G0} = 50.46 \mu\text{m}$ ,  $a_0 = 0.699$ , the capillary radius  $R_{cap}$  is set according to  $r_0$  in table 5.1, the evolution of the maximum laser amplitude during the propagation is shown in Figure 5.20.



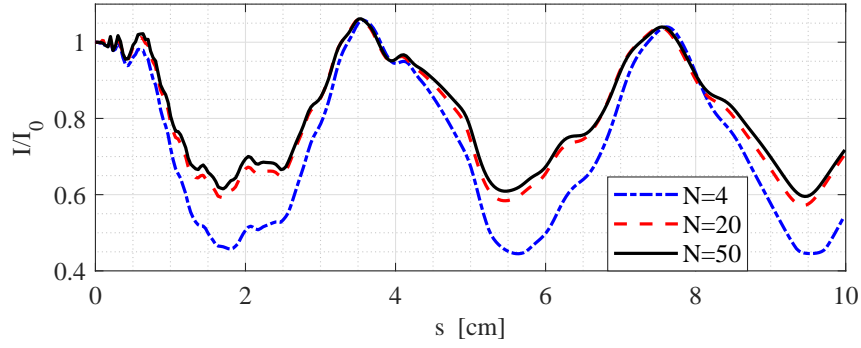


FIGURE 5.20: The evolution of the laser amplitude of the Flattened Gaussian beams of order  $N = 4$  and  $N = 50$  in the capillary without plasma.

According to the analysis in the previous section, the amplitude oscillation is due to the dephasing process between the hybrid modes, the beating length increases with the hybrid mode number while the energy decreases fast with the mode number, thus the low frequency oscillation of the amplitude is the result of the dephasing between  $EH_{11}$  and  $EH_{12}$  modes, the period should be the beating length of the  $EH_{12}$  mode  $L_{b2}$ , it is proportional to  $R_{cap}^2$  as shown in to formula 5.13. The capillary radius for FGB of higher order is slightly smaller than hat of lower order(i.e.  $1.916w_{G0}$  for  $N = 50$  while  $1.928w_{G0}$  for  $N = 4$ ), thus the oscillation period for the case  $N = 50$  (solid black line in figure 5.20) is slightly shorter than that of case  $N = 4$  (dashed blue line in figure 5.20). The minimum amplitude occurs near the half beating length of the  $EH_{12}$  mode, the amplitude of the oscillation decreases with the order of the FGB, because less energy is coupled to second modes and higher modes according to table 5.1, and also can be found by comparing figure 5.17 and Figure 5.18. However, for  $N = 20$  and  $N = 50$ , the oscillations of the laser amplitude is quite similar.

In the previous analysis, even with a FGB of order  $N = 50$ , the modulation of the radial profile occurs near 1.7 cm, this is verified by simulation results, the evolution of the radial profile in the first 2 cm is shown in Figure 5.21, the modulation is clearly identified at 1.7 cm.

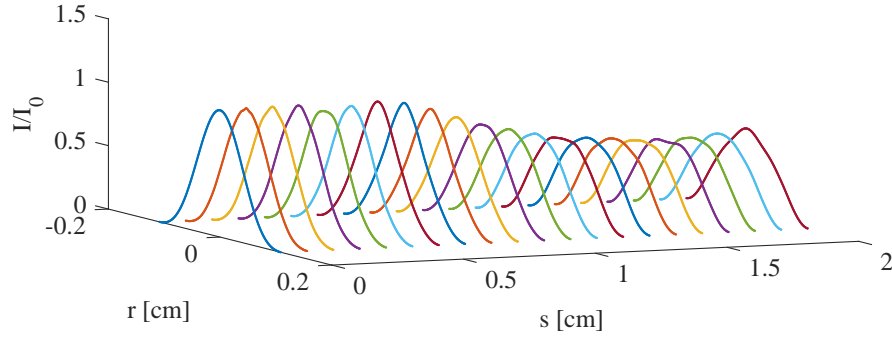


FIGURE 5.21: The evolution of the radial profile of the Flattened Gaussian beams of order  $N = 50$  in the capillary without plasma.

The simulation results are in agreement with the analytical results, comparing with the Gaussian beam, the diffraction induced fast oscillation of the laser amplitude is eliminated with the FGB, and with less energy being coupled to higher order modes which calls to the modulation of near axis field, thus the FGB is expected to have advantages on driving the wakefield in the dielectric capillary.

Then the effects of the plasma to the laser propagation is checked. With a FGB of order  $N = 4$ , the propagation in the capillary with plasma density of  $1, 2, 3, 5 \times 10^{17} \text{cm}^{-3}$  are studied, the maximum laser amplitude during the propagation is shown in Figure 5.22, the self-focusing effect is more prominent with the increase of plasma density, and below a density of  $3 \times 10^{17} \text{cm}^{-3}$ , the plasma has less effect on the laser propagation.

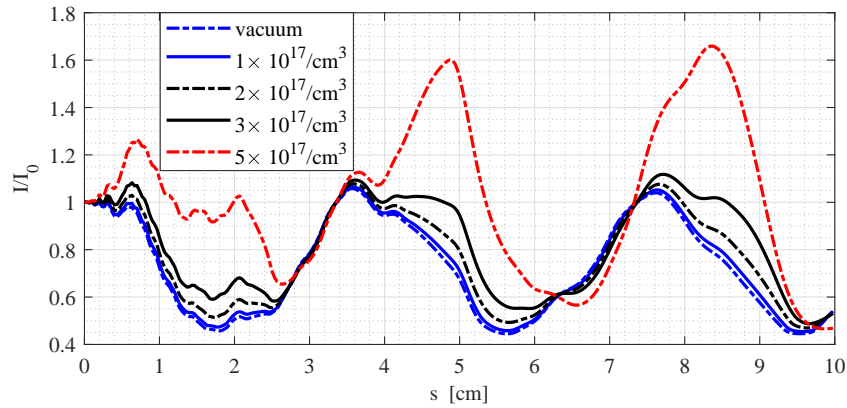


FIGURE 5.22: The evolution of the maximum amplitude of the Flattened Gaussian beams of order  $N = 4$  in the capillary with different plasma density.

Since the potential of the plasma wave excited by the the laser is related to the integration of the laser profile as shown in equation 2.119, the radial profile of a FGB varies from a Gaussian beam, with the plasma density being set to  $2 \times 10^{17} \text{cm}^{-3}$ , the longitudinal and radial electric field at capillary entrance excited by a Gaussian beam and a FGB

of order 4 with the same laser amplitude is shown in Figure 5.23 and Figure 5.24. The longitudinal field is almost the same because they both follow a Gaussian distribution, while the transverse field changed a lot,  $E_r/r$  is smaller for the FGB.

As the focusing strength  $K$  of the wakefield is related to  $E_r/r$ , for a FGB of order  $N$ ,  $K$  has been derived and is given by  $K_N = K_{cof.N} K_0$ , where  $K_0$  is the focus strength of the Gaussian case ( $N=0$ ),  $K_{cof.N}$  takes the form that

$$k_{cof.N} = \frac{1}{(N+1)^3} \sum_{n=0}^N (-1)^n C_n^N \left( \sum_{n=0}^N (-1)^n C_n^N + \sum_{n=0}^N (-1)^n C_n^N (-n) \right) \quad (5.14)$$

But one should be noted that the period of betatron oscillation is in a length scale of several 0.1 cm refer to Figure 4.26a and 5.26a, neither the laser amplitude nor the radial profile of laser is fixed in this scale refer to Figure 5.20 and 5.19, the 'uniform focusing channel' condition for the transverse matching condition in equation 3.21 is not valid here.

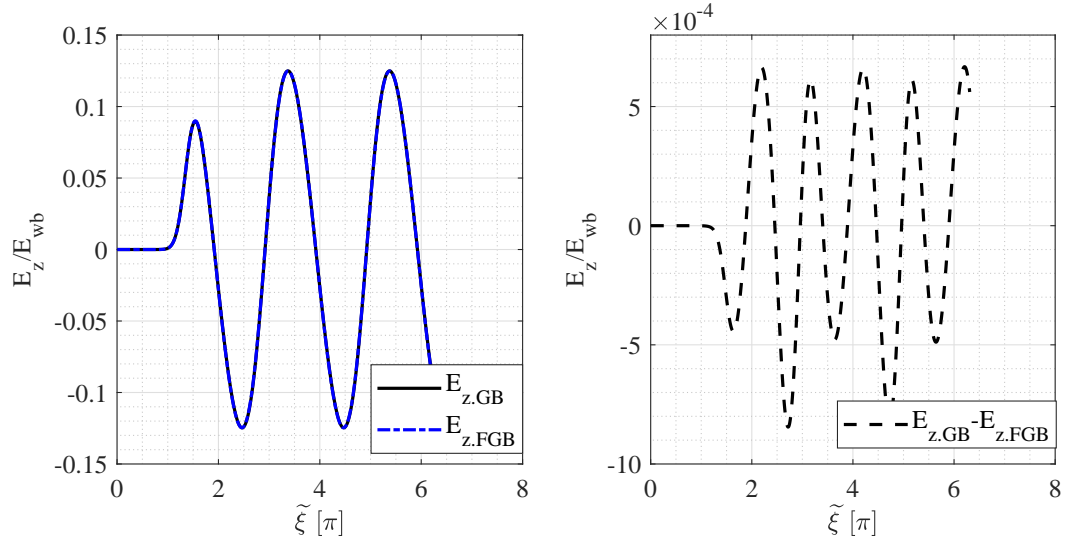


FIGURE 5.23: The excited longitudinal electric field with a GB and a FGB of order 4, with the same laser amplitude.

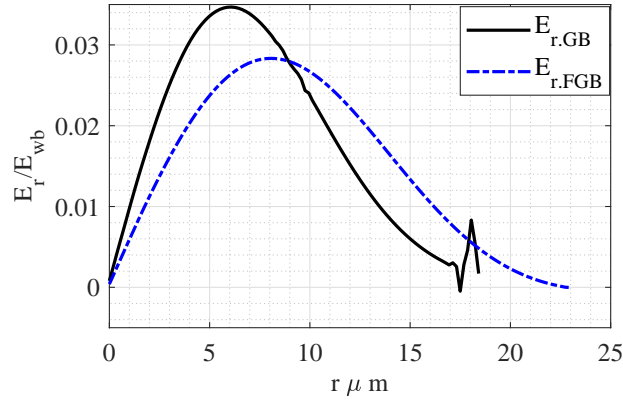


FIGURE 5.24: The excited radial electric field with a GB and a FGB of order 4, with the same laser amplitude.

To study the acceleration of the electrons, an electron bunch is injected at phase  $\tilde{\xi} = 0.92\pi$  at the capillary entrance, the electron bunch is the same as that in the previous study with a Gaussian laser profile in Figure 5.12. The trapped electrons versus propagation length is shown in Figure 5.25, almost no (0.002%) electrons are lost with a FGB of order  $N = 4$ , no electrons are lost in the capillary with a FGB of order  $N = 20$  and  $N = 50$ . This is a significant improvement compared to the Gaussian case in Figure 5.11

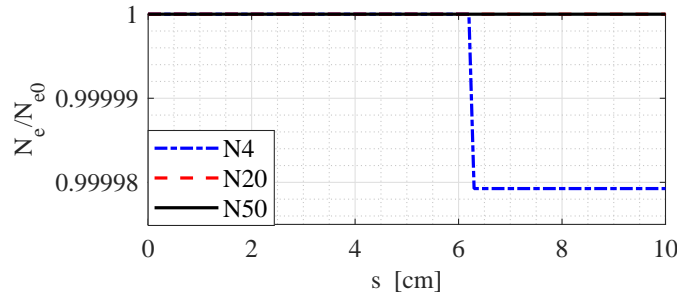
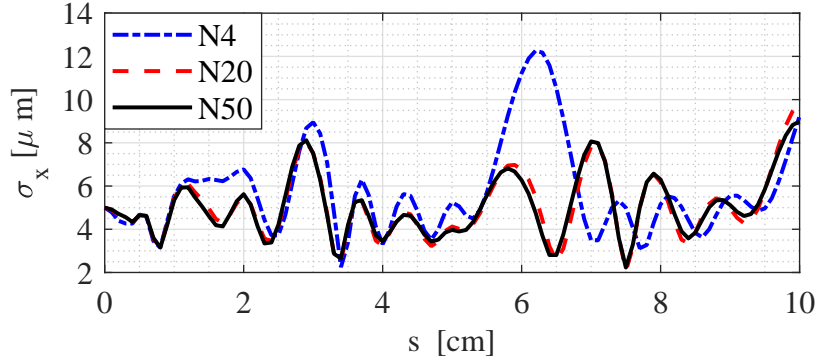


FIGURE 5.25: The electrons number during the propagation with plasma wave excited by FGB of order  $N = 4, 20, 50$ .

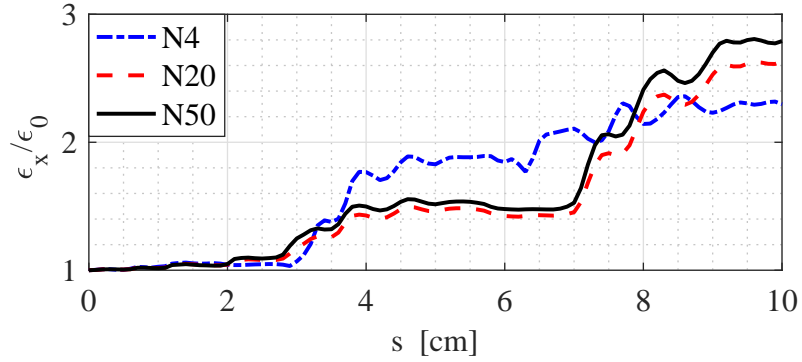
The evolution of the RMS bunch size, the normalized emittance and the energy spread of the electron bunch are shown in Figure 5.26, there is less difference between  $N = 20$  and  $N = 50$ , for  $N = 4$  electrons lost at  $s = 6.2\text{cm}$ , where the bunch size has a maximum value. The emittance doesn't increase at  $1.8\text{cm}$  and  $5.4\text{cm}$  where the radial laser profile is modulated, that means the defocusing field is weak and has less effect on the electrons. The emittance has a sharp increase from  $s = 3\text{cm}$  and  $s = 7\text{cm}$ , where the phase shift between  $EH_{11}$  and  $EH_{12}$  mode is  $\sim 3/2\pi$ ,  $dE/ds$  reaches it's maximum value, thus the field varies fast, and also the amplitude of the field is increasing, the fast change of the field amplitude and profile lead to the increase of emittance. But referring to

the final emittance of the electron bunch, the FGB of order  $N = 4$  seems has a better performance, this may due to the relatively lower electric field.

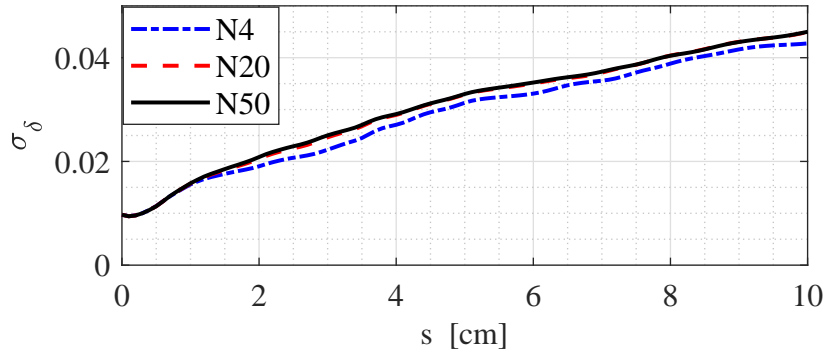
The energy spread increases from 1% to  $\sim 4\%$  during the 10 cm's propagation due to the gradient of the electric field, the longitudinal phase space of the electrons at the capillary entrance and the capillary exit with a driven FGB of  $N = 4, 20, 50$  are shown in Figure 5.27



(A) The RMS bunch size during the propagation with plasma wave excited by FGB of order  $N = 4, 20, 50$ .



(B) The normalize emittance during the propagation with plasma wave excited by FGB of order  $N = 4, 20, 50$ .



(C) The energy spread during the propagation with plasma wave excited by FGB of order  $N = 4, 20, 50$ .

FIGURE 5.26: Evolution of electron bunch parameters during the propagation with plasma wave excited by FGB of order  $N = 4, 20, 50$ .

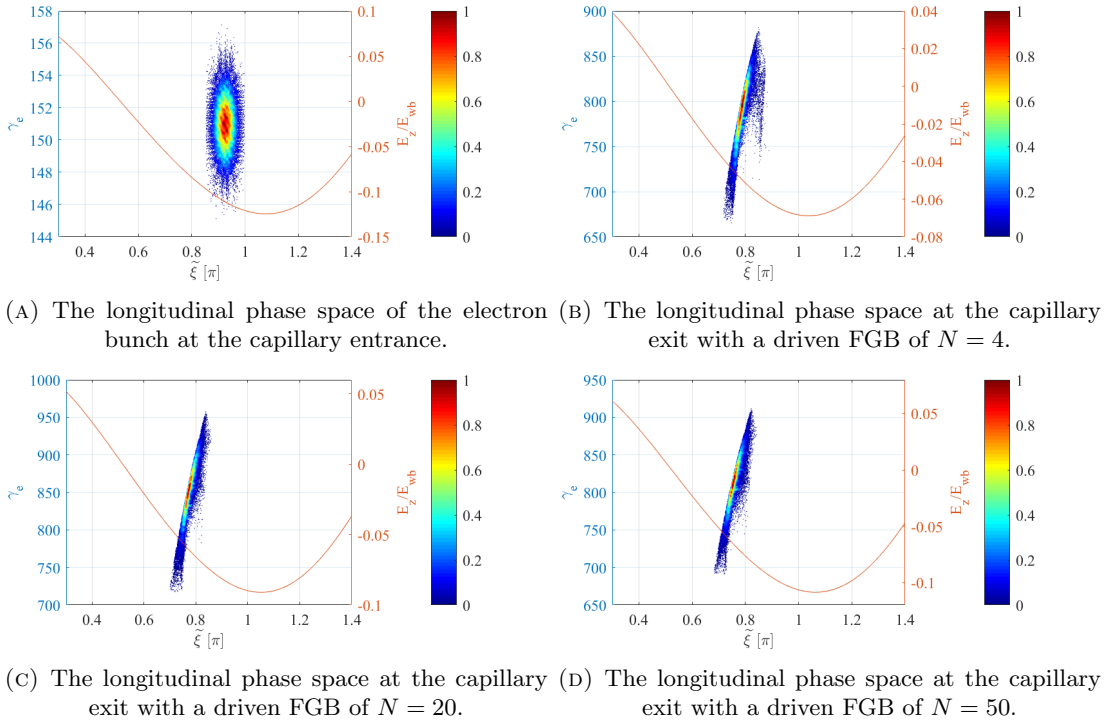


FIGURE 5.27: The longitudinal phase space of the electron bunch at the capillary entrance and exit, with a driven FGB of order  $N = 4, 20, 50$ .

With a drive FGB of order  $N = 20$  and  $N = 50$ , the phase space of the electron bunch at the capillary exit is similar. For both case, especially for  $N = 4$ , there are a few electrons who get less energy and falls to the low energy region, since they are kicked by the defocusing force induced by the radial profile modulation, the same as the case of a Gaussian drive beam discussed in section 5.1, but the number of kicked electrons is significantly decreased with a higher order Flattened Gaussian driven beam.

### 5.3 Extending the acceleration length for the ESCULAP frame

In the previous section, we have shown that, to extend the acceleration length with a dielectric capillary tube, the laser radial profile has a large effect on the acceleration process of the electron bunch. With a Gaussian radial profile, the diffraction at the capillary entrance and the dephasing between hybrid modes leads to the oscillation of the laser profile and amplitude, more than 50% electrons are lost during the propagation. While with a focused FGB the diffraction at capillary entrance can be eliminated, and also less laser energy is coupled to higher modes, almost no electrons are lost during the propagation. In this section, the Flattened Gaussian laser and the dielectric capillary are used to extend the acceleration range for the ESCULAP project.

Looking at the guiding of the laser beam with a hollow dielectric capillary for the ESCULAP project as shown in Figure 5.28.

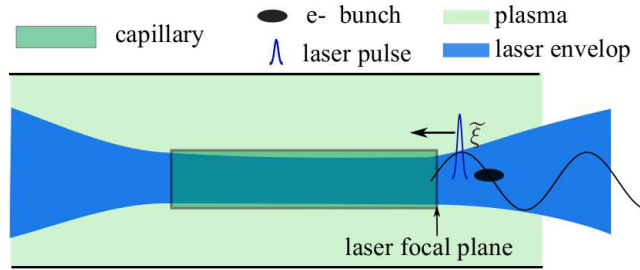


FIGURE 5.28: The upgraded configuration of the ESCULAP project with a dielectric capillary to guide the laser

However, one should note that, with the same laser energy, the laser amplitude at the focal plane and the evolution of the on axis laser amplitude are different for the Flattened Gaussian beam and the Gaussian beam, thus the best injection condition are changed.

With the parameters of the LASERIX laser beam ( $E_L=2$  J  $\tau_L=45$  fs FWHM duration,  $w_{G0}=50.46$   $\mu\text{m}$ ), the laser amplitude at the focal plane are summarized in Table 5.2,  $N$  is the order of the FGB,  $N = 0$  indicates the GB.

TABLE 5.2: The laser amplitude at the focal plane with different radial profile

N	0	1	2	4	5	8	10	20	50
$a_0$	0.69876	0.62499	0.59591	0.56906	0.56147	0.54747	0.54176	0.52743	0.51481

Since the laser plasma interaction starts several centimeters before the laser focal plane, the radial profiles of the FGB of different orders at 5 cm before the focal plane are shown in Figure 5.29.

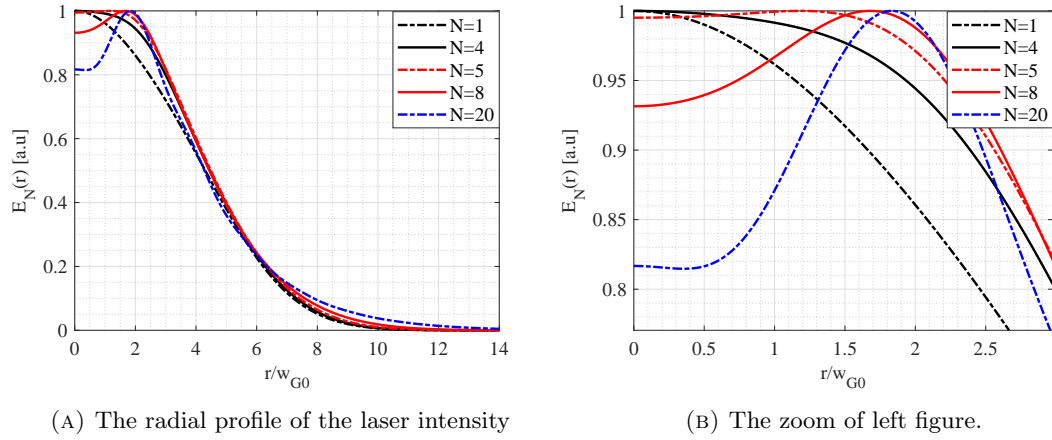


FIGURE 5.29: The radial profiles of the laser intensity at 5 cm before the laser focal plane. The radial profiles before focusing follow a Flattened Gaussian distribution of order 1, 4, 5, 8, 20.

With  $N$  larger than 4, the near axis field is modulated near the injection plane, thus  $N$  should be smaller than 4 for the configuration of the ESCULAP project as shown in Figure 5.28. With the increase of  $N$ , less energy is coupled to the higher engine modes when propagating in the capillary, this is beneficial for the electron beam quality, however, the laser amplitude decreases at the focal plane, more laser energy is collimated by the capillary according to Table 5.1 and 5.2. One should make a compromise between the energy efficiency and the beam quality, in the following study,  $N$  is set to 4 mainly concerning on the beam quality.

The optimal injection condition depends on the evolution of the on axis laser amplitude from the injection plane to one Rayleigh length before the focal plane. In the following study, the laser energy is fixed to 2 J, the laser amplitude at the focal plane yields  $a_0 = 0.56906$ .

The on axis laser intensity versus distance to focal plane for a GB and a FGB of order  $N = 4$  are shown in Figure 5.30, due to previous simulation results, the velocity bunching mainly takes place from  $-4.5$  cm to  $-1$  cm for the GB case, the laser intensity of the FGB is higher than that of the GB in this section, however by shifting the evolution curvature of 'FGB@ $N = 4$ ' 0.5 cm to the right, it almost coincides with that of the Gaussian case between  $-4.5$  cm and  $-1$  cm, that means the same velocity bunching can be achieved with the FGB, by injecting the electrons 5 cm before the laser focal plane.



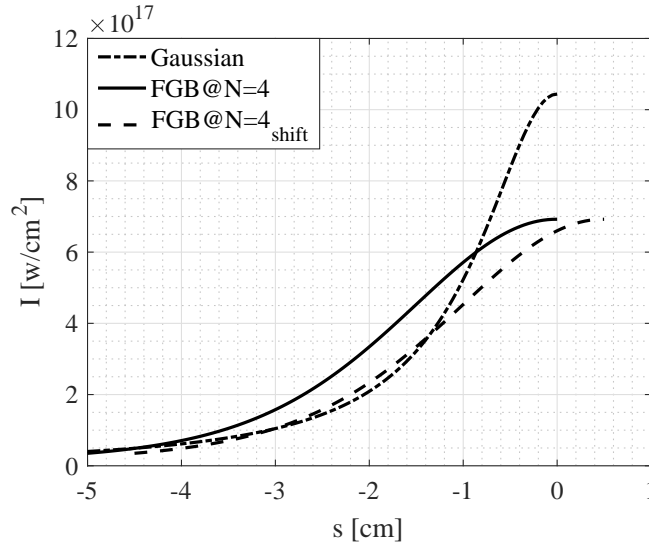


FIGURE 5.30: The upgraded configuration of the ESCULAP with a dielectric capillary to guide the laser.

The self-focusing effect should also be checked to set the capillary radius, the simulation is done without and with plasma (plasma density  $2 \times 10^{17}/\text{cm}^3$ ), when it propagates to the laser focal plane, the radial profiles of the laser are shown in Figure 5.31. With plasma, the zero crossing radius is  $\sim 93.99 \mu\text{m}$ , without plasma, the zero crossing radius is  $\sim 97.28 \mu\text{m}$ .

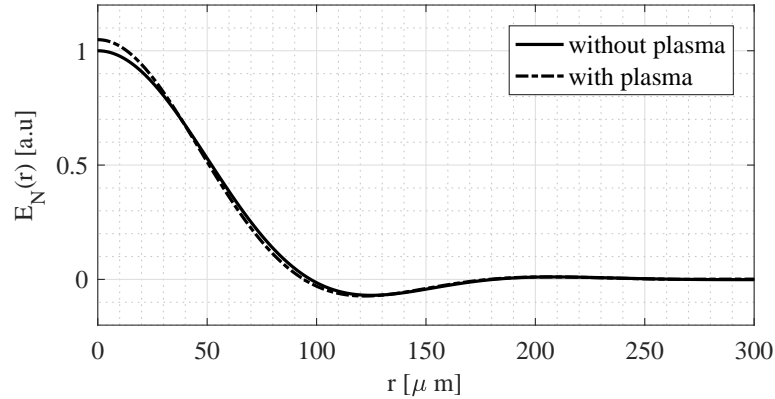


FIGURE 5.31: The radial profile of the laser at 5 cm before the

By setting the capillary radius to  $\sim 93.99 \mu\text{m}$ , and start the interaction 5 cm before the laser focal plane ( $\tilde{s}_f = 5$ ), The laser intensity and the captured electrons during the propagation is checked in Figure 5.32, the laser intensity is shown with the left axis, the fast fluctuation is efficiently suppressed. The trapped electron numbers is shown with the right axis, the low energy electrons are collimated by the capillary entrance, and 6.58 pC out of the 7.81 pC of electrons are accelerated to 15 cm after the capillary entrance. The electrons are mainly lost when the laser intensity reaches it's local minimum value, since

the radial profile of the laser beam changes fast there, and the focusing field is relatively weaker.

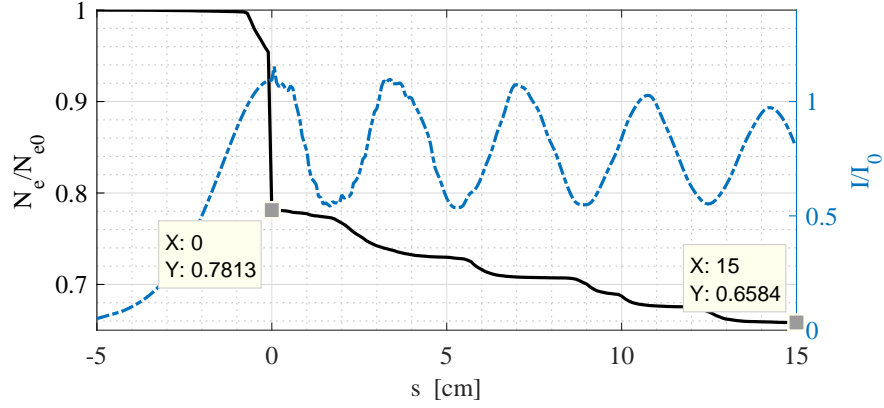


FIGURE 5.32: The maximum laser intensity during the propagation and the number of the accelerated electrons

The longitudinal phase space of the electron bunch at the capillary entrance, 2.6 cm after the capillary, 5 cm after the capillary and 14 cm after the capillary are reported in Figure 5.33.

From the evolution of the phase space, one can find that, at the capillary entrance, the bunch head has more energy than the bunch tail, while the bunch tail get more energy from the plasma wave during the propagation, at 2.6 cm after the capillary entrance, the bunch head has the same energy with the bunch tail, the energy spread reaches it's minimum value, after that the bunch tail may have more energy than the head, the energy spread increases during the propagation. The normalized FWHM bunch energy spread is shown in Figure 5.34.

The energy distribution at 2.6 cm and 14 cm after the capillary entrance is shown in Figure 5.35.

Thus to get a minimum energy spread, the capillary length should be set to  $\sim 2.6$  cm, the FWHM energy yields  $\sim 1.20\%$ . However, without capillary guiding and with the Gaussian radial laser profile, the  $\gamma_e$  at plasma exit is also  $\sim 280$ , the same with the 2.6 cm capillary guiding. With a long capillary, the electrons can be accelerated to higher energy, but the energy spread increases fast during the propagation, i.e. with a 15 cm capillary, the electron bunch is boosted to 370 MeV, with an FWHM energy spread of  $\sim 10\%$ .

The increase of the energy spread is mainly due to the gradient of the acceleration field. Note that, during the propagation in the capillary tube, the electron bunch is faster

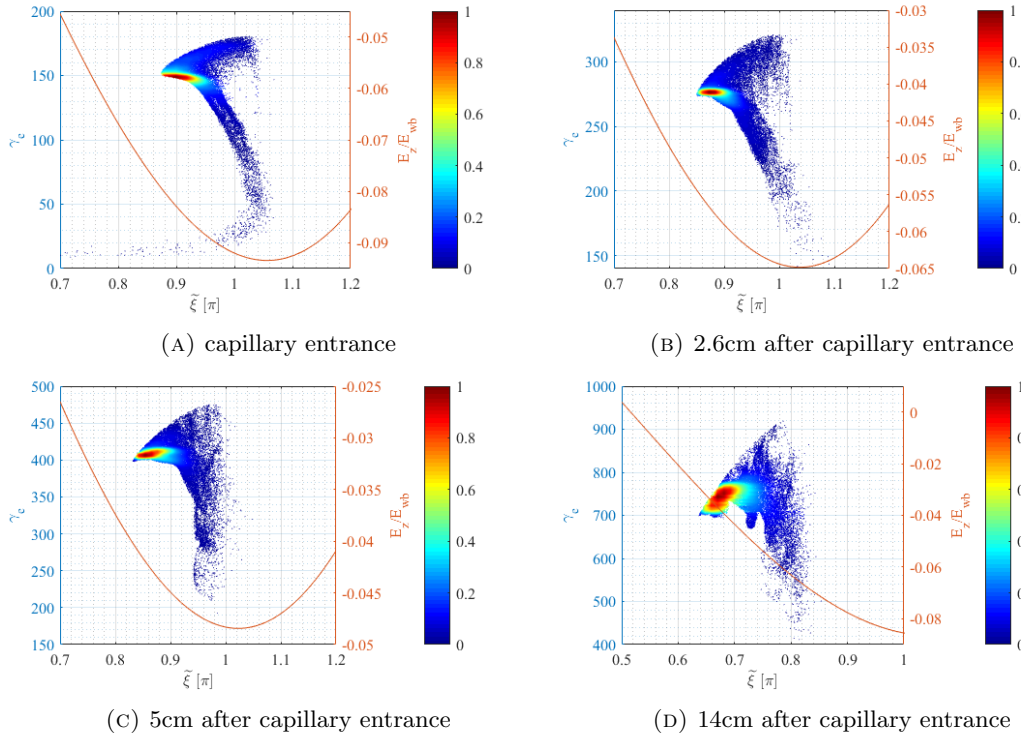


FIGURE 5.33: The longitudinal phase space of the electron bunch when propagates in the capillary

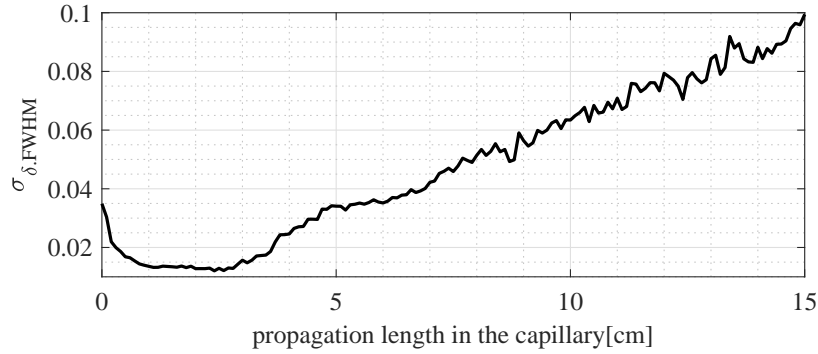


FIGURE 5.34: The normalized FWHM energy spread of the electron bunch during the propagation in the capillary

than the plasma wave and moves away from the acceleration field crest (see Figure 5.35) where the field gradient is minimum.

To achieve a higher energy electron beam with smaller energy spread, the electron bunch should be accelerated to higher energy before slipping away from the field crest, thus a stronger wakefield at the laser focal plane is required. This can be realized by focusing the laser beam to a smaller size, while in this case, the electron bunch should also be focused to a smaller size at the plasma entrance, a stronger solenoid is required (0.85 T in previous study). As the electron bunch after acceleration has a small volume ( $\sim 3$  fs in duration and  $\sim 3 \mu\text{m}$  in radius), a second stage acceleration with higher acceleration

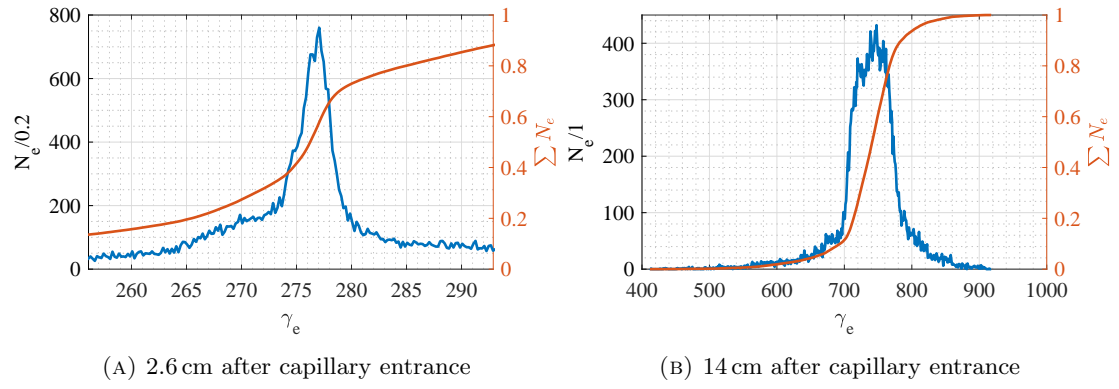


FIGURE 5.35: The distribution of the electron energy at different position

field can also be implemented. These will be the investment of the future. In this thesis, we tried to suppress the increase of the energy spread by an up plasma density ramp, this will be discussed in the next section.

## 5.4 Compensating the dephasing effect with a plasma up density ramp

With the Flattened Gaussian laser beam being guided by a hollow dielectric capillary, the electron bunch can be accelerated to 370 MeV in 15 cm's propagation as discussed in previous section, while the electron bunch moves away from the field crest and the energy spread increases during the propagation. It has been shown in [25, 108, 109] that with a tailored plasma density profile, the electron bunch can be fixed at the field crest. Here a linearly increased plasma density is used to partially compensate the dephasing, the linearly increased density profile is generated with the cell shown in Figure 5.36, the density ramp can be adjusted by changing the gas flux in "inlet2".

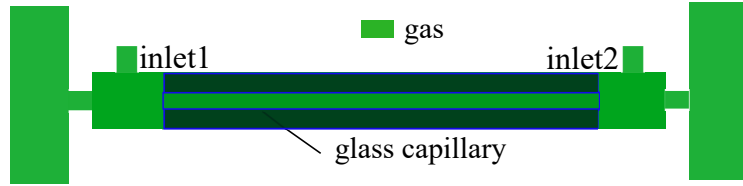


FIGURE 5.36: The cell used to generate a linearly increased plasma density in the glass capillary

Assume a liner density ramp with  $n_e(s) = n_0(1 + ks)$ , according to 4.5, the equation of motion is given by

$$\frac{d\beta_e\gamma_e}{ds} = -\sqrt{\pi}\frac{a_0^2}{4\sqrt{2}}k_p(s)k_p(s)L\exp(-k_p(s)^2L^2/8)\cos\tilde{\xi}\exp\left(\frac{-2r^2}{r_s^2}\right) \quad (5.15a)$$

$$\frac{d\tilde{\xi}}{ds} = d(k_p(s)d\xi) = \frac{\partial k_p(s)}{\partial s}\frac{\xi}{k_p(s)} + k_p(s)\left(\beta_g(s) - \frac{\beta_e\gamma_e}{\sqrt{1+\beta_e^2\gamma_e^2}}\right) \quad (5.15b)$$

Where  $k_p(s) = \frac{1}{c}\sqrt{\frac{n_e(s)e^2}{\epsilon_0 m_e}}$ , the first part in 5.15b is the phase slip induced by the density gradient, while the second part is introduced by the velocity difference between the electron bunch and the plasma wave. The first part is approximately  $0.5k\phi$ , in proportional to the density gradient and the initial phase, that means, to achieve equal dephasing compensation, the electron bunch can be injected in the wave packet far away from the laser pulse to reduce the required density gradient. However, in this thesis the electron bunch is injected in the first wave packet to avoid the generation of a pre electron bunch as discussed in section 4.4.1.

Equation 5.15 is solved with the initial phase being  $\tilde{\xi} = 0.92\pi$ , the initial energy being  $\gamma_e = 155$ , and  $a_0 = 0.57$ , with  $n_0 = 2 \times 10^{17}/\text{cm}^3$ ,  $n_e(s) = n_0(1 + ks)$ , The  $\phi - \gamma_e$  evolves from  $s = 0$  to  $s = 10$  with different density ramp  $k$  is shown in Figure 5.37

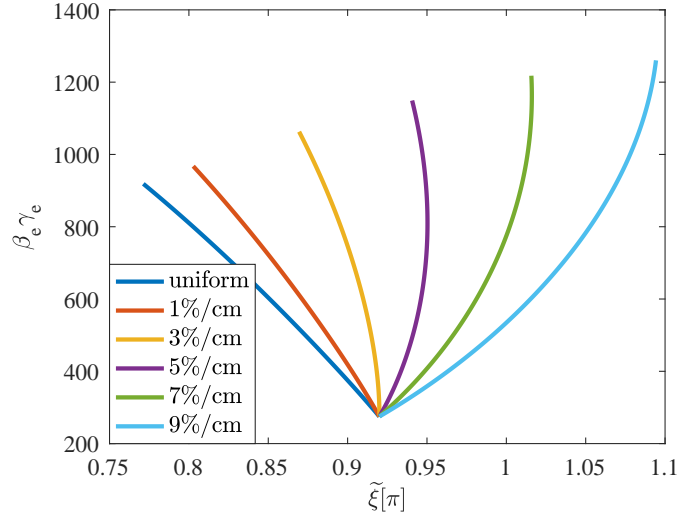


FIGURE 5.37: The evolution of the electron momenta  $\beta_e \gamma_e$  and acceleration phase in the 10cm capillary tube after laser focal plane, various plasma density ramp are studied, the electron starts with  $\beta_e \gamma_e = 155$ ,  $\tilde{\xi} = 0.92\pi$

A density gradient larger than 0.05/cm is required to make the electron bunch close to the field crest.

With  $k = 0.001, 0.005, 0.007, 0.009$  in unit of /cm, a density ramp is introduced from 2.6 cm after the capillary entrance, the number of captured electrons is shown in Figure 5.38, the corresponding energy spread is shown in Figure 5.39

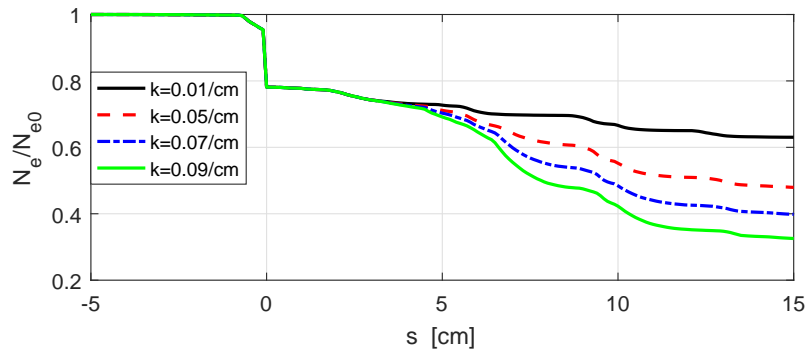


FIGURE 5.38: The number of the captured electrons during the propagation in the capillary tube, with different plasma density gradient

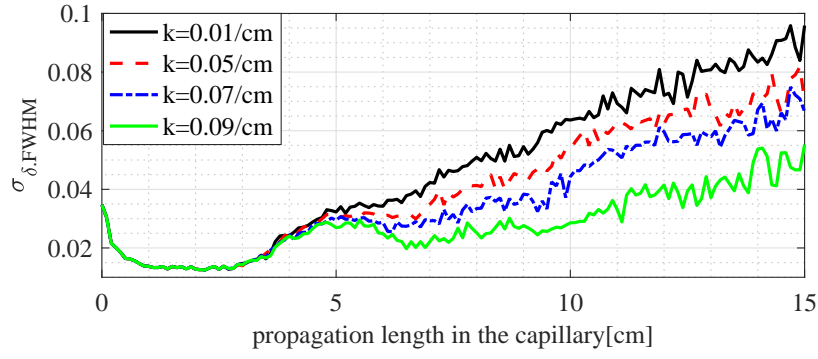


FIGURE 5.39: The evolution of the energy spread in the capillary tube, with different plasma density gradient

More electrons are lost with the increase of the density gradient  $k$ , because the electron bunch is closer to the field crest, some electrons are situated in the defocusing force. The increase of the energy spread can be efficiently suppressed with a larger density gradient, however, the FWHM energy spread after 15 cm's propagation in the plasma is still larger than 5%. To reduce the loss of electron and the increase of the energy spread, a shorter electron bunch is strongly desired

## 5.5 summary

In this chapter, the guiding of the laser beam with a hollow dielectric capillary is studied, the simulation results show that with a Gaussian radial profile of the laser intensity, even in the best match condition, the diffraction at the capillary entrance leads to a fast fluctuation of the laser intensity. As a result, the radial profile is modulated, at some positions, the maximum laser intensity is not suited on axis, a transverse defocusing force appears at the focusing phase, electrons are lost during the propagation.

To eliminate the diffraction at the capillary entrance, the use of a focused Flattened Gaussian profile is proposed, the intensity of a focused Flattened Gaussian profile falling fast to zero at the laser focal plane. The simulation results show that with a focused FGB the diffraction at the capillary entrance can be efficiently suppressed, thus electrons can be accelerated in more than 10 Rayleigh length without loss.

In the capillary, the laser energy is coupled to a family of hybrid modes  $EH_{1n}$ , the dephasing between hybrid modes may also modulates the radial profile of the laser intensity and lead to an increase of the electron beam emittance, this can only be suppressed with a real mono mode beam.

For the ESCULAP configuration, a Flattened Gaussian radial laser profile is then used to drive the plasma, and a hollow dielectric capillary is used to guide the laser. More than 83% electrons can be accelerated to high energy, i.e. 370 MeV in 15 cm. However, the energy spread increases quickly during the propagation due to the large field gradient, i.e. the energy spread increased to  $\sim 10\%$  after 15 cm's propagation. A minimum FWHM energy spread of 1.2% is achieved at 2.6 cm after the capillary, with  $\langle \gamma_e \rangle \sim 280$ .

To suppress the increase of the energy spread, an up plasma density ramp is used to reduce the plasma wave length, thus the electron bunch is closer to the field crest where a minimum field gradient is achieved. With the increase of the density gradient, the energy spread can be suppressed to  $\sim 5$  after 15 cm's propagation. However, more electrons are lost during the propagation, because more electrons are situated at the defocusing phase, a shorter electron bunch at the laser focal plane is strongly desired to suppress the loss of the electrons and the increase of the energy spread.



## Chapter 6

# Conclusion

With the low energy electron bunch (10 MeV) from the RF gun PHIL and the 2 J (41.8 TW) laser beam from LASERIX, the overall design of a Laser Plasma Wakefield Accelerator has been studied by simulation. The laser beam has a duration of 38 fs, it is focused to 50  $\mu\text{m}$  in the focal plane yielding a laser intensity of  $1 \times 10^{18} \text{W}/\text{cm}^2$ .

Normally the external electron bunch should be compressed to a small volume (several femtoseconds in duration, several micrometers in radius) to match the high gradient electric field in the plasma, this is very challenging for a 10 MeV 10 pC electron bunch since the space charge effect is significant. While with the configuration concerned in this thesis, the plasma starts several Rayleigh lengths before the laser focal plane to focus the electron bunch transversely and compress the electron bunch longitudinally, the required bunch volume at the plasma entrance is relaxed to tens of femtoseconds (half the plasma period) in duration and tens of micrometers in radius.

A dogleg chicane has been designed to compress the electron bunch before being injected into the plasma, space charge effect and CSR effect have been mainly checked in the simulation, the results indicate that the space charge effect may stretch the electron bunch and lead to an over compression, this can be compensated by slightly reducing the energy chirp of the electron bunch at the dogleg entrance, the CSR has less effect on the electron bunch due to the low charge. As a result, the electron bunch has been compressed to  $\sim 70$  fs, whereas it lengthens quickly after the dogleg, thus it should be injected in the plasma quickly. The plasma density has been chosen to achieve a plasma wave which is longer than two times the length of the electron bunch. The plasma starts several Rayleigh lengths before the laser focal plane, in this section, velocity bunching is performed to compress the electron bunch since the relative position of the electrons is not frozen, the injection phase and the distance between the plasma start plane and the laser focal plane have been varied to optimize the velocity bunching process, the

optimal injection condition for plasma densities of  $1.5 \times 10^{17}/\text{cm}^3$ ,  $2.0 \times 10^{17}/\text{cm}^3$  and  $2.5 \times 10^{17}/\text{cm}^3$  have been summarized in this thesis. With a plasma density of  $2.0 \times 10^{17}/\text{cm}^3$ , the electron bunch has been compressed to 3 fs at the laser focal plane (3.4 fs at the plasma exit), the energy spectrum at the plasma exit has a sharp peak and long tail, the FWHM energy spread yields 1.2%. The simulation results also indicate that, the tolerance to the injection timing error of the electron bunch is 12 fs with respect to the resulted energy spectrum with various injection phase as shown in Figure 4.17.

In the velocity bunching process,  $\sim 25\%$  of the electrons are lost and the relative positions of electrons changes, so it is difficult to define a transverse matching condition at the injection plane. Thus a solenoid has been used after the dogleg to focus the electron bunch immediately to reduce the distance between the plasma and the dogleg exit (the electron bunch lengthens quickly). The transverse beam size has been varied to suppress the oscillation of the bunch envelop and the emittance in the plasma, with the optimum case presented in the thesis, the emittance at the plasma exit is smaller than  $1 \mu\text{m}$ . While it is notable that, to focus the electron bunch with a solenoid, the bunch size at the focal point depends on the position of the focal point, this makes the tuning of the bunch size more complicated. The angular divergence of the electron bunch after acceleration has been efficiently reduced to 0.17 mrad, by terminating the plasma 5.5 cm after the laser focal plane, where the bunch size increases linearly with the propagation length.

The guiding of the laser beam with a hollow dielectric capillary has also been studied to extend the acceleration length, the laser beam in a capillary has been described with a family of hybrid modes  $EH_{1n}$ . It has been presented that with a Gaussian intensity profile for laser, the diffraction at the capillary entrance and the dephasing between hybrid modes will modulate the laser profile and lead to the loss of electrons. While with a focused Flattened Gaussian profile, the diffraction at the capillary entrance can be efficiently suppressed, electrons can be accelerated over ten Rayleigh lengths, while the emittance increases fast due to the modulation of the laser profile resulting from dephasing between hybrid modes. To maintain the low emittance, a mono mode laser beam should be used, a plasma channel or some other technique can also be considered to guide the laser beam.

The tolerance to the synchronisation error and alignment error are still need to be checked in the future.

# Bibliography

- [1] Richard B Neal. The stanford two mile accelerator. Technical report, Stanford Linear Accelerator Center, Menlo Park, CA (US), 1968.
- [2] JW Wang et al. R&d of accelerator structures at slac. Technical report, Stanford Linear Accelerator Center (SLAC), 2007.
- [3] TO Raubenheimer, H Trautner, F Perriollat, G Carron, P Pearce, JC Godot, Daniel Schulte, P Royer, Steffen Döbert, Rudolf Bossart, et al. *A 3 TeV  $e^+e^-$  Linear Collider Based on CLIC Technology*. Number CERN-2000-008. CERN, 2000.
- [4] John Galayda. The linac coherent light source-ii project. 2014.
- [5] Massimo Altarelli, R Brinkmann, M Chergui, W Decking, B Dobson, S Düsterer, G Grübel, W Graeff, H Graafsma, J Hajdu, et al. The european x-ray free-electron laser. *Technical design report, DESY*, 97:1–26, 2006.
- [6] LHC Study Group and European Organization for Nuclear Research. *Design study of the Large Hadron Collider (LHC): a multiparticle collider in the LEP tunnel*. Number 3. Not Avail, 1991.
- [7] Toshiki Tajima and John M Dawson. Laser electron accelerator. *Physical Review Letters*, 43(4):267, 1979.
- [8] Donna Strickland and Gerard Mourou. Compression of amplified chirped optical pulses. *Optics communications*, 55(6):447–449, 1985.
- [9] F Amiranoff, S Baton, D Bernard, B Cros, D Descamps, F Dorchies, F Jacquet, Victor Malka, JR Marques, G Matthieussent, et al. Observation of laser wakefield acceleration of electrons. *Physical Review Letters*, 81(5):995, 1998.
- [10] K Nakajima, T Kawakubo, H Nakanishi, A Ogata, Y Kato, Y Kitagawa, R Kodama, K Mima, H Shiraga, K Suzuki, et al. A proof-of-principle experiment of laser wakefield acceleration. *Physica Scripta*, 1994(T52):61, 1994.

- [11] A Modena, Z Najmudin, AE Dangor, CE Clayton, KA Marsh, C Joshi, Victor Malka, CB Darrow, C Danson, D Neely, et al. Electron acceleration from the breaking of relativistic plasma waves. *nature*, 377(6550):606, 1995.
- [12] Donald Umstadter, S-Y Chen, A Maksimchuk, G Mourou, and R Wagner. Nonlinear optics in relativistic plasmas and laser wake field acceleration of electrons. *Science*, 273(5274):472–475, 1996.
- [13] WP Leemans, P Catravas, E Esarey, CGR Geddes, Cs Toth, R Trines, CB Schroeder, BA Shadwick, J Van Tilborg, and J Faure. Electron-yield enhancement in a laser-wakefield accelerator driven by asymmetric laser pulses. *Physical review letters*, 89(17):174802, 2002.
- [14] Victor Malka, S Fritzler, E Lefebvre, M-M Aleonard, F Burgy, J-P Chambaret, J-F Chemin, K Krushelnick, G Malka, SPD Mangles, et al. Electron acceleration by a wake field forced by an intense ultrashort laser pulse. *Science*, 298(5598):1596–1600, 2002.
- [15] Jérôme Faure, Yannick Glinec, A Pukhov, S Kiselev, S Gordienko, E Lefebvre, J-P Rousseau, F Burgy, and Victor Malka. A laser-plasma accelerator producing monoenergetic electron beams. *Nature*, 431(7008):541, 2004.
- [16] CGR Geddes, Cs Toth, J Van Tilborg, E Esarey, CB Schroeder, D Bruhwiler, C Nieter, J Cary, and WP Leemans. High-quality electron beams from a laser wakefield accelerator using plasma-channel guiding. *Nature*, 431(7008):538, 2004.
- [17] Stuart PD Mangles, CD Murphy, Zufikar Najmudin, Alexander George Roy Thomas, JL Collier, Aboobaker E Dangor, EJ Divall, PS Foster, JG Gallacher, CJ Hooker, et al. Monoenergetic beams of relativistic electrons from intense laser-plasma interactions. *Nature*, 431(7008):535, 2004.
- [18] Wim P Leemans, Bob Nagler, Anthony J Gonsalves, Cs Toth, Kei Nakamura, Cameron GR Geddes, ESCB Esarey, CB Schroeder, and SM Hooker. GeV electron beams from a centimetre-scale accelerator. *Nature physics*, 2(10):696, 2006.
- [19] WP Leemans, AJ Gonsalves, H-S Mao, K Nakamura, C Benedetti, CB Schroeder, Cs Tóth, J Daniels, DE Mittelberger, SS Bulanov, et al. Multi-gev electron beams from capillary-discharge-guided subpetawatt laser pulses in the self-trapping regime. *Physical review letters*, 113(24):245002, 2014.
- [20] AJ Gonsalves, K Nakamura, J Daniels, H-S Mao, C Benedetti, CB Schroeder, Cs Tóth, J van Tilborg, DE Mittelberger, SS Bulanov, et al. Generation and

- pointing stabilization of multi-gev electron beams from a laser plasma accelerator driven in a pre-formed plasma waveguide. *Physics of Plasmas*, 22(5):056703, 2015.
- [21] AJ Gonsalves, K Nakamura, J Daniels, C Benedetti, C Pieronek, TCH de Raadt, S Steinke, JH Bin, SS Bulanov, J van Tilborg, et al. Petawatt laser guiding and electron beam acceleration to 8 gev in a laser-heated capillary discharge waveguide. *Physical Review Letters*, 122(8):084801, 2019.
- [22] SJ Yoon, JP Palastro, D Gordon, TM Antonsen, and HM Milchberg. Quasi-phase-matched acceleration of electrons in a corrugated plasma channel. *Physical Review Special Topics-Accelerators and Beams*, 15(8):081305, 2012.
- [23] Phillip Sprangle, B Hafizi, JR Penano, RF Hubbard, A Ting, CI Moore, DF Gordon, A Zigler, D Kaganovich, and TM Antonsen Jr. Wakefield generation and gev acceleration in tapered plasma channels. *Physical Review E*, 63(5):056405, 2001.
- [24] W Rittershofer, CB Schroeder, E Esarey, FJ Grüner, and WP Leemans. Tapered plasma channels to phase-lock accelerating and focusing forces in laser-plasma accelerators. *Physics of Plasmas*, 17(6):063104, 2010.
- [25] A Pukhov and I Kostyukov. Control of laser-wakefield acceleration by the plasma-density profile. *Physical Review E*, 77(2):025401, 2008.
- [26] J Luo, M Chen, WY Wu, SM Weng, ZM Sheng, CB Schroeder, DA Jaroszynski, E Esarey, WP Leemans, WB Mori, et al. Multistage coupling of laser-wakefield accelerators with curved plasma channels. *Physical review letters*, 120(15):154801, 2018.
- [27] Kazuhisa Nakajima. Seamless multistage laser-plasma acceleration toward future high-energy colliders. *Light: Science and Applications*, 7:1–3, 2018.
- [28] Guo-Zheng Sun, Edward Ott, YC Lee, and Parvez Guzdar. Self-focusing of short intense pulses in plasmas. *The Physics of fluids*, 30(2):526–532, 1987.
- [29] AB Borisov, AV Borovski, OB Shiryaev, VV Korobkin, AM Prokhorov, JC Solem, TS Luk, K Boyer, and CK Rhodes. Relativistic and charge-displacement self-channeling of intense ultrashort laser pulses in plasmas. *Physical Review A*, 45(8):5830, 1992.
- [30] E Esarey, CB Schroeder, BA Shadwick, JS Wurtele, and WP Leemans. Nonlinear theory of nonparaxial laser pulse propagation in plasma channels. *Physical review letters*, 84(14):3081, 2000.

- [31] DF Gordon, B Hafizi, RF Hubbard, JR Penano, P Sprangle, and A Ting. Asymmetric self-phase modulation and compression of short laser pulses in plasma channels. *Physical review letters*, 90(21):215001, 2003.
- [32] Jérôme Faure, Yannick Glinec, JJ Santos, F Ewald, J-P Rousseau, S Kiselev, A Pukhov, T Hosokai, and Victor Malka. Observation of laser-pulse shortening in nonlinear plasma waves. *Physical review letters*, 95(20):205003, 2005.
- [33] J Schreiber, C Bellei, SPD Mangles, C Kamperidis, S Kneip, SR Nagel, CAJ Palmer, PP Rajeev, MJV Streeter, and Z Najmudin. Complete temporal characterization of asymmetric pulse compression in a laser wakefield. *Physical review letters*, 105(23):235003, 2010.
- [34] J Faure. Plasma injection schemes for laser-plasma accelerators. *arXiv preprint arXiv:1705.10542*, 2017.
- [35] Arthur Pak, KA Marsh, SF Martins, W Lu, WB Mori, and C Joshi. Injection and trapping of tunnel-ionized electrons into laser-produced wakes. *Physical Review Letters*, 104(2):025003, 2010.
- [36] C McGuffey, AGR Thomas, W Schumaker, T Matsuoka, V Chvykov, FJ Dollar, G Kalintchenko, V Yanovsky, A Maksimchuk, K Krushelnick, et al. Ionization induced trapping in a laser wakefield accelerator. *Physical Review Letters*, 104(2):025004, 2010.
- [37] M Chen, E Esarey, CB Schroeder, CGR Geddes, and WP Leemans. Theory of ionization-induced trapping in laser-plasma accelerators. *Physics of Plasmas*, 19(3):033101, 2012.
- [38] CGR Geddes, K Nakamura, GR Plateau, Cs Toth, E Cormier-Michel, E Esarey, CB Schroeder, JR Cary, and WP Leemans. Plasma-density-gradient injection of low absolute-momentum-spread electron bunches. *Physical review letters*, 100(21):215004, 2008.
- [39] Hyyong Suk, Nick Barov, James Benjamine Rosenzweig, and E Esarey. Plasma electron trapping and acceleration in a plasma wake field using a density transition. In *The Physics Of High Brightness Beams*, pages 404–417. World Scientific, 2000.
- [40] AV Brantov, T Zh Esirkepov, M Kando, H Kotaki, V Yu Bychenkov, and SV Bulanov. Controlled electron injection into the wake wave using plasma density inhomogeneity. *Physics of Plasmas*, 15(7):073111, 2008.

- [41] E Esarey, RF Hubbard, WP Leemans, A Ting, and P Sprangle. Electron injection into plasma wakefields by colliding laser pulses. *Physical Review Letters*, 79(14):2682, 1997.
- [42] G Fubiani, E Esarey, CB Schroeder, and WP Leemans. Beat wave injection of electrons into plasma waves using two interfering laser pulses. *Physical Review E*, 70(1):016402, 2004.
- [43] H Kotaki, S Masuda, M Kando, JK Koga, and K Nakajima. Head-on injection of a high quality electron beam by the interaction of two laser pulses. *Physics of Plasmas*, 11(6):3296–3302, 2004.
- [44] Clément Rechatin, Jérôme Faure, Agustin Lifschitz, Victor Malka, and E Lefebvre. Plasma wake inhibition at the collision of two laser pulses in an underdense plasma. *Physics of plasmas*, 14(6):060702, 2007.
- [45] Timon Mehrling. *Theoretical and numerical studies on the transport of transverse beam quality in plasma-based accelerators*. Dissertation, Universität Hamburg, Hamburg, 2014. URL <http://bib-pubdb1.desy.de/record/191881>. Dissertation, Universität Hamburg, 2014.
- [46] Ralph Assmann, Ingmar Hartl, Markus Hüning, Matthias Groß, Franz Kaertner, Yuancun Nie, Andreas Maier, Brian Foster, Axel Rühl, Christopher Behrens, et al. Sinbad-a proposal for a dedicated accelerator research facility at desy. 2014.
- [47] U Dorda, R Assmann, R Brinkmann, K Flöttmann, I Hartl, M Hüning, F Kärtner, A Fallahi, B Marchetti, Y Nie, et al. SINBAD-The accelerator R&D facility under construction at DESY. *Nuclear Instruments and Methods in Physics Research Section A*, 829:233–236, 2016.
- [48] Paul Andreas Walker, PD Alesini, AS Alexandrova, Maria Pia Anania, NE Andreev, I Andriyash, A Aschikhin, RW Assmann, T Audet, A Bacci, et al. Horizon 2020 eupraxia design study. In *Journal of Physics: Conference Series*, volume 874, 2017.
- [49] Andrea R Rossi, Alberto Bacci, Marco Belleveglia, et al. The external-injection experiment at the SPARC.LAB facility. *Nuclear Instruments and Methods in Physics Research Section A*, 740:60–66, 2014.
- [50] Benno Zeitler, Florian Gruener, and Klaus Floettmann. *Phase Space Linearization and External Injection of Electron Bunches into Laser-Driven Plasma Wakefields at REGAE*. PhD thesis. University Hamburg, Diss. 2016.

- [51] Jun Zhu. Design study for generating sub-femtosecond to femtosecond electron bunches for advanced accelerator development at sinbad. 2017.
- [52] J Zhu, RW Assmann, M Dohlus, U Dorda, and B Marchetti. Sub-fs electron bunch generation with sub-10-fs bunch arrival-time jitter via bunch slicing in a magnetic chicane. *Physical Review Accelerators and Beams*, 19(5):054401, 2016.
- [53] Julia Grebenyuk, Ralph Assmann, Ulrich Dorda, and Barbara Marchetti. Plasma acceleration with external injection at sinbad. In *Beam Dynamics and Optimization (BDO), 2014 20th International Workshop on*, pages 1–2. IEEE, 2014.
- [54] M Belleveglia, M Castellano, E Chiadroni, G Di Pirro, A Gallo, M Ferrario, G Gatti, C Vaccarezza, A Bacci, L Serafini, et al. Plasma acceleration experiment at sparclab with external injection. In *International Particle Accelerator Conference*, page 2169, 2012.
- [55] Benno Zeitler, Klaus Floettmann, and Florian Grüner. Linearization of the longitudinal phase space without higher harmonic field. *Physical Review Special Topics-Accelerators and Beams*, 18(12):120102, 2015.
- [56] Tim Gehrke. Design of permanent magnetic solenoids for regae. Technical report, Deutsches Elektronen-Synchrotron (DESY), 2013.
- [57] Max Hachmann, Klaus Flöttmann, Tim Gehrke, and Frank Mayet. Design and characterization of permanent magnetic solenoids for regae. *Nuclear Instruments and Methods in Physics Research Section A: Accelerators, Spectrometers, Detectors and Associated Equipment*, 829:270–273, 2016.
- [58] M Alves, C Arnault, D Auguste, JL Babigeon, F Blot, J Brossard, C Bruni, S Cavalier, JN Cayla, V Chaumat, et al. Phil photoinjector test line. *Journal of Instrumentation*, 8(01):T01001, 2013.
- [59] Fabien Ple, Moana Pittman, Gerard Jamelot, and Jean-Paul Chambaret. Design and demonstration of a high-energy booster amplifier for a high-repetition rate petawatt class laser system. *Optics letters*, 32(3):238–240, 2007.
- [60] Elsa Baynard, Christelle Bruni, Kevin Cassou, Vincent Chaumat, Nicolas Delerue, Julien Demailly, Denis Douillet, Nouredine El Kamchi, David Garzella, Olivier Guilbaud, et al. Status report of the esculap project at orsay: External injection of low energy electrons in a plasma. *Nuclear Instruments and Methods in Physics Research Section A: Accelerators, Spectrometers, Detectors and Associated Equipment*, 909:46–48, 2018.



- [61] M Santarsiero, D Aiello, R Borghi, and S Vicalvi. Focusing of axially symmetric flattened gaussian beams. *Journal of Modern Optics*, 44(3):633–650, 1997.
- [62] Helmut Wiedemann. *Particle accelerator physics*. Springer, 2015.
- [63] Thomas P Wangler. *RF Linear accelerators*. John Wiley & Sons, 2008.
- [64] Karl L Brown and Roger V Servranckx. First-and second-order charged particle optics. In *AIP conference proceedings*, volume 127, pages 62–138. AIP, 1985.
- [65] Klaus Floettmann. Some basic features of the beam emittance. *Physical Review Special Topics-Accelerators and Beams*, 6(3):034202, 2003.
- [66] Accelerator Research Division, AR: Divisional reports - 1965. URL <https://cds.cern.ch/record/1597939>.
- [67] LINEAR SPACE CHARGE FORCES. Theory and technique of beam envelope simulation.
- [68] Luca Serafini and James B Rosenzweig. Envelope analysis of intense relativistic quasilaminar beams in rf photoinjectors: ma theory of emittance compensation. *Physical Review E*, 55(6):7565, 1997.
- [69] Michiko G Minty and Frank Zimmermann. Beam techniques—beam control and manipulation. *USPAS lectures, June*, 1999.
- [70] Settimio Mobilio, Federico Boscherini, and Carlo Meneghini. *Synchrotron Radiation*. Springer, 2016.
- [71] Lev Davidovich Landau. *The classical theory of fields*, volume 2. Elsevier, 2013.
- [72] Ya. S. Derbenev, J. Rossbach, V. D. Shiltsev, and E. L. Saldin. Microbunch radiative tail - head interaction. 1995.
- [73] Evgenij L Saldin, Evgeny A Schneidmiller, and MV Yurkov. On the coherent radiation of an electron bunch moving in an arc of a circle. *Nuclear Instruments and Methods in Physics Research Section A: Accelerators, Spectrometers, Detectors and Associated Equipment*, 398(2-3):373–394, 1997.
- [74] JB Murphy, S Krinsky, and RL Gluckstern. Longitudinal wakefield for synchrotron radiation. In *Particle Accelerator Conference, 1995., Proceedings of the 1995*, volume 5, pages 2980–2982. IEEE, 1995.
- [75] A He, F Willeke, L.H Yu, and L Yang. Design of low energy bunch compressors with space charge effects. *Physical Review Special Topics-Accelerators and Beams*, 18(1):014201, 2015.

- [76] K Flöttmann, T Limberg, and Ph Piot. Generation of ultrashort electron bunches by cancellation of nonlinear distortions in the longitudinal phase space. *TESLA-FEL Report: TESLA-FEL*, 6:2001, 2001.
- [77] TI Smith. Intense low emittance beams for free electron lasers. In *Proceedings of the 1986 Linear Accelerator Conference (LINAC86)(SLAC, Stanford, CA, 1986)*, page 421, 1986.
- [78] Benno Zeitler. *Phase Space Linearization and External Injection of Electron Bunches into Laser-Driven Plasma Wakefields at REGAE*. Dissertation, Universität Hamburg, Hamburg, 2017. URL <http://bib-pubdb1.desy.de/record/317605>. Dissertation, Universität Hamburg, 2016.
- [79] Huang Rui-Xuan, He Zhi-Gang, Li Wei-Wei, and Jia Qi-Ka. Velocity bunching in travelling wave accelerator with low acceleration gradient. *Chinese Physics C*, 38(5):057004, 2014.
- [80] Wai Lau, Ming-Chang Chou, Nuan-Ya Huang, An-ping Lee, and Juhao Wu. Design of a dogleg bunch compressor with tunable first-order longitudinal dispersion. In *38th Int. Free Electron Laser Conf.(FEL'17), Santa Fe, NM, USA, August 20-25, 2017*, pages 309–312. JACOW, Geneva, Switzerland, 2018.
- [81] P Emma and R Brinkmann. Emittance dilution through coherent energy spread generation in bending systems. In *Particle Accelerator Conference, 1997. Proceedings of the 1997*, volume 2, pages 1679–1681. IEEE, 1997.
- [82] Dmitry Kayran and Vladimir N Litvinenko. Novel method of emittance preservation in erl merging system in presence of strong space charge forces. In *Particle Accelerator Conference, 2005. PAC 2005. Proceedings of the*, pages 2512–2514. IEEE, 2005.
- [83] Yichao Jing, Yue Hao, and Vladimir N Litvinenko. Compensating effect of the coherent synchrotron radiation in bunch compressors. *Physical Review Special Topics-Accelerators and Beams*, 16(6):060704, 2013.
- [84] Stefan Karsch. Applications of high-intensity laser-pulses – overview, 2017. URL [https://www.physik.uni-muenchen.de/lehre/vorlesungen/sose\\_17/applications\\_of\\_high-intensity\\_laser-pulses/index.html](https://www.physik.uni-muenchen.de/lehre/vorlesungen/sose_17/applications_of_high-intensity_laser-pulses/index.html).
- [85] Nikolai B Delone and Vladimir P Krainov. *Multiphoton processes in atoms*, volume 13. Springer Science & Business Media, 2012.

- [86] Nikolai Borisovich Delone and Vladimir Pavlovich Krainov. Tunneling and barrier-suppression ionization of atoms and ions in a laser radiation field. *Physics-Uspekhi*, 41(5):469–485, 1998.
- [87] Christer Z Bisgaard and Lars Bojer Madsen. Tunneling ionization of atoms. *American Journal of Physics*, 72(2):249–254, 2004.
- [88] Steeve Augst, David D Meyerhofer, Donna Strickland, and See-Leang Chin. Laser ionization of noble gases by coulomb-barrier suppression. *JOSA B*, 8(4):858–867, 1991.
- [89] Robert J Goldston and Paul Harding Rutherford. *Introduction to plasma physics*. CRC Press, 1995.
- [90] George B Arfken and Hans J Weber. *Mathematical methods for physicists*, 1999.
- [91] Carlo Benedetti, CB Schroeder, Eric Esarey, Francesco Rossi, and WP Leemans. Numerical investigation of electron self-injection in the nonlinear bubble regime. *Physics of Plasmas*, 20(10):103108, 2013.
- [92] D Umstadter, JK Kim, and E Dodd. Laser injection of ultrashort electron pulses into wakefield plasma waves. *Physical review letters*, 76(12):2073, 1996.
- [93] T Mehrling, J Grebenyuk, FS Tsung, K Floettmann, and J Osterhoff. Transverse emittance growth in staged laser-wakefield acceleration. *Physical Review Special Topics-Accelerators and Beams*, 15(11):111303, 2012.
- [94] Paul Andreas Walker, PD Alesini, AS Alexandrova, Maria Pia Anania, NE Andreev, I Andriyash, A Aschikhin, RW Assmann, T Audet, A Bacci, et al. Horizon 2020 eupraxia design study. In *Journal of Physics: Conference Series*, volume 874, 2017.
- [95] Eric Esarey, Jonathan Krall, and Phillip Sprangle. Envelope analysis of intense laser pulse self-modulation in plasmas. *Physical review letters*, 72(18):2887, 1994.
- [96] Eric Esarey, Phillip Sprangle, Jonathan Krall, and Antonio Ting. Self-focusing and guiding of short laser pulses in ionizing gases and plasmas. *IEEE Journal of Quantum Electronics*, 33(11):1879–1914, 1997.
- [97] Brigitte Cros. Laser-driven plasma wakefield: Propagation effects. *arXiv preprint arXiv:1705.10566*, 2017.
- [98] B Cros, C Courtois, G Matthieussent, A Di Bernardo, D Batani, N Andreev, and S Kuznetsov. Eigenmodes for capillary tubes with dielectric walls and ultraintense laser pulse guiding. *Physical Review E*, 65(2):026405, 2002.

- [99] Phillip Sprangle, Eric Esarey, Jonathan Krall, and G Joyce. Propagation and guiding of intense laser pulses in plasmas. *Physical review letters*, 69(15):2200, 1992.
- [100] E Esarey, A Ting, and P Sprangle. Optical guiding and beat wave phase velocity control in the plasma beat wave accelerator. In *AIP Conference Proceedings*, volume 193, pages 71–86. AIP, 1989.
- [101] DJ Spence and Simon Mark Hooker. Investigation of a hydrogen plasma waveguide. *Physical Review E*, 63(1):015401, 2000.
- [102] DJ Spence, Arthur Butler, and Simon Mark Hooker. Gas-filled capillary discharge waveguides. *JOSA B*, 20(1):138–151, 2003.
- [103] Arthur Butler, DJ Spence, and Simon Mark Hooker. Guiding of high-intensity laser pulses with a hydrogen-filled capillary discharge waveguide. *Physical Review Letters*, 89(18):185003, 2002.
- [104] Stefan Karsch, Jens Osterhoff, Antonia Popp, TP Rowlands-Rees, Zs Major, Matthias Fuchs, Benjamin Marx, Rainer Hörlein, Karl Schmid, Laszlo Veisz, et al. Gev-scale electron acceleration in a gas-filled capillary discharge waveguide. *New Journal of Physics*, 9(11):415, 2007.
- [105] CGR Geddes, Cs Toth, J Van Tilborg, E Esarey, CB Schroeder, J Cary, and WP Leemans. Guiding of relativistic laser pulses by preformed plasma channels. *Physical review letters*, 95(14):145002, 2005.
- [106] Eric Esarey, Phillip Sprangle, Jonathan Krall, and Antonio Ting. Overview of plasma-based accelerator concepts. *IEEE Transactions on Plasma Science*, 24(2):252–288, 1996.
- [107] Bradley Allan Shadwick, Carl B Schroeder, and Eric Esarey. Nonlinear laser energy depletion in laser-plasma accelerators. *Physics of Plasmas*, 16(5):056704, 2009.
- [108] T Katsouleas. Physical mechanisms in the plasma wake-field accelerator. *Physical Review A*, 33(3):2056, 1986.
- [109] P Sprangle, B Hafizi, JR Penano, RF Hubbard, A Ting, A Zigler, and TM Antonsen Jr. Stable laser-pulse propagation in plasma channels for gev electron acceleration. *Physical review letters*, 85(24):5110, 2000.
- [110] Wei Lu, M Tzoufras, C Joshi, FS Tsung, WB Mori, J Vieira, RA Fonseca, and LO Silva. Generating multi-gev electron bunches using single stage laser

- wakefield acceleration in a 3d nonlinear regime. *Physical Review Special Topics-Accelerators and Beams*, 10(6):061301, 2007.
- [111] T Garvey et al. Construction of the alpha-x photoinjector cavity. In *EPAC*, volume 6, page 1277.
- [112] Bruce E Carlsten. New photoelectric injector design for the los alamos national laboratory xuv fel accelerator. *Nuclear Instruments and Methods in Physics Research Section A: Accelerators, Spectrometers, Detectors and Associated Equipment*, 285(1-2):313–319, 1989.
- [113] Jun Zhu. *Design Study for Generating Sub-femtosecond to Femtosecond Electron Bunches for Advanced Accelerator Development at SINBAD*. PhD thesis, Hamburg U., Dept. Math., 2017.
- [114] Robert Joel England. *Longitudinal shaping of relativistic bunches of electrons generated by an RF photoinjector*. University of California, Los Angeles, 2007.
- [115] K Wang, E Baynard, C Bruni, K Cassou, V Chaumat, N Delerue, J Demailly, D Douillet, N El Kamchi, D Garzella, et al. Longitudinal compression and transverse matching of electron bunch for external injection lpwa at esclap. *Nuclear Instruments and Methods in Physics Research Section A: Accelerators, Spectrometers, Detectors and Associated Equipment*, 2017.
- [116] Ji Qiang, Steve Lidia, Robert D Ryne, and Cecile Limborg-Deprey. Three-dimensional quasistatic model for high brightness beam dynamics simulation. *Physical Review Special Topics-Accelerators and Beams*, 9(4):044204, 2006.
- [117] Martin Dohlus and Torsten Limberg. CSRtrack: faster calculation of 3d csr effects. In *Proceedings of the 2004 FEL Conference*, pages 18–21, 2004.
- [118] Martin Reiser. *Theory and design of charged particle beams*. John Wiley & Sons, 2008.
- [119] Timon Johannes Mehrling. Theoretical and numerical studies on the transport of transverse beam quality in plasma-based accelerators. 2014.
- [120] XL Xu, JF Hua, YP Wu, CJ Zhang, F Li, Y Wan, C-H Pai, W Lu, W An, P Yu, et al. Physics of phase space matching for staging plasma and traditional accelerator components using longitudinally tailored plasma profiles. *Physical review letters*, 116(12):124801, 2016.

- [121] BS Paradkar, B Cros, P Mora, and G Maynard. Numerical modeling of multi-gev laser wakefield electron acceleration inside a dielectric capillary tube. *Physics of Plasmas*, 20(8):083120, 2013.
- [122] Patrick Mora and Thomas M Antonsen, Jr. Kinetic modeling of intense, short laser pulses propagating in tenuous plasmas. *Physics of Plasmas*, 4(1):217–229, 1997.
- [123] Sepehr Morshed, TM Antonsen, and JP Palastro. Efficient simulation of electron trapping in laser and plasma wakefield acceleration. *Physics of Plasmas*, 17(6):063106, 2010.
- [124] E Baynard, C Bruni, K Cassou, V Chaumat, N Delerue, J Demailly, D Douillet, N El Kamchi, D Garzella, O Guilbaud, et al. Modeling of laser-plasma acceleration of relativistic electrons in the frame of esculap project. *Nuclear Instruments and Methods in Physics Research Section A: Accelerators, Spectrometers, Detectors and Associated Equipment*, 2018.
- [125] Alexander Roth. *Vacuum technology*. Elsevier, 2012.
- [126] Ke Wang, C Bruni, K Cassou, V Chaumat, N Delerue, D Douillet, N El Kamchi, S Jenzer, V Kubytskyi, P Lepercq, et al. A start to end simulation of the laser plasma wakefield acceleration experiment at esculap. In *Journal of Physics: Conference Series*, volume 1067, page 042013. IOP Publishing, 2018.
- [127] Xiangkun Li, Phu Anh Phi Nghiem, and Alban Mosnier. Toward low energy spread in plasma accelerators in quasilinear regime. *Physical Review Accelerators and Beams*, 21(11):111301, 2018.
- [128] Eugene Hecht. *Optics*. Pearson Education, 2016.
- [129] F Gori. Flattened gaussian beams. *Optics Communications*, 107(5-6):335–341, 1994.
- [130] Philip M Morse and Herman Feshbach. Methods of theoretical physics. *American Journal of Physics*, 22(6):410–413, 1954.

**Titre :** Étude d'un accélérateur à champ de sillage laser-plasma avec un faisceau d'électrons de 10 MeV injectés depuis un photoinjecteur

**Mots clés :** Accélérateur laser-plasma, compression de paquet d'électrons, transport de faisceau d'électrons, simulations du début à la fin, capillaire diélectrique creux

**Résumé :** Nous étudions l'accélération d'un faisceau d'électrons provenant d'un photoinjecteur RF lorsque celui-ci est injecté dans le champ électrique à très fort gradient créé par un laser de forte puissance dans un plasma. Dans cette thèse la configuration d'une telle expérience est étudiée et des simulations du début à la fin sont présentées. Étant donné qu'un faisceau ultra-court d'électrons (quelques femto secondes) est nécessaire pour atteindre une faible dispersion en énergie dans le plasma, le faisceau d'électrons de 10 MeV provenant du photoinjecteur est comprimé en deux étapes. Le premier étage utilise une chicane coudée qui comprime le paquet d'électrons jusqu'à une durée de 69fs, puis un deuxième étage qui utilise la méthode de regroupement par différence de célérité dans le plasma et qui comprime le paquet jusqu'à 4 fs avant qu'il ne soit accéléré. Le paquet d'électrons est comprimé transversalement avant d'être injecté dans le plasma. Le paquet d'électrons est focalisé transversalement avant d'être injecté dans le plasma. Une longue cellule plasma est utilisée pour créer le plasma en commençant plusieurs longueurs de Rayleigh avant

le plan focal du laser, ce qui permet un regroupement par différence de célérité dans la première partie du plasma avec des contraintes relâchées sur la taille transverse du paquet d'électrons. La cellule plasma s'étend plusieurs longueurs de Rayleigh après le plan focal du laser pour supprimer la divergence angulaire du paquet d'électrons. Nous démontrons que le paquet d'électrons à la sortie du plasma a une énergie de plus d'une centaine de MeV avec une émittance plus petite que 1  $\mu\text{m}$ , une charge plus grande que 7pC et une dispersion en énergie plus petite que 1.5% (largeur à mi-hauteur). Pour étendre la longueur d'accélération nous avons étudié le guidage du laser par un capillaire diélectrique creux et les résultats montrent que même dans le cas optimal le profile Gaussian usuel d'un laser n'est pas optimal, principalement à cause de la diffraction du laser sur les bords à l'entrée du capillaire. Un profile gaussian aplati est donc suggéré pour supprimer cette diffraction et il est montré que dans ce cas les électrons peuvent être accélérés sur plus de 10 longueurs de Rayleigh.

**Title :** Design study of a Laser Plasma Wakefield Accelerator with an externally injected 10 MeV electron beam coming from a photoinjector

**Keywords :** Laser Plasma Wakefield Accelerator, electron bunch compression, electron beam transport, start to end simulations, hollow dielectric capillary

**Abstract :** The acceleration of an externally injected 10 MeV electron bunch coming from a RF photoinjector in a high gradient electric field excited in a plasma by a high power laser is studied. In this thesis the configuration of such an experiment is studied and start to end simulations are presented. As an ultrashort electron bunch (several femtoseconds) is required to maintain a low energy spread beam in the plasma, the 10 MeV electron bunch coming from the photoinjector is compressed in two stages. The first stage is realized using a dogleg chicane which compresses the electron bunch to 69 fs, the second stage is realized with velocity bunching in the plasma that further compresses the electron bunch to 3 fs before efficient acceleration. The electron bunch is transversely focused with a solenoid before being injected into the plasma. A long cell is used to create a plasma starting several Rayleigh lengths before the laser focal

plane, allowing the velocity bunching in the first part of the plasma and relaxing constraints on the transverse bunch size. The cell extends several Rayleigh lengths after the laser focal plane to suppress the angular divergence of the electron bunch. We demonstrate that the electron bunch at the exit of the plasma has an energy of more than one hundred MeV, with an emittance smaller than 1  $\mu\text{m}$ , a charge greater than 7 pC and a FWHM energy spread smaller than 1.5%. To extend the acceleration section, the guiding of the laser beam with a hollow dielectric capillary is studied, the results show that even in the best matching conditions, the usual laser Gaussian transverse profile is not optimum, mainly because of the diffraction of the laser on the edges at the entrance of the capillary, a flattened Gaussian laser profile is then suggested to suppress this diffraction and the electrons can be accelerated over more than ten Rayleigh lengths.

